UNIVERSITY OF
BIRMINGHAM

Mixed Anion Complex Hydrides for Hydrogen Storage

by

Philip A. Chater

Supervisor: Dr Paul A. Anderson

A thesis submitted to The University of Birmingham for
the degree of Doctor of Philosophy

The School of Chemistry
College of Engineering and Physical Sciences
The University of Birmingham

December 2009

To Zo

Abstract

The first examples of a new class of mixed anion complex hydride have been synthesised and characterised. The structures of three amide-borohydride complex hydrides of lithium and sodium, $Li_4BH_4(NH_2)_3$, $Li_2BH_4NH_2$ and $Na_2BH_4NH_2$, have been solved by powder diffraction methods and characterised by infrared and Raman spectroscopy.

The thermal decomposition of these hydrogen rich materials was investigated and hydrogen was observed as the major gaseous product in all cases. Ammonia was observed as a minor product with the amount of ammonia release dependent on the sample composition and experimental set-up. Powder diffraction was used to identify the solid decomposition products and decomposition pathways are proposed. Two competing decomposition pathways, one forming metal hydride and boron nitride, the other forming metal nitridoborate, were identified for the lithium system and suggested for the sodium system.

In-situ and *ex-situ* powder diffraction, differential scanning calorimetry and temperature programmed desorption were used to investigate the lithium amide-borohydride system in detail and a phase diagram was proposed. The reactions of metal hydrides with $Li_4BH_4(NH_2)_3$ were tested and were found to reduce the amount of ammonia released. A reversible hydrogen storage reaction was observed upon reaction with magnesium hydride, which was investigated with gravimetric methods and *ex-situ* powder diffraction to elucidate the reaction pathway.

Acknowledgements

There are many to whom I owe a great deal of thanks. First and foremost is my supervisor, Paul Anderson, who's help and guidance throughout this PhD has been invaluable.

Many thanks to all members of Paul's group. Thanks to Jim Prendergast (for being there from day one), Martin Viertelhaus, Matt Turnbull (for oh so many things!), Alvaro Mayoral Garcia, Ian Evans, Alex Kersting, David Hewett, Chao Zhao (aka Ivan), Tom Carey and Heather O'Brien.

Thanks to the rest of 5th floor Chemistry, past and present, for help and entertainment (and Tom Marsh).

Thanks to Simon Johnson for first suggesting a PhD in the first place and for much help along the way. Many thanks to Bill David for many opportunities, valuable discussions and for introducing me to Topas.

Many thanks for all of the Metallurgy and Materials departement, especially David Book for generous provision of equipment and Allan Walton, Vicky Mann and Dan Reed (quite literally couldn't have done it without your help!).

Thanks to the excellent beamline scientists Andy Fitch and Irene Margiolaki at ESRF and Ron Smith and Richard Ibberson at ISIS.

Finally, thanks to all of those who have helped on a personal level; Dan Wilson for putting up with a rather uncommunicative person sitting on the sofa with a laptop, my brother Mark and my parents for unwavering support and lastly, but by no means least, Zoe - thank you for being there with me throughout!

Contents

Chapter 1

Introduction

There is an urgent need to find a replacement for fossil fuels, which we are heavily reliant upon for the provision of the vast majority of our energy needs. Fossil fuels are very convenient sources of energy and supply almost all of our mobile energy needs in the form of petroleum. As supplies of fossil fuels dwindle, the requirement for a replacement energy vector becomes increasingly pressing. Whether hydrogen can fill that role depends on whether technical challenges associated with the production, storage and use of hydrogen can be overcome [1]. Of these challenges, the problem of the storage of hydrogen remains arguably the most challenging.

World energy demand has risen at an alarming rate since the industrial revolution [2]. In a pre-industrial age all of our energy requirements were met by plant life *via* photosynthesis. Plants provided food for humans and animals (both a source of food and transport) and solid fuel to burn for warmth. Upon the advent of the steam engine the amount of physical work done was no longer proportional just to the amount of humans or animals alive, and fuel (in the form of coal) could be used to increase productivity. Since the industrial revolution world energy consumption has continued to increase, mostly fuelled by fossil fuels. The use of fossil fuels releases CO_2 into the atmosphere that was previously locked away underground. CO_2 is a greenhouse gas and the increase in the amount of atmospheric CO_2 caused by the burning of fossil fuels has been linked with global

climate change [3].

Hydrogen already supplies us with almost all of our energy *via* nuclear fusion in the sun. This energy can be harnessed directly *via* solar cells or solar furnaces, or in the form of photosynthesis (either directly as biofuels or indirectly by the fossilisation of plant life from millions of years ago). It is important to note that the amount of energy reaching Earth from the sun remains relatively constant. Harnessing enough of this energy to meet our demands remains challenging. In using fossil fuels we are utilising the sun's energy stored millions of years ago in plant matter. Once fossil fuel resources are depleted we will have to return to using the energy from the sun in real-time, as we did in pre-industrial times, or become increasingly reliant on energy from nuclear fission/fusion. As such, we are forced to become more ingenious in the ways in which the sun's energy can be harnessed and used in an efficient manner.

1.1 Hydrogen Production

Hydrogen is by far the most abundant element in the known universe. It is very common on Earth in the form of its oxidation product, H_2O, and in the various hydrocarbons that make up the planet's living matter. The gaseous elemental form, which can be used as a fuel, is not available and therefore hydrogen must first be synthesised if it is to be used [4].

The majority of the hydrogen produced at present is made from fossil fuels *via* steam reformation and the water gas shift reactions:

$$\text{-}(CH_2)\text{-}_n + H_2O \rightarrow CO + (n+1)H_2 \tag{1.1}$$

$$CO + H_2O \rightarrow CO_2 + H_2 \tag{1.2}$$

The use of fossil fuels in this reaction, and the net release of CO_2, means that hydrogen produced in this fashion meets neither the requirements for independence from fossil fuels or the need to reduce CO_2 emissions. In order for hydrogen

production to be described as sustainable it must be made using an essentially limitless energy source and without the net increase in the amount of CO_2, or other harmful by-products, released.

Electrolysis

The electrolysis of water to produce hydrogen and oxygen is potentially the cleanest way of synthesising hydrogen, although this depends on the source of electricity. The source of electricity is connected to two electrodes, typically made of an inert metal, which are placed in the water. Hydrogen is produced at the negative cathode and oxygen is produced at the anode.

$$2H^+_{(aq)} + 2e^- \rightarrow H_{2(g)} \tag{1.3}$$

$$2H_2O_{(l)} \rightarrow O_{2(g)} + 4H^+_{(aq)} + 4e^- \tag{1.4}$$

This is not a thermodynamically favourable process and as such an electrical potential must be applied. An electrolyte is introduced to the water to increase the rate of electrolysis. The typical efficiency achievable for electrolysis is around 65% [5], although efficiencies reaching 85% are possible [6].

Electrolysis using electricity from renewable energy sources such as photovoltaics, wind turbines, hydroelectricity and geothermal power provide potentially limitless sources of 'green' hydrogen. Electricity produced from nuclear power addresses the problem of CO_2 release, but produces harmful by-products in the form of radioactive waste. Although not strictly renewable because of the rare nature of the nuclear isotopes required for nuclear fission, nuclear power has the greatest potential to replace fossil fuel based sources in the short to mid-term and meet our growing energy demands.

Thermal Production

The direct thermal dissociation of H_2O to form H_2 and O_2 is thermodynamically a highly unfavourable process. Temperatures in excess of 2000°C are required to

achieve this, and the resultant gases need to be separated at these temperatures if the hydrogen produced is to be used. Solar furnaces that focus large amounts of light energy from the sun onto a small area have been designed that are capable of achieving the temperatures required in a renewable fashion [7].

Bio-hydrogen

Hydrogen can be produced from biological matter in two main ways: gasification and fermentation. Gasification is essentially the same process as the extraction of hydrogen from fossil fuels. The biomass is thermally broken down to H_2, CO and CH_4 to which steam is added to ultimately produce H_2 and CO_2. Although biomass gasification releases CO_2, it is CO_2 that was absorbed by the plant material during photosynthesis, and as such the process of biomass production followed by gasification is described as CO_2 neutral.

Many bacteria and algae also produce small amounts of hydrogen alongside the majority product, oxygen. The anaerobic fermentation of biomass in the absence of light favours hydrogen production [8, 9]. Suitable biomass can be fed into a reactor containing an appropriate bacterium or algae which then can digest it to form hydrogen. The digestion process also produces CO_2. However, the ability to use 'low quality' biomass such as waste products and sewage makes this process doubly attractive.

1.2 Hydrogen as a Fuel

The use of hydrogen as a fuel follows an observed trend away from carbon based fuels like coal and oil to more energy dense, hydrogen rich fuels like natural gas [2]:

$$C_{(s)} \rightarrow \text{-}(CH_2)\text{-}_{n\,(l)} \rightarrow CH_{4(g)} \rightarrow H_{2(g)} \tag{1.5}$$

Chemical potential energy is the energy associated with valence electrons in atoms and molecules, and their potential to form more stable arrangements upon re-

action. Hydrogen is an attractive source of chemical potential energy as it is made up of only one proton and one electron, giving it the best ratio of valence electrons available for reaction per mass [10].

Once produced, hydrogen is the cleanest burning fuel, with water being the only combustion product when burnt in oxygen. It is a very energy rich fuel, with a lower heating value[†] (LHV, 120.1 MJ kg^{-1}) three times that of petroleum (42.5 MJ kg^{-1}) [11]. The chemical potential of hydrogen can either be harnessed by combustion in an internal combustion engine (ICE) to produce mechanical power, in the same way that petroleum is currently used, or electrochemically using a fuel cell to produce electrical power.

1.2.1 Hydrogen Internal Combustion Engines

The use of hydrogen in an internal combustion engine is not a new idea, with the first ICE produced, designed and built by François Isaac de Rivaz of Switzerland in 1807, designed to run on a mixture of hydrogen and oxygen [12]. Hydrogen gas can be used directly in a modern petroleum internal combustion engine with relatively minor modifications, such as the use of a higher piston compression ratio and reduction resistant oil as a lubricant, as well as an exhaust system that can withstand water vapour [13].

ICEs are a very well established technology, with many years of refinement in reliability and efficiency. Despite many improvements, the efficiency of ICEs as energy conversion devices is fundamentally limited by thermodynamics. In an ICE, combustion of a fuel-air mix results in an expansion of gas which is used to do work. According to Carnot's theorem the efficiency of no such process may exceed that of a Carnot cycle. The maximum theoretical efficiency of a Carnot cycle is limited by the ratio of the combustion temperature of the fuel to the

[†]The lower heating value for a fuel is the amount of heat released upon combustion after returning the combustion products to 150°C. This value discounts the latent heat of vaporisation of any water produced, which is typically of no practical use. For hydrogen, the LHV is 15.4% less than the higher heating value (HHV), which includes all of the energy of the combustion reaction.

temperature of the exhaust gas, which typically gives a theoretical efficiency of around 40%, which has been achieved in modern diesel engines. Relatively few car manufacturers have investigated hydrogen ICEs. Out of the major automobile companies, only Mazda Motor Corporation and BMW maintain an active research programme, both of which rely on hydrogen stored at high pressure.

1.2.2 Hydrogen Fuel Cells

Fuel cells are electrochemical energy conversion devices, where the chemical potential of a reaction is used to drive an electrical current around a circuit. There are many types of fuel cells, which are characterised by the electrolyte used: alkaline, phosphoric acid, molten carbonate, solid oxide and polymer membrane electrolytes are the most common. Fuel cells produce electricity continuously, as long as the fuels are supplied. The use of fuel cells with hydrogen from a sustainable source is seen by many as the ultimate in clean energy usage [14].

Polymer electrolyte membrane fuel cells, also known as proton exchange membrane (PEM) fuel cells, have very fast start-up times. They can operate with high efficiency at temperatures around 65°C [15], making them particularly attractive for mobile applications. Hydrogen gas is supplied at the anode, where a catalyst (typically platinum) splits the hydrogen into its component protons and electrons. The polymer membrane allows only the protons to permeate through it, forcing the electrons to travel along an external circuit providing electrical power. Air containing oxygen is flowed past the cathode. The electrons from the circuit recombine with the protons and oxygen at the cathode to form water. In practice many PEM fuel cells are used in combination to produce a fuel cell stack so that higher power densities can be achieved. Many automotive manufacturers have produced cars containing PEM fuel cells such as Honda's FXC Clarity (2007) and General Motors' Chevrolet Equinox Fuel Cell (2009).

PEM fuel cells are adversely affected by the presence of contaminants in the hydrogen supply [16]. The presence of 30 ppm NH_3 in the hydrogen supply has

been shown to cause a rapid drop in fuel cell performance which could not be completely recovered once the NH_3 was removed.

1.2.3 The Hydrogen versus Battery Debate

Hydrogen is not the only technology suggested as a replacement for fossil fuels. As mentioned previously, hydrogen has to be synthesised, typically by electrolysis. The hydrogen is then converted back to electrical energy in a fuel cell for use in mobile applications. These energy conversions significantly reduce the efficiency of the system compared with using the electricity directly in batteries [17]. The energy density, efficiency and cycling lifetime of batteries have significantly improved in recent years and lithium ion batteries have been used to power automobiles such as the Tesla Roadster (2006).

The huge advantage of batteries is that the infrastructure for implementation is already in place, whereas moving towards hydrogen as a fuel will require significant investment. The problem with batteries is that, unlike a fuel cell which can run continuously given a sufficient fuel source, batteries require recharging which can take many hours. In practice, most fuel cell vehicles may use a combination of batteries and a fuel cell to meet the energy demands associated with automotive transport [18].

1.3 Hydrogen Storage Methods

The storage of hydrogen involves the reduction in volume of hydrogen from its natural state as a diatomic gas, which occupies a massive 11 m^3 kg^{-1} at standard temperature and pressure, to a more usable volumetric density. Increases in volumetric density can easily be achieved by various methods such as compression or liquefaction. However this is always at the expense of gravimetric density. To clarify, the volumetric density of hydrogen can easily be increased through compression, but the pressure vessel required to store hydrogen at high pressures

reduces the gravimetric capacity of the system. An ideal hydrogen storage system is a compromise between increasing the volumetric capacity of the system while maintaining a usable gravimetric hydrogen capacity.

There are a number of methods that have been investigated for hydrogen storage which can broadly be separated into two groups: the storage of molecular or atomic/ionic hydrogen. A hydrogen storage system for molecular hydrogen increases the volumetric density by physical compression of the gas, by liquefaction or by adsorption on surfaces. Atomic hydrogen can be stored by reaction of hydrogen gas to form metal hydrides or complex hydrides.

1.3.1 Compressed Gas Storage

Storage of hydrogen at high pressure is currently the most widely used and understood technology. Many of the technological and safety problems associated with the storage and handling of the gas at high pressure have been resolved with infrastructure requirements for transport and handling of hydrogen already in existence. The most common high pressure vessels are made from steel, and hydrogen can be stored at a pressure of 200 bar. The mass of steel required means that only approximately 1 wt% of hydrogen can be stored [4] and increasing to higher pressures means that even thicker pressure vessel walls are required.

The use of light-weight high-density carbon fibre or composite gas cylinders has been developed, which can store hydrogen at pressures of up to 1000 bar giving a theoretical hydrogen capacity of 10 wt% [4]. Attaining such high hydrogen pressures requires a large amount of physical work to be done on the gas in terms of compression, which is energy that cannot be reclaimed upon using the gas [19]. The handling of gas at such high pressures introduces a series of engineering challenges as the gas pressure leaving the pressure vessel must be stepped down in pressure so that it can be used. There are also safety concerns with storing gas at very high pressures. A range of hybrid pressure vessels which combine metal hydrides with a high pressure tank have also been proposed [20].

1.3.2 Cryogenic Liquid Storage

The condensation of hydrogen into a liquid requires cryogenic temperatures of below −252°C. This low temperature must be maintained in order to minimise loss of hydrogen through boil-off. Cryogenic hydrogen stores are designed to minimise heat flow from the surroundings to the hydrogen within. The process of liquefaction is very energy intensive, requiring approximately 30% of the chemical potential energy of the hydrogen liquefied [21]. All of the components used for the delivery and storage of hydrogen must also be cooled which incurs a further energy cost. Because of this, liquefaction is not a very energy efficient method of hydrogen storage.

1.3.3 Physisorption

Like all gases, hydrogen will adsorb onto solid surfaces *via* attractive Van der Waals-type interactions. The energy of these interactions is typically very low (2-20 kJ mol^{-1} H_2 [2]), and thermal energy at room temperature is enough to desorb the majority of hydrogen from the surface. Low temperatures (typically $N_{2(l)}$, boiling point −196°C, is used as coolant) are used to maximise this interaction.

The strongest binding of hydrogen will occur when the hydrogen is bound in a single layer on the surface; subsequent layers will be less tightly bound. Materials for hydrogen storage *via* physisorption are typically very high surface area solids such as zeolites [22], high surface area carbon [23], metal-organic frameworks (MOFs) [24] or polymers of intrinsic microporosity (PIMs) [25]. Materials such as zeolites and MOFs have the potential to increase the strength of the hydrogen binding by the inclusion of metal ions within the structures. Purely surface interactions can give rise to hydrogen capacities of approximately 1.6 wt% [2, 22], whereas gravimetric capacities of 6.7 wt% have been reported for MOFs where binding to metal centres is believed to increase the hydrogen capacity [21].

1.3.4 Metallic Hydrides

Many metals and alloys reversibly react with hydrogen to produce metal hydrides. Alkali metals tend to form stoichiometric ionic hydrides, such as NaH, whereas transition metal hydrides tend to form variable composition interstitial hydrides of variable composition, such as $PdH_{0.6}$ [26]. Hydrogen gas is dissociated at the metal surface and diffuses into the metal. The reversible transition back to the metal can either be achieved by increasing the temperature or by reducing the pressure.

The interaction of hydrogen with a metal to form an interstitial hydride can be described in terms of a pressure-composition isotherm, as illustrated in figure 1.1 [2]. At low pressures hydrogen dissolves in low concentrations into the metal lattice forming a solid solution (MH_x in figure 1.1). Increasing the pressure causes more hydrogen to become absorbed, leading to the formation of an ordered hydride phase (MH_n in figure 1.1). A plateau region forms where MH_x and MH_n coexist. Here the composition of the metal hydride can be changed radically with minor changes in the pressure or temperature. This is the region of interest for hydrogen storage applications. Above a certain temperature (T_c in figure 1.1) the plateau behaviour is lost and there a continuous transition between MH_x and MH_n.

Metallic hydrides have very high volumetric hydrogen densities, although the presence of relatively heavy metals means that gravimetric capacities of only a few wt% are typical. For example, $LaNi_5H_{6.5}$ is an excellent hydrogen store, releasing all of its hydrogen at H_2 pressures below 2 bar, but only contains 1.5 wt% H_2. Moving to lighter elements improves the gravimetric content, for example Mg_2NiH_4 contains 3.6 wt%, but requires temperatures above 280°C for hydrogen release. Incorporation of transition metal additives by mechanical alloying has been shown to improve this temperature slightly [27].

Magnesium hydride offers the highest gravimetric hydrogen capacity of the

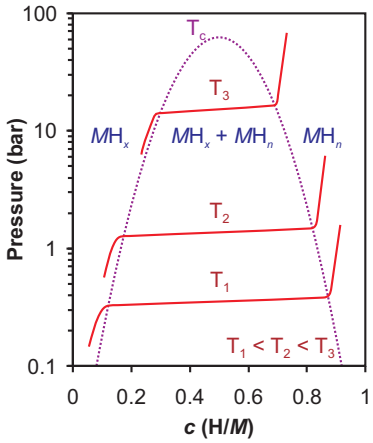

Figure 1.1: A typical pressure-composition(c)-temperature(T) plot for a metal hydride.

reversible hydrides (7.7 wt%). However, it suffers from impractically slow rates of de/rehydrogenation [28]. Attempts to improve the kinetics by inclusion of precious metals [29] and chemical activation with $LiBH_4$ [30] have shown some improvement, but temperatures of around 300°C are still required for appreciable rates.

1.3.5 Complex Hydrides

The term complex hydride is generally given to materials where hydrogen is covalently bonded to a central atom in an anion [31]. These ionic hydrides containing ions such as AlH_4^- (aluminium hydrides), BH_4^- (borohydrides) and NH_2^-/NH^{2-} (amides/imides) have amongst the highest gravimetric hydrogen capacities known. Complex hydrides of most alkali and alkaline-earth metals, as well as of many transition metals, are known [32, 31].

Aluminium Hydrides

Aluminium hydrides[†] of Li and Na can be synthesised from the elements or by the reaction of the metal hydride with aluminium halides in solution [33]. $LiAlH_4$

[†]Aluminium hydrides are sometimes referred to as 'alanates'.

and $NaAlH_4$ have high gravimetric hydrogen densities (10.5 wt% and 7.4 wt% respectively) and decompose with the release of hydrogen at 201°C and 265°C respectively, in a two stage process;

$$3MAlH_4 \rightarrow M_3AlH_6 + 2Al + 3H_2 \rightarrow 3MH + 3Al + 9/2H_2. \tag{1.6}$$

High kinetic barriers to the de/rehydrogenation reactions limited the use of aluminium hydrides as hydrogen storage materials until Bogdanović and Schwickardi [34] demonstrated that doping with Ti vastly improved the kinetics of reversible storage in $NaAlH_4$. Hydrogen was released from 150°C and rehydrogenation was achieved in 5 hours at 170°C and a hydrogen pressure of 152 bar. Further improvements have been achieved through the ball milling of aluminium hydrides with various transition metal chlorides [35]. Similar effects have been noted for $LiAlH_4$ [36]. Cycling studies of Ti-doped $NaAlH_4$ have shown that a reversible capacity of 3-4 wt% is achievable [37].

Borohydrides

Borohydrides, also known as tetrahydroborates,[‡] have been known for many years [38, 39] and are widely used in organic synthesis as powerful reducing agents. Interest in their potential use as hydrogen storage materials was sparked in 2003 by Züttel *et al.* [40], who demonstrated a reduction in the temperature of hydrogen release from $LiBH_4$ upon the introduction of SiO_2.

Borohydrides can be synthesised by the reaction of organo-metal solutions [38] or metal hydrides [41] with diborane gas:

$$2MH_x + xB_2H_6 \rightarrow 2M(BH_4)_x \tag{1.7}$$

The direct synthesis from the elements (or using the metal hydride) has also been claimed at high temperatures (550–700°C) and hydrogen pressures of 30–150 bar (reference 10 in [40]).

[‡]Borohydrides are, to a lesser extent, sometimes referred to as 'boronates'.

The majority of transition metal borohydrides are synthesised by the metathesis of the transition metal chloride with $LiBH_4$ or $NaBH_4$ in THF or diethyl ether [39]. Mechanochemical syntheses have also been reported where high energy ball milling is used to induce the same metathesis in the solid state [42]. Mixed metal borohydrides have also been prepared by thermal [43] and mechanochemical [44] means.

Of all the readily accessible borohydrides, $LiBH_4$ has the highest gravimetric hydrogen content (18.5 wt%)† and has received possibly the most attention. $LiBH_4$ decomposes above 370°C [45] to give LiH as the only crystalline product, suggesting the reaction:

$$2LiBH_4 \rightarrow 2LiH + 2B + 3H_2 \uparrow \text{[46]} \tag{1.8}$$

giving a theoretical hydrogen capacity of 13.9 wt%. The decomposition is exothermic with the standard reaction enthalpy, ΔH_r^0, calculated to be 66.6 kJ mol^{-1} and observed experimentally to be 74 kJ mol^{-1} [45]. Computational studies on the decomposition pathway proposed the presence of various intermediate species [47, 48] and Raman spectroscopy suggested the presence of $[B_{12}H_{12}]^{2-}$ upon decomposition of $LiBH_4$ [49]. Nuclear magnetic resonance spectroscopy studies later confirmed the presence of $[B_{12}H_{12}]^{2-}$ upon the decomposition of various borohydrides [50] suggesting that the above proposed reaction (equation 1.8) is only part of the story. The exact mechanism of decomposition remains the subject of some debate. The hydrogenation of decomposed $LiBH_4$ has been demonstrated under the relatively harsh conditions of 600°C and a hydrogen pressure of 350 bar [51]. A reversibility of 8.3 wt% hydrogen (60% of the theoretical capacity) has been demonstrated within 200 minutes [45].

Although $LiBH_4$ has limited reversibility, it has been shown that the introduction of MgH_2 gives an alternative decomposition pathway:

$$2LiBH_4 + MgH_2 \leftrightarrow 2LiH + MgB_2 + 4H_2 \tag{1.9}$$

†Only $Be(BH_4)_2$, which is toxic and readily sublimes at room temperatures [32], has a higher gravimetric content of 20.9 wt%.

which has more favourable thermodynamics [52] while maintaining a high theoretical gravimetric hydrogen capacity of 11.6 wt%. Hydrogen is released in this reaction from 270°C, which is significantly below that observed for $LiBH_4$. The reaction pathway was shown to proceed by the decomposition of MgH_2 to form Mg, which in turn reacted with $LiBH_4$ to form MgB_2 and LiH [53]. Hydrogenation equating to 6.5 wt% was observed at 330°C and 7 bar H_2 which increased to around 10 wt% at 400°C and 24 bar [52]. The reverse of reaction 1.9 has also been demonstrated for NaH and CaH_2 [54].

The thermal decomposition of a range of borohydrides has been investigated and a general inverse correlation between decomposition temperature and the electronegativity of the metal was established [55]. For mixed metal borohydrides, this relationship has been observed to hold for the average electronegativity of the metals [43, 56]. Not all borohydrides decompose with the release of hydrogen. Borohydrides with the lowest decomposition temperatures, such as $Zn(BH_4)_2$ (T_{dec} 85-140°C), decompose to the metal with the release of extremely flammable and toxic diborane [32, 42]. It has recently been suggested that the mechanism for hydrogen release from all borohydrides involves the release of diborane, the subsequent decomposition of which gives rise at higher temperatures to hydrogen and boron [57]. If this is proven to be the case, then working toward the lowering in temperature of borohydride decomposition must go hand in hand with the development of new catalysts for the decomposition of diborane.

Amides

Amides of the alkali metals are readily formed by the reaction of the molten metal with ammonia, from the metal-ammonia solution by the addition of an Fe_2O_3 catalyst or by the reaction of the metal hydride with ammonia [58]. In isolation, lithium amide decomposes with the release of ammonia gas to form lithium imide [59]:

$$2LiNH_2 \rightarrow Li_2NH + NH_3 \tag{1.10}$$

For this reaction it is not classed as a hydrogen storage material in isolation. In 2002, Chen *et al.* [60] reported that lithium nitride could absorb around 9.3 wt% hydrogen at moderate temperatures and pressures in a two step reaction:

$$Li_3N + 2H_2 \leftrightarrow Li_2NH + LiH + H_2 \leftrightarrow LiNH_2 + 2LiH \tag{1.11}$$

This reaction was found to be completely reversible and has the potential to release 10.4 wt% hydrogen. These reactions of $LiNH_2$ and Li_2NH with LiH were shown to release hydrogen in preference to ammonia. The first step, from lithium nitride, was found not to be readily reversible, with very slow hydrogen uptake and hydrogen release only at temperatures in excess of 320°C in a vacuum [60]. The amide-imide step:

$$LiNH_2 + LiH \leftrightarrow Li_2NH + H_2 \tag{1.12}$$

is readily reversible with favourable thermodynamics ($\Delta H = -45$ kJ mol^{-1} [60]) and desirable gravimetric hydrogen capacity (6.5 wt%). This reaction has been the subject of intensive study [61, 62, 63, 64, 65]. The hydrogen released was attributed to the "redox reaction" between $H^{\delta+}$ in $LiNH_2$ and $H^{\delta-}$ in LiH [61].

Mixed metal amide–hydride systems based on Li–Mg and Li–Ca have also been proposed [66]. The replacement of LiH in reaction 1.12 with MgH_2 was found to give a mixed Li–Mg imide, and reversibility was proven at 200°C and a hydrogen pressure of 35 bar [67]. Other investigations demonstrated that the reversible reaction involved magnesium amide and lithium hydride [66, 68, 69],

$$Mg(NH_2)_2 + 2LiH \leftrightarrow Li_2Mg(NH)_2 + 2H_2, \tag{1.13}$$

which had a lower reaction enthalpy than that of the pure lithium system ($\Delta H = -34$ kJ mol^{-1} [67]).

The equivalent Li–Ca system is summarised in equation 1.14. The reaction at 300°C starting from either Li or Ca amide resulted in the same mixed Li–Ca imide [70]. Significant hydrogen release approaching the theoretical maximum

gravimetric capacity was observed at 200°C, although at these lower temperatures separate imides Li_2NH and CaNH are formed rather than the mixed imide [71]. Partial reversibility has also been demonstrated [71].

$$2LiNH_2+CaH_2 \rightarrow Li_2NH+CaNH+2H_2 \rightarrow Li_2Ca(NH)_2+2H_2 \leftrightarrow Ca(NH_2)_2+2LiH \tag{1.14}$$

1.4 Hydrogen Storage Targets

The use of hydrogen in a mobile application, such as vehicular transport, offers the greatest challenge towards system design. The criteria for a practical hydrogen store for mobile applications have been outlined by the U.S. Department of Energy [72]. The originally very optimistic targets have recently been superseded and current targets for the gravimetric capacity of a hydrogen storage system are 5.5 wt% in the year 2015 with an ultimate goal of 7.5 wt%. Targets have also been set for the hydrogen delivery temperature of -40 to 85°C and delivery pressures of 5 bar for fuel cell applications (35 bar for ICE applications). Recharging would ideally take place on-board within 2.5 minutes. Not only must the system be completely and rapidly reversible, it must also be capable of 1500 de/rehydrogenation cycles and meet safety/toxicity requirements. On top of all of these demands, any hydrogen storage system must also be of low enough cost for widespread acceptance into the marketplace.

It should be noted that these criteria are for the entire hydrogen storage system. This includes the balance of plant, which is the general term for all of the other systems, components and structures, such as pressure regulation and heat exchangers, that are required for any hydrogen storage system to be used in conjunction with a fuel cell or ICE. It is generally assumed that the inclusion of the balance of plant will, at least in the first incarnation of the technology, reduce the gravimetric capacity of any material that makes up the hydrogen store by half.

These targets constrain the nature of storage materials and systems that can be used in mobile applications. In order for a fuel cell or ICE to run on hydrogen, a constant supply of hydrogen is required at a pressure of at least 1 bar; somewhere in the range 5 - 20 bar is generally accepted. For a high pressure, low temperature (physisorption) store this means that 1 bar is the lowest limit of usable hydrogen in the system without addition of a compressor to supply the fuel cell or ICE. This limitation seriously reduces the hydrogen storage capacity reported for many systems such as MOFs and PIMs. In practice, more hydrogen may be removed by warming the tank. However, this will then incur a further energy cost in re-cooling the tank during the next refuelling. These types of materials may find application in stationary hydrogen stores where the materials demands are less stringent.

Similarly, for chemical hydrides, artificially high hydrogen capacities are frequently quoted by including all of the hydrogen in the material. This is misleading as typically it is very difficult to expel all of the hydrogen from chemical hydrides at moderate temperatures. A case in point is ammonia borane, NH_3BH_3, which contains an attractive 19.6 wt% hydrogen. Only 6.5 wt% of this hydrogen is readily released at moderate temperatures ($\approx$100°C), with the full 19.6 wt% not released until above 900°C. Also problems such as the release of undesirable side products (e.g. borazine in the case of ammonia borane) can reduce the amount of hydrogen released. This problem may be addressed by the introduction of selective catalysts. However, these are typically predominantly transition metal salts, which will further decrease the gravimetric capacity. Hydrogen capacities for chemical hydrides should be derived from the hydrogen releasing reaction, rather than the hydrogen content of the materials involved. This gravimetric capacity will then be reduced further in a hydrogen store once the balance of plant is included.

In summary, an ideal hydrogen storage system must have a high gravimetric (and volumetric) hydrogen capacity, release pure hydrogen at a temperature of

−40 to 85°C, rapidly rehydrogenate at moderate pressures, not degrade appreciably upon cycling and maintain a high efficiency of energy storage at a low cost. This is an extremely demanding set of criteria and one which no single system has met to date.

1.5 Thermodynamics and Hydrogen Storage

The relationship between the thermodynamic properties of a hydride and its hydrogen storage properties is an important one, which has been described in detail by Grochala and Edwards [32], a summary of which will be presented and discussed here. From the decomposition reaction of a metal hydride:

$$\mathrm{MH}_n \rightarrow \mathrm{M} + {}^{n}/_{2}\mathrm{H}_{2(\mathrm{g})} \tag{1.15}$$

and the corresponding thermodynamic description:

$$\Delta G^{\ominus}_{\mathrm{dec}} = \Delta H^{\ominus}_{\mathrm{dec}} - T\Delta S^{\ominus}_{\mathrm{dec}} \tag{1.16}$$

the behaviour of the hydride upon heating can be established. In this case, $\Delta H^{\ominus}_{\mathrm{dec}}$ is equal to the negative standard enthalpy of formation of the hydride, $\Delta H^{\ominus}_{\mathrm{f}}$. The entropy term is dominated by the gaseous evolution of molecular hydrogen so that:

$$\Delta S^{\ominus}_{\mathrm{dec}} \approx S(\mathrm{H}_2)^{\ominus} = 130.7 \text{ J K}^{-1}\mathrm{mol}^{-1} \tag{1.17}$$

which is the entropy change associated with the transformation of hydrogen from an ordered solid to a disordered gas. In order for the thermal decomposition of the hydride to proceed, the entropic contribution needs to overcome the enthalpic contribution. At a certain temperature, known as the formal decomposition temperature of the hydride, T_{dec}, the standard Gibbs enthalpy for the decomposition reaction (equation 1.15), $\Delta G^{\ominus}_{\mathrm{dec}}$, decreases below zero. In order for the thermal decomposition to proceed:

$$0 = \Delta H^{\ominus}_{\mathrm{dec}} - ({}^{n}/_{2})T_{\mathrm{dec}}S(\mathrm{H}_2)^{\ominus} \tag{1.18}$$

and so the formal decomposition temperature (in degrees Kelvin) can be shown to be:

$$T_{\mathrm{dec}} = \left(\frac{\Delta H^{\ominus}_{\mathrm{dec}}}{n}\right)\left(\frac{2}{S(\mathrm{H_2})^{\ominus}}\right) \tag{1.19}$$

where ${}^{\Delta H^{\ominus}_{\mathrm{dec}}}/_{n}$ is the negative enthalpy of formation of the hydride per hydrogen atom stored. From this it can be shown that in order to reach an equilibrium pressure of 1 bar at room temperature (27°C, 300 K) the ideal standard enthalpy of formation of the hydride per hydrogen atom stored can be estimated to be +19.6 kJ $\mathrm{mol_H}^{-1}$.

Although this is a very useful estimate, it by no means rules out systems that do not meet this criteria. If we now consider moving from equilibrium by changing the volume of the system, then:

$$\Delta G = -S\Delta T + V\Delta p \tag{1.20}$$

and

$$\Delta H = T\Delta S + V\Delta p \tag{1.21}$$

which are two of Gibbs' four differential equations derived from the first and second laws of thermodynamics [73]. From equation 1.20 at constant pressure:

$$\frac{\delta G}{\delta T} = -S \tag{1.22}$$

Differentiating with respect to the extent of the reaction, ξ, at constant temperature and pressure gives:

$$\frac{\delta}{\delta \xi}\left(\frac{\delta G}{\delta T}\right) = -\frac{\xi S}{\delta \xi} \tag{1.23}$$

which can be rearranged to:

$$\frac{\delta}{\delta T}\left(\frac{\delta G}{\delta \xi}\right) = -\frac{\xi S}{\delta \xi} \tag{1.24}$$

In equation 1.24, ${}^{\delta G}/_{\delta \xi}$ is the Gibbs function of reaction at constant temperature and pressure for equilibrium conditions and ${}^{\delta S}/_{\delta \xi}$ is the entropy of reaction under the same conditions, frequently symbolised as ΔG and ΔS respectively.

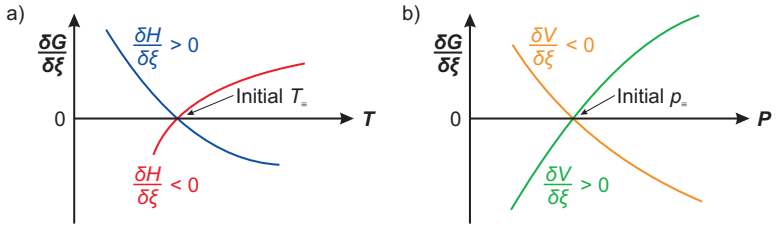

Figure 1.2: Schematic change in Gibbs function of reaction with changes in (a) temperature and (b) pressure for systems initially in equilibrium.

From equation 1.21 at constant pressure:

$$\delta S = \frac{\delta H}{T} \tag{1.25}$$

which, when combined with equation 1.24 gives:

$$\frac{\delta}{\delta T}\left(\frac{\delta G}{\delta \xi}\right) = -\frac{1}{T}\frac{\delta H}{\delta \xi} \tag{1.26}$$

For a system at a given temperature and pressure, it follows that in order for the reaction to advance further the condition is:

$$\frac{\delta G}{\delta \xi} < 0 \tag{1.27}$$

and for the reverse:

$$\frac{\delta G}{\delta \xi} > 0 \tag{1.28}$$

The effect on composition of altering the temperature at constant pressure is most easily predicted from a sketch of $^{\delta G}/_{\delta \xi}$ as a function of T, shown in figure 1.2(a).

From equation 1.26, when $^{\delta H}/_{\delta \xi} > 0$, i.e. an endothermic reaction, the slope of the curve in figure 1.2(a) is negative. $^{\delta G}/_{\delta \xi}$ becomes negative and decomposition proceeds when the temperature is increased, which therefore increases the entropy of the system. When $^{\delta H}/_{\delta \xi} < 0$, i.e. an exothermic reaction, the slope of the curve in figure 1.2(a) is positive. $^{\delta G}/_{\delta \xi}$ becomes positive, and decomposition proceeds, when the temperature is decreased. These observations gives the generalisation that higher temperatures favour higher enthalpy.

The effect of a pressure change on a system initially at equilibrium and constant temperature can also be deduced. From equation 1.20 at constant temperature:

$$\frac{\delta G}{\delta p} = V \tag{1.29}$$

Again differentiating with respect to the extent of the reaction, ξ, at constant temperature and pressure gives:

$$\frac{\delta}{\delta \xi}\left(\frac{\delta G}{\delta p}\right) = \frac{\delta V}{\delta \xi} \tag{1.30}$$

which can be rearranged to give:

$$\frac{\delta}{\delta p}\left(\frac{\delta G}{\delta \xi}\right) = \frac{\delta V}{\delta \xi} \tag{1.31}$$

which gives the rate of change of the Gibbs function of the reaction with pressure at constant temperature. The significance of this is shown in figure 1.2(b) showing ${}^{\delta G}/_{\delta \xi}$ as a function of p. When ${}^{\delta V}/_{\delta \xi} > 0$, i.e. the case where the volume of the system increases with the progression of the reaction, which is the case for all hydrogen releasing systems, the slope of the curve is positive. Since ${}^{\delta G}/_{\delta \xi} = 0$ at equilibrium, it must become positive when the pressure is increased and so the reaction must reverse, i.e. the hydride must reform, so that the volume of the system decreases. To put this in simplistic terms, a higher pressure favours a smaller volume, or systems that appear irreversible at moderate pressures may be made to be reversible at high pressures.

For use in vehicular applications it is widely accepted that, in order to supply an adequate amount of hydrogen at the required rate to keep a fuel cell supplying an adequate amount of power, the system will need to run at higher pressures than 1 bar. Also, in order to achieve fast recharging times, an increased pressure of rehydrogenation will almost certainly be required. Clearly, operating at higher pressures the whole wealth of thermodynamic data available at room temperature and pressure can not be used in its original form. Even the oft quoted value of 130.7 J K^{-1} mol^{-1} for the entropy change associated with the transformation

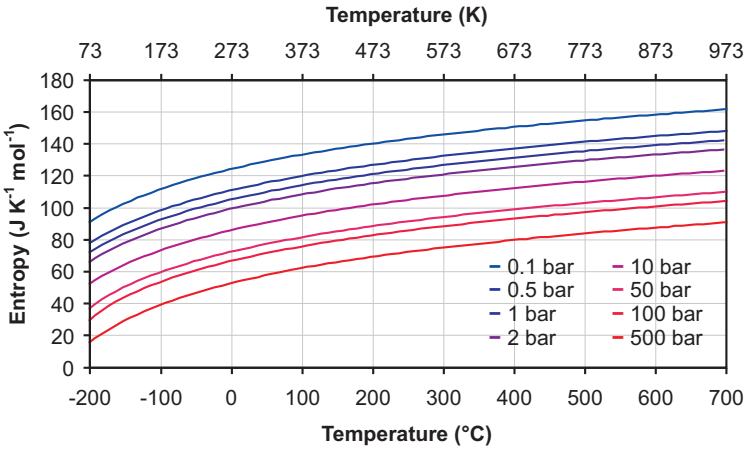

Figure 1.3: Variation of entropy of hydrogen with temperature and pressure as calculated from the equation of state [74].

to gaseous hydrogen is not sacrosanct, as the entropy of hydrogen has a strong dependence on temperature and pressure (figure 1.3). The use of a hydrogen storage material under non-standard conditions will affect the thermodynamics of the hydrogen storage process. In summary, systems that appear at the outset to be irreversible may not be thermodynamically irreversible at all temperatures and pressures. Whether materials fail to release sufficient amounts of hydrogen at the pressures required by fuel cells or ICEs, or whether systems that are not hydridable at lower pressures become readily reversible at higher pressures, will depend on how their thermodynamic properties change with pressure. A separate issue entirely, and one which is not easily predicted, is whether the kinetics of the reaction will be rapid enough for application in a hydrogen storage system.

1.6 Aims

Complex hydrides were identified as the area of hydrogen storage most likely to produce a new hydrogen storage material that fulfils the demands for high gravimetric hydrogen content. The most promising reversible hydrogen storage system based on complex hydrides at the beginning of this work exploited the interaction of protic $H^{\delta+}$ in $LiNH_2$ and hydridic H^- in LiH [61]. The aim of the project was to investigate new hydrogen storage systems based on $NH_2{}^-$ and $BH_4{}^-$, which also contains hydridic $H^{\delta-}$ [75].

Chapter 2

Experimental

2.1 Solid State Synthesis

Due to the reactivity of all of the materials used towards atmospheric moisture and oxygen, all manipulations were performed under inert conditions. Samples were weighed out using an analytical balance (up to ±0.1 mg accuracy) in the desired mole ratio in an argon filled glove box (MBraun, UniLab, <1 ppm O_2, <0.1 ppm H_2O) and intimately ground together by hand using a pestle and mortar.

2.1.1 Synthesis under Inert Gas

Samples were prepared in the glove box, transferred to a quartz reaction tube ($\frac{1}{2}''$ O/D), sealed with a Young's tap T-piece *via* an Ultra-torr® fitting, and removed from the glove box. The design of the T-piece allowed inert gas to be flowed past the end of the reaction tube to purge the gas line of air before opening the Young's tap. Typically a sintered glass disk of No.2 porosity was placed between the sample tube and the gas flow. Although in principle any gas can be connected to this flowing system only argon or hydrogen (5%) in nitrogen were used. Bubblers containing concentrated H_2SO_4 were fitted to the inlet and exhaust of the gas supply. The quartz reaction tube was then clamped in place

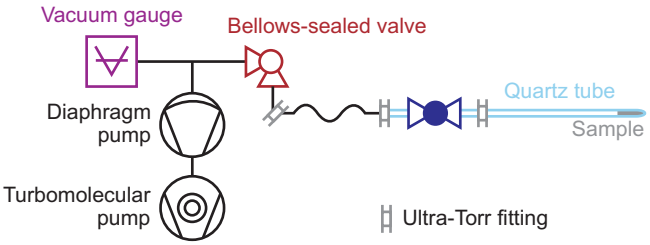

Figure 2.1: Schematic diagram of the vacuum line setup with the principal components labelled.

inside a vertical tube furnace (Lenton Furnaces, LTF 12/25/250 fitted with a Eurotherm 3216P1 controller and an insulation plug at the base of the work tube to improve thermal uniformity) so that the sample was at the centre of the hot zone of the furnace. Ramp rates of 1–2°C min^{-1} were used to ensure that the furnace did not overshoot the desired temperature. For a typical reaction the sample was held at the desired temperature for 12 hours before the furnace power was turned off and allowed to cool at a rate of around 1–2°C min^{-1}.

2.1.2 Synthesis under High Vacuum

Samples were prepared in a glove box, transferred to a quartz reaction tube and sealed with a right angled Young's tap *via* an Ultra-torr® fitting. The sample was then removed from the glove box, connected to a vacuum line (figure 2.1) and evacuated to approximately 1.0×10^{-6} mbar (Oerlikon Leybold Vacuum, PT70B vacuum station with a dry diaphragm fore pump and a turbomolecular pump). The quartz tube was then sealed at the Young's tap, removed from the vacuum line and sealed using an oxygen–natural gas torch. The sealed evacuated quartz tube containing the sample was then placed inside a muffle furnace (Carbolite, *CSF 1200*) and heated at a ramp rate of 1–2°C min^{-1} to ensure that the furnace did not overshoot the desired temperature. Typical reaction times were 12 hours.

2.2 Crystallography and Diffraction

Crystallography and diffraction are intrinsically linked in solid state chemistry. Crystallography describes the way atoms are arranged in the solid state and diffraction is used as the main probe into the atomic arrangements.

2.2.1 Crystallography

In a crystalline solid, the atoms adopt a regular arrangement with respect to each other in three dimensions which is known as a lattice. In an ideal crystal, the arrangement of atoms can be represented by a repeating unit known as the "unit cell". The unit cell is the smallest repeating unit which shows the full symmetry of the crystal structure. The entire crystal lattice can be generated from the unit cell using only translational symmetry. The lattice is defined as a set of points in space where the surroundings of one point is identical to all other points. Lattice points and unit cells are intrinsically linked in a bulk ideal crystal structure. The three lengths of the unit cell edges (a, b and c) and angles between them (α, β and γ) are known as the lattice parameters.

There are 7 primitive (P) lattice systems which may be described by unit cells of different shapes. Introduction of body centring (I) and face centring (F and C) translations produces a total of 14 lattice types, known as the Bravais lattices (figure 2.2). The unit cell of each Bravais lattice has an intrinsic symmetry, made up of a collection of mirror planes and rotational symmetry axes, which will be reflected in any crystal structure which adopts that lattice type [76].

Crystal Structures

Crystal structures are described by their lattice parameters, the atomic positions within the unit cell and by the internal symmetry. Atomic positions are expressed as fractional coordinates in each direction along the unit cell from one corner of the cell. Upon the addition of atoms to a unit cell, further translational

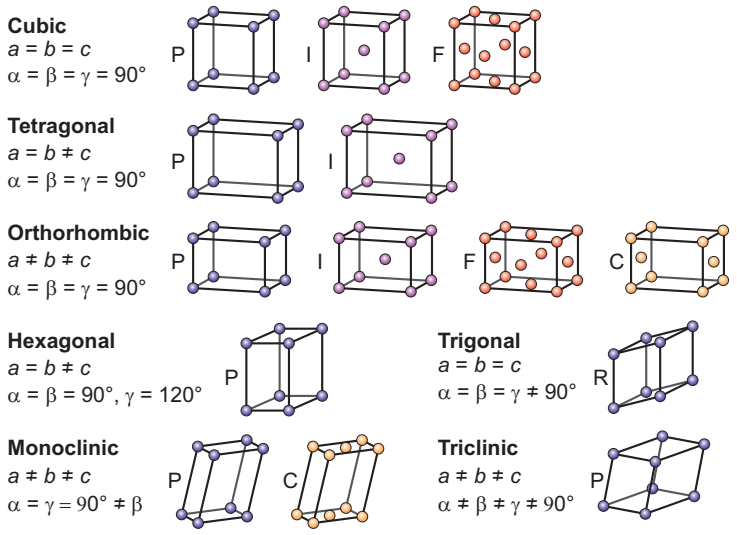

Figure 2.2: The 14 Bravais lattices.

symmetry elements to those required to describe the Bravais lattices must be considered. Atomic arrangements can also give rise to screw axes and glide planes. Combination of all of the symmetry arrangements possible in a 3-D object gives rise to 230 "space groups". The space group completely describes the symmetry of the crystal structure [76].

Lattice Planes

In order for the application of crystallography to diffraction, an unambiguous description of directions and especially planes in crystals is required. Directional vectors in a lattice are defined as passing through the unit cell origin. An arbitrary point on the direction vector to be assigned is chosen and represented as fractions of the unit cell lengths, a, b and c. The fractions are then expressed as the ratio of whole numbers placed in square brackets in the conventional form $[uvw]$. Directional coordinates proceeding in the opposite direction to the crystal axis are negative by convention. For example, a vector proceeding in a negative direction along the a axis is represented as $[\bar{1}00]$. Some examples of directional vectors are shown in figure 2.3.

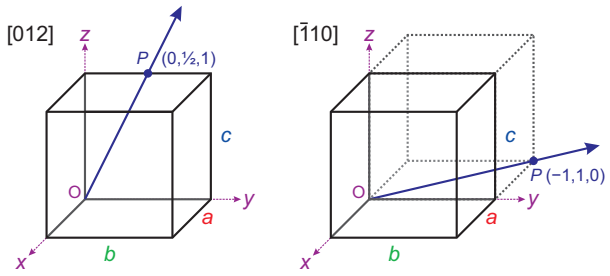

Figure 2.3: Examples of lattice vectors.

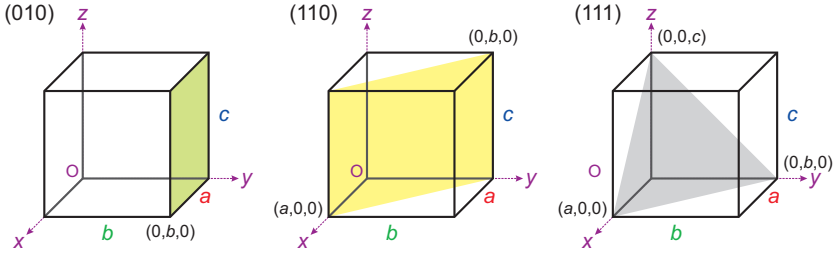

Figure 2.4: Lattice planes with different Miller indices.

The orientation of a lattice plane is defined by considering how the plane intersects the unit cell axes. The plane is defined by in the inverse of the fractional intercept along each lattice vector (x, y and z), which lie parallel with the unit cell edges (a, b and c). Indexing the planes in this way leads to the assignment of Miller indices of the form (hkl) for the plane. Some examples of lattice planes with their Miller indices are shown in figure 2.4. Depending on the symmetry of the lattice some or many of the planes will be equivalent to others, such as the (100), (010) and (001) planes in a cubic lattice. The number of equivalent planes is known as the multiplicity. The set of equivalent planes are denoted $\{hkl\}$. Although usually defined as a plane in a single unit cell, it is important to recognise that an infinite number of equivalent parallel planes exist in the lattice which are separated by a perpendicular distance (d_{hkl}). This plane separation is the shortest possible reciprocal lattice vector which is orthogonal to the lattice plane (hkl).

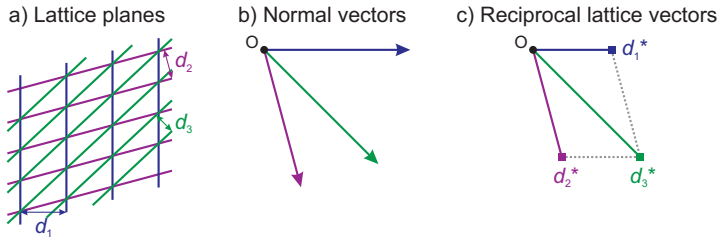

Figure 2.5: Lattice planes and their equivalent reciprocal lattice. (a) Three sets of lattice planes perpendicular to the plane of the paper (purple, blue and green), (b) the normal directions to the planes from a common origin (O) and (c) the sets of planes represented as reciprocal lattice vectors.

The Reciprocal Lattice

So far only the description of a crystal structure by the use of a lattice and unit cell has been considered, i.e. a representation of the atomic arrangement in three dimensional space (also known as the direct lattice). For an appreciation of how diffraction occurs in a crystalline solid, an alternative related description is useful, which is termed the reciprocal lattice.

Each set of lattice planes, described in the previous section, can be represented by their perpendicular (normal) vector. All that is needed for a complete description of a set of lattice planes is their direction in the crystal and their separation (d_{hkl}), also known as d-spacing. These normal vectors can then be used to define a new set of reciprocal lattice points.

The construction of a reciprocal lattice from sets of lattice planes is shown in figure 2.5. The lengths of the normal vectors (d_n^* in figure 2.5(c)), are inversely proportional to the d-spacing in the real lattice:

$$d^*_{(hkl)} = K/d_{(hkl)} \tag{2.1}$$

where K is a proportionality constant.[†] The end points of the reciprocal lattice vectors (represented by squares in figure 2.5(c)) are reciprocal lattice points. Each point on the reciprocal lattice represents a crystallographic plane and can be assigned (hkl) values. These reciprocal lattice points make a new unit cell

[†]In X-ray diffraction K is normally, by convention, the X-ray wavelength.

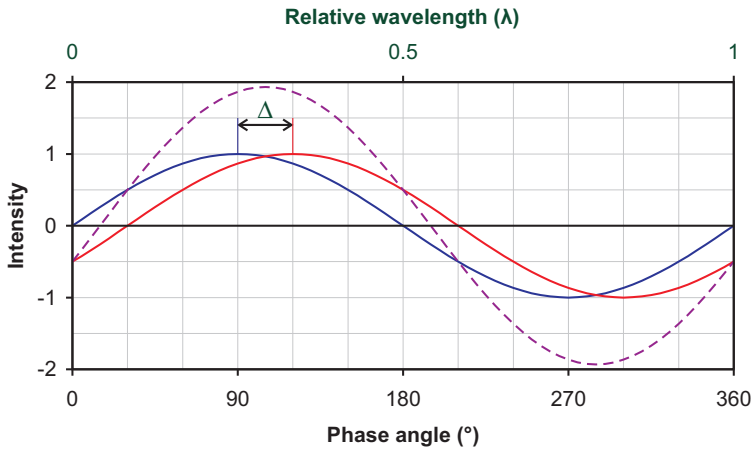

Figure 2.6: The superposition of two waves (red and blue) giving rise to interference (purple).

which is repeated in all directions in the reciprocal lattice. The value of the description of a unit cell in terms of a reciprocal lattice will become evident in the following section.

2.2.2 Diffraction

Diffraction is a special case of the interaction of a wave with matter. In order to describe the process of diffraction it is first useful to explore the properties of waves which make diffraction possible. All types of waves travelling through the same medium may interact and undergo the processes superposition, which can give rise to constructive and destructive interference. In the case of two waves of the same wavelength travelling in the sample direction, the observed intensity at any point is determined by the "phase shift" between the waves. The phase shift is normally represented a linear shift, Δ, in the length units of the wavelength. If the phase shift is zero this will give rise to completely constructive interference as an increased intensity will be observed. If the phase shift is equal to half of the wavelength this will give rise to completely destructive interference. An example of the superposition of two phase-mismatched waves giving rise to interference is shown in figure 2.6.

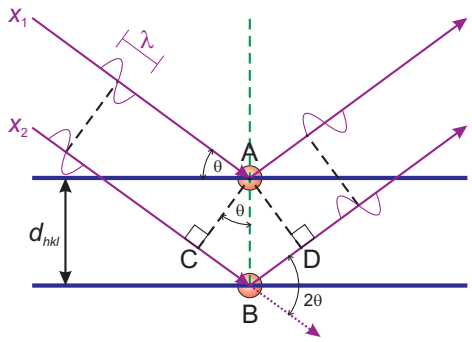

Figure 2.7: The geometry used for simplified derivation of Bragg's law.

Diffraction in crystalline materials arises when waves are scattered from atoms at different positions in the sample. The difference in path length will result in a phase shift between the waves, and superposition of the waves will result in differences in the detected intensity. The measured intensities can therefore give information about the relative positions of the atoms. Diffraction only occurs if the wavelength of radiation used is of the order of the separation distance of the scattering centres. X-rays have a wavelength which is comparable to atomic separations and so makes them an ideal probe for crystalline materials.

The Bragg Equation

Treatment of diffraction as the reflection of X-rays by equally spaced lattice planes (i.e. planes with the same Miller indices, described previously) gives rise to the Bragg equation. If two X-rays (x_1 and x_2 in figure 2.7) are scattered from consecutive planes, the second wave travels a longer distance (from C to B before, and from B to D after reflection). Applying simple trigonometry to the geometrical arrangement shown in figure 2.7 gives the path difference (Δ) in terms of the plane separation ($d_{(hkl)}$) and the incident angle of the radiation (θ):

$$\Delta = (CB + BD) = (d_{(hkl)} \sin\theta + d_{(hkl)} \sin\theta) = 2d_{(hkl)} \sin\theta. \qquad (2.2)$$

Superposition resulting in constructive interference only occurs if the path difference is equal to a multiple of the wavelength (i.e. the waves return to being in

phase):

$$\Delta = n\lambda, \text{ where } n = 0, \pm 1, \pm 2, ... \tag{2.3}$$

Complete destructive interference results from all non-integer values of n. Combining equations 2.2 and 2.3 gives the Bragg equation:

$$n\lambda = 2d \sin\theta \tag{2.4}$$

In reality, X-rays are strongly penetrating and scattering can occur at thousands of consecutive planes in a single crystallite. Also, X-rays are scattered by the electron cloud of constituent atoms, not by the crystal planes.

It is worth clarifying at this point how the Bragg equation is applied in a diffraction experiment. A single wavelength impinges onto the sample at a defined angle θ. The intensity of scattered radiation at an angle 2θ is measured. Angles corresponding to the d-spacing of a lattice plane *via* the Bragg equation are said to obey Bragg's law and may have a significant diffracted intensity. The Bragg law still holds even if scattering occurs from atoms located at different positions within the lattice plane.

The Ewald Sphere

The Bragg equation describes the geometrical requirements for diffraction in terms of the d-spacing of lattice planes. As discussed in section 2.2.1, each lattice plane can be described in terms of a perpendicular vector, which gives rise to the reciprocal lattice. It can also be shown that diffraction occurs when a scattering vector is a vector of the reciprocal lattice. The "Ewald sphere of reflection" is a convenient method for demonstrating this [77].

An imaginary sphere of radius $1/\lambda$ is centred on a single crystal (figure 2.8(a)). The reciprocal lattice is viewed as a tangent to the sphere with the lattice origin at the point where the incident radiation would exit the sphere. The imaginary single crystal, and with it the reciprocal lattice, is rotated through the angle 2θ

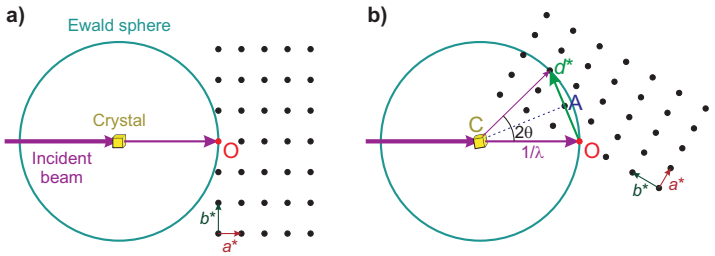

Figure 2.8: The geometry used for the description of the Ewald's sphere of reflection. The circles represent points of the reciprocal lattice in the a^*b^* plane.

until a second lattice point coincides with the Ewald sphere (figure 2.8(b)) [78]. By trigonometry:

$$\sin\theta = \frac{OA}{CO} = \frac{d^*/2}{1/\lambda} \tag{2.5}$$

which can be rearranged to give Bragg's law:

$$\lambda = \frac{2\sin\theta}{d^*} = 2d\sin\theta \tag{2.6}$$

Further rotation of the crystal will result in different lattice points falling on the Ewald sphere, and therefore result in diffraction from the associated lattice plane. The lowest observable d-spacing in a diffraction experiment is determined by the diameter of the Ewald sphere $(2/\lambda)$. It should be noted that only scattering in the a^*b^* plane (in the plane of the paper in figure 2.8), i.e. reciprocal lattice points with $(hk0)$, was considered here. The Ewald sphere of reflection is a three dimensional phenomenon and as such diffraction will occur when a lattice point contacts at any point on the 3-D sphere.

Single crystal diffraction exploits the sphere of reflection by controlling the relative orientation of the crystal and detecting the trajectory and intensity of the diffracted radiation. For each crystal orientation, 2-D scattering information can be obtained relating to the atomic positions. By changing the crystal orientation a 3-D picture of the atomic positions, and therefore the crystal structure, can be constructed.

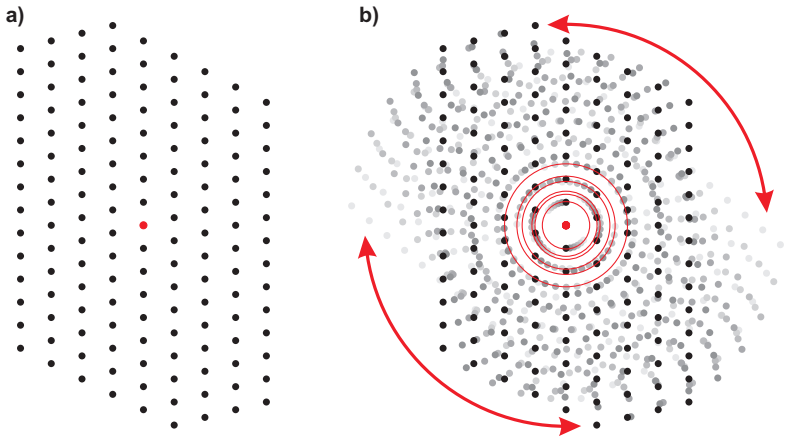

Figure 2.9: Schematic comparison of the observed reciprocal lattice for (a) a single crystal and for (b) a powder.

2.2.3 Powder Diffraction

A powder sample contains many randomly orientated crystallites. Whereas for a single crystal sample the reciprocal lattice is easily observed in the Ewald sphere of reflection (figure 2.9(a)) the simultaneous presence of every crystal orientation in a powder results in the spreading out of reciprocal space (figure 2.9(b)) [77]. The main challenge associated with powder diffraction is therefore that of the systematic overlap of Bragg peaks caused by the projection of 3-D reciprocal lattice on to the 1-D angular 2θ axis. This results in a large reduction in the amount of direct data compared to single crystal diffraction methods. There is, however, a large amount of data contained in the various aspects of a powder diffraction pattern, illustrated in figure 2.10. This 1-D powder diffraction data can in many cases be used to reconstruct the 3-D nature of the structure, as well as providing a great wealth of information on the bulk and micro-structural properties of the material. The various aspects of a powder diffraction pattern will now be discussed in turn.

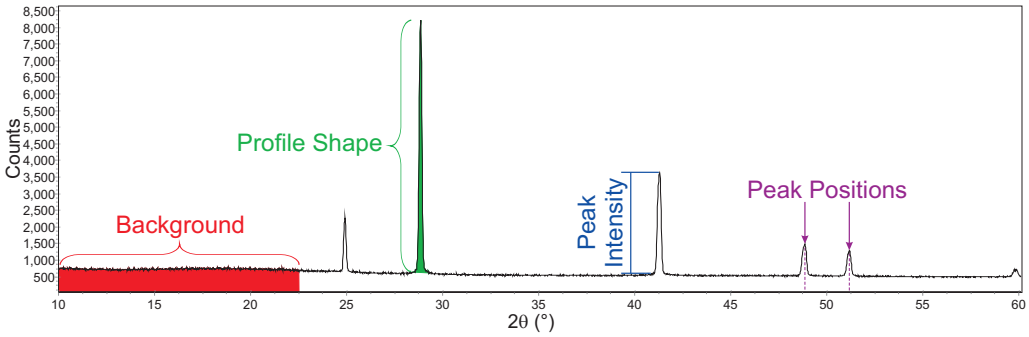

Figure 2.10: A typical powder X-ray diffraction pattern.

Background

The background is typically caused by instrumental factors like detector noise or experimental factors such as the sample container used. Sample effects such as absorption and fluorescence, local effects, amorphous phases and incoherent scattering can also contribute. Typically information contained in the background is disregarded in typical analysis of diffraction patterns, although more specialist techniques such as Pair Distribution Function (PDF) analysis use the diffuse scattering component of the background to determine the short range ordering in materials.

Profile Shape

Peak profile shapes have a number of contributions, some from the instrumental factors such as the radiation source being used, instrument characteristics and set-up, and some from the sample such as particle (grain) size and crystallinity. Aside from instrumental factors, the greatest contribution to the peak shape is frequently due to crystallite size. The Bragg law (equation 2.4) is only completely valid when the crystallite size is essentially infinite; for a crystallite of a finite size the diffracted intensity of the Bragg peak will spread over a region where the size and peak shape are related to the crystallite size and shape. The degree of Bragg peak broadening due to the sample can be used to estimate the crystallite

size using relationships such as the Scherrer equation [79].

Peak Position

Bragg peak positions for each phase present are determined by the wavelength of radiation used for powder diffraction and the unit cell size, shape and symmetry, which has been discussed in detail in section 2.2.1. The peak positions correspond to the separation distances of lattice planes in the unit cell (the Bragg law). Instrumental factors such as zero point error or sample height error can also contribute to shifts in the observed peak positions.

Peak Intensity

Peak intensities are predominantly affected by atomic positions and thermal vibrations, phase fractions and preferred orientation effects. The multiplicity of the lattice plane giving rise to the peak will affect the intensity (see section 2.2.1). It is important to distinguish which parameters affect the *overall* intensities for a phase, and which affect the *relative* intensities of the phase Bragg peaks.

The absolute intensity of a diffraction pattern is dependent on experimental factors such the data collection time and the scattering power of the sample and instrumental factors such as the intensity of the radiation source and the efficiency of the detector. The relative overall intensity of the Bragg peaks for one phase compared to another is predominantly due to the relative abundance of that phase. A small crystallite size of a phase will cause broadening of the Bragg peaks, as mentioned previously, which has the effect of an apparent decrease in intensity. Thermal motion of the atoms in a crystal structure can also diminish the diffracted intensity due to that phase. Effects such as micro-absorption (when the sample absorbs the diffracted radiation) can also attenuate the intensity, but this is minimal for lightly absorbing materials.

The relative intensity of Bragg peaks for a certain phase is dependent on the types, positions and (to a lesser extent) thermal motions of the atoms present in

the structure. Certain symmetry elements of a crystal structure can lead to complete absence of symmetry related Bragg peaks. In a powder diffraction pattern, the sample is assumed to be a collection of crystallites in a completely random orientation. If the crystallites are of a certain size and shape they may align with each other, especially in the case of plate-like or needle-shaped crystallites. This phenomenon is known as preferred orientation. This ordering of crystallites results in a disproportionate amount of diffracted intensity from lattice planes in the aligned crystallographic plane.

2.3 X-ray Powder Diffraction

An X-ray diffraction (XRD) experiment consists of a monochromatic source of radiation which shines onto the sample and a detector which is positioned in a defined geometry relative to the source and sample. The components of an X-ray diffractometer will now be discussed in turn.

X-ray Source

In a standard laboratory based X-ray diffractometer, X-rays are produced when electrons are accelerated and collided with a metal anode target inside a vacuum tube. The high energy electrons induce a cascade of electronic transitions in the atoms of the target. Upon relaxation, well defined electronic transitions within the atoms lead to the emission of radiation of characteristic wavelengths (figure 2.11(a)). The most common target element, and the only type used in this study, is Cu, although Mo, Cr, Fe and Co are also common.

Monochromation

The X-ray radiation emitted from a metal anode source is a divergent beam containing a spectrum of X-rays. The spectrum contains characteristic discrete wavelengths, which correspond to atomic transitions of the metal. A continuous

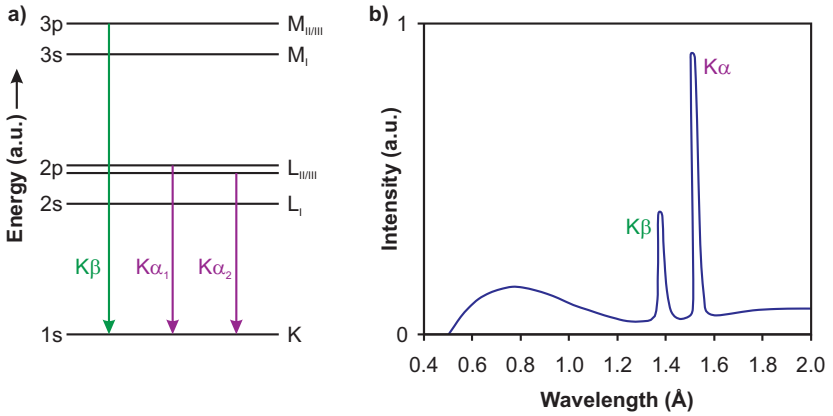

Figure 2.11: (a) Energy level diagram for a neutral Cu atom and (b) an X-ray spectrum from a Cu X-ray source [77].

background spectrum is also present, predominantly caused by *Bremsstrahlung* (literally "brake radiation") released by the deceleration of the high energy electrons upon contacting the metal target. A typical X-ray spectrum for a Cu X-ray source is shown in figure 2.11(b). For X-ray diffraction, a single intense wavelength of focused radiation is required. Monochromation is used to select the most intense part of the X-ray spectrum, corresponding to an electronic transitions of the target metal.

Two types of monochromation are common in laboratory based diffractometers. Crystal monochromators are single crystals set to a particular orientation, θ_m, so that the desired X-ray wavelength (λ) satisfies the equation:

$$\lambda = 2d_{(hkl)} \sin \theta_m \tag{2.7}$$

where $d_{(hkl)}$ is the d-spacing of an intense Bragg reflection. Typically crystal monochromators are made from Si, Ge, quartz or graphite. Göbel mirror monochromators are curved multi-layer crystals made up of alternating strongly and weakly scattering materials. The mirror reflects only monochromatic radiation, the wavelength of which is determined by the multi-later spacing, producing a parallel X-ray beam. The degree of monochromation from a Göbel mirror is typically insufficient to differentiate between Cu Kα_1 and Kα_2.

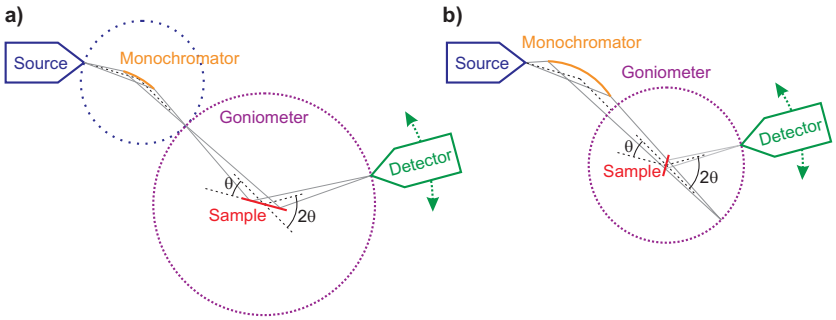

Figure 2.12: Comparison of (a) Bragg-Brentano and (b) Debye-Scherrer geometries for X-ray diffraction. The principal components of the X-ray diffractometer are labelled.

Detection

The most common detector is a scintillation counter. X-rays hitting a phosphorescent screen emit photons which are detected and amplified using a photon multiplier. The signal intensity is directly proportional to the amount of X-rays hitting the detector. This is classed as a point detector as it can only collect data at a single 2θ angle at a time. In order to decrease data collection time, position sensitive detectors (PSD) were developed which can collect data over a 2θ range. The detector records the 2θ angle at which each X-ray was detected.

Goniometer

The geometric nature of the diffraction phenomenon means that the accurate relative positioning of the X-ray beam, sample, and detector are essential. A goniometer is used to measure and control the relative angles of each component. There are two common geometries used in powder diffraction experiments; reflection (Bragg-Brentano) and transmission (Debye-Scherrer). The geometric considerations for both geometries are shown in figure 2.12.

Synchrotron X-ray Sources

A synchrotron is a particle accelerator where charged particles are accelerated to relativistic speeds and held in a (usually) circular orbit by magnetic fields. Syn-

chrotron radiation is emitted when the charged particles change their velocity. A wide range of wavelengths are released which can be selected using suitable monochromation. Modern synchrotron X-ray sources use insertion devices, such as wigglers and undulators, to produce high intensity, highly collimated and polarised radiation.

2.3.1 Synchrotron X-ray Diffraction

Synchrotron X-ray diffraction data were collected in Debye-Scherrer geometry on the high-resolution powder diffraction beam line ID31 at the European Synchrotron Radiation Facility (ESRF), in Grenoble, France, at a wavelength and step-size of ~ 0.8 Å and 0.003° respectively. Samples were loaded in a glove bag under flowing nitrogen into borosilicate capillaries of 0.9 mm diameter sealed at one end. Once the samples were well packed the capillary was plugged with a 0.7 mm diameter glass rod, removed from the glove bag and sealed on a gas torch. No signs of oxidation of samples from the loading and sealing procedure were observed.

Sealed capillaries were spun at 100 r.p.m perpendicular to the X-ray beam to improve randomization of the individual crystallite orientations. The exact wavelength and the zero point were determined from reflections of a silicon standard. For standard samples, scan times of 15 minutes were used. No noticeable radiation damage, in the form of anisotropic peak shift or broadening, was observed during this time.

2.3.2 Laboratory X-ray Diffraction

Laboratory powder X-ray diffraction data were collected on a Siemens D5000 diffractometer in transmission (Debye-Scherrer) geometry. A copper X-ray source was monochromated using a germanium monochromator to give Cu Kα_1 radiation at a wavelength of 1.54056 Å. Samples were prepared by grinding in an argon filled glove box and sealed from the atmosphere between two layers of Scotch®

Magic™ tape. Samples were rotated in the plane perpendicular to the X-ray beam.

2.4 Neutron Diffraction

Neutrons predominantly interact with the nuclei of atoms, in contrast to X-rays which interact with the electron cloud. As such, the scattering power of an atom in a neutron diffraction experiment is often very different to the equivalent X-ray experiment. Neutron diffraction is significantly more sensitive to some light atoms such as hydrogen. The difference in scattering mechanisms of neutrons and X-rays means that the two techniques give complementary information.

Neutrons can be produced either in a nuclear reactor or by the process of "spallation". Spallation is when a heavy metal target is bombarded with pulses of high energy protons. In both cases, the high energy neutrons released are slowed down by collisions with a moderator. The wave–particle duality of matter means that the slowed neutrons, travelling at approximately 2000 m s^{-1}, have a de Broglie wavelength in the region 1–2 Å; this wavelength makes neutrons suitable for structural studies by diffraction.

Neutron diffraction was performed at the ISIS spallation neutron source at the Rutherford Appleton Laboratory, Oxfordshire. Samples were manipulated inside an argon filled glove box and sealed inside a vanadium can with an iridium wire seal.

2.5 Rietveld Analysis

A fundamental cornerstone of Rietveld analysis is that, given enough information, an accurate diffraction pattern can be calculated for a given crystal structure. Rietveld analysis relies on a structural model built from parameters that describe the unit cell size and shape, and atomic positions, occupancies and thermal motions. This is then combined with experimental parameters that describe the

peak profile and background shapes to calculate a diffraction pattern. These parameters are varied using a least-squares method until the agreement between the measured and calculated diffraction profiles is optimised. This process is essentially the minimisation of the residual, S_y, in the equation:

$$S_y = \sum_i w_i (y_i - y_{ci})^2 \tag{2.8}$$

where

$w_i = 1/y_i$,

y_i =observed intensity at the ith step,

y_{ci} = calculated intensity at the ith step, and the sum is over all data points [80, 81].

The Rietveld method is one of refinement, rather than elucidation, and as such the choice of the correct starting model is essential. The aim is to determine an accurate model for the crystal structures of each phase present in a given diffraction pattern. The contributions to the diffraction pattern (see section 2.2.3) will now be discussed in relation to how they are modelled in Rietveld refinement.

Background

No diffraction pattern is completely free of background. The contributions to the background are of little interest in Rietveld refinement. However, the background must still be described. The background is generally described by geometrical functions that best fit the shape of the background. Typical background functions range from linear interpolation functions [82] to polynomial equations such as the Chebyschev polynomial [83]. The ability of a background function to fit the observed background depends heavily on the number of parameters in the background function, as illustrated for a Chebyschev polynomial function in figure 2.13.

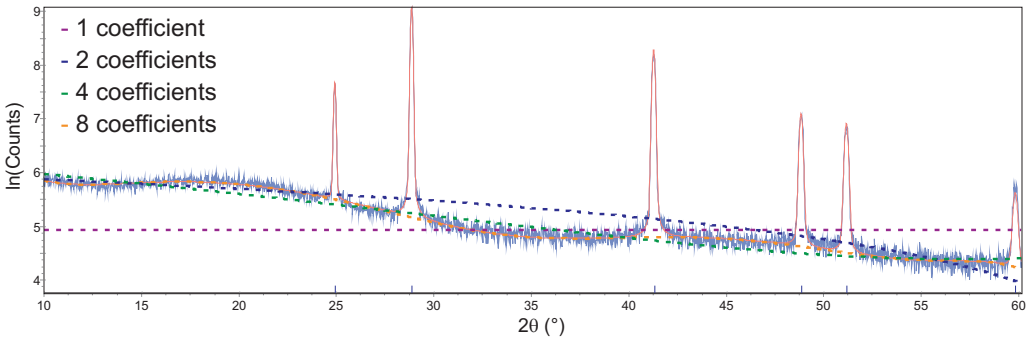

Figure 2.13: Fitting of a Chebyschev polynomial background function with 1, 2, 4 and 8 coefficients.

Peak Profile Functions

The peak shapes have to be modelled for each phase present. Although there are a number of instrumental and sample contributions to the peak shape, is it normally sufficient to model the peak shape using a geometric function. Two of the most common mathematical descriptions of symmetric peak shapes are the Gaussian and Lorentzian peak profile shapes [83]. As single peak shapes these rarely adequately describe the peak profile of an observed diffraction pattern. In practise a more complex peak function is used, such as the pseudo-Voigt peak shape which combines Lorentzian and Gaussian functions with refinable parameters for the width and intensity of each component peak shape. The combination of Lorentzian and Gaussian functions to give pseudo-Voigt peak shape is illustrated in figure 2.14. There is also an angular dependence of the peak width, with wider peaks observed at higher angle. As such there is also a need to model the angle-dependent shape features [84].

Peak Positions

Peak positions are easily calculated by geometric considerations of the separation of lattice planes of the unit cell (see section 2.2.1). The lattice parameters of the unit cell are the refinable parameters. Instrumental factors affecting the peak positions, such as a zero point error or some other sample displacement correction,

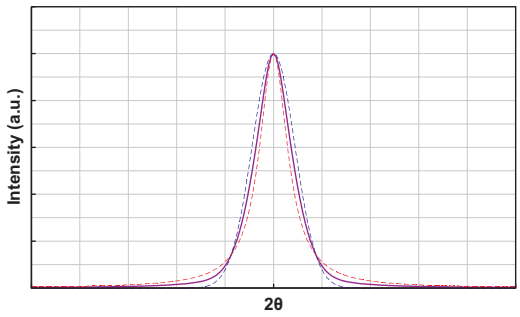

Figure 2.14: Pseudo–Voigt peak profile (purple) with the contributing Lorentzian (red) and Gaussian (blue) components shown.

can also be refined.

Peak Intensities

The calculation to give the intensity of a Bragg peak is of the form:

$$I_{(hkl)} = K_{(hkl)} F^2_{(hkl)} m_{(hkl)} A_{(hkl)} Lp_{(hkl)} \tag{2.9}$$

the terms of which are described below.

$K_{(hkl)}$: a proportionality constant;

$F^2_{(hkl)}$: the "structure factor", which describes the interaction of the diffracted radiation with the atoms in the lattice;

$m_{(hkl)}$: the multiplicity of the Bragg reflection;

$A_{(hkl)}$: an absorption correction factor which depends on the sample composition and apparent sample thickness in the direction of diffraction;

$Lp_{(hkl)}$: contains the Lorentz factor, which corrects for the probability of observing a Bragg reflection at the diffraction angle, and a radiation polarisation factor.

The structure factor contains the component of atomic positions, and as such is of most interest. $F_{(hkl)}$, is given by:

$$F_{(hkl)} = \sum_j f_j N_j exp[2\pi i(hx_j + ky_j + lz_j)]exp[-M_j] \tag{2.10}$$

where

f_j is the atomic scattering factor of the jth atom type,

N_j in the site occupancy of the jth atomic site,

x_i, y_i and z_i are the position parameters of the jth atom in the unit cell, and

M_j is the apparent reduction is scattering powder due to thermal motion. M_j is calculated from:

$$M_j = 8\pi^2 B_j^2 \sin^2\theta/\lambda^2 \tag{2.11}$$

where B_j is related to the root-mean-square thermal displacement of the jth atom parallel to the diffracted beam by a factor of $1/(8\pi^2)$.

In Rietveld refinement, the calculated intensity at any point in the diffraction pattern is the sum of all contributions from overlapping Bragg peaks together with corrections for sample effects like preferred orientation and the background intensity. Iterative refinement of parameters, like atomic positions, followed by the recalculation of the resultant calculated diffraction and comparison with the observed diffraction pattern results[†] in a structural model which best matches the observed data.

Numerical Criteria of Fit

In order to determine the quality of the fit of the calculated diffraction pattern to the observed pattern, a number of statistical measures have been introduced. Statistical measures relating to the fit of the diffraction pattern to the crystal structure of interest include the 'R-structure factor':

$$R_{\mathrm{F}} = \frac{\sum |[I_{(hkl)}(\text{`obs'})]^{1/2} - [I_{(hkl)}(\text{calc})^{1/2}]|}{\sum [I_{(hkl)}(\text{`obs'})]^{1/2}} \tag{2.12}$$

[†]If false minima can be avoided.

and the 'R-Bragg factor':

$$R_{\text{Bragg}} = \frac{\sum |I_{(hkl)}(\text{`obs'}) - I_{(hkl)}(\text{calc})|}{\sum I_{(hkl)}(\text{`obs'})} \tag{2.13}$$

Both of these measures compare the observed and calculated intensity at the position of Bragg reflections predicted by the unit cell of the structure. As such, they rely on the correct determination of the unit cell to predict where Bragg reflections are observed, and so are biased towards the starting model.

Measures based on the whole pattern fitting of the observed and calculated diffraction pattern intensities at each point (y_i) include 'R-pattern':

$$R_{\text{p}} = \frac{\sum |y_i(\text{obs}) - y_i(\text{calc})|}{\sum y_i(\text{obs})} \tag{2.14}$$

and 'R-weighted pattern':

$$R_{\text{wp}} = \left[\frac{\sum w_i [y_i(\text{obs}) - y_i(\text{calc})]^2}{\sum w_i [y_i(\text{obs})]^2} \right]^{1/2} \tag{2.15}$$

where w_i is the weighting given to data point i based on the estimated error in the measured intensity. The best possible R-value for a data set, taking into account the errors in measured intensity, is called 'R-expected':

$$R_{\text{exp}} = \left[\frac{N - P - C}{\sum w_i y_{oi}^2} \right]^{1/2} \tag{2.16}$$

where N is the number of observables, P the number of refined parameters and C the number of constraints used. This enables the definition of a further statistical measure:

$$\chi^2 = \left[\frac{R_{\text{wp}}}{R_{\text{exp}}} \right]^2 \tag{2.17}$$

which is a particularly valuable statistic as it includes the number of refinable parameters used to calculate the fit. Increasing the number of refined parameters will normally improve the fit to the observed data. However, if the amount of improvement is small compared to the quality of the data then the improvement in χ^2 will be small. A very small value of χ^2 can also result from when errors in the structural model are outweighed by errors associated with poor quality data.

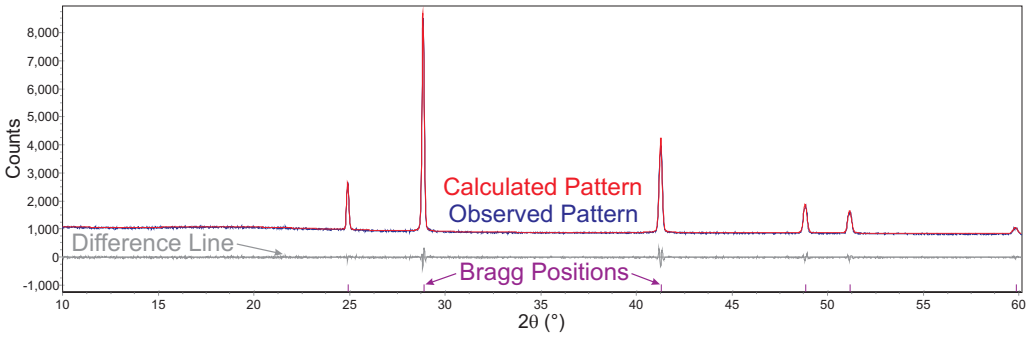

Figure 2.15: A typical Rietveld refinement plot.

R_{wp} is the most relevant statistical value for the process of Rietveld refinement, although it is vulnerable to giving high values if not all of the peaks are accounted for or if the background is inadequately described. R_{wp} can also give artificially low values if there is a large, well fitted background. For this reason, background corrected versions of these statistical measures are also possible, for example, for the background corrected R-weighted pattern:

$$R_{\mathrm{wp}}{}' = \left[\frac{\sum w_i[y_i(\mathrm{obs}) - y_i(\mathrm{calc})]^2}{\sum w_i[y_i(\mathrm{obs}) - \mathrm{Bkg}_i]^2}\right]^{1/2} \tag{2.18}$$

Visual Criteria of Fit

Although the numerical criteria of fit are very useful, and indeed necessary for the computational application of Rietveld refinement to proceed and reach an ultimate value, they can not be used in isolation. A Rietveld plot is used to display visually how good the calculated fit is to the observed data. An example of a Rietveld plot is shown in figure 2.15. The observed data is plotted and overlaid with the calculated diffraction pattern. The difference between the observed and calculated data is shown below the diffraction patterns; for a perfect fit this should be a straight line. Tick marks indicating the calculated Bragg positions for each phase present are typically shown below the difference line so that the contributions to the calculated pattern by different phases can be more easily identified.

2.5.1 Quantitative Phase Analysis

It has been shown that Rietveld analysis can provide very accurate estimates of the relative and/or absolute abundances of component phases in a mixture. The effectiveness of this technique, known as quantitative phase analysis (QPA), has been demonstrated with X-ray and neutron powder diffraction data [85, 86, 87]. QPA relies on the relationship:

$$W_p = \frac{S_p(ZMV)_p}{\sum_{i=1}^{n} S_i(ZMV)_i} \tag{2.19}$$

where W is the relative weight fraction of phase p in a mixture of n phases, and S, Z, M and V are the Rietveld scale factor, the number of formula units per unit cell, the mass of the formula unit (in atomic mass units) and the unit cell volume (in Å^3), respectively [77]. If an internal standard phase, s, is added to the phase mixture in the weight fraction W_s, then the absolute weight fractions of the other identified components p are given by:

$$W_p = \frac{W_s S_p(ZMV)_p}{S_s(ZMV)_s} \tag{2.20}$$

Where this method is employed, a reduction from unity of the sum of the determined weight fractions of the n identified components can provide an estimate of the amount of non-crystalline or amorphous material in the sample.

Any effect which can affect Bragg peak intensity (see section 2.2.3), such as preferred orientation, extinction, micro-absorption and sample representability, can cause deviation of determined weight fractions from the true values. Of these factors, preferred orientation has been identified as causing the most deviation and so efforts must be made to include preferred orientation in the Rietveld analysis or reduce its effects during data collection [77, 88]. The effects of extinction are most pronounced when mixture components have radically different crystallite and grain sizes. Extinction effects are most prominent for large crystallite sizes on the order of several microns [89]. The effects of micro-absorption are most prominent when phases present have very different absorption coefficients.

QPA is most widely used in the characterisation of mineralogical samples and of cements [87]. Because of the nature of these multi-phase powders, with large ranges of particle size, crystallinity and chemical composition, effects such as preferred orientation, extinction and micro-absorption frequently need to be included to obtain accurate results. Typically the particle and grain size of the components of a sample are determined *via* microscopy in order for various correction factors to be applied in the Rietveld analysis.

Testing Quantitative Phase Analysis

In order to test how accurate QPA results can be without knowledge of the microstructure of the phases, and in order to develop a refinement strategy to be used throughout this body of work, QPA was performed on powder diffraction data supplied by the International Union of Crystallography Commission on Powder Diffraction 'round robin' on the determination of quantitative phase abundance from diffraction data [88]. Powder diffraction data from samples containing various known quantities of corundum (Al_2O_3), fluorite (CaF_2) and zincite (ZnO) was supplied together with data for the pure components. The diffraction data were collected on a Philips 3020 diffractometer in reflection (Bragg-Brentano) geometry. Radiation from a copper X-ray source was monochromated using a graphite monochromator to give Cu K$\alpha_{(1+2)}$ radiation.

The powder diffraction data was analysed using the computer program Topas [90]. Initially diffraction patterns from pure samples of the constituent materials were used. The radiation was modelled using a suitable emission profile and Lorentz-polarisation factor, and a specimen displacement (sample height) error was included. The lattice parameters, atomic positions, thermal parameters and pseudo-Voigt peak shape parameters were refined for each phase. A Chebyshev polynomial with 12 parameters was used to describe the background. Once Rietveld refinement of the pure phases gave a good quality fit to the observed diffraction data, the atomic positions and thermal parameters were then fixed.

The correlation between thermal parameters and scale factor in the calculation of Bragg peak intensity meant that thermal parameters were not refined for multi-phase sample. These models were then used in the quantitative phase analysis of the mixtures.

During QPA, background parameters and a specimen displacement parameter were refined for each diffraction pattern, and lattice parameters, a peak shape function, and scale factor were refined for each phase present. Topas reported relative abundances of each phase as a weight percent (wt%), calculated as in equation 2.19, together with an estimated standard error.† The resultant determined phase fractions for each phase present, compared to the actual given weighed component for each mixture, is shown in figure 2.16. All of the determined values were correct to within 2 wt%. The determined standard errors are small relative to true error from the real values and this should be taken into account when interpreting these results. It should be emphasised that this level of accuracy was achieved without taking into account any of the possible effects of absorption, extinction or preferred-orientation, and the results were completely repeatable.

These values compare favourably to values quoted for quantitative analysis of the same samples by X-ray fluorescence (XRF), shown in figure 2.17. Although the values for XRF are much more accurate and precise, giving the correct value to less than 1 wt%, XRF is typically poor for light elements and performing XRF on air sensitive materials is non-trivial. XRF is also of no use in determining the relative amounts of different phases with very similar chemical compositions. As such, QPA was identified as a more effective method for determining phase abundance.

†The standard error reported by Topas is from the error in the determined value of the scale factor for each phase and does not represent other sources of errors discussed previously.

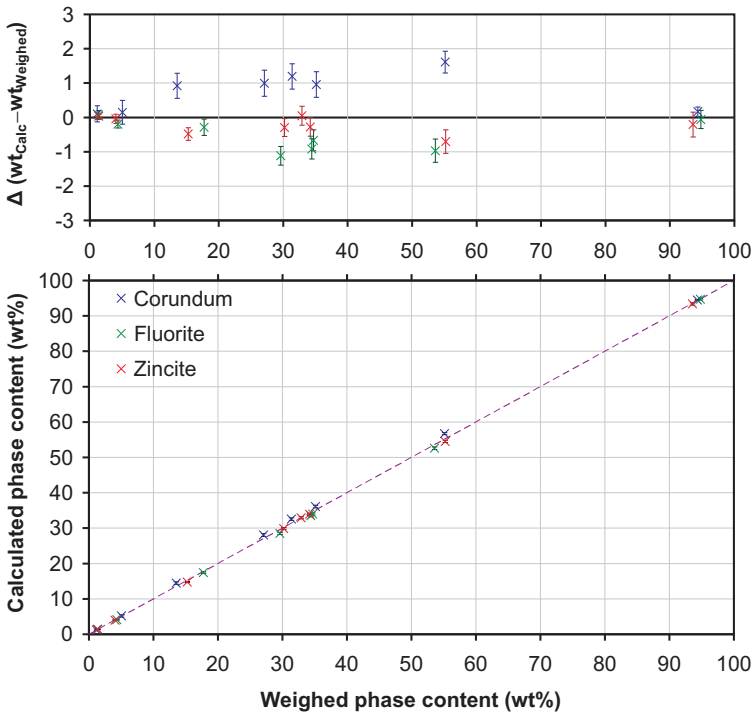

Figure 2.16: Calculated phase content data from quantitative phase analysis against the true weighed values for various mixtures. Error bars shown are 3×standard error.

Quantitative Phase Analysis Refinement Strategy

In this study, QPA been applied to study the reactions of light metal complex hydrides. The particle size and crystallinity of the components of these samples were presumed to be similar for each phase component. The homogeneity of the samples was ensured by grinding by hand using a pestle and mortar. Absorption by such light elements is assumed to be minimal, with a typical calculated linear absorption factor, μ, of less than 4 cm^{-1} [91]. In the majority of cases, synchrotron X-ray diffraction data has been used for QPA. Samples were loaded in capillaries, giving a small cylindrical radius and therefore minimal absorption. Rapid sample spinning during data collection essentially removed the possible effects of preferred orientation.

Throughout this work a consistent refinement strategy for QPA was adopted, where atomic positions and thermal parameters were determined by diffraction

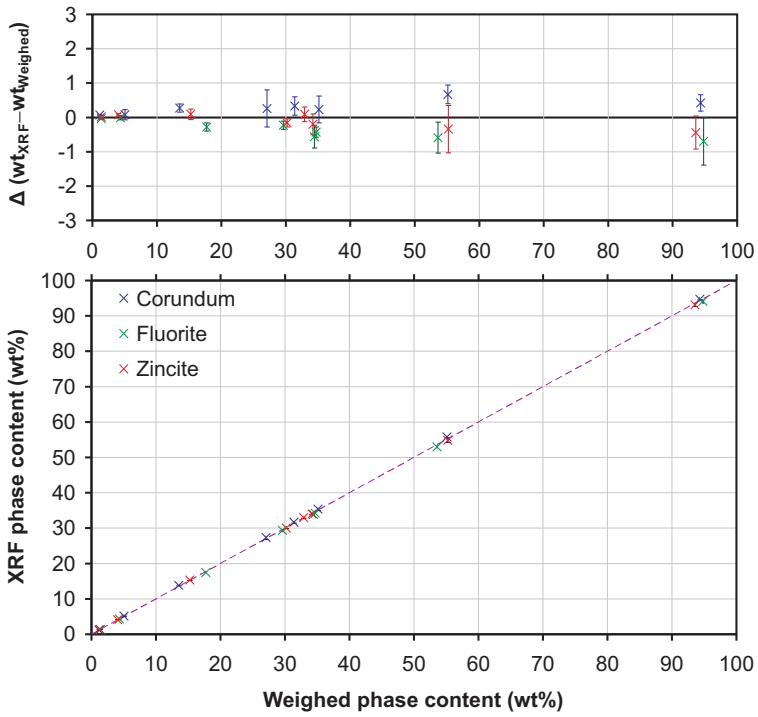

Figure 2.17: Phase content data from XRF against the true weighed values for various mixtures. Error bars are shown are 3×standard error.

from a sample of the pure phase, which were then fixed when looking at QPA in multi-phase samples. Unless specifically mentioned, only lattice parameters, peak shape function parameters and a scale function were refined for each phase present.

2.6 Mass Spectrometry

Mass spectrometry is an analytical technique which measures the amount of gaseous charged ion species with a certain mass to charge (m/z) ratio. Mass spectrometers are capable of scanning across a range of m/z values and determining the relative amount of each observed. Certain m/z ratios corresponding to species of interest can be selectively detected to determine the amount in a given analyte. Ions are charged species and, as such, can be manipulated with the use of electromagnetic fields. Mass spectrometry uses electromagnetic fields to

separate ions in the gas phase at very low pressures to detect species according to their m/z values. The maintenance of very low pressures by the use of a vacuum system is essential to the m/z separation process so that ions do not collide with other species during the mass selection process. A mass spectrometry experiment consists of three main processes: ionisation, separation and detection [92].

Ionisation

Ionisation converts the atoms/molecules of the analyte into gas-phase ionic species by the removal or addition of an electron or proton. Although there are many forms of ionisation used in mass spectrometry, the most common for gaseous analytes, and the only one used in this work, is electron ionisation (also known as electron impact, EI).

An electron beam generated from a tungsten filament is used to knock an electron from analyte atoms or molecules to create a singly charged cation. The energy of the electron beam is usually tuned so as to cause a significant amount of singly ionised species, but without multiple ionisation. The selection of species by m/z ratio means that the presence of exclusively singly charged species is preferable. The cations are then accelerated through a voltage and focused towards the analyser where separation occurs.

Fragmentation of ionic species can frequently occur upon ionisation. Excess energy from the ionisation process can cause the ionised species to break up into smaller species, the charged portion of which will also be detected at the corresponding lower m/z ratio. Molecules will frequently display a characteristic fragmentation pattern depending on the ionisation energy used. For larger organic molecules the fragmentation pattern is often used for phase identification. Fragmentation is an important feature of mass spectrometry that cannot be ignored. For the analytical determination of an analyte the fragmentation behaviour of the species must be understood.

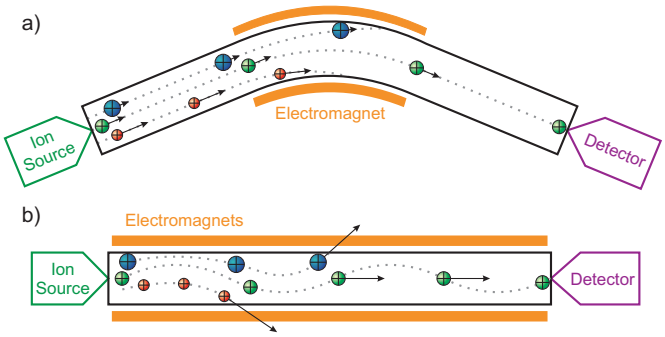

Figure 2.18: Comparison between (a) magnetic sector and (b) quadrupole mass spectrum analysers.

Separation

The separation of ionic species according to m/z ratio takes place in the analyser. The analyser in the first mass spectrometers was essentially a tunable electromagnet, known as a magnetic sector analyser. The degree to which a charged species is deflected in a magnetic field depends on its mass and charge (m/z). Lighter species get deflected more than heavier species of the same charge in the same magnetic field. The mass spectrometer scans through m/z values by varying the strength of the magnetic field so that different m/z values are successively aimed at the detector.

The most common method of ion selection is now the quadrupole mass analyser. Rather than bending charged particles in radius depending on their m/z values, quadrupole mass analysers use an electric field oscillating at radio frequency to selectively stabilise or destabilise the path of cations passing through it. The frequency of oscillation is used to select which m/z value is stabilised, and therefore which cations reach the detector at the expense of all other m/z values that get scattered, neutralised in collisions, and therefore are not detected. The mechanisms of magnetic sector and quadrupole mass analysers are compared in figure 2.18.

Detection

The detector measures the ion current generated by ions with each m/z value hitting the detector, amplifies the signal and then outputs the data as a mass spectrum. For large ion currents produced by majority components of the analyte a Faraday cup detector is used to collect and measure the separated ions. A Faraday cup is a conductive cup which emits electrons when a charged particle hits the inner surface. The current, which is directly related to the numbers of ions detected, is then amplified and recorded. If much larger sensitivity is required, a (secondary) electron multiplier is used. In an electron multiplier the electrons produced by the collision of the ion of interest are amplified in a series of electrodes, each at an increased potential. This creates a cascade of electrons for each electrode resulting in an amplification and corresponding increase in sensitivity of the order of $\times 10^6$.

Overview

A schematic of the type of mass spectrometer used in this study is shown in figure 2.19. The analyte is contained in a carrier gas of argon and is sampled through a heated capillary. The gas then passes into the vacuum system of the mass spectrometer with the small diameter of the capillary limiting the amount of gas entering the vacuum system so that a low enough pressure for mass spectrometry is maintained. The entire vacuum system is heated to reduce the amount of water present, which is ubiquitous (at low concentrations) in high vacuum applications.

In this study, mass spectrum data was first collected over the m/z range of 1 to 50 to identify what species were present. The mass spectrometer was then used in multiple ion monitoring (MIM) mode to detect only the ions of interest to increase the rate of data collection.

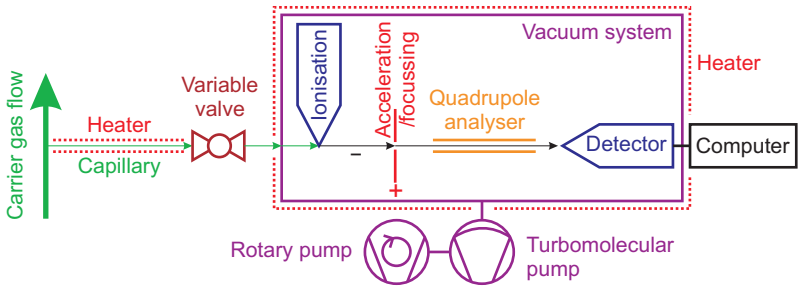

Figure 2.19: Schematic diagram of a mass spectrometer with the principal components labelled.

2.7 Temperature Programmed Desorption

Temperature programmed desorption (TPD) is the generic term for controlled heating of a sample while the desorption products are monitored. A sample is heated at a controlled rate in an atmosphere or in a vacuum while the gaseous desorption products are observed by mass spectrometry. In this study the thermal desorption properties of samples have been investigated using two home assembled temperature programmed desorption (TPD) apparatus, which are differentiated by the method of characterisation of the desorption products.

2.7.1 TPD-MS

Temperature programmed desorption under flowing argon was monitored using a mass spectrometer (TPD-MS). A mass flow controller (Hastings 200 Series, Teledyne) was used to control the flow of argon past the sample at a constant rate of 100 ml min^{-1}. The sample ($\sim$ 0.1 g) was weighed into a quartz reaction tube (7 mm O/D, 4 mm I/D) inside an argon filled glove box and sealed vertically in the reaction chamber. The sealed reaction chamber was then transferred onto the TPD apparatus without exposing the sample to atmosphere. A barrel heater surrounding the reaction chamber was controlled by an internal thermocouple which was in contact with the sample. The position of the thermocouple within the sample meant that endothermic and exothermic events were sometimes visible

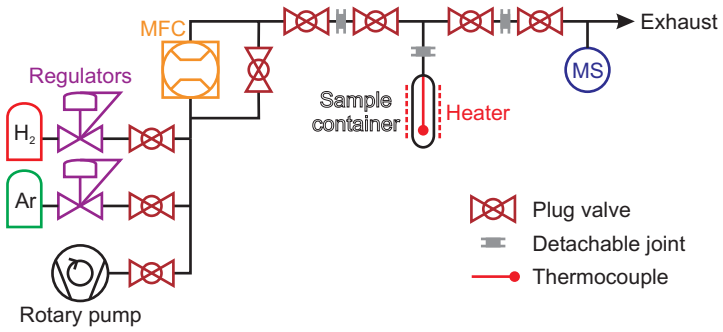

Figure 2.20: Schematic diagram of the TPD-MS apparatus with the principal components labelled.

in the temperature trace of the TPD. The gaseous desorption products were monitored using a quadrupole mass spectrometer (HPR-20, Hiden Analytical). Depending on the amount of sample, and therefore the amount of gas desorbed, the desorbed gases were monitored using a Faraday cup or secondary electron multiplier (SEM) detector for large and small samples respectively. A schematic diagram of the TPD-MS setup is shown in figure 2.20.

Calibration

In order to determine the true total sensitivity of the mass spectrometer towards hydrogen and ammonia, a calibration gas was used (BOC Speciality Gases, 4736 ppm H_2, 4898 ppm NH_3, balance Ar). Determining NH_3 in a mass spectrometer is problematic because the main $NH_3^{\bullet+}$ mass fragment has the same m/z value as the $OH^{\bullet+}$ fragment of water, which is ubiquitous in high vacuum systems such as a mass spectrometer. For this reason, the $NH_2^{\bullet+}$ fragment of NH_3, which is approximately 80% of the intensity of the $NH_3^{\bullet+}$ fragment, was used to determine the true amount of NH_3.

The calibration gas was flowed into the TPD apparatus *via* the mass flow controller in the same way as the argon carrier gas in the TPD-MS experiments. The observed partial pressures (P_n) for mass channels (m/z) 2 ($H_2^{\bullet+}$), 16 ($NH_2^{\bullet+}$), 17 ($NH_3^{\bullet+}/OH^{\bullet+}$), 18 ($H_2O^{\bullet+}$), 28 ($N_2^{\bullet+}$), 32 ($O_2^{\bullet+}$) and 40 ($Ar^{\bullet+}$) were recorded

until a consistent signal was reached. In order to determine the background signal for the desired mass channels 2 ($H_2^{\bullet+}$) and 16 ($NH_2^{\bullet+}$), the equivalent mass spectrum data were also collected for the pure argon carrier gas.

The total mass spectrum signal is dependent on the total amount of gas entering the mass spectrometer, so the observed partial pressure signals for mass channels 2 and 16 (P_2 and P_{16}) were converted to a fraction (x_2 and x_{16}) of the observed argon signal (P_{40}).

$$x_2 = \frac{P_2}{P_{40}} \qquad\qquad x_{16} = \frac{P_{16}}{P_{40}} \tag{2.21}$$

The observed fractional signals from the 2 and 16 mass channels for the pure carrier gas (x_2^0 and x_{16}^0) were then deducted from the fractional signal for the 2 and 16 mass channels for the calibration gas (x_2 and x_{16}). Relative sensitivity (RS) values for H_2 and NH_3 (R_{H_2} and R_{NH_3}) were then determined by dividing the background subtracted fraction signals for $H_2^{\bullet+}$ and $NH_2^{\bullet+}$ by the true molar fraction from the calibration gas certificate (4.736×10^{-3} and 4.898×10^{-3} respectively).

$$R_{H_2} = \frac{x_2 - x_2^0}{4.736 \times 10^{-3}} \qquad\qquad R_{NH_3} = \frac{x_{16} - x_{16}^0}{4.898 \times 10^{-3}} \tag{2.22}$$

The determined RS values were then used to correct the observed signals for $H_2^{\bullet+}$ and $NH_2^{\bullet+}$ obtained from TPD-MS experiments to give true values for H_2 and NH_3.

Upon collection of TPD-MS data for a sample the same mass channels were recorded as for the calibration using the same data collection routine. The MS data was collected for an appropriate time before the TPD heating profile was started so that background signals for the $m/z = 2$ and 16 (x_2^0 and x_{16}^0) mass channels could be determined. The MS data were again converted to a fraction of the argon signal (x_2 and x_{16}, equation 2.21). For the m/z 2 and 16 mass channels, the background signal determined before starting the heating profile was subtracted from subsequent signals and the corrected fractional signal was

divided by the determined RS values to give the corrected molar fractions of H_2 and NH_3 in the gas stream ($x^*_{H_2}$ and $x^*_{NH_3}$).

$$x^*_{H_2} = \frac{x_2 - x^0_2}{R_{H_2}} \qquad x^*_{NH_3} = \frac{x_{16} - x^0_{16}}{R_{NH_3}} \tag{2.23}$$

The corrected TPD-MS data could now be used to give accurate values for the relative amounts of H_2 and NH_3 released.

The inclusion of a mass flow controller in the TPD-MS experiment allowed for the molar fractions for H_2 and NH_3 in the gas stream to be processed further to produce pseudo–gravimetric data. The argon carrier gas flowed at a constant rate of 100 ml min^{-1} while the corrected MS data provided the mole fraction of H_2 and NH_3 present at each time ($x^*_{H_2}(t)$ and $x^*_{NH_3}(t)$) at regular time intervals (δt, in minutes) determined by the MS data collection rate.[†] Therefore, during the timescale of one MS data collection the volume of each gas (V_{H_2} and V_{NH_3}) and the total volume (in ml) of each gas released in a certain time interval ($V(t)$) could be determined.

$$V_{H_2}(t) = \sum_{t=0}^{t} 100 \times \delta t \times x^*_{H_2}(t) \qquad V_{NH_3}(t) = \sum_{t=0}^{t} 100 \times \delta t \times x^*_{NH_3}(t) \tag{2.24}$$

The molar volumes of H_2 and NH_3 at room temperature and pressure are 24.804 l mol^{-1} and 24.532 l mol^{-1} respectively [74]. The volume of gas released were used to provide an estimate of the number of moles of H_2 and NH_3 released by multiplying by 4.032×10^{-5} mol ml^{-1} and 4.076×10^{-5} mol ml^{-1} respectively. If the sample mass and molecular mass were known then the number of moles of each gas released could then be expressed in terms of the number of moles of the starting sample.

A simulated gravimetric plot could now also be prepared by a further data manipulation. Once the moles of gas released was known, then calculating the mass of each gas released (m_{H_2}) was trivial by multiplying by the molecular mass of the gas (2.02 g mol^{-1} for H_2). The mass of gas released was then deducted

[†]The data collection rate was approximately three complete mass spectra per minute.

from the starting mass of the sample (m_S, in g) and expressed as a percentage of the starting mass to give simulated wt% data.[†]

$$\text{wt\%(t)} = 100 \times \frac{m_S - \sum_{t=0}^{t} V_{H_2}(t) \times 4.032 \times 10^{-5} \times 2.02}{m_S} \tag{2.25}$$

Although this form of data analysis is convoluted, it allows for a more complete analysis of the desorbed gases in relation to the starting sample. This TPD-MS setup is much more resistant to ill behaved samples which melt and bubble and could easily damage more delicate thermo-gravimetric analysis (TGA) instruments which provide a more direct method of quantification. The TPD experimental setup is also relatively easily modified to fit most requirements. In summary, TPD-MS can be a valuable analytical technique which, after calibration, can give data far beyond simply which gases are released at what temperatures.

2.7.2 TPD-RGA

Temperature programmed desorption in high vacuum was measured using the Mass Analysis of Residuals in Vacuum INstrument (MARVIN). Approximately 1 mg of sample was added to a quartz reaction tube (7 mm O/D, 4 mm I/D) inside an argon filled glove box. This tube was then placed into a larger quartz tube which was fitted with an inline Young's tap *via* an Ultra-Torr® fitting. Gases desorbed were monitored using an MKS MicroVision Plus quadrupole residual gas analyser (RGA).

An RGA is essentially the quadrupole mass analyser from a mass spectrometer (see section 2.6). In order for the RGA to function properly a high level of vacuum must be maintained. To facilitate this, the glassware used was dried and degassed under high vacuum (approximately 5×10^{-7} mbar) at 500°C overnight before transferring to an argon glove box to load the sample. The sample was attached

[†]The example shown here includes only hydrogen in the wt% calculation. In principle a combination of any calibrated gas can be used.

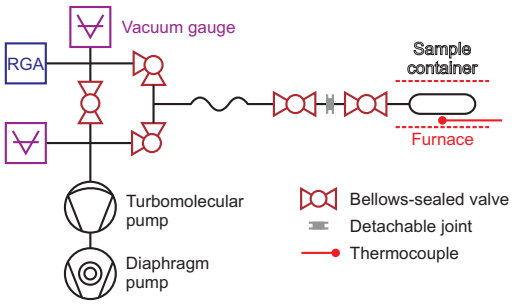

Figure 2.21: Schematic diagram of TPD-RGA apparatus with the principal components labelled.

onto the vacuum system and degassed to high vacuum for a period of a few hours. Before heating the sample, the RGA filament was turned on to allow it to degas. Only once the partial pressure values measured had reached a steady nominal value was the measurement started. An external furnace was used to heat the sample and a thermocouple placed on the outer quartz tube was used to monitor the sample temperature. A schematic diagram of the TPD-RGA setup of MARVIN is shown in figure 2.21.

Unlike for TPD-MS, the TPD-RGA experiment is very difficult to calibrate accurately due to the very small sample size and differences in pumping rates for different gases in the vacuum system. As such, data from TPD-RGA experiments were only qualitative in the form of what gases were released in approximate relative amounts at each temperature. The partial pressure values directly from the RGA software are quoted.

2.8 Intelligent Gravimetric Analysis

An Intelligent Gravimetric Analyser (IGA, Hiden Analytical) is a pressure controlled thermo-gravimetric balance with complete environmental control. The sample is loaded in a crucible[†] and placed on a hang-down attached to a microbalance head. The weight of the sample is then monitored under different

[†]Quartz crucibles were prepared in-house for this study

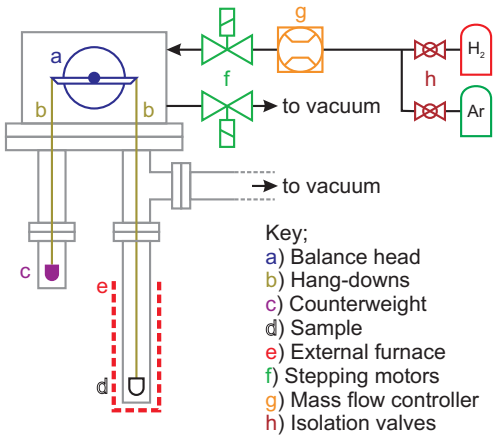

Figure 2.22: Schematic diagram of an IGA with the principal components labelled.

environmental conditions so that weight changes can be observed upon changing temperature and pressure. The sample, microbalance head and counterweight all share the same environment which helps to reduce the effects of buoyancy on the observed sample mass. The temperature of the sample is controlled using an external furnace which surrounds the reaction tube housing the sample hang-down. Sample temperature is monitored by a positive temperature coefficient (PTC) sensor located next to the sample. A schematic diagram of an IGA is shown in figure 2.22.

2.8.1 Pressure Control Mode

The IGA used in this study had stepping motors on the gas inlet/outlet so that the pressure inside the reactor could be precisely controlled from 50 mbar to 20 bar. A variety of gases could be connected to the IGA inlet, although in this study only Ar or H_2 were connected. In pressure control mode, a pressure set point and ramp rate is selected. The IGA then admits gas up to the desired pressure by continually admitting small amounts of gas *via* the inlet stepping motor. The pressure is then maintained at the set-point value by the continual admission of small amounts of gas while the sample mass is monitored. The

outlet is connected to a vacuum system and pressure is reduced by continually bleeding small amounts of gas into this vacuum system. Pressure control mode was used to observe hydrogenation of samples under an atmosphere of hydrogen.

2.8.2 Flowing Gas Mode

For thermal desorption data, a constant flow of gas within the IGA reactor could be controlled *via* external mass flow controllers. A pressure and flow rate is set for Ar, H_2, or any mix of the two, which then flowed directly over and around the sample. A flow of pure argon at a rate of 100 ml min^{-1} at 1 bar was used to monitor the thermal desorption properties upon heating a sample in IGA-MS measurements. A mass spectrometer (Hiden Analytical, HPR20-QIC Atmospheric Gas Analysis System) was used to monitor gases released from the head-space above the sample.

2.8.3 Inert Sample Loading

The use of a portable glove box allowed for samples to be loaded onto and removed from the IGA without contact with air. After the dry mass of the sample crucible had been recorded, approximately 100 mg of sample was loaded into the crucible inside an argon filled glove box and sealed inside a sample cartridge. The cartridge was then removed from the glove box and inserted into a portable glove box attached to the IGA. The portable glove box was then purged of air by cycling between 1050 mbar and 1250 mbar of argon 100 times. The sample cartridge was then opened and the sample crucible was transferred on to the balance hang-down using a mechanical arm.

2.9 Differential Scanning Calorimetry

Differential scanning calorimetry (DSC) is the calorimetric measurement of the exothermic and endothermic processes occurring upon the controlled heating and

cooling of a sample. Useful information on the temperature and enthalpy of phase transitions such as melting, crystallisation and reactions can be obtained. DSC involves the measurement of the change of the difference in the rate of heat flow (power) to/from a sample relative to a (thermally inert) reference sample when both are subjected to the same temperature program regime.

DSC is a more advanced derivative of differential thermal analysis (DTA) [93]. In the case of DTA, a sample and a reference material are both heated in the same furnace and the difference in temperature between the sample and the reference, measured by appropriately placed thermocouples, is plotted as a function of time or furnace temperature. If the sample undergoes an endothermic event, such as melting, the sample temperature will lag behind that of the reference material until the melting event is complete and normal heating can be resumed. In this way the temperatures at which exothermic and endothermic events occur can be observed. The data obtained from DTA experiments is normally semi-quantitative at best. DSC allows for the collection of truly quantitative calorimetric data.

The principles involved in a DSC measurement share many similarities to the more basic DTA experiment. In a heat flux DSC measurement, it is the heat flow to/from the sample (and reference) which is recorded, rather than the sample temperature. As such, this has a much more direct relation to the enthalpy of the thermal event being observed. The exchange of heat to the sample (and reference) mainly takes place *via* a well defined pathway, through a material with a known thermal resistance [94]. The temperature of this conduction pathway (typically a metal disk) is monitored for the sample and the reference and the temperature difference between the two is proportional to the difference in heat flow rates for the sample and reference. In a DSC experiment the sample environment is normally controlled. A schematic of a typical heat flow DSC experimental setup is shown in figure 2.23.

In order for quantifiable data to be obtained from a DSC measurement, the sample mass must be accurately known and careful calibration is required. Accu-

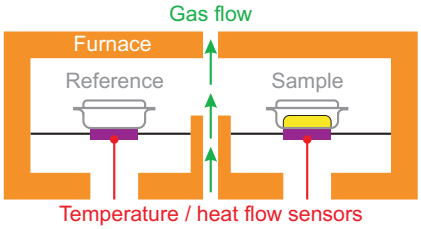

Figure 2.23: Experimental setup for a DSC measurement with the principle components labelled.

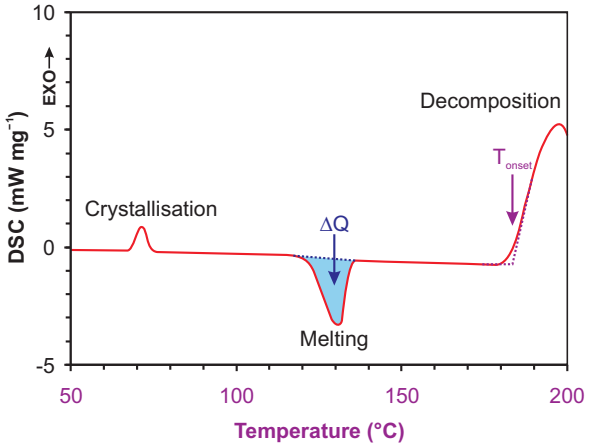

Figure 2.24: Example of a typical DSC trace. The method of determining ΔQ and T_{onset} values are shown in blue and purple respectively.

rate temperature data is achieved using a multi-point calibration using the melting point of high purity metals in the temperature range desired. The observed melting point transition temperature is then used to produce a temperature calibration curve. The observed transition temperature frequently depends on the heating rate used and so this calibration must be performed for each heating rate used. The calibration of the observed heats of reaction also needs to be carried out, typically using a phase transition with a well defined enthalpy associated with it. Consistent sample sizes should also be used as a larger sample size will often cause an apparent increase in onset temperature of any observed event due to thermal lag.

A typical DSC measurement in shown in figure 2.24. The corrected measured value quoted is in units of mW mg^{-1}. If the sample mass and molecular formula

is known, molar enthalpy values can be derived from a properly calibrated DSC measurement. The area of a thermal event gives the heat flow (ΔQ) for that event per mass of sample. A baseline for the thermal event must be determined as the heat capacity of the sample will cause a deviation from a zero value for the heat flow at each point. The onset temperature of thermal events is determined from where the tangent at the maximum rate of change of heat flow meets the baseline. This value is less sensitive to factors such as sample size and heating rate than onset values determined from visual inspection.

DSC measurements were performed on a calibrated DSC 204 HP Phoenix, NETZSCH, which was housed inside a flowing argon glove box. Samples of approximately 8 mg were loaded into a shallow Al pan fitted with a lid. The sample was spread over the base of the sample pan to improve thermal uniformity and the sample mass was recorded to and accuracy of 0.001 mg. The reference used was an empty Al sample pan, with lid. A constant atmosphere of 4 bar Ar was achieved inside the DSC at a flow rate of 100 ml min^{-1}. Typical experiments involved a ramp at 2°C min^{-1} to 250°C, a dwell time at 250°C of 20 minutes followed by cooling at 2°C min^{-1} to room temperature.

2.10 Infrared Spectroscopy

The energy of infrared radiation is of the order of the energy required for the vibration of chemical bonds. If the energy of the incident photon corresponds to the energy gap between the vibrational ground state of a molecule and an excited state, the photon may be absorbed to excite the molecule to a higher vibrational state. The infrared spectrum results from transitions between vibrational energy states. Typical molecular transitions from the ground vibrational state ($\nu = 0$) to the first excited state ($\nu = 1$) correspond to the mid-infrared region of the electromagnetic spectrum (400 cm^{-1} to 4000 cm^{-1}) and these are the transitions most frequently observed.

In order for a vibration to be infrared active it must result in a change in the molecular dipole moment. Asymmetric stretching vibrations tend to cause a greater change in the molecular dipole moment and therefore normally result in more intense absorption bands than the equivalent symmetric stretch. Molecular symmetry can cause certain vibrations to be degenerate with others resulting in more intense absorption bands, whereas other vibrations can be rendered completely forbidden by symmetry.

The amount of infrared radiation absorbed by the sample at each wavelength is used to generate an infrared spectrum. Infrared radiation is passed through the sample and the intensity (I) at each wavelength in compared to the intensity of a blank (I_0, the infrared radiation without the sample present). The absorbance (A) is calculated and plotted as a function of wavelength.

$$A_\lambda = -\log_{10}(I/I_0) \tag{2.26}$$

In the case of Fourier transform infrared spectroscopy (FTIR), all wavelengths of infrared radiation are passed through the sample at the same time. Fourier transform is a mathematical process which then separates out the resulting waveform into its constituent wavelengths.

FTIR spectra were acquired on a Nicolet Magna FTIR spectrometer at a resolution of 2 cm^{-1}. Samples were ground with dried KBr inside an argon filled glove box and pressed into disks. The sample–KBr disks were quickly removed from the glove box and loaded into the spectrometer where dry nitrogen was passed over the sample during data collection.

2.11 Raman Spectroscopy

Raman spectroscopy is a form of vibrational spectroscopy where vibrations in molecules and crystals are observed by the process of Raman scattering. A single wavelength of radiation (from infrared to ultraviolet) is used to irradiate the

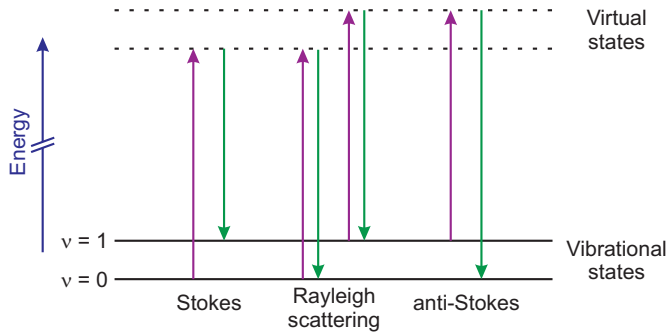

Figure 2.25: Diagram of the Raman and Rayleigh scattering processes. The incident energy and scattered energy are represented in purple and green respectively.

sample. The radiation scattered from the molecules which is shifted by one vibrational unit of energy is detected. It is the difference in energy from that of the incident radiation which is of interest in vibrational spectroscopy.

In scattering, the incident light interacts with the molecule and polarises the electron cloud surrounding the constituent nuclei of the molecule to form a short-lived excited state known as a "virtual state". The energy of this state depends on the energy of the incident radiation. This state is unstable and quickly relaxes with the release of a photon of a different energy. In the majority of scattering events, only electron cloud distortion is involved in the scattering process and the difference in energy between the incident photon and the scattered photon will be very small due to the relatively light nature of electrons. This scattering process, known as Rayleigh scattering, can be regarded as essentially elastic in nature. In a small proportion of scattering events nuclear motion may be induced in the molecule. In this case a significant amount of energy may be transferred between the photon and the molecule. In these inelastic "Raman scattering" events the energy of the scattered photon differs from that of the incident photon by the energy of the motion induced in the molecule. For vibrational Raman spectroscopy, the nuclear motions of interest induced in the inelastic scattering events are of the form of molecular vibrations.

A schematic illustration of the energy exchanged during these scattering

events is shown in figure 2.25. The vast majority of scattering events are of the elastic Rayleigh type, with essentially no change in the energy of photons involved. The Raman scattering process from the lowest energy (ground) vibrational state leads to the absorption of energy by the molecule and the resulting excitation to a higher energy (excited) vibrational state. The resulting scattered photon will be reduced in energy by the energy of that vibrational state, which is known as Stokes scattering. If a molecule in an excited vibration state ($\nu = 1$ in figure 2.25) undergoes scattering, the vibrational energy can be transferred to the scattered photon, increasing the energy relative to the incident radiation. This process is known as anti-Stokes scattering. At room temperature the majority of molecules are in their lowest energy vibrational state ($\nu = 0$ in figure 2.25) and so Stokes scattering is the dominant form of Raman scattering which is used for vibrational Raman spectroscopy. As the amount of thermal energy (temperature) increases, the relative amount of anti-Stokes to Stokes scattering will increase.

In order for a molecular vibration to be Raman active, the vibration must cause a change in the magnitude or direction of the polarisability of the molecule. The most intense bands in Raman spectra are usually due to symmetrical vibrations compared with asymmetric vibrations which are relatively weak. The symmetry of the molecule determines what vibrations are Raman active.

Raman spectra were collected on a Renishaw InVia Raman microscope using a Ar ion laser at a wavelength of 488 nm. Samples were loaded into an Instec sample cell in an argon filled glove box. The sample cell was then transferred onto the Raman microscope and Ar gas was flowed over the samples at a pressure of 1 bar during data collection.

Chapter 3

$Li_4BH_4(NH_2)_3$

3.1 Introduction

When this research was started there were no known mixed anion complex hydrides. Initial investigations were into 1:1 reactions of $LiBH_4$ and $LiNH_2$ but it was found that excess $LiBH_4$ remained. $2LiNH_2$ + $LiBH_4$ mixtures were found to form almost completely a new cubic phase with only small amounts of $LiBH_4$ remaining. This was initially attributed to Li_2O impurities in the $LiNH_2$ causing there to be less $LiNH_2$ present than expected. During this research it became clear that the true stoichiometry was 1:3 and the structure of this mixed anion complex hydride, $Li_4BH_4(NH_2)_3$, was solved. The spectroscopic and hydrogen desorption properties of this new phase were investigated.

3.2 Experimental

Lithium amide and lithium borohydride (Sigma-Aldrich, 95% purity) were ground together in a 3:1 ratio in an argon filled glove box (>10 ppm O_2, >1 ppm H_2O) and heated under argon gas at 190°C. The sample was reground and annealed at 190°C to improve the crystallinity of the sample. Powder synchrotron X-ray diffraction data were collected on the ID31 diffractometer at the ESRF, Grenoble,

at a wavelength and stepsize of 0.80102 Å and 0.003°, respectively. The sample was loaded into a glass capillary inside a nitrogen filled glove bag and sealed on a miniature gas torch. Neutron powder diffraction data were collected on GEM at the ISIS spallation neutron source at the Rutherford Appleton Laboratory. The sample was sealed inside a vanadium can with an iridium wire seal, inside an argon filled glove box.

3.3 Crystal Structure Determination

The crystal structure of $Li_4BH_4(NH_2)_3$ was determined in collaboration with Professor W. I. F. David, ISIS Facility, Rutherford Appleton Laboratories, Oxfordshire, from powder diffraction data using the computer program Topas [90]. During the structural determination the stoichiometry of the pure phase was established and the resulting structure was found to be closely related to the $LiNH_2$ structure.

3.3.1 Infrared Spectroscopy

Infrared spectroscopy was performed in order to determine whether the BH_4^- and NH_2^- groups remained intact from the starting materials. The infra-red spectrum of the amide–borohydride phase, analysed in more detail in section 3.5 (figure 3.21), shows the characteristic BH_4^- and NH_2^- stretches centred around 2300 cm^{-1} and 3300 cm^{-1}, respectively, confirming that these groups remain intact.

3.3.2 Indexing

The regular spacing of observed Bragg reflections suggested a cubic lattice. A trial-and-error method utilising ChekCell [95] to provide a graphical indication of fit gave a lattice parameter of ≈ 10.7 Å. Investigation of the systematic absences of the diffraction pattern indicated that the phase has body centred symmetry

Table 3.1: Special positions available in each possible space group.

$I23$	$I2_13$	$Im\bar{3}$	$I432$	$I\bar{4}3m$	$Im\bar{3}m$
No. 197	No. 199	No. 204	No. 211	No. 217	No. 229
$24f$ (x,y,z)	$24c$ (x,y,z)	$48h$ (x,y,z)	$48j$ (x,y,z)	$48h$ (x,y,z)	$96l$ (x,y,z)
$12e$ $(x,1/2,0)$	$12b$ $(x,0,1/4)$	$24g$ $(0,y,z)$	$24i$ $(1/4,y,\bar{y}+1/2)$	$24g$ (x,x,z)	$48k$ (x,x,z)
$12d$ $(x,0,0)$	$8a$ (x,x,x)	$16f$ (x,x,x)	$24h$ $(0,y,y)$	$24f$ $(x,1/2,0)$	$48j$ $(0,y,z)$
$8c$ (x,x,x)		$12e$ $(x,0,1/2)$	$24g$ $(x,1/2,0)$	$12e$ $(x,0,0)$	$48i$ $(1/4,y,\bar{y}+1/2)$
$6b$ $(0,1/2,1/2)$		$12d$ $(x,0,0)$	$16f$ (x,x,x)	$12d$ $(1/4,1/2,0)$	$24h$ $(0,y,y)$
$2a$ $(0,0,0)$		$8c$ $(1/4,1/4,1/4)$	$12e$ $(x,0,0)$	$8c$ (x,x,x)	$24g$ $(x,0,1/2)$
		$6b$ $(0,1/2,1/2)$	$12d$ $(1/4,1/2,0)$	$6b$ $(0,1/2,1/2)$	$16f$ (x,x,x)
		$2a$ $(0,0,0)$	$8c$ $(1/4,1/4,1/4)$	$2a$ $(0,0,0)$	$12e$ $(x,0,0)$
			$6b$ $(0,1/2,1/2)$		$12d$ $(1/4,0,1/2)$
			$2a$ $(0,0,0)$		$8c$ $(1/4,1/4,1/4)$
					$6b$ $(0,1/2,1/2)$
					$2a$ $(0,0,0)$

with $I23$, $I2_13$, $Im\bar{3}$, $I432$, $I\bar{4}3m$ and $Im\bar{3}m$ (see table 3.1) as the most probable space groups. This assignment was confirmed by Prof. David using the computer program DASH [96]. The lattice constant and unit cell volume were refined in a Pawley fit using Topas [90] as 10.66445(1) Å and 1212.875(3) Å^3, respectively.

3.3.3 Determining Stoichiometry and Crystallographic Density

While work on the structure solution of this cubic phase was in progress, a paper was published on the composition $Li_3BN_2H_8$ [97]. A new body-centred cubic phase was identified with a lattice constant of $a = 10.76$ Å and a sample density, as measured by a He gas pycnometer, of 0.96 g cm^{-3}. Our previous experiments at the 1:2 stoichiometry had always produced the body-centred cubic phase with an excess of $LiBH_4$ as illustrated in figure 3.1. For a presumed 1:2 stoichiometry of the cubic phase to account for the excess of $LiBH_4$ a substantial impurity in the $LiNH_2$ would be required. Although there was a Li_2O impurity observed in the diffraction pattern of $LiNH_2$ this was not enough to account for the excess of $LiBH_4$ observed.

Preliminary experiments were performed by heating different mixtures of $LiBH_4$ and $LiNH_2$ over the entire composition range. A body-centred cubic phase

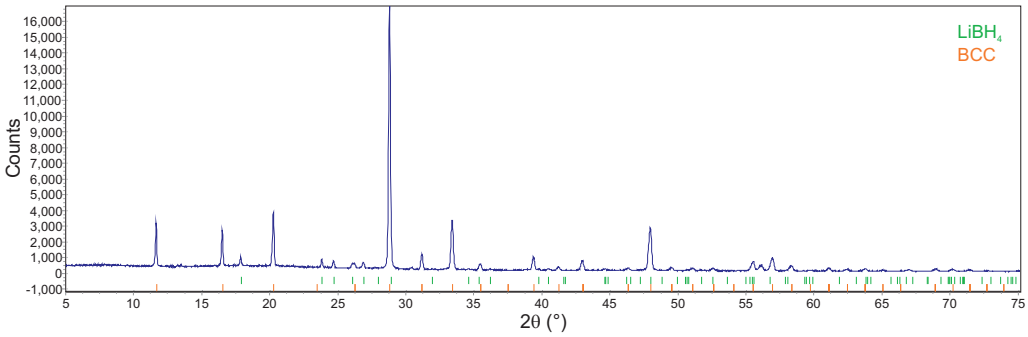

Figure 3.1: Powder X-ray diffraction pattern of the products of the reaction $2LiNH_2 + LiBH_4$. Bragg reflection positions for $LiBH_4$ and the BCC lattice are shown in green and orange respectively.

with a unit cell of around 10.7 Å was always present across the full composition range. The 20:80 composition contained an amide impurity while $LiBH_4$ was detected in the 30:70 composition. We concluded that the most likely composition was 25:75.

The case for a 1:3 stoichiometry, rather than the 1:2 stoichiometry proposed, is backed up by consideration of the volumes of the single formula unit of the starting materials, the crystallographic densities and the multiplicity of Wyckoff positions present in the most probable space groups. Assuming that the $LiBH_4$ and $LiNH_2$ formula units occupy a similar volume (54.2 $Å^3$ [98] and 32.6 $Å^3$ [99], respectively) in the new phase to that of the starting materials, we arrive at $Z = 10.16$ for a 1:2 ratio material. For a 1:3 stoichiometry, this leads to a value of 7.98 formula units in the unit cell, which is a strong indication that there are 8 formula units of $Li_4BH_4(NH_2)_3$ in the unit cell ($Z = 8$).

The calculated crystallographic density for a 1:3 stoichiometry with $Z = 8$ is 0.99 g cm^{-3}, which is close to the reported value of 0.96 g cm^{-3} [97] for a ball milled "$Li_3BN_2H_8$" phase. For a density of 0.96 g cm^{-3}, the calculated number of 1:2 stoichiometry formula units, Z, is 10.35.

Of the Wyckoff positions available in the most probable space groups (see table 3.1), it is possible to have a 1:3 stoichiometry with $Z = 8$ by occupying sites

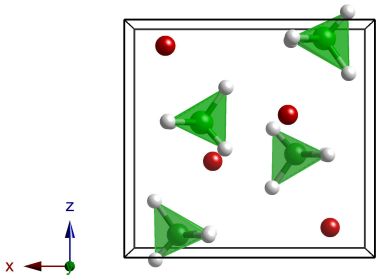

Figure 3.2: Crystal structure of $LiBH_4$ [98]. Boron is shown in green, lithium in red and hydrogen in grey. The unit cell is shown in black.

of 8 and 24 multiplicity with B and N atoms, respectively. A 1:2 stoichiometry is possible for $Z = 10$, which is close to the values of $Z = 10.16$ calculated by considering the unit cell volumes of the starting materials, with space groups $Im\bar{3}$, $I432$ and $Im\bar{3}m$ by occupying sites of 2 and 8 multiplicity for B atoms and sites of 16 and 24 multiplicity for N atoms. This arrangement, even when optimised to maximise inter-atomic distances, still generates distances of as little as 2.32 Å, which is much less than the observed B-B and N-N distances in $LiBH_4$ (3.71 Å) and $LiNH_2$ (3.36 Å), respectively.

From these observations we concluded that the structure was most likely $Li_4BH_4(NH_2)_3$ with 8 formula units in the unit cell.

3.3.4 Producing a Model

The structures of the starting materials, $LiBH_4$ [98] and $LiNH_2$ [99] (figures 3.2 and 3.3, respectively), were investigated as possible starting points for structural determination.

It was noted that four tetragonal unit cells of $LiNH_2$ ($a = 5.037$ Å, $c = 10.278$ Å) aligned in the ab plane would give a pseudo-cubic structure of a similar size to the observed unit cell of the new phase (figure 3.4). The $LiNH_2$ structure was normalised so that each atom was on idealised coordinates, as shown in table

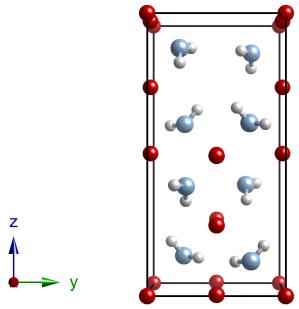

Figure 3.3: Crystal structure of $LiNH_2$ [99]. Nitrogen is shown in blue, lithium in red and hydrogen in grey. The unit cell is shown in black.

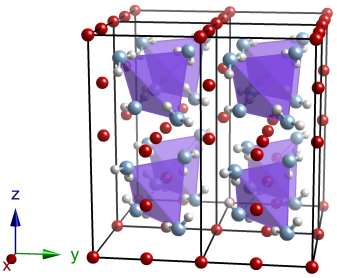

Figure 3.4: Four unit cells of $LiNH_2$ giving a pseudo-cubic structure. Nitrogen is shown in blue, lithium in red and hydrogen in grey. The unit cells are shown in black.

Table 3.2: Literature structure of $LiNH_2$ and idealised atomic positions.

Atom	Site	Jacobs [99]	Normalised
N	8g (x,y,z)	(0.2284,0.2452,0.1148)	($^1/_4$,$^1/_4$,$^1/_8$)
Li(1)	2a (0,0,0)	(0,0,0)	(0,0,0)
Li(2)	2c (0,$^1/_2$,$^1/_4$)	(0,$^1/_2$,$^1/_4$)	(0,$^1/_2$,$^1/_4$)
Li(3)	4f (0,$^1/_2$,z)	(0,$^1/_2$,0.0042)	(0,$^1/_2$,0)

Hydrogen atom positions have been disregarded.

3.2 and figure 3.5, and re-sized so that $c = 2a = 10.66$ Å, the size of the cubic $Li_4BH_4(NH_2)_3$ unit cell.

This structure (figure 3.5) was transformed to a cubic unit cell and then interrogated for symmetry elements using the computer program Endeavour [100].

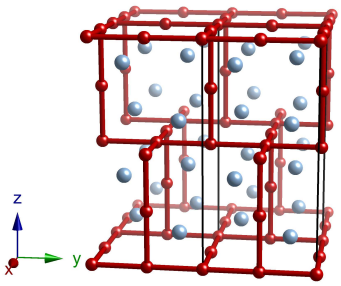

Figure 3.5: Idealised pseudo-cubic $LiNH_2$ structure. Nitrogen is shown in blue and lithium is shown in red. The unit cell of the parent $LiNH_2$ structure is shown in black. Hydrogen atoms are disregarded.

Although this structure could not be generated in cubic symmetry[†] the body-centred arrangement of N atoms could be recreated in body-centred cubic symmetry by occupation of 8 and 24 multiplicity sites in the space groups $I23$ and $I2_13$. The availability of two different sites of 8 and 24 multiplicity allow for B and N in a 1:3 ratio in both of these space groups. The difference between the idealised B/N arrangement in $I23$ and $I2_13$ is down to the relative ordering of the B/N atoms, as shown in figures 3.6 and 3.7, respectively. In $I23$ there are local clusters of boron whereas in $I2_13$ the boron atoms are more evenly distributed throughout the unit cell. Preliminary Rietveld refinements using Topas [90] including just B and N atoms (the most prominent X-ray scatterers) in these two symmetries showed little differentiation between the two symmetries.

Although it is not possible to generate the lithium atomic arrangement from the $LiNH_2$ structure in cubic symmetry, a slight rearrangement of the lithium lattice can give a possible structure which can be generated in $I2_13$, as shown in figure 3.8 and listed in table 3.3.

Both symmetries, $I23$ and $I2_13$, can generate lithium atoms at $(^l/_4,^m/_4,^n/_4)$ (where l,m,n = 0,1,2,3) sites, similar to the positions observed in the $LiNH_2$, as listed in table 3.4.

[†]The highest possible symmetry to generate this structure was $P2$.

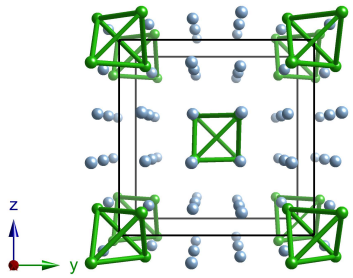

Figure 3.6: Idealised body centred boron/nitrogen arrangement in $I23$. Boron is shown in green and nitrogen is shown in blue. The unit cell is shown in black.

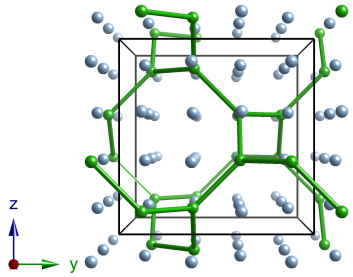

Figure 3.7: Idealised body centred boron/nitrogen arrangement in $I2_13$. Boron is shown in green and nitrogen is shown in blue. The unit cell is shown in black.

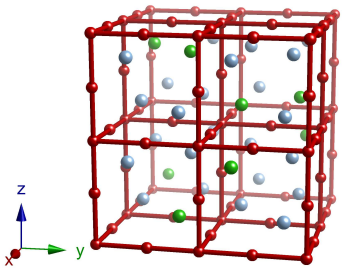

Figure 3.8: Idealised body centred Li/B/N arrangement in $I2_13$. Boron is shown in green, nitrogen in blue and lithium in red.

Table 3.3: Atomic coordinates for a model Li/B/N structure in $I2_13$.

Atom	Site	Coordinates
B	8a (x,x,x)	(0.125,x,x)
N	24c (x,y,z)	(0.375,0.375,0.125)
Li(1)	8a (x,x,x)	(0.000,x,x)
Li(2)	12b (x,0,1/4)	(0.000,0,1/4)
Li(3)	12b (x,0,1/4)	(0.500,0,1/4)

Table 3.4: Possible Li positions in $I23$ and $I2_13$.

Atom	$I23$ Site	Coordinates	$I2_13$ Site	Coordinates
Li(1)	2a (0,0,0)	(0,0,0)	8a (x,x,x)	(0,x,x)
Li(2)	6b (0,1/2,1/2)	(1/4,x,x)	8a (x,x,x)	(1/4,x,x)
Li(3)	8c (x,x,x)	(1/4,1/4,1/4)	12b (x,0,1/4)	(0,0,1/4)
Li(4)	12d (x,0,0)	(1/4,0,0)	12b (x,0,1/4)	(1/4,0,1/4)
Li(5)	12e (x,1/2,0)	(1/4,1/2,0)	12b (x,0,1/4)	(1/2,0,1/4)
Li(6)	24f (x,y,z)	(1/4,1/2,3/4)	12b (x,0,1/4)	(3/4,0,1/4)

This model, with boron and nitrogen forming a body centred lattice occupying half of the ($^{[2l+1]}/_8$,$^{[2m+1]}/_8$,$^{[2n+1]}/_8$) (where l,m,n = 0,1,2,3) and lithium atoms occupy a total of half of the possible ($^l/_4$,$^m/_4$,$^n/_4$) (where l,m,n = 0,1,2,3) sites, was then used for full Rietveld refinement.

3.3.5 Rietveld Refinement

Rietveld refinement was first performed against the synchrotron X-ray powder diffraction data using Topas [90]. At this stage both symmetries, $I23$ and $I2_13$, were considered. The B/N positions were refined, then fixed while occupancies of each of the possible Li sites (listed in table 3.4) were refined between values of 0 and 1. After refinement in both symmetries the $I2_13$ structure became favoured. The occupancies of sites Li(2) (1/4,1/4,1/4), Li(3) (0,0,1/4) and Li(6) (3/4,0,1/4) from table 3.4 tended towards a value of 1 while the other site occupancies reached zero. This leads to a total of 32 lithiums in the unit cell, the required amount for $Li_4BH_4(NH_2)_3$ with $Z = 8$. The resultant $I2_13$ preliminary structure is shown in

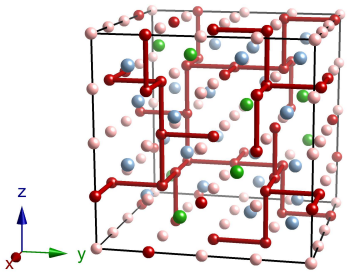

Figure 3.9: Refined B/N positions and remaining Li sites. Boron is shown in green, nitrogen in blue, lithium in red and unoccupied lithium sites in pink. The unit cell is shown in black.

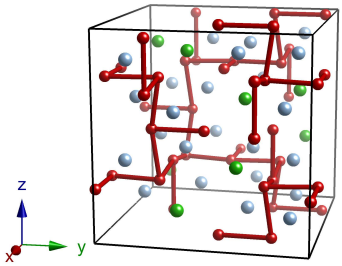

Figure 3.10: Refined Li/B/N positions. Boron is shown in green, nitrogen in blue and lithium in red. The unit cell is shown in black.

figure 3.9. For $I23$, the best fits were achieved for structures with the incorrect number of lithium atoms present and partially occupied lithium sides.

The determined lithium site occupancies were then fixed at a value of 1, and all of the atomic positions refined. This resulted in minor movements of the lithium atoms from their idealised arrangement, as shown in figure 3.10.

Hydrogen atoms were then introduced by adding rigid bodies for the BH_4^- and NH_2^- ions. The NH_2^- ion was placed at the refined nitrogen position and allowed to rotate while the bond length and bond angle were refined from the starting values of 1.0 Å and 107°. The B occupies a site symmetry of point group type 3, i.e. it lies on the three fold rotational axis of the cubic unit cell,

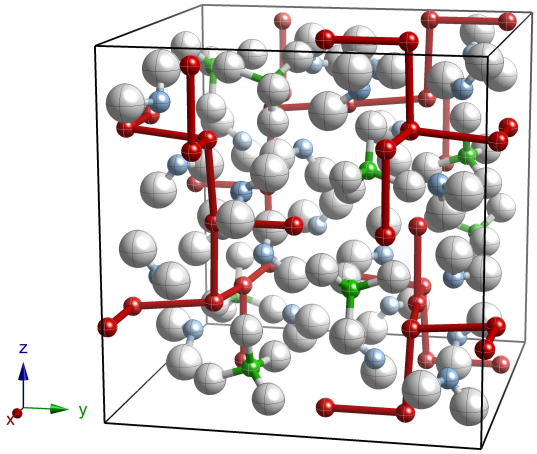

Figure 3.11: Refined crystal structure of $Li_4BH_4(NH_2)_3$. Boron is shown in green, nitrogen in blue, lithium in red and hydrogen in white. Atoms are represented as thermal ellipsoids of 75% probability. The unit cell is shown in black.

therefore adding a tetrahedral BH_4^- rigid body at this position will generate more hydrogen atoms than required. To accommodate this, the occupancy of hydrogen sites were merged when they approached within 0.7 Å of each other. Upon refinement, one of the hydrogen atoms moved towards a (x,x,x) position whereas the other hydrogen atoms moved on top of each other on a general (x,y,z) position, allowing the four hydrogen atoms of the BH_4^- to be generated with only two hydrogen positions.

The powder neutron diffraction data was now introduced for a joint refinement with the synchrotron X-ray diffraction data using the refined structure from the X-ray data as a starting point. Thermal parameters (B_{iso}) were refined from starting values of 1 Å^2. The thermal parameters for each type of atom (Li, B, N, H(B) and H(N)) were constrained at the same value. The resultant crystal structure and Rietveld plots for the X-ray and neutron data are shown in figures 3.11, 3.12 and 3.13, respectively, and the refined crystallographic data, and the bond distances and angles compared with those of $LiBH_4$ and $LiNH_2$, are shown in tables 3.5 and 3.6, respectively.

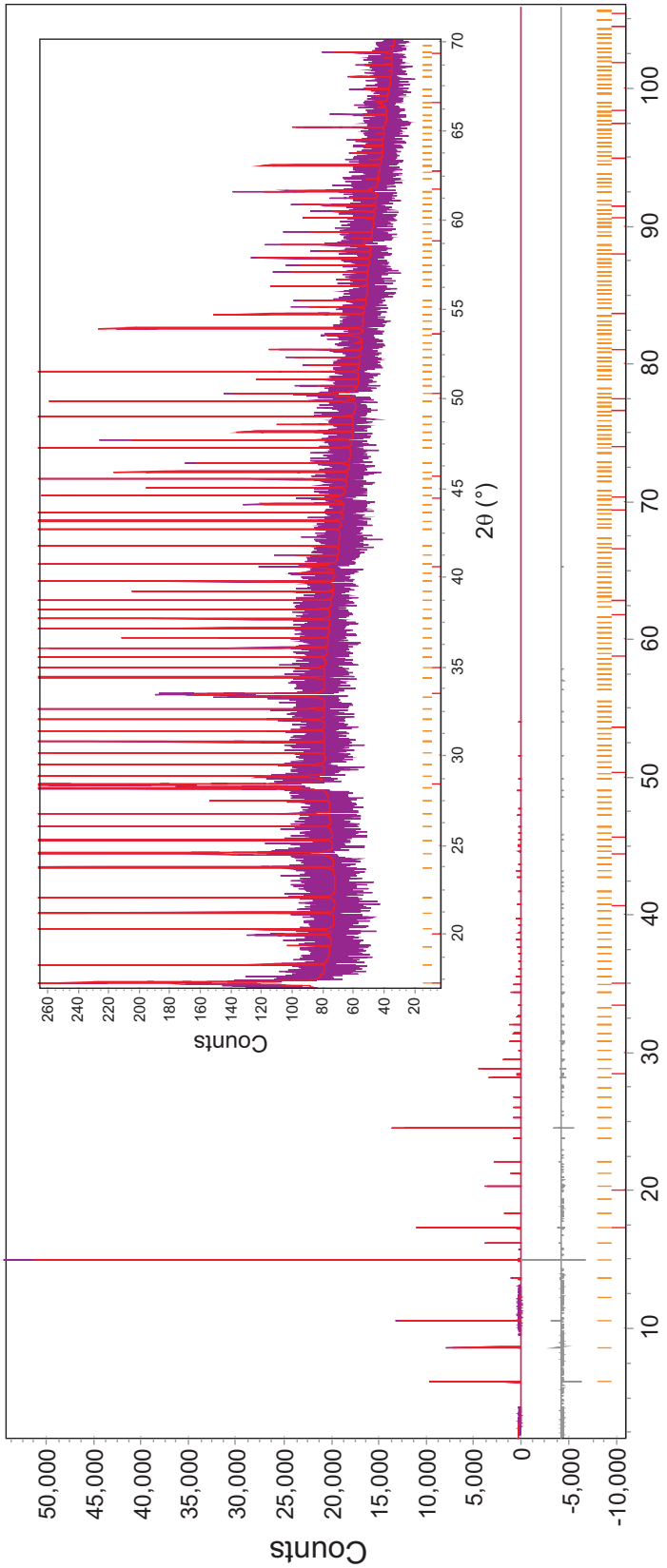

Figure 3.12: Final Rietveld plot for X-ray diffraction data of $Li_4BH_4(NH_2)_3$ showing observed (purple), calculated (red) and difference (grey) plots. The insert shows the low d-spacing region at a magnified scale. Peak positions for $Li_4BH_4(NH_2)_3$ (orange) and Li_2O (red) are indicated.

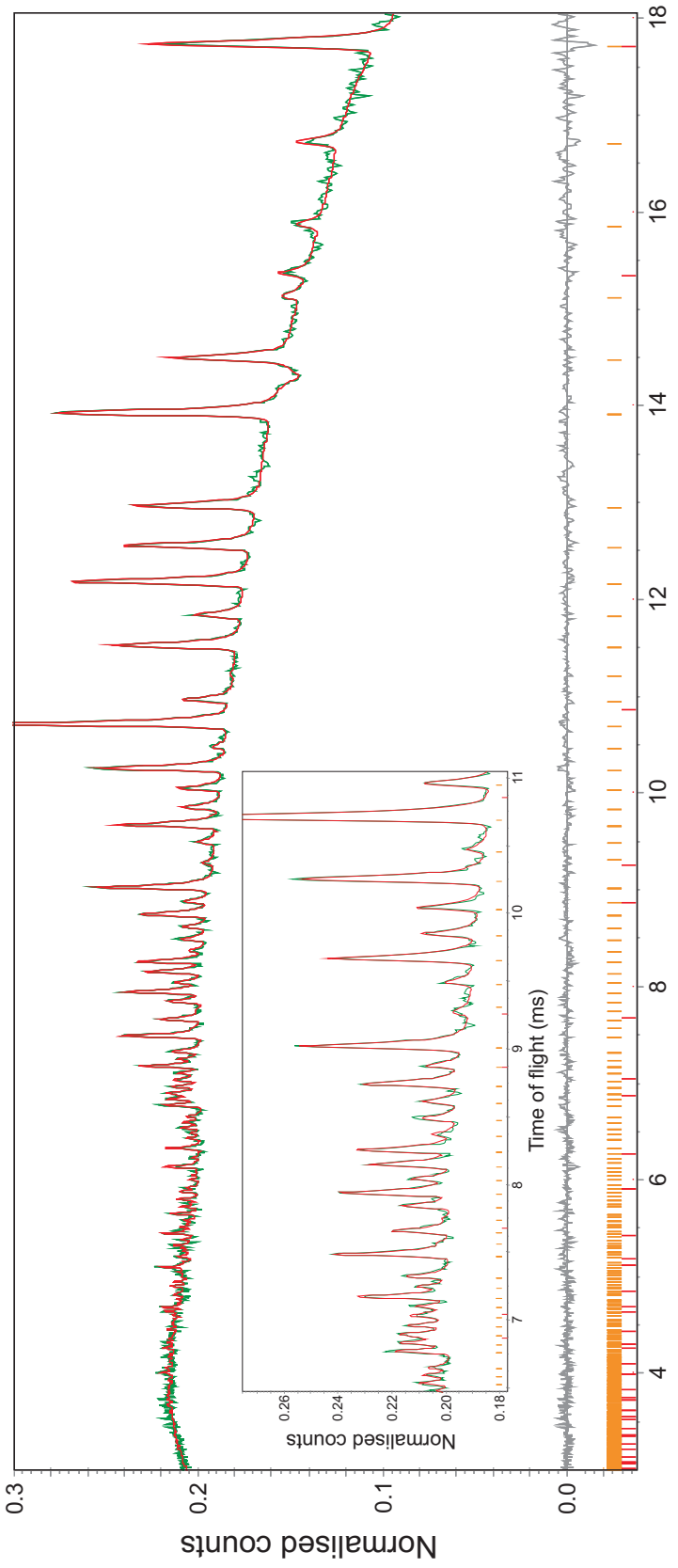

Figure 3.13: Final Rietveld plot for neutron diffraction data of $Li_4BH_4(NH_2)_3$ showing observed (green), calculated (red) and difference (grey) plots. The insert shows the low d-spacing region at a magnified scale. Peak positions for $Li_4BH_4(NH_2)_3$ (orange) and Li_2O (red) are indicated.

Table 3.5: Refined crystallographic data for $Li_4BH_4(NH_2)_3$.

Atom	Site	x/a	y/a	z/a	B_{iso}/Å
Li(1)	12b	0.9572(14)	0	1/4	1.5(1)
Li(2)	12b	0.7378(16)	0	1/4	Li(1)
Li(3)	8a	0.2722(12)	x	x	Li(1)
B	8a	0.1354(5)	x	x	1.4(2)
H(1)	8a	0.0721(15)	x	x	4.1(2)
H(2)	24c	0.0969(10)	0.1361(9)	0.2480(8)	H(1)
N	24c	0.1559(3)	0.3899(2)	0.3668(3)	1.8(1)
H(3)	24c	0.1533(12)	0.4467(15)	0.4394(12)	5.6(1)
H(4)	24c	0.0733(12)	0.3328(12)	0.3768(14)	H(3)

Space group $I2_13$, $a = 10.66445(1)$ Å.
X-ray data: $R_{wp} = 13.8$, $R_{exp} = 10.6$, $\chi^2 = 1.7$.
Neutron data: $R_{wp} = 0.821$, $R_{exp} = 0.726$, $\chi^2 = 1.3$.

Table 3.6: Selected refined inter atomic distances (Å) and angles (°) for $Li_4BH_4(NH_2)_3$ together with literature data for $LiBH_4$, $LiBD_4$, $LiNH_2$ and $LiND_2$.

Bond	$Li_4BH_4(NH_2)_3$	$LiBH_4$	$LiBD_4$[†]	$LiNH_2$	$LiND_2$
B-H	1.17(2)	1.04(2)	2×1.208(3)	-	-
	3×1.271(11)	1.25(1)	1.213(7)	-	-
	-	2×1.28(1)	1.224(5)	-	-
H-B-H	3×107.6(4)	85.1(4)	107.2(3)	-	-
	3×111.3(5)	103.2(5)	2×108.0(3)	-	-
	-	2×114.3(3)	110.1(3)	-	-
	-	2×120.0(5)	2×111.6(4)	-	-
N-H	0.985(13)	-	-	0.70(10)	0.967(5)
	1.043(15)	-	-	0.76(12)	0.978(6)
H-N-H	104.9(6)	-	-	123(1)	104.0(4)
Li-B	2.530(14)	2.475(4)	2.371(7)	-	-
	3× 2.685(10)	2×2.521(2)	2×2.523(4)	-	-
	-	2.542(4)	2.538(7)	-	-
Li-N	3×2.035(13)	-	-	4×2.059(3)	4×2.065(3)
	2×2.056(11)	-	-	2×2.064(9)	2×2.078(6)
	2×2.097(9)	-	-	2×2.212(9)	2×2.191(6)
	2×2.212(8)	-	-	4×2.213(3)	4×2.210(3)
Li-Li	2.34(2)	2×3.449(4)	2×3.494(8)	4×2.519(7)	4×2.51584(4)
	3×2.44(2)	-	-	2×2.524(7)	2×2.55(1)
	3×3.46(2)	-	-	4×3.598(7)	4×3.59214(3)
Reference	[101]	[98]	[102]	[99]	[103]
Volume per cation (Å^3)	37.90234(9)	54.1713(8)	54.615(11)	32.596	32.4569(17)

[†]This determination was performed at 3.5 K (−269.5°C).

The B-H bond lengths in $Li_4BH_4(NH_2)_3$ are similar to those observed in $LiBH_4$ [98]. Interestingly, as with the reported $LiBH_4$ structure, one B-H bond is significantly shorter (1.17 Å) than the other three (1.27 Å). The BH_4^- ion in the literature structure of $LiBH_4$, which was determined by synchrotron X-ray powder diffraction, deviates greatly from an ideal symmetric tetrahedron and we considered that this maybe be down to an inaccurate structural determination of the hydrogen positions because of the use of only X-rays. A later neutron powder diffraction study of $^7Li^{11}BD_4$ [102] showed much less deviation from an ideal tetrahedron at 3.5 K (−269.5°C) and 87°C. The observed mismatch in $Li_4BH_4(NH_2)_3$ is possibly due to the boron being on a site symmetry of point group type 3, only allowing refinement of two different B-H bond lengths; the true local structure may deviate from this symmetry and therefore the observed bond lengths may not be accurate.

N-H bond lengths are elongated compared with those observed in $LiNH_2$ [99] and the N-D bond lengths observed in $LiND_2$ [103]. N-H bond lengths will typically be underestimated in Rietveld refinements using X-ray data due to X-ray interactions with the strong N-H bond polarisation [104], as evidenced by the large discrepancy in the reported distances between $LiNH_2$ [99] (0.70(10) Å and 0.76(12) Å) determined using X-ray data and $LiND_2$ (0.967(5) Å and 0.978(6) Å [103] and 0.99(4) and 1.00(3) [105]) determined using neutron data. It is very likely that the observed elongation in N-H bond distance in $Li_4BH_4(NH_2)_3$ is due to a genuine weakening and concurrent lengthening of the N-H bond.

The $Li_4BH_4(NH_2)_3$ structure is closely related to the $LiNH_2$ structure, which becomes more clear when a slightly larger range ($-1/4$ to $+5/4$ in all crystallographic directions) is plotted along side an equivalent volume of the $LiNH_2$ structure, as shown in figures 3.14 and 3.15, respectively. Comparing figures 3.14 and 3.15 it can be seen how the larger BH_4^- anion displaces the regular lithium lattice of the $LiNH_2$ structure. It is worth noting that the replacement of an NH_2^- anion in the unit cell of $Li_4BH_4(NH_2)_3$ by an additional BH_4^- would nec-

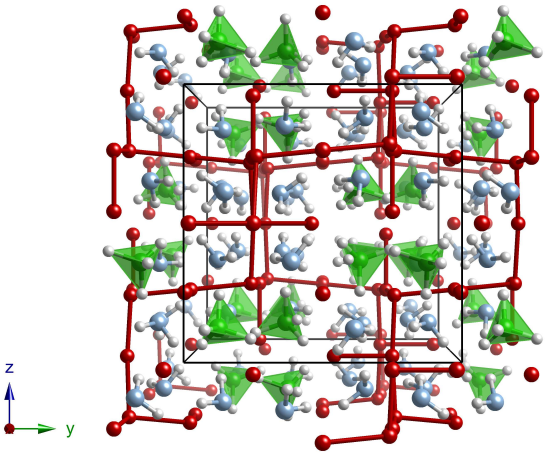

Figure 3.14: Extended crystal structure of $Li_4BH_4(NH_2)_3$. Boron is shown in green, nitrogen in blue, lithium in red and hydrogen in white. The unit cell is shown in black.

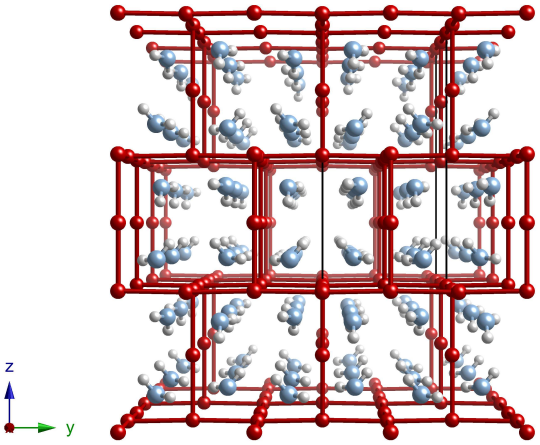

Figure 3.15: Extended crystal structure of $LiNH_2$. Nitrogen is shown in blue, lithium in red and hydrogen in white. The unit cell is shown in black.

essarily result in shorter distances between BH_4^- ions than in the stoichiometric compound. This may be the reason why the material appears to prefer the 1:3 stoichiometry.

3.4 Alternative Crystal Structure Determinations

There are currently five published crystal structures of $Li_4BH_4(NH_2)_3$; two structural determinations were performed concurrently with our own work and two were later determinations. Of the later determinations, one used the reported structures as a starting point and one was performed from scratch using a deuterated sample. For convenience, the five structures will be referred to (in order of article submission date) as the *Filinchuk* [106], *Noritake* [107], *Chater* [101], *Yang* [108] and *Wu* [104] structures. Two separate density functional theory (DFT) studies have also been undertaken by *Herbst et al.* [109] and *Siegel et al.* [110], where the reported structures of *Filinchuk*, and *Filinchuk* and *Chater*, respectively, were optimised.

The determined lattice parameters for each structure solution were 10.6794(10) Å (10.6723(10) Å for domain 2), 10.656(2) Å, 10.66445(1) Å, 10.664519(52) Å and 10.6645(1) Å (at 295 K, 10.5803(1) Å at 5 K), respectively, and 10.611 Å and 10.60 Å for the DFT studies.

The *Filinchuk* [106] structure solution was performed on X-ray diffraction data from single crystals. A 2:1 mixture of $LiNH_2$ and $LiBH_4$ was ball milled, enclosed in sealed capillary tubes. The sample was then re-melted, cooled slowly to crystallise the sample and measured on a single crystal diffractometer. Diffraction from a segment of the capillary showed five randomly inter-grown domains and the structure was solved using diffraction data from the two largest domains. Within one estimated standard error the refined values for the atomic coordinates for the two domains agreed.

The *Noritake* [107] structure solution used powder synchrotron X-ray diffraction data and was collected on a sample prepared by mechanically milling a 1:3 mixture of $LiBH_4$ and $LiNH_2$. Rietveld analysis confirmed that $LiNH_2$, Li_2O and Fe (from the milling process) were also present.

The *Yang* [108] structure solution was performed using constant wavelength

neutron diffraction data from a natural abundance sample prepared by ball milling of $3LiNH_2 + LiBH_4$, followed by annealing at 170°C for 2 days.

The *Wu* [104] structure solution was performed on an isotopically enriched sample of nominal composition $^{6/7}Li_3{}^{11}BN_2D_8$ prepared from a 1:2 mixture of $^7Li^{11}BD_4$ and $LiND_2$ by repeatedly annealing at 140°C. Constant wavelength (λ = 1.5403(2) Å) high resolution powder neutron diffraction data were collected, which showed predominantly the body centred cubic $^{6/7}Li_4{}^{11}BD_4(ND_2)_3$ phase with a small amount (4.84(2) weight %) of $^7Li^{11}BD_4$.

3.4.1 Crystal Structure Comparison

With the exception of the *Noritake* [107] structure, the determined crystal structures for $Li_4BH_4(NH_2)_3$ generally agree quite closely. Although the origin choice of unit cell for the *Chater* [101] and *Wu* [104] structures were the same, in order to map the reported atomic coordinates of *Filinchuk* [106] and *Yang* [108] onto these atomic positions an origin shift of $(-1/4, -1/4, -1/4)$, inversion of each of the axes and swapping the a and c axes are required. The determined atomic parameters for the agreeing structures, after transforming to the same unit cell origin and axes choice, are shown in table 3.7.

The *Noritake* [107] crystal structure determined was also cubic in space group $I2_13$. However, it was inconsistent with the other four structures. This structure, which exhibited fractional occupation of the Li sites (giving a stoichiometry of $Li_{3.99(1)}BH_4(NH_2)_3$), is shown in figure 3.16, and the structural parameters are shown in table 3.8.

Although the resultant arrangement of the B/N lattice is very similar to the other structural determinations, the rest of the model is very different. The fact that the authors have arrived at an incorrect structural determination could be attributed to the relatively poor crystallinity of the mechanically milled sample. Other syntheses that employed milling, those of *Filinchuk* [106] and *Yang* [108], also included an annealing step which improved the crystallinity of the samples.

Table 3.7: Comparison of different crystal structure determinations.

		Parameter	*Chater*	*Filinchuk*	*Yang*†	*Wu*‡	*Herbst*	*Siegel*
		a (Å)	10.66445(1)	10.6794(10)	10.664519(52)	10.6645(1)	10.611	10.60
		V (Å^3)	1212.875(3)	1218.0(2)	1212.897(17)	1212.919(3)	1194.7	1191.0
Atom	Site							
Li(1)	12b	x	0.9572(14)	0.9626(2)	0.96320(246)	0.9659(5)	0.9690	0.970
	(x,0,1/4)	B_{iso}	1.5(1)	3.17(4)	-	1.7(3)	-	-
Li(2)	12b	x	0.7378(16)	0.7263(2)	0.72801(310)	0.7428(4)	0.7315	0.732
	(x,0,1/4)	B_{iso}	Li(1)	2.42(4)	-	1.4(4)	-	-
Li(3)	8a	x	0.2722(12)	0.26670(16)	0.73283(243)	0.2730(4)	0.7663	0.266
	(x,x,x)	B_{iso}	Li(1)	2.41(6)	-	2.7(4)	-	-
B	8a	x	0.1354(5)	0.13640(10)	0.13986(142)	0.1379(2)	0.1371	0.137
	(x,x,x)	B_{iso}	1.4(2)	2.35(3)	-	0.87(16)	-	-
H(1)	8a	x	0.0721(15)	0.0779(14)	0.07062(467)	0.0697(3)	0.0705	0.071
	(x,x,x)	B_{iso}	4.1(2)	3.9(6)	-	6.0(3)	-	-
H(2)	24c	x	0.0969(10)	0.1031(12)	0.11183(503)	0.0975(5)	0.1037	0.103
	(x,y,z)	y	0.1361(9)	0.1306(14)	0.12706(352)	0.1337(6)	0.1319	0.133
		z	0.2480(8)	0.2377(14)	24777(173)	0.2437(5)	0.2475	0.247
		B_{iso}	H(1)	4.5(3)	-	6.5(2)	-	-
N	24c	x	0.1559(3)	0.1552(9)	0.15394(59)	0.1547(5)	0.1520	0.152
	(x,y,z)	y	0.3899(2)	0.3907(7)	0.38978(51)	0.3884(6)	0.3884	0.388
		z	0.3668(3)	0.3654(7)	0.36208(43)	0.3679(6)	0.3666	0.367
		B_{iso}	1.8(1)	2.08(2)	-	1.7(6)	-	-
H(3)	24c	x	0.1533(12)	0.1469(16)	0.14810(393)	0.1416(6)	0.1424	0.143
	(x,y,z)	y	0.4467(15)	0.4400(16)	0.47031(289)	0.4467(5)	0.4437	0.445
		z	0.4394(12)	0.4251(17)	0.41793(376)	0.4374(6)	0.4455	0.445
		B_{iso}	5.6(1)	4.7(3)	-	4.58(16)	-	-
H(4)	24c	x	0.0773(12)	0.0891(16)	0.09513(408)	0.0732(7)	0.0719	0.071
	(x,y,z)	y	0.3328(12)	0.3449(14)	0.30087(372)	0.3422(7)	0.3341	0.335
		z	0.3768(14)	0.3645(14)	0.37362(294)	0.3706(6)	0.3674	0.368
		B_{iso}	H(3)	3.9(3)	-	2.37(8)	-	-

†The reported *Yang* structure did not include thermal parameters.
‡The quoted hydrogen positions in this table are deuterium positions.

Table 3.8: Refined crystallographic data for the *Noritake* $Li_4BH_4(NH_2)_3$ structure [107].

Atom	Site	g	x/a	y/a	z/a	B_{iso}/Å
N(1)	12b	1.0	0.2544(7)	0	1/4	2.7(1)
N(2)	12b	1.0	0.7895(3)	0	1/4	N(1)
B	8a	1.0	0.0285(3)	x	x	1.4(2)
Li(1)	24c	0.58(1)	0.1068(10)	0.3775(7)	0.1587(8)	0.5(1)
Li(2)	24c	0.75	0.3755(7)	0.1493(10)	0.3311(7)	Li(1)
H(1)	24c	1.0	0.278(3)	0.094(3)	0.233(3)	4.4(4)
H(2)	24c	1.0	0.769(3)	0.096(2)	0.258(4)	H(1)
H(3)	8a	1.0	0.088(3)	x	x	H(1)
H(4)	24c	1.0	-0.032(6)	-0.032(7)	0.088(2)	H(1)

Space group $I2_13$, $a = 10.656(2)$ Å.

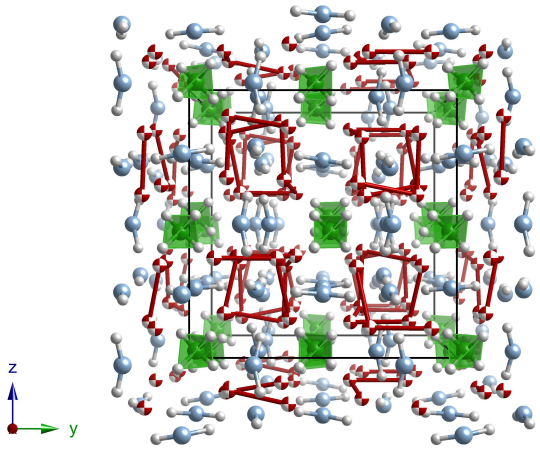

Figure 3.16: *Noritake* structure of $Li_4BH_4(NH_2)_3$. Boron is shown in green, nitrogen in blue, partially occupied lithium sites in half red, half white and hydrogen in white. The unit cell is shown in black.

The main differences between the other experimental structural solutions are mostly due to inherent differences between the methods of data collection. This is highlighted by the different bond distances and angles obtained for the different structures, as shown in table 3.9.

The *Filinchuk* [106] structure is based entirely on X-ray data, which results in shorter bonds to hydrogen due to a significant proportion of the X-ray scattering taking place from the bond rather than the hydrogen atom, which is particularly pronounced for the strongly polarised N-H bond. The observed lattice parameter was also slightly larger (10.6794(10) Å compared to an average of 10.6645 Å for the other structures). This could be due to partial replacement of NH_2^- with the larger BH_4^- caused by the 1:2 stoichiometry starting mixture, which would affect the determination of the local structure around the NH_2^-.

Although the atomic coordinates of the *Yang* [108] structure largely agree with the other determinations, there are significant differences. The lithium lattice of the *Yang* structure is significantly different. This is apparent in the abnormally short B-Li(3) bond distance (1.72(3) Å) observed. The lithium lattice appears

Table 3.9: Selected refined interatomic distances (Å) and angles (°) for six $Li_4BH_4(NH_2)_3$ structure determinations.

Bond	*Chater*	*Filinchuk*	*Yang*	*Wu*	*Herbst*	*Siegel*
Reference	[101]	[106]	[108]	[104]	[109]	[110]
B-H(1)	1.17(2)	1.082(15)	1.28(5)	1.260(4)	1.224	1.213
B-H(2)	1.271(11)	1.140(13)	1.20(3)	1.209(7)	1.225	1.222
H(1)-B-H(2)	111.3(5)	109.7(5)	110.2(9)	108.2(3)	111.0	111.2
H(2)-B-H(2)	107.6(4)	109.3(5)	108.7(9)	110.7(3)	107.9	107.7
N-H(3)	0.985(13)	0.83(2)	1.05(3)	0.977(9)	1.027	1.029
N-H(4)	1.043(15)	0.86(2)	1.14(4)	1.000(9)	1.027	1.027
H(3)-N-H(4)	104.9(6)	106.4(9)	125.9(8)	99.6(5)	103.4	103.6
B-Li(1)	2.685(10)	2.653(2)	2.67(2)	2.638(3)	2.595	2.586
B-Li(3)	2.530(14)	2.410(2)	1.72(3)	2.495(5)	2.375	2.371
N-Li(1)	2.097(9)	2.113(8)	2.09(2)	2.157(7)	2.140	2.151
N-Li(2)	2.056(11)	2.117(8)	2.10(2)	2.048(7)	2.112	2.114
N-Li(2)	2.212(8)	2.157(8)	2.19(2)	2.231(6)	2.169	2.166
N-Li(3)	2.035(13)	2.069(9)	2.33(3)	2.032(7)	2.069	2.070

Bond distances, angles and estimated standard deviations were calculated from the reported structures using VESTA [111]. Errors were not reported for the DFT calculated structures of *Herbst* and *Siegel*.

to be deformed from the regular $LiNH_2$-type lattice towards the larger BH_4^- ion, rather than away as it appears in the other structures. The NH_2^- bond angle is also much larger than in the other determinations (125.9°) which is an indication that there may be something wrong with the determination. The *Yang* structure was performed solely using neutron diffraction data on a natural abundance sample, meaning that the data will be strongly affected by the large incoherent neutron scattering cross section of H and the high neutron absorption of naturally occurring Li (containing ^{6}Li) and B (containing ^{10}B), which could have affected the quality of their data and the subsequent Rietveld refinement.

The determined atomic positions of *Wu* [104], in particular the deuterium positions, should be the most accurate. The use of neutron diffraction data eliminates the problems associated with X-rays, namely the low scattering cross section of H and scattering by electron density within chemical bonds, which caused short distances to hydrogen in the *Filinchuk* [106] structure. The *Chater*

[101] solution attempts to remove this problem using both X-ray and neutron diffraction data. However, because of the lack of isotopic enrichment in the samples, the neutron data will be affected by incoherent scattering from H and absorption by Li and B. The use of a fully enriched $Li_4{}^{11}BD_4(ND_2)_3$ phase should also eliminate these problems. The $BD_4{}^-$ tetrahedron observed is also distorted, but to a slightly lesser extent than that of the *Chater* structure and is more similar to that observed in $LiBD_4$ [102]. The $ND_2{}^-$ bond angle, however, is unusually low (99.6(5)°) compared to that of the $LiND_2$ structure (104.0(4)°). The inaccuracies in the *Wu* $NH_2{}^-$ positions may be due to a small amount substitution for $BH_4{}^-$ in the structure. The original starting composition was borohydride rich, nominally $Li_3BN_2D_8$. The quoted weight fractions for the phases $Li_4{}^{11}BD_4(ND_2)_3$ and $Li^{11}BD_4$ were 95.16(5)% and 4.84(2)% respectively, whereas, assuming that the starting materials were pure and 100% isotopically enriched, they should be 88.6% and 11.4%, respectively, for a pure $Li_4{}^{11}BD_4(ND_2)_3$ stoichiometry. This reduction in the amount of observed $Li^{11}BD_4$ could be due to inclusion of excess $LiBD_4$ in the $Li_4{}^{11}BD_4(ND_2)_3$ structure.

In conclusion, the *Chater* [101] structure agrees well with the reported structures of *Filinchuk* [106] and *Wu* [104]. The structure proposed by *Noritake* [107] is almost certainly incorrect. The structure proposed by *Yang* [108], despite using the published structures of *Filinchuk* and *Chater* as a starting point for refinement, also appears to be incorrect. The computational studies of *Herbst* [109] and *Siegel* [110] confirm that the structures of *Chater*, *Filinchuk* and *Wu* are essentially correct, with the main differences lying in the H bond lengths.

The structure of *Filinchuk* [106] underestimates the bond lengths because it relies on X-ray data only. The structure of *Wu* [104] should give the most accurate atomic positions but gives an unusually low bond angle for the $ND_2{}^-$, most probably due to partial replacement of $ND_2{}^-$ with $BD_4{}^-$ because of an incorrect reaction stoichiometry. Although the *Chater* [101] structure seems to give an inaccurate result for the $BH_4{}^-$ geometry, which may be due to the high neutron

absorption of naturally occurring boron, the NH_2^- geometry seems to reflect most closely that reported in compounds such as $LiND_2$. The true definitive structure for $Li_4BH_4(NH_2)_3$ therefore appears to lie somewhere between that of the *Chater* and *Wu* structures.

3.5 Spectroscopy

In order to investigate the bonding within $Li_4BH_4(NH_2)_3$, Fourier Transform Infrared (FTIR) spectroscopy and Raman spectroscopy were performed and compared with that of the parent materials, $LiBH_4$ and $LiNH_2$. The spectra of all materials were found to be dominated by the internal vibrations of the complex anions, and group theory and comparisons with the literature were used to assign the spectra.

The borohydride anion

The ideal BH_4^- ion would have tetrahedral symmetry (point group T_d). However, in $LiBH_4$ and $Li_4BH_4(NH_2)_3$ the borohydride ion occupies a crystallographic site of lower symmetry. For $LiBH_4$, the borohydride ion lies on a mirror plane and contains three crystallographically distinct hydrogen atoms (two of single multiplicity and one of double multiplicity) leading to assignment of point group C_s. In the case of $Li_4BH_4(NH_2)_3$, the borohydride ion lies on the three fold rotational axis with two crystallographically distinct hydrogen atoms (one of single multiplicity and one of triple multiplicity) leading to assignment of point group C_{3v}. The three different symmetries of borohydride ion are illustrated in figure 3.17.

For the ideal tetrahedral BH_4^- ion it is possible to derive the normal vibrational modes using Cartesian displacement vectors for each of the atoms as the basis set. The reducible representation for this basis set (Γ_{red}) is given in table 3.10 and the irreducible representation (Γ_{irr}) is given in table 3.11, where the

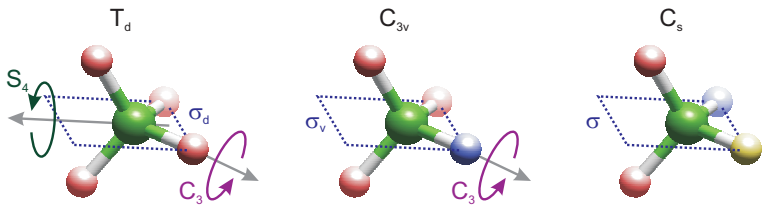

Figure 3.17: Three possible symmetries of the BH_4^- anion with the symmetry elements labelled. Symmetry equivalent hydrogen atoms are shown in the same colour.

Table 3.10: Point group table for T_d

	E	$8C_3$	$3C_2$	$6S_4$	$6\sigma_d$	Linear, rotations	Quadratic
A_1	1	1	1	1	1	-	$x^2+y^2+z^2$
A_2	1	1	1	-1	-1	-	-
E	2	-1	2	0	0	-	$(2z^2-x^2-y^2, x^2-y^2)$
T_1	3	0	-1	1	-1	(R_x,R_y,R_z)	-
T_2	3	0	-1	-1	1	(x,y,z)	(xy,xz,yz)
Γ_{red}	15	0	-1	-1	3		

Table 3.11: Deconvolution of Γ_{irr} for the ideal T_d symmetry BH_4^-.

	Γ_{irr}	Γ_{trans}	Γ_{rot}	Γ_{vib}	Γ_{IR}	Γ_{Raman}	Fundamental mode
A_1	1	0	0	1	0	1	ν_1
A_2	0	0	0	0	0	0	-
E	1	0	0	1	0	1	ν_2
T_1	1	0	1	0	0	0	-
T_2	3	1	0	2	2	2	ν_3, ν_4

translational (Γ_{trans}) and rotational modes (Γ_{rot}) are removed to give the normal vibrational modes (Γ_{3n-6}), of which the IR (Γ_{IR}) and Raman (Γ_{Raman}) active modes are shown and assigned fundamental modes.

For the ideal tetrahedron the fundamental modes ν_1 (A_1), ν_2 (E), ν_3 (T_2) and ν_4 (T_2) correspond to the singly degenerate symmetric stretch, the doubly degenerate symmetric bend, the triply degenerate asymmetric stretch and the triply degenerate asymmetric bend, respectively, as illustrated in figure 3.18.

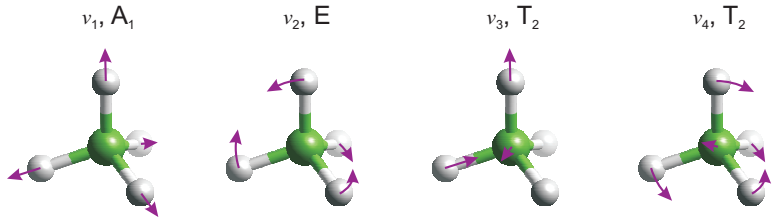

Figure 3.18: Vibrational modes of the BH_4^- anion.

Table 3.12: Correlation table for T_d, C_{3v} and C_s point groups.

C_s	E			σ		
A′	1			1		
A″	1			-1		
C_{3v}	E	$2C_3$		$3\sigma_\nu$		Species of C_s
A_1	1	1		1		A′
A_2	1	1		-1		A″
E	2	-1		0		A′ + A″
T_d	E	$8C_3$	$3C_2$	$6S_4$	$6\sigma_d$	Species of C_{3v}	Species of C_s
A_1	1	1	1	1	1	A_1	A′
A_2	1	1	1	-1	-1	A_2	A″
E	2	-1	2	0	0	E	A′ + A″
T_1	3	0	-1	1	-1	A_2 + E	A′ + 2A″
T_2	3	0	-1	-1	1	A_1 + E	2A′ + A″

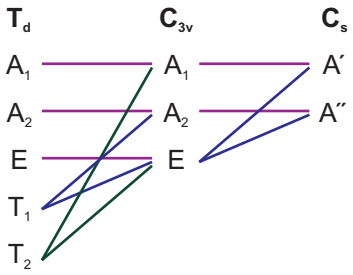

Figure 3.19: Correlation diagram for T_d, C_{3v} and C_s symmetries.

The effect of reducing the ideal tetrahedral symmetry of the BH_4^- ion to C_{3v} and C_s of $Li_4BH_4(NH_2)_3$ and $LiBH_4$, respectively, can be seen by constructing a symmetry correlation table (table 3.12) and the corresponding correlation diagram (figure 3.19).

For C_{3v}, the ν_1 (A_1) symmetric stretch remains, the doubly degenerate ν_2 (E)

Table 3.13: Point group table for C_{2v}.

	E	C_2 (z)	σ_v (xz)	σ_v (yz)	Linear, rotations	Quadratic
A_1	1	1	1	1	z	x^2, y^2, z^2
A_2	1	1	-1	-1	R_z	xy
B_1	1	-1	1	-1	x, R_y	xz
B_2	1	-1	-1	1	y, R_x	yz
Γ_{red}	9	-1	1	3		

symmetric bend remains doubly degenerate and two triply degenerate ν_3 and ν_4 (T_2) stretches split to A_1 and E modes. In the case of even lower symmetry $LiBH_4$ anion (C_s) the ν_1 (A_1) symmetric stretch remains (A'), the doubly degenerate ν_2 (E) symmetric bend splits to A' and A'' and two triply degenerate ν_3 and ν_4 (T_2) stretches split to $2A' + A''$ modes. As such, we may expect some of the fundamental vibrational modes of the BH_4^- anion to split so that more vibrations are observed. However, in practice the degree of splitting observed will depend on the energy difference between the split stretching modes of the same symmetry and therefore the degree to which the stretching modes mix.

The amide anion

The ideal NH_2^- ion would be bent, like the water molecule (point group C_{2v}). However, in $LiNH_2$ and $Li_4BH_4(NH_2)_3$ the amide ion lies on a general position giving a symmetry of C_s.

The vibrational modes for the ideal bent NH_2^- ion are easily derived using Cartesian displacement vectors for each of the atoms as the basis set. The reducible representation (Γ_{red}) for this basis set is given in table 3.13 which is then reduced to an irreducible representation (Γ_{irr}) and in table 3.14 the translational (Γ_{trans}) and rotational modes (Γ_{rot}) are removed to give the normal vibrational modes (Γ_{3n-6}), of which the IR (Γ_{IR}) and Raman (Γ_{Raman}) active modes are shown and assigned fundamental modes.

For the ideal bent NH_2^- the fundamental modes ν_1 (A_1), ν_2 (A_1) and ν_3 (B_2)

Table 3.14: Deconvolution of Γ_{irr} for C_{2v} NH_2^-.

	Γ_{irr}	Γ_{trans}	Γ_{rot}	Γ_{vib}	Γ_{IR}	Γ_{Raman}	Fundamental mode
A_1	3	1	0	2	2	2	ν_1, ν_2
A_2	1	0	1	0	0	0	-
B_1	2	1	1	0	0	0	-
B_2	3	1	1	1	1	1	ν_3

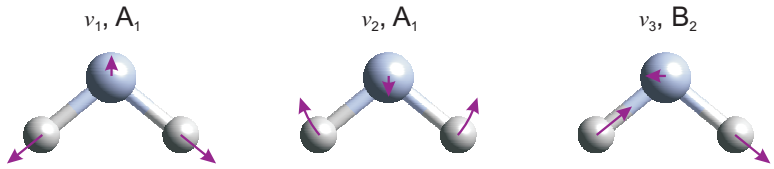

Figure 3.20: Vibrational modes of the NH_2^- anion.

Table 3.15: Correlation table for C_{2v} and C_s point groups.

C_s	E		σ		
A'	1		1		
A''	1		-1		
C_{2v}	E	C_2 (z)	σ_v (xz)	σ_v (yz)	Species of C_s
A_1	1	1	1	1	A'
A_2	1	1	-1	-1	A''
B_1	1	-1	1	-1	A''
B_2	1	-1	-1	1	A'

correspond to the singly degenerate modes of the symmetric stretch, the bend and the asymmetric bend, respectively, as illustrated in figure 3.20. Unlike for the borohydride anion, the reduction in symmetry does not change the number of observed vibrational modes that can be observed, as shown in table 3.15, and all of the possible vibrational modes have A' symmetry are IR and Raman active.

Results

The FTIR and Raman spectra of $Li_4BH_4(NH_2)_3$, together with the spectra of the starting materials $LiBH_4$ and $LiNH_2$, are shown in figures 3.21 and 3.22, respectively.

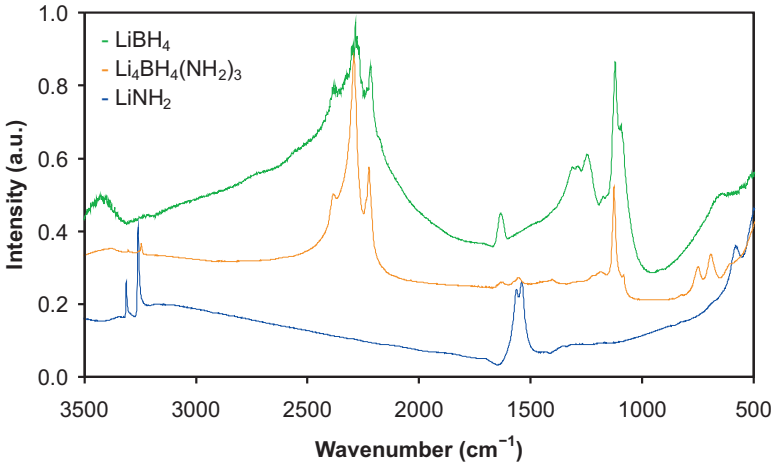

Figure 3.21: Infra-red spectrum of $Li_4BH_4(NH_2)_3$ (orange) together with spectra of $LiBH_4$ (green) and $LiNH_2$ (blue) for comparison.

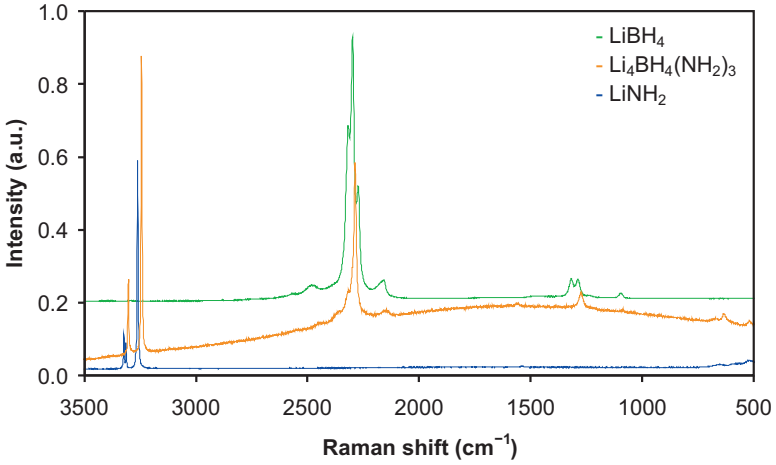

Figure 3.22: Raman spectrum of $Li_4BH_4(NH_2)_3$ (orange) together with spectra of $LiBH_4$ (green) and $LiNH_2$ (blue) for comparison.

Table 3.16: Literature (Lit.) and observed (Obs.) FTIR stretching modes ($\tilde{\nu}$) and assignments (Ass.) for $LiBH_4$ and $LiNH_2$ with observed data for $Li_4BH_4(NH_2)_3$.

$LiBH_4$				$LiNH_2$				$Li_4BH_4(NH_2)_3$	
Lit. [112]†		Obs.		Lit. [114]		Obs.		Obs.	
$\tilde{\nu}$	Ass.	$\tilde{\nu}$	Ass.	$\tilde{\nu}$	Ass.	$\tilde{\nu}$	Ass.	$\tilde{\nu}$	Ass.
1089	ν_4	1120	ν_4					1126	ν_4 (BH_4^-)
1254	$3\nu_L$	1250	$3\nu_L$					-	-
1284	ν_2	1293	ν_2					-	-
1323	ν_2'	1317	ν_2'					-	-
				1539	ν_2	1543	ν_2	1560 (b)	ν_2 (NH_2^-)
				1561	ν_2'	1566	ν_2'	-	-
2176	$2\nu_4$	2219	$2\nu_4$					2225	$2\nu_4$ (BH_4^-)
2277	ν_3	2284	ν_3					2295	ν_3 (BH_4^-)
2307	ν_3'	-	-					-	-
2350	ν_3''	-	-					-	-
2387 (sh)	$\nu_2 + \nu_4$	2386	com					2388	com
2423	$\nu_2' + \nu_4$	-	-					-	-
				3258	ν_s	3259	ν_1	3246	ν_1 (NH_2^-)
				-	-	-	-	3258	ν_1' (NH_2^-)
				3310	ν_{as}	3313	ν_3	3305	ν_3 (NH_2^-)
				3315	ν_{as}'	-	-	3313	ν_3' (NH_2^-)

b, broad; com, combination bands; ext, external vibrations; sh, shoulder.

† This spectra was obtained at −193°C (80 K).

The infrared and Raman spectra of $LiBH_4$ have been fully assigned by Harvey *et al.* [112] and Gomes *et al.* [113] and the vibrational spectra of $LiNH_2$ has also been investigated and partially assigned by Bohger *et al.* [114]. Using these literature assignments and the analysis discussed in the previous subsections the observed FTIR and Raman spectra of $Li_4BH_4(NH_2)_3$, $LiNH_2$ and $LiBH_4$ have been fully assigned, the results of which are shown in tables 3.16 and 3.17, respectively.

Enlarged sections of the FTIR and Raman spectra relating to the internal modes of the borohydride and amide anions are shown in figures 3.23 and 3.24, respectively. For the FTIR spectra, vibrational modes of $LiBH_4$ were typically observed at higher wavenumbers than for the literature spectra due to the liter-

Table 3.17: Literature (Lit.) and observed (Obs.) Raman shifts ($\tilde{\nu}$) and assignments (Ass.) for $LiBH_4$ and $LiNH_2$ with observed data for $Li_4BH_4(NH_2)_3$.

$LiBH_4$				$LiNH_2$				$Li_4BH_4(NH_2)_3$	
Lit. [113]		Obs.		Lit. [114]		Obs.		Obs.	
$\tilde{\nu}$	Ass.	$\tilde{\nu}$ †	Ass.	$\tilde{\nu}$	Ass.	$\tilde{\nu}$ †	Ass.	$\tilde{\nu}$ †	Ass.
189	ext	190	ext	-	-	236.7	ext	230	ext
255	ext	256	ext	-	-	273.7	ext	265	ext
285	ext	-	-	-	-	291.2	ext	300	ext
				-	-	327.1	ext	327	ext
				-	-	343.8	ext	380	ext
				-	-	516.2	ext	516	ext
				-	-	582.3	ext	630	ext
				-	-	654.7	ext	666	ext
1090	ν_4	1095.5	ν_4					1086	ν_4 (BH_4^-)
1099	ν_4'	-	-					-	-
1235	$3\nu_L$	1235	$3\nu_L$					-	-
1286	ν_2	1287.2	ν_2					1273.9	ν_2 (BH_4^-)
1316	ν_2'	1317.3	ν_2'					-	-
				1539	δ_{HNH}	1539.1	ν_2	-	-
				1561	δ_{HNH}	-	-	1558.6	ν_2 (NH_2^-)
2157	$2\nu_4$	2161.6	$2\nu_4$					2139	$2\nu_4$ (BH_4^-)
2177	$2\nu_4'$	2189.1	$2\nu_4'$					2154	$2\nu_4'$ (BH_4^-)
2275	ν_3	2273.3	ν_3					-	-
2301	ν_1	2297.4	ν_1					2286.4	ν_1 (BH_4^-)
2321 (sh)	ν_3'	2318.1	ν_3'					2316 (sh)	ν_3 (BH_4^-)
2391	com	2377	com					2360 (b)	com
2491	com	2479.8	com					2442 (b)	com
2572	com	2566	com					-	-
				3258	ν_s	3261.6	ν_1	3244	ν_1 (NH_2^-)
				3310	ν_{as}	3313.2	ν_3	3302.1	ν_3 (NH_2^-)
				3315	ν_{as}'	3323.6	ν_3'	3304.9	ν_3' (NH_2^-)

b, broad; com, combination bands; ext, external vibrations; sh, shoulder.

† Vibrations quoted to one decimal place were calculated using peak fitting with the computer program WiRE [115]. Vibrations quoted to one decimal place were from observed maxima.

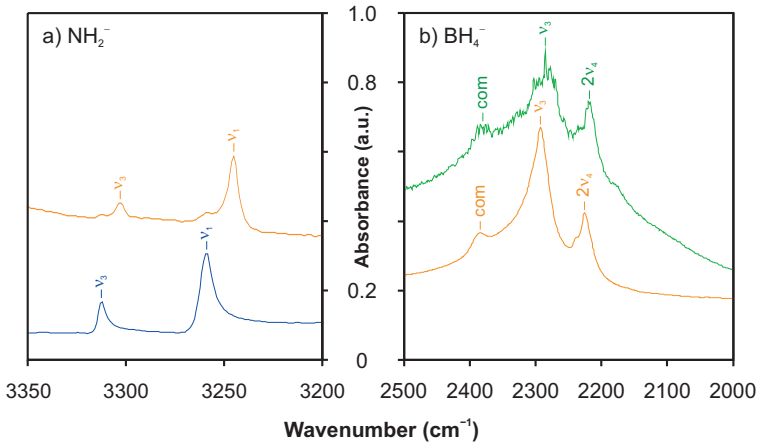

Figure 3.23: FTIR spectra of (a) the NH_2^- region and (b) the BH_4^- region of $LiNH_2$, $LiBH_4$ and $Li_4BH_4(NH_2)_3$. Observed spectra for $LiBH_4$, $LiNH_2$ and $Li_4BH_4(NH_2)_3$ are shown in green, blue and orange, respectively.

ature spectra being collected at −193°C (80 K) [112]. The ν_2 and ν_2' symmetric bends of the BH_4^- ion, which are forbidden in the ideal tetragonal symmetry, are observed. This provides confirmation of the C_s symmetry of the borohydride ion in the $LiBH_4$ crystal structure, where these vibrations are infrared active. The observed Raman spectrum for $LiBH_4$ was similar to the literature spectra, with observed vibrational modes within a few wavenumbers of the literature values, with the main difference being with ν_4 (triply degenerate asymmetric bend) related stretches. For the $LiNH_2$ Raman spectrum, only one NH_2^- bending mode (ν_2) was observed compared to two in the literature spectrum and in the observed FTIR spectrum. All of the symmetric and asymmetric bond stretching modes (ν_1, ν_3 and ν_3') were observed at slightly higher wavenumbers in both the FTIR and Raman spectra.

In the Raman spectrum of $Li_4BH_4(NH_2)_3$, the bands due to each complex anion bond were observed at lower wavenumbers than in the starting materials. This was most significant for the amide bond stretches, where this lowering was also observed in the FTIR spectrum.[†] This observed bond weakening is consis-

[†]In the FTIR spectrum of $Li_4BH_4(NH_2)_3$ there were also a set of much less intense vibrations at the same wavenumbers as observed for $LiNH_2$ (3258 cm^{-1} and 3313 cm^{-1}) which may have been due to a small $LiNH_2$ impurity in this sample.

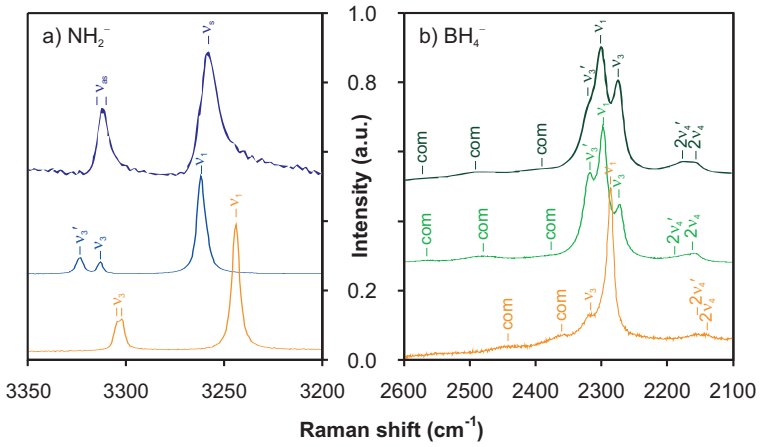

Figure 3.24: Raman spectra of (a) the NH_2^- region and (b) the BH_4^- region of $LiNH_2$, $LiBH_4$ and $Li_4BH_4(NH_2)_3$. Observed spectra for $LiBH_4$, $LiNH_2$ and $Li_4BH_4(NH_2)_3$ are shown in green, blue and orange, respectively. Literature spectra for $LiBH_4$ [113] and $LiNH_2$ [114] are shown in dark green and dark blue, respectively.

tent with the longer B-H and N-H bond lengths observed in the crystal structure of $Li_4BH_4(NH_2)_3$ (table 3.6) and is strong evidence for the accuracy of the crystallographically determined bond lengths (as opposed to the shorter bond lengths suggested by Filinchuk *et al.* [106]).

The absence of the librational mode of the BH_4^- anion ($3\nu_L$, 1235 cm^{-1}) in both the FTIR and Raman spectra of $Li_4BH_4(NH_2)_3$ could be an indication that the BH_4^- is more constrained in this structure than in $LiBH_4$. Only a single broad asymmetric stretch (ν_3) is observed in the Raman spectrum of $Li_4BH_4(NH_2)_3$ (2316 cm^{-1}), as opposed to the two seen for $LiBH_4$ (2273.3 cm^{-1} and 2318.1 cm^{-1}) which is consistent with the higher symmetry (C_{3v}) borohydride anion in the crystal structure of $Li_4BH_4(NH_2)_3$ compared to $LiBH_4$ (C_s).

The ν_2 symmetrical bending mode of the BH_4^- anion, which was present in the FTIR spectrum of $LiBH_4$, was absent from the spectrum of $Li_4BH_4(NH_2)_3$. This infrared vibrational mode is forbidden in the ideal tetragonal BH_4^- ion (T_d), however is allowed in the C_{3v} symmetry in the $Li_4BH_4(NH_2)_3$ structure. The symmetric stretch, ν_1, is also absent from the FTIR spectrum of $Li_4BH_4(NH_2)_3$.

Symmetric stretches are typically less intense than asymmetric stretches in infrared spectra. However, the complete absence of these vibrational modes is an indication that the borohydride ion in $Li_4BH_4(NH_2)_3$ may be more symmetrical than implied by the crystal structure.

The formation of $Li_4BH_4(NH_2)_3$ from $LiBH_4$ and $LiNH_2$ has a desirable weakening effect on the B-H and N-H bond strengths with respect to hydrogen release. This could contribute to the different hydrogen releasing decomposition pathway of $Li_4BH_4(NH_2)_3$ compared to that of $LiBH_4$ and $LiNH_2$ (see section 3.7).

3.6 In-situ Formation

The formation of $Li_4BH_4(NH_2)_3$ on heating $LiBH_4$ and $LiNH_2$ was investigated in an *in-situ* powder synchrotron X-ray diffraction experiment. A sample of $LiBH_4$ + $LiNH_2$ in a 1:1 ratio was intimately ground by hand in an argon atmosphere glovebox before transfer to the ESRF, Grenoble, where it was loaded into a capillary and measured on beamline ID31.

Synchrotron X-ray diffraction data were collected at a wavelength of 0.80022(1) Å and rebinned from the original step size of 0.002° to 0.006° to improve the signal-to-noise ratio. Data were collected in the range 2° to 43° 2θ (d-spacing 22.9 to 1.09 Å) with a data collection time of around 3.4 minutes per scan. A cryostream was used to heat the sample at a ramp rate of 1.5°C min^{-1} from room temperature to 150°C. The temperatures quoted are the average temperatures over the entire scan.

Refinement Strategy

Powder diffraction data were analysed using Topas [90]. For each data set a zero point error and an 18 parameter Chebyshev background function were refined. For each phase present, lattice parameters, a pseudo-Voigt peak shape function with 6 parameters and scale factor were refined. Atomic coordinates

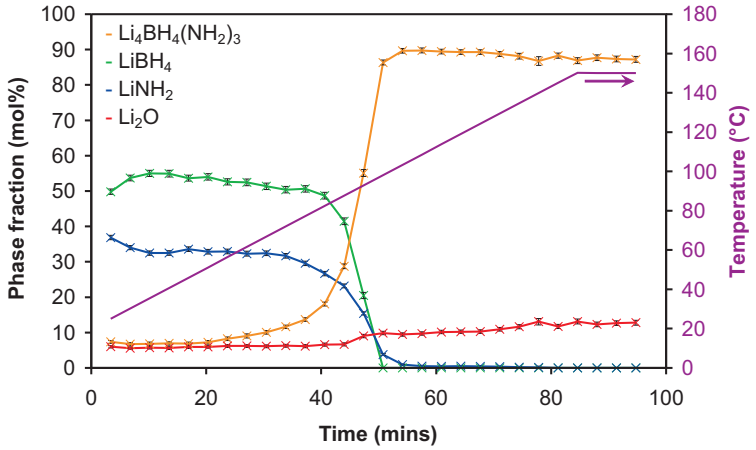

Figure 3.25: Phase fractions present during the formation of $Li_4BH_4(NH_2)_3$ upon heating a mixture of $LiBH_4$ + $LiNH_2$.

and thermal parameters were taken from reported structures and were not refined as the quality of data recorded with such short scan times did not allow for meaningful refinement of atomic positions. The weight percent reported by Topas from QPA (see section 2.5.1) for each compound present, together with the estimated standard error, were converted into mole percent values. Molar masses per lithium ion, i.e. calculated from the chemical formula scaled to one Li (e.g. $Li(BH_4)_{0.25}(NH_2)_{0.75}$), were used to make the mole percent values comparable.

Results

Figure 3.25 shows a summary of the phase fractions obtained from the refinements at each stage of the temperature ramp and figure 3.26 shows this information presented in the form of a "phase map" at each temperature. From this data it is clear that $Li_4BH_4(NH_2)_3$ was present from the start of the experiment, before the heating ramp had begun. This is attributed to room temperature formation of $Li_4BH_4(NH_2)_3$ in the 5 days between preparation of the starting mixture and running the experiment. It has previously been reported that the reaction of $LiBH_4$ with $LiNH_2$ can occur to a significant extent from a mixture of ball milled reagents within 12 days [97].

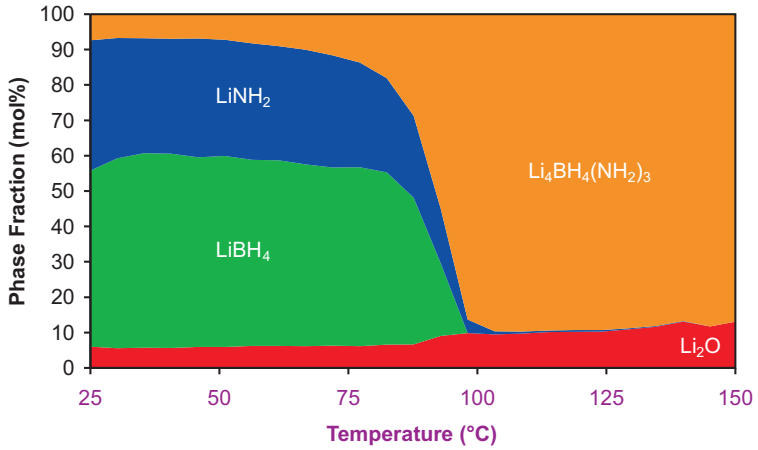

Figure 3.26: Phase map showing phases present during the formation of $Li_4BH_4(NH_2)_3$ upon heating a mixture of $LiBH_4$ + $LiNH_2$.

Despite the original prepared starting mixture being weighed out in a starting $LiBH_4$:$LiNH_2$ ratio of 1:1, the observed BH_4^-:NH_2^- ratio at the start of the experiment (taking into account the $Li_4BH_4(NH_2)_3$ present) was around 1:0.6, with $LiBH_4$ in the majority. This shortfall in NH_2^- is in part due to the Li_2O present in the $LiNH_2$ starting material which was not taken into account during weighing. Also, at lower temperatures the observed lattice parameter of the $Li_4BH_4(NH_2)_3$ phase (figure 3.27) was lower than expected for a pure stoichiometric phase. Combined with the relatively broad peak shape of this phase this could be an indication that this phase is sub-stoichiometric and disordered with respect to the larger BH_4^- ion, giving the formula $Li_4(BH_4)_{(1-x)}(NH_2)_{(3+x)}$.

A gradual and steady rise in the amount of $Li_4BH_4(NH_2)_3$ was observed until 80°C when the increase became more rapid until 100°C when the transformation is essentially complete. The anomaly in the data point at 78 minutes (figure 3.25) was due to an error in data collection that resulted in diffraction data only being collected to 25° 2θ. Interestingly, the decrease in the amount of $LiBH_4$ observed was more rapid than decrease of $LiNH_2$ and this phase was completely absent at lower temperatures than the more persistent $LiNH_2$. This could be interpreted as the $LiBH_4$ readily combining with $LiNH_2$ to form the body centred cubic

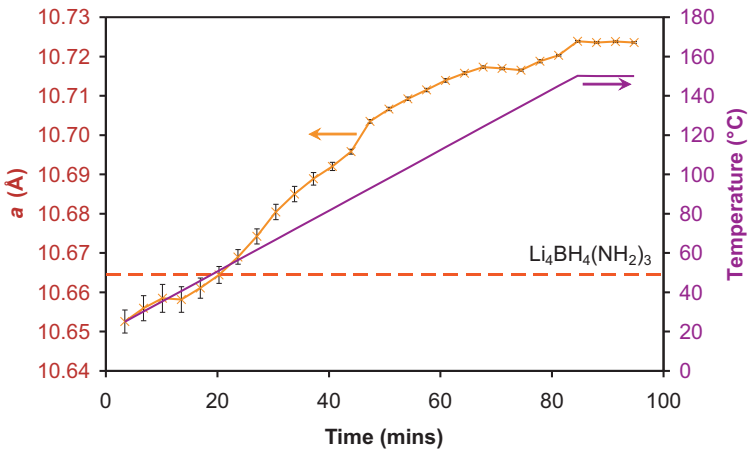

Figure 3.27: Lattice parameter of $Li_4BH_4(NH_2)_3$ present upon heating a mixture of $LiBH_4$ and $LiNH_2$. The literature value for $Li_4BH_4(NH_2)_3$ [101] is shown as a dotted line.

$Li_4BH_4(NH_2)_3$ phase which may initially be disordered and BH_4^- rich on a local scale while some unreacted $LiNH_2$ remains. Upon further heating the BH_4^- may then diffuse throughout the structure and become ordered until finally all of the $LiNH_2$ is consumed to give the stoichiometric and ordered $Li_4BH_4(NH_2)_3$ structure.

The transformation in the diffraction patterns during the heating experiment can be followed in the 2-dimensional contour plot of a selected 2θ range (figure 3.28). From this figure it is possible to see loss of the Bragg peaks due to $LiBH_4$ and $LiNH_2$ with the concurrent appearance of the (222) peak of $Li_4BH_4(NH_2)_3$ in the region 80 to 100°C. The thermal expansion of $LiNH_2$ and $Li_4BH_4(NH_2)_3$ was also observed in the gradual shift to lower angle of the relevant diffraction peaks.

The positions of the Bragg peaks due to $LiBH_4$ did not all vary linearly with temperature, with a much larger shift in the (002) peak. Upon heating, the $LiBH_4$ unit cell was observed to change with an increase in the a and c lattice parameters with a concurrent decrease in the b lattice parameter, resulting in an overall increase in unit cell volume with temperature (figure 3.29).

This was consistent with a move towards the high temperature hexagonal

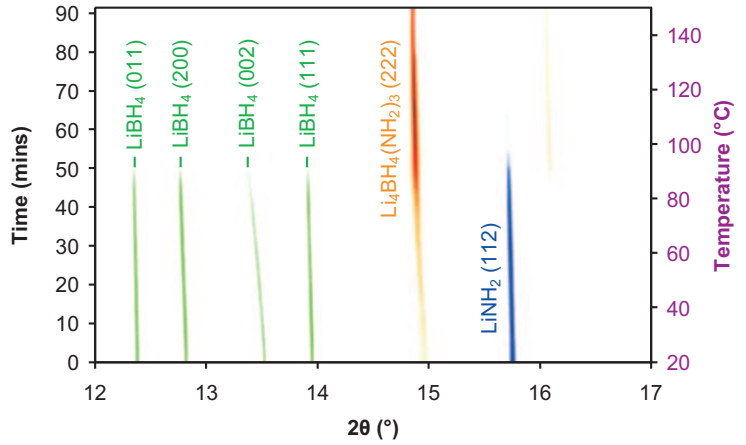

Figure 3.28: 2-D contour plot of powder diffraction data during the formation of $Li_4BH_4(NH_2)_3$. A representative portion of the diffraction data containing Bragg peaks from the majority phases is shown and the Bragg peaks are labelled. The Bragg peaks of $LiBH_4$, $LiNH_2$ and $Li_4BH_4(NH_2)_3$ are coloured in green, blue and orange, respectively.

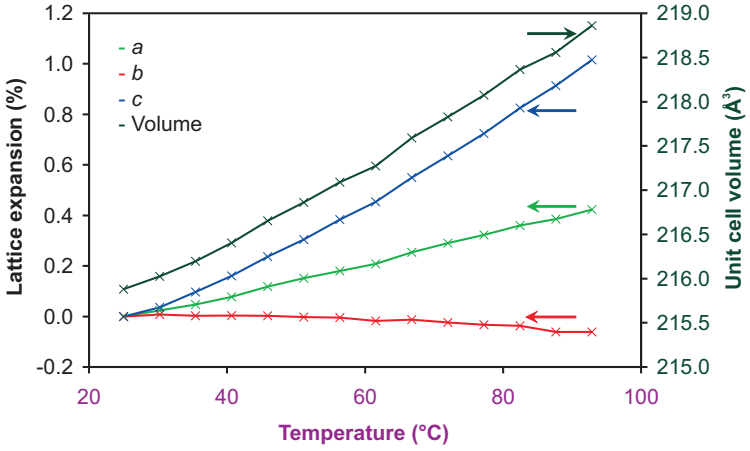

Figure 3.29: Variation of the unit cell parameters and unit cell volume of $LiBH_4$ upon heating during the formation of $Li_4BH_4(NH_2)_3$.

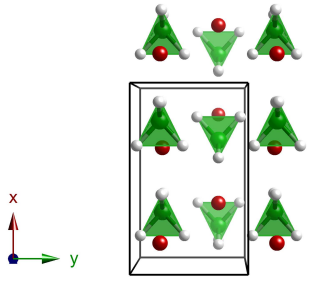

Figure 3.30: Crystal structure of the room temperature form of $LiBH_4$. Li^+ ions are shown in red and BH_4^- ions are shown as green tetrahedra.

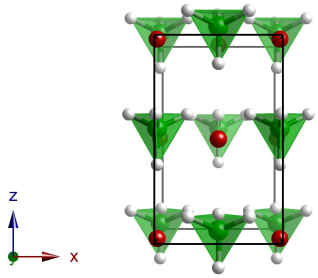

Figure 3.31: Crystal structure of high temperature form of $LiBH_4$ transformed into an orthorhombic maximal *translationengleiche* subgroup. Li^+ ions are shown in red and BH_4^- ions are shown as green tetrahedra.

form of $LiBH_4$. However, none of the high temperature ($P6_3mc$) form is observed as it had completely reacted below the transition temperature of around 105°C [40]. Figure 3.30 shows the crystal structure of the orthorhombic ($Pnma$) room temperature form of $LiBH_4$ [98] and figure 3.31 shows the literature structure for the hexagonal ($P6_3mc$) high temperature (135°C) form [98] transformed to the corresponding orthorhombic maximal *translationengleiche* subgroup ($Cmc2_1$) using PowderCell [116].

When converted to the orthorhombic maximal *translationengleiche* subgroup, this gives the lattice parameters 7.4068, 4.2763 and 6.9484 Å which correspond to $a = 7.17858$ (3.18% expansion), $b = 4.43686$ (3.62% contraction) and $c = 6.80321$

Å (2.13% expansion) in the room temperature literature structure respectively. The lattice parameters of $LiBH_4$ observed at 90°C were $a = 7.19966(8)$, $b = 4.42614(4)$ and $c = 6.86801(7)$, still some way from what would be expected for the high temperature form. Looking at the lattice parameters of the transformed high temperature unit cell it might be expected that it would be the a lattice parameter which should undergo the larger expansion, rather than the c lattice parameter. This larger lattice expansion in the c parameter was probably due to an increase in librational motion of the BH_4 unit around the c axis. It is hypothesised that the large expansion of the c axis is a prerequisite for the reorientation of the BH_4 unit which goes with the transformation to the high temperature form. After reorientation the c axis could then relax back to the value observed in the high temperature structure.

Although the phase composition diagrams (figures 3.25 and 3.26) are an accurate reflection of the crystalline phases present there was some evidence that there may be some amorphous material present at higher temperatures. Firstly, molar phase fraction of Li_2O observed increased, which should not be due to oxidation when sealed inside a capillary. Secondly, the observed BH_4^-:NH_2^- ratio at the end of the experiment was 3:1 (the stoichiometry of $Li_4BH_4(NH_2)_3$) rather than the 1:1 starting mixture, indicating that there was some borohydride present which had not been accounted for. Although the $Li_4BH_4(NH_2)_3$ structure can support over-stoichiometry with respect to BH_4^- (discussed in more detail in chapter 5), this could not account for such a large discrepancy. Reactions at borohydride rich stoichiometries have shown that these mixtures can melt at temperatures as low as 100°C (see section 5.4). Using the average calculated weight fraction for Li_2O over the first four diffraction patterns as an internal standard, the weight fractions could be recalculated to estimate any amorphous content, as shown in figure 3.32.

Although the errors associated with this calculation were large, there was a clear indication of amorphous content from around 90°C which rose to ∼53 wt%.

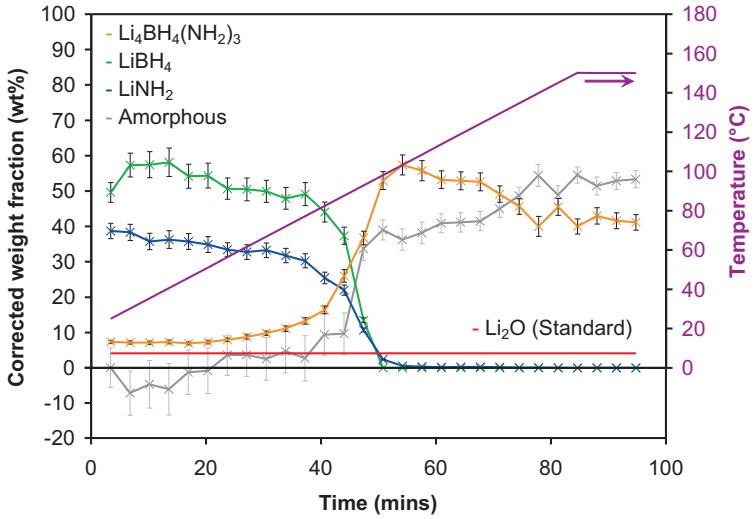

Figure 3.32: Corrected phase weight fractions present during the formation of $Li_4BH_4(NH_2)_3$ upon heating a mixture of $LiBH_4$ + $LiNH_2$ after normalisation for Li_2O.

From 100°C, where $Li_4BH_4(NH_2)_3$ was the only observed crystalline phase, this implied that the amorphous content corresponded to a borohydride rich melt to make up for the shortfall in observed borohydride. Although pure $LiBH_4$ melts at 268°C [117],[†] a melting point determination of a $LiBH_4$ + $LiNH_2$ mixture showed the loss of crystallinity at around 100°C. In summary, the use of Li_2O as an inert internal standard during QPA provided a valuable insight into an amorphous phase present upon heating $LiBH_4$ + $LiNH_2$ which was present alongside $Li_4BH_4(NH_2)_3$.

3.7 Thermal Decomposition

3.7.1 In-situ Decomposition

The gaseous thermal desorption products from $Li_4BH_4(NH_2)_3$ were investigated using TPD-MS, IGA-MS and TPD-RGA. The decomposition pathway was found to depend on the type of desorption method performed with either hydrogen or

[†]The melting point of $LiNH_2$ is 380°C [117].

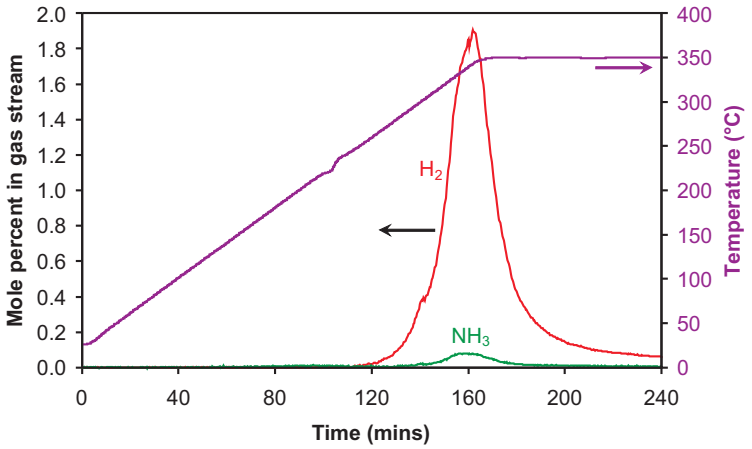

Figure 3.33: Thermal decomposition analysis of $Li_4BH_4(NH_2)_3$ in a TPD apparatus. The temperature trace is shown in purple and the mole percents of H_2 and NH_3 released are shown in red and green respectively.

ammonia and hydrogen released.

TPD-MS

Thermal desorption data from pure $Li_4BH_4(NH_2)_3$ heated at a ramp rate of 2°C min^{-1} to 350°C are shown in figure 3.33. The endothermic event in the temperature trace starting at 220°C was due to the melting of $Li_4BH_4(NH_2)_3$. The hydrogen signal started to increase from 245°C, with significant hydrogen release from 270°C which peaked around 340°C. At the peak of desorption, only 4 mol% of the gas released was NH_3. There was a shoulder on the hydrogen trace at 300°C, which could indicate a two step desorption. Hydrogen release continued, although much more slowly, after reaching the maximum temperature of 350°C.

Figure 3.34 shows the TPD-MS data processed so as to give gravimetric data, as discussed in section 2.7. The observed weight loss from mass spectrometry data over the total heating time was only 7.6 wt%, less than that predicted if all of the hydrogen was released from $Li_4BH_4(NH_2)_3$ (11.1 wt% H_2).

Results from PXRD after decomposition (figure 3.35) showed Li_3BN_2 ($P2_1/c$) as the major product (with a small amount of the $I4_1/amd$ polymorph). However,

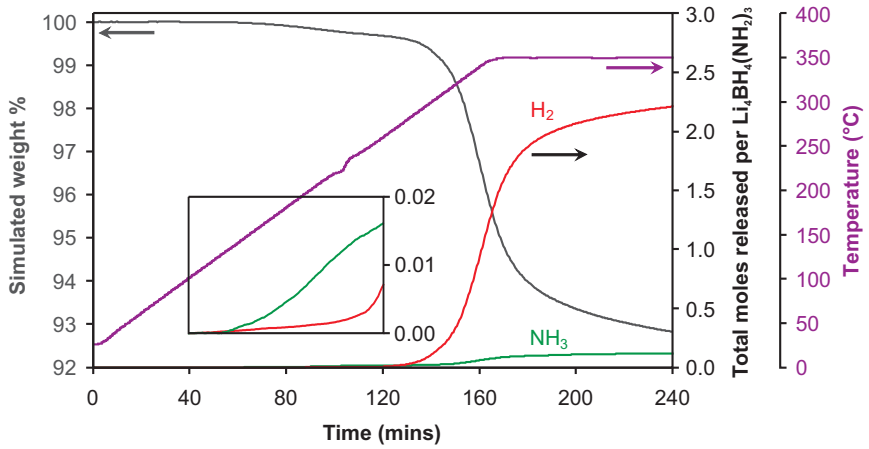

Figure 3.34: Thermal decomposition analysis of $Li_4BH_4(NH_2)_3$ in a TPD apparatus with simulated gravimetric data. The temperature trace is shown in purple and the mole percents of H_2 and NH_3 released are shown in red and green respectively and the simulated gravimetric data is shown in grey. The inset shows a magnified y scale area.

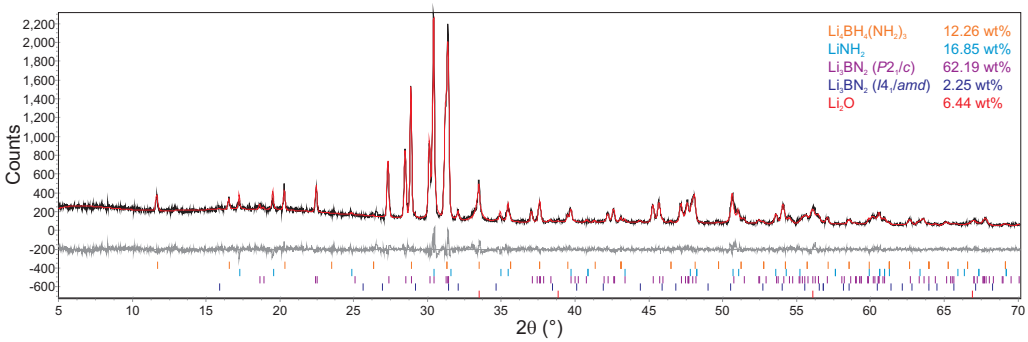

Figure 3.35: Powder XRD of $Li_4BH_4(NH_2)_3$ after heating to 350°C in a TPD-MS apparatus. Bragg peak positions due to $Li_4BH_4(NH_2)_3$ (orange), $LiNH_2$ (light blue), Li_3BN_2 ($P2_1/c$) (purple), Li_3BN_2 ($I4_1/amd$) (dark blue) and Li_2O (red) are indicated.

a significant amount of $Li_4BH_4(NH_2)_3$ and $LiNH_2$ also remained. This accounts for why only a 7.6 wt% loss was observed, less than if all of the $Li_4BH_4(NH_2)_3$ present had decomposed. The inset in figure 3.34 shows that gas release started from 145°C with ammonia release preempting the release of hydrogen. This is possible evidence for hydrogen release occuring *via* an ammonia mediated reaction.

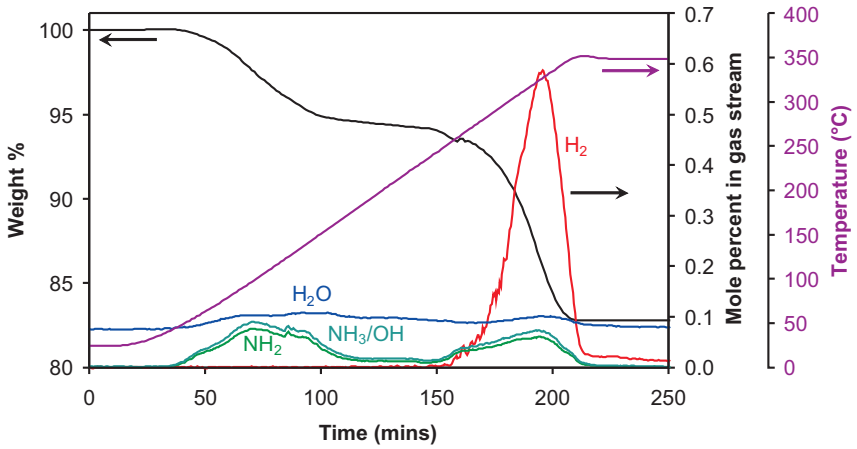

Figure 3.36: Thermo-gravimetric analysis of $Li_4BH_4(NH_2)_3$ in an IGA. The gravimetric trace is shown in black, the temperature trace is shown in purple and the mole percents of H_2, NH_3/OH, NH_2 and H_2O observed at the mass spectrometer are shown in red, and green, teal and blue respectively.

IGA-MS

A sample of $Li_4BH_4(NH_2)_3$ (104 mg) was inertly loaded into an IGA connected to a mass spectrometer. Figure 3.36 shows the thermogravimetric data overlaid with the mass spectrometric data for the observed desorption products. The sample heated in the IGA showed a two stage desorption trace: the onset temperature for the first desorption was 40°C, peaking at 95°C, and the second desorption onset temperature was 240°C, peaking at 320°C, ending at a final weight loss of 17.3 wt%.

Interestingly, the first low temperature desorption was completely absent in the mass spectrum of the TPD-MS experiment (figure 3.33). A total mass loss of 17.3 wt% was not consistent with hydrogen, which makes up only 11.1 wt% of $Li_4BH_4(NH_2)_3$, being the majority desorption product. The mass spectrometry data confirmed that the first desorption was due only to ammonia and the second, higher temperature desorption, was due to ammonia and hydrogen. The weight loss associated with the first desorption was approximately 5.8 wt%, equivalent to the loss of around 2.5 NH_3 molecules from the unit cell (eight formula units) of $Li_4BH_4(NH_2)_3$.

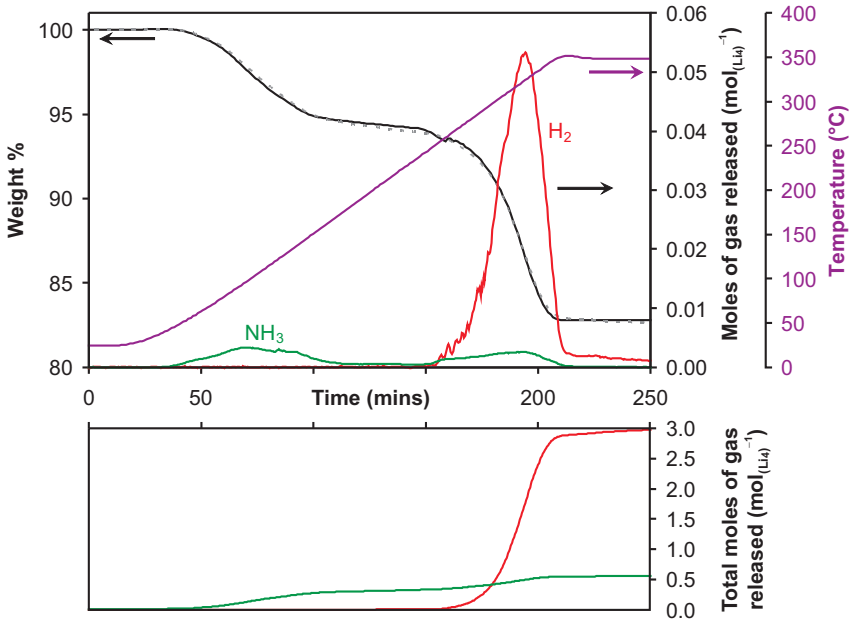

Figure 3.37: Thermo-gravimetric analysis of $Li_4BH_4(NH_2)_3$ in an IGA. The gravimetric trace is shown in black, the fitted calculated gravimetric trace from mass spectroscopy data is shown in grey, the temperature trace is shown in purple. The number of moles of H_2 and NH_3 released per mole of $Li_4BH_4(NH_2)_3$ are shown in red and green respectively and a cumulative plot for these gases is shown below.

Although the mass spectrometer was not specifically calibrated for H_2 and NH_3 (library data for gas relative sensitivities were used), because we have gravimetric data for the weight loss associated with gas release the relative amounts of H_2 and NH_3 can be calculated. Figure 3.37 shows the IGA-MS data where the calculated mass loss due to the amount of desorbed gases has been fitted to the observed mass loss by refining the relative H_2:NH_3 sensitivity (based on the m/z 16 fragment, $NH_2^{\bullet+}$).[†] As such, the amount of moles of each gas released could now be expressed per mole of $Li_4BH_4(NH_2)_3$ (figure 3.37).

After this correction had been applied, it could be seen that the second, higher temperature mass loss was made up predominantly H_2 with 4.9 mol% NH_3 (slightly larger than the 4 mol% NH_3 observed in the TPD-MS measurement).

The amount of mass loss due to H_2 and NH_3 could now be deconvoluted and

[†]The mass spectrum data for H_2 and NH_3 were background subtracted and averaged over the time frame of a minute before fitting to the observed mass loss data.

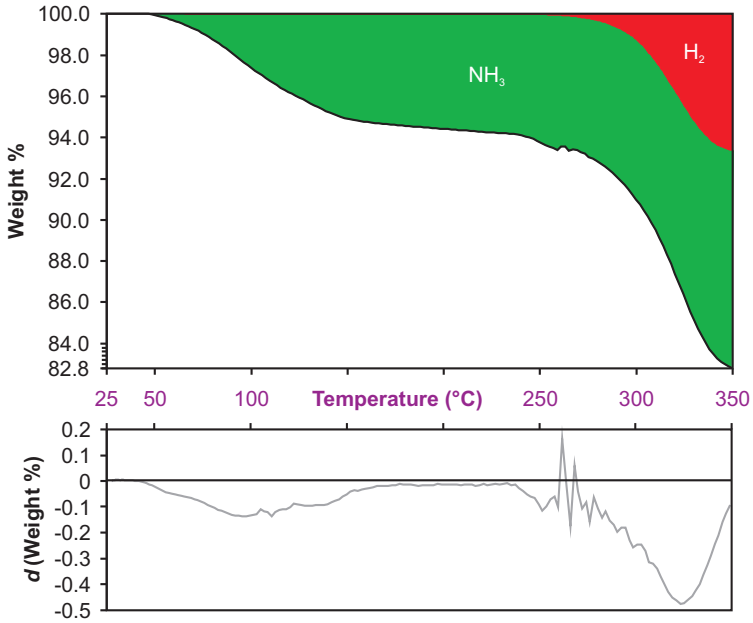

Figure 3.38: Thermo-gravimetric analysis of $Li_4BH_4(NH_2)_3$ in an IGA. The gravimetric trace is shown in black, proportion of the mass loss due to H_2 and NH_3 are shown in red and green respectively and the differential gravimetric trace is shown below in gray.

plotted as a function of temperature, as shown in figure 3.38 together with the first differential of the mass loss signal. From figures 3.37 and 3.38 it can be seen that, in total, 3.0 mol H_2 (6.6 wt%) and 0.55 mol NH_3 (10.6 wt%) was released. Hydrogen release started from 245°C, which was the same temperature as in the TPD-MS experiment.

The closeness of value of 0.55 mol NH_3 released to 0.5 is an indication that the ammonia release could be due to the excess of $LiNH_2$ present in $Li_4BH_4(NH_2)_3$ when compared to the $LiBH_4$ + $2LiNH_2$ ratio required to produce the decomposition product, Li_3BN_2. We hypothesise that this ∼0.5 mol NH_3 released is due to the known decomposition pathway of lithium amide to form lithium imide with the release of ammonia;

$$2LiNH_2 \rightarrow Li_2NH + NH_3 \uparrow, \tag{3.1}$$

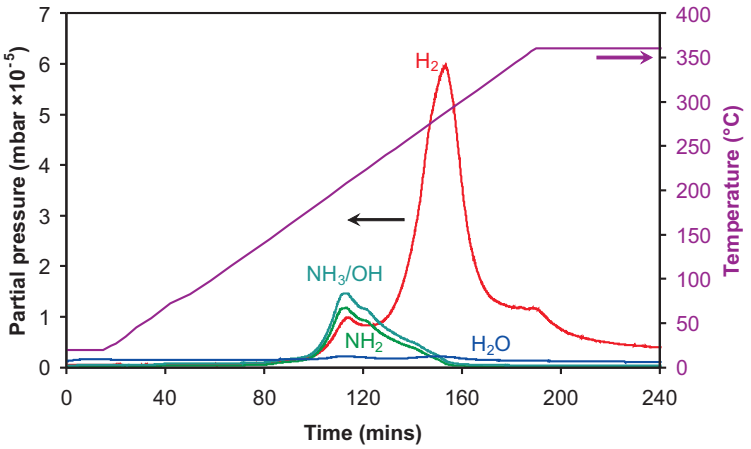

Figure 3.39: TPD-RGA analysis of $Li_4BH_4(NH_2)_3$. The temperature trace is shown in purple and the partial pressures of H_2, NH_3/OH, NH_2 and H_2O are shown in red, and green, teal and blue respectively.

giving the overall decomposition reaction for $Li_4BH_4(NH_2)_3$ in the IGA as;

$$Li_4BH_4(NH_2)_3 \rightarrow Li_3BN_2 + {}^1/_2Li_2NH + 4H_2 \uparrow + {}^1/_2NH_3 \uparrow . \qquad (3.2)$$

Only 7.65 of the 10 hydrogen atoms in one unit formula of $Li_4BH_4(NH_2)_3$ were accounted for in the gaseous products. From equation 3.2 it can be seen that only 9.5 are expected to be desorbed, but this is still a shortfall of 1.85 hydrogen atoms. We expect that the solid products after the IGA-MS measurement would contain some unreacted $Li_4BH_4(NH_2)_3$, as was the case with the TPD-MS measurement. Problems during the inert unloading of the sample after IGA-MS measurement meant that the sample oxidised so that meaningful powder XRD data could not be collected to confirm this.

TPD-RGA

A sample of $Li_4BH_4(NH_2)_3$ (1.2 mg) was inertly loaded onto TPD-RGA apparatus. Thermal desorption data was collected at a ramp rate of 2°C min^{-1} to 350°C and the results are shown in figure 3.39.

A small ammonia release was observed from 50°C, corresponding well with the low temperature ammonia release seen in the IGA-MS experiment. However,

this was less pronounced in the TPD-RGA experiment. Significant hydrogen release started at 145°C, which was concurrent with ammonia release. The major decomposition took place in a two step process; the first peaked at 210°C which was made up of hydrogen and ammonia and the second higher temperature step peaked at 290°C and is made of predominantly hydrogen. Interestingly, the second larger hydrogen release started from 240°C, just below the onset temperature observed in the TPD-MS and IGA-MS experiments. Decomposition in the high vacuum of the TPD-RGA experiment appeared to lower the observed decomposition temperature of $Li_4BH_4(NH_2)_3$ with respect to the TPD-MS and IGA-MS experiments.

Discussion

Clearly from the various different methods of exploring the gasseous thermal decomposition products investigated, the desorption profile of $Li_4BH_4(NH_2)_3$ was strongly dependent on the experimental setup. The thermal desorption data from each experiment are compared in figure 3.40. The general trend observed showed that although lower desorption temperatures appear to be achieved, this tended to be at the detriment of hydrogen purity. Interestingly the onset temperature of the major hydrogen desorption temperature appeared to be fairly consistent at $\sim$ 245°C, suggesting that the observed differences in decomposition temperature maybe be due to kinetic effects in the experimental setups.

Of the experimental set-ups tested, the TPD-MS experiment was closest to that which could be implemented in a hydrogen storage/delivery system. Ideally, hydrogen desorption would also have been tested under a pressure of hydrogen, although this would make analysis using mass spectrometry more difficult.

3.7.2 Ex-situ Synchrotron X-ray Powder Diffraction

A range of partially decomposed samples of $Li_4BH_4(NH_2)_3$ were prepared by heating at 4°C min^{-1} to the desired temperature and holding for 4 hours. A reaction

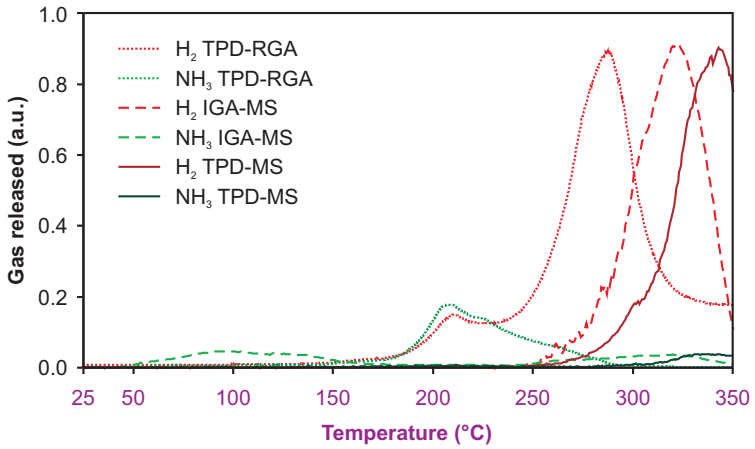

Figure 3.40: Comparison of TPD-MS, IGA-MS and TPD-RGA thermal desorption data for $Li_4BH_4(NH_2)_3$.

time of 4 hours was used so that the observed products would be intermediate between the immediate kinetic desorption products and the thermodynamically stable products at each temperature and so be more representative of the phases present during dynamic heating experiments. Temperatures investigated ranged from 200°C to 360°C in 20°C steps. The solid crystalline products were then determined using synchrotron X-ray powder diffraction.

Refinement Strategy

Synchrotron X-ray powder diffraction data were collected at a wavelength of 0.80157(1) Å and rebinned from the original step size of 0.003° to 0.006° to improve the signal-to-noise ratio. Data were collected in the range 2° to 68° 2θ (d-spacing 23.0 to 0.72 Å) with a data collection time of around 12 minutes. Powder diffraction data were refined using Topas [90]. For each data set a zero point error and an 18 parameter Chebyshev background function were refined. For each phase present, lattice parameters, a pseudo-Voigt peak shape function with 6 parameters and scale factor were refined. Atomic coordinates were taken from reported structures and were not refined. Preliminary attempts to refine atomic positions gave improvements in the visual and statistical fit, however, re-

sulted in chemically poor results. It was decided that a data time of 12 minutes was insufficient for a full Rietveld refinement. Where isotopic thermal parameters were given in the reported structure they were included in the structure and a single coefficient was refined as a scale factor for the thermal parameters.

The relativistic form factors for the formal charges on boron and nitrogen in these species (B^{3+} and N^{3-}) are not included in the elastic photon–atom scattering data used by Topas, so neutral atoms were used throughout in the refinements for all atoms. For some phases a single parameter was refined to modify the occupancy of each site as an approximation to charge segregation within the compound. For example, for Li_3BN_2 a single parameter (x in equations 3.3, 3.4 and 3.5) was refined where for a value of 0 all of the atoms are neutral, and for a value of 1 the atomic charges equate to Li^+, B^{3+} and N^{3-}.

$$\mathrm{Li_{occ}} = 1 - (1/3)x \tag{3.3}$$

$$\mathrm{B_{occ}} = 1 - (3/5)x \tag{3.4}$$

$$\mathrm{N_{occ}} = 1 + (3/7)x \tag{3.5}$$

Attempts to refine the charge segregation in this way resulted in insignificant improvement in the statistical fit and so occupancies were fixed at 1 for neutral atoms.

Topas reported weight percent values from QPA for each compound present with an estimated standard error. Molar percents and standard errors were calculated from the weight percent values. In order to maintain consistency, molar masses per lithium atom were used, i.e. for $Li_4BH_4(NH_2)_3$ a quarter of the molar mass was used ($Li(BH_4)_{0.25}(NH_2)_{0.75}$). Where a new phase could not be identified this could not be included in the mol% calculations and was therefore disregarded in the resultant phase composition diagrams.

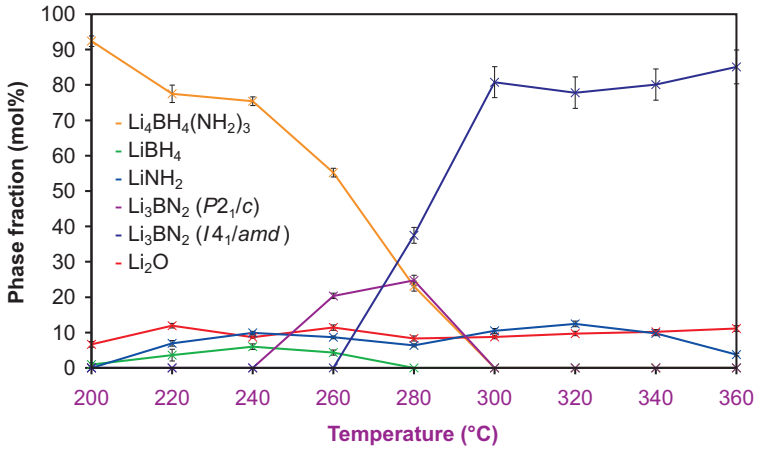

Figure 3.41: Molar phase fractions after heating $Li_4BH_4(NH_2)_3$ at various temperatures.

†An unidentified phase was present in these samples which could not be included in the composition calculations.

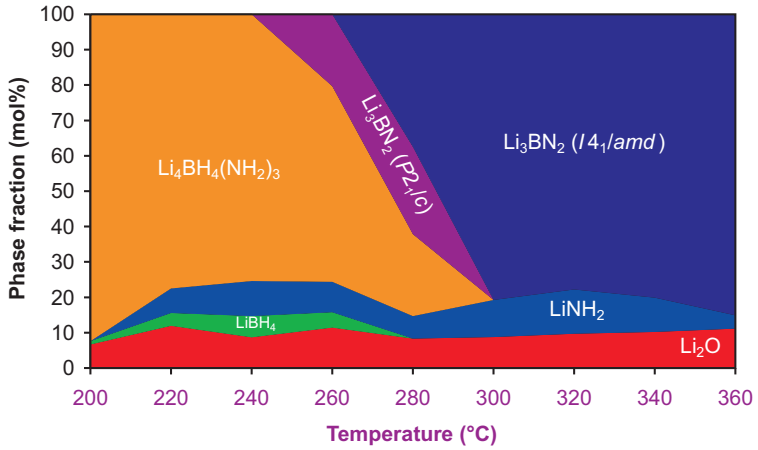

Figure 3.42: Total molar phase fractions after heating $Li_4BH_4(NH_2)_3$ at various temperatures

†An unidentified phase was present in these samples which could not be included in the composition calculations.

Results

Table 3.18 shows the results from the Rietveld refinement of the powder diffraction patterns. Figures 3.41 and 3.42 show how the molar percentage of each phase varied with reaction temperature.

At 200°C $Li_4BH_4(NH_2)_3$ [101] persisted as the major product with a small

Table 3.18: Results from Rietveld refinement of powder diffraction data from samples of $Li_4BH_4(NH_2)_3$ heated to various temperatures. Mole % values are calculated per lithium for each phase.

	Reference	200°C	220°C	240°C†	260°C†	280°C	300°C	320°C	340°C	360°C
$Li_4BH_4(NH_2)_3$	[101]									
a (Å)	10.66445(1)	10.66121(1)	10.65888(4)	10.66089(8)	10.66359(8)	10.65657(12)	-	-	-	-
Volume (Å^3)	1212.875(3)	1211.768(4)	1210.97(13)	1211.66(2)	1212.58(3)	1210.19(5)	-	-	-	-
Weight %	-	94.6(3)	80.9(5)	77.8(3)	59.0(3)	25.8(2)	-	-	-	-
Mole %	-	92.4(5)	77.5(8)	75.4(4)	55.2(4)	23.1(5)	-	-	-	-
$LiBH_4$	[98]									
a (Å)	7.17858(4)	7.180(2)	7.1780(13)	7.1796(4)	7.1784(5)	-	-	-	-	-
b (Å)	4.43686(2)	4.4372(10)	4.4366(7)	4.4346(2)	4.4348(3)	-	-	-	-	-
c (Å)	6.80321(4)	6.803(2)	6.805(2)	6.8104(5)	6.8085(5)	-	-	-	-	-
Volume (Å^3)	216.685(3)	216.7(1)	216.69(7)	216.83(2)	216.75(3)	-	-	-	-	-
Weight %	-	1.0(2)	3.6(5)	6.0(3)	4.5(3)	-	-	-	-	-
Mole %	-	0.98(15)	3.6(5)	6.0(3)	4.3(2)	-	-	-	-	-
$LiNH_2$	[99]									
a (Å)	5.037	-	5.04043(10)	5.03949(4)	5.03972(5)	5.03961(6)	5.04740(11)	5.04881(11)	5.05180(14)	5.0491(3)
c (Å)	10.278	-	10.2712(4)	10.27032(14)	10.2691(2)	10.2653(2)	10.2608(4)	10.2595(4)	10.2515(5)	10.2556(11)
Volume (Å^3)	260.77	-	260.950(14)	260.830(5)	260.821(7)	260.715(7)	261.41(2)	261.52(2)	261.63(2)	261.45(4)
Weight %	-	-	7.3(3)	10.3(2)	9.37(14)	7.23(9)	12.17(15)	14.45(17)	11.37(15)	4.43(12)
Mole %	-	-	6.9(3)	9.89(15)	8.66(14)	6.39(15)	10.5(2)	12.4(3)	9.7(2)	3.75(12)
Li_3BN_2 ($P2_1/c$)	[118]									
a (Å)	5.1502(2)	-	-	-	5.1435(5)	5.14847(19)	-	-	-	-
b (Å)	7.0824(2)	-	-	-	7.0977(5)	7.0876(2)	-	-	-	-
c (Å)	6.7908(2)	-	-	-	6.7678(3)	6.77413(12)	-	-	-	-
β (°)	112.956(2)	-	-	-	112.703(5)	112.8515(19)	-	-	-	-
Volume (Å^3)	228.08	-	-	-	227.93(3)	227.790(12)	-	-	-	-
Weight %	-	-	-	-	19.1(2)	24.19(14)	-	-	-	-
Mole %	-	-	-	-	20.4(2)	24.7(5)	-	-	-	-
Li_3BN_2 ($I4_1/amd$)	[119]									
a (Å)	6.5992(2)	-	-	-	-	6.59772(8)	6.59696(5)	6.59701(5)	6.59732(5)	6.59700(5)
c (Å)	10.3483(7)	-	-	-	-	10.34871(17)	10.35031(11)	10.34961(10)	10.34872(10)	10.34953(10)
Volume (Å^3)	450.664(16)	-	-	-	-	450.478(13)	450.444(9)	450.421(8)	450.424(8)	450.416(9)
Weight %	-	-	-	-	-	36.67(18)	81.23(16)	78.20(18)	80.90(17)	87.00(18)
Mole %	-	-	-	-	-	37.5(7)	80.8(15)	77.8(15)	80.1(15)	85.1(16)
Li_2O										
Weight %	-	4.5(3)	8.18(16)	5.91(8)	8.0(3)	6.1(2)	6.61(10)	7.35(10)	7.73(11)	8.57(16)
Mole %	-	6.6(3)	11.9(2)	8.70(11)	11.4(3)	8.3(2)	8.75(17)	9.7(2)	10.2(2)	11.2(3)

†An unidentified phase was present in these samples which could not be included in the composition calculations.

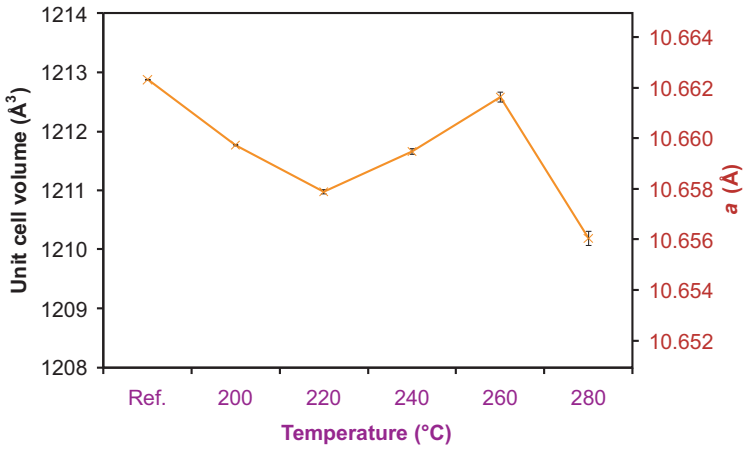

Figure 3.43: Unit cell volume of $Li_4BH_4(NH_2)_3$ at various temperatures. The literature value (Ref.) is shown for comparison [101].

amount of $LiBH_4$ [98] present (1.0(2) mol%). Upon heating to 220°C the $Li_4BH_4(NH_2)_3$ started to dissociate to $LiBH_4$ and $LiNH_2$ [99], present at 3.6(5) and 7.3(3) mol%, respectively, increasing to 6.3(3) and 10.34(16) mol% after heating to 240°C. For a simple disproportionation of $Li_4BH_4(NH_2)_3$ we should observe a 25:75 ratio in the appearance of $LiBH_4$ and $LiNH_2$ (taking into account the original excess $LiBH_4$ observed at 200°C). The observed ratios are 27(6):73(5) at 220°C and 34(4):66(3) at 240°C. The large errors associated with these calculated ratios (due to the errors in calculating out the weight fractions of $LiBH_4$ at low quantities) makes drawing definite conclusions about this ratio impossible. There is also potential for non-stoichiometry in $Li_4BH_4(NH_2)_3$ to account for any discrepancy (see chapter 5). A decrease in unit cell volume of $Li_4BH_4(NH_2)_3$ would be an indication of partial substitution of BH_4^- for the smaller NH_2^-. However, figure 3.43 shows that the $Li_4BH_4(NH_2)_3$ unit cell was fairly consistent with a maximum change of only 0.2% from the literature value [101] with no noticeable trend to back up a theory of non-stiochiometry.

After heating at 240°C minor new reflections were observed in the powder diffraction pattern which could not be indexed or identified. Some of these reflections were also present after heating to 260°C (see table 3.19).

Table 3.19: Unidentified reflections after partial decomposition of $Li_4BH_4(NH_2)_3$.

240°C			260°C		
2θ (°)	d (Å)	I_{rel} (%)	2θ (°)	d (Å)	I_{rel} (%)
6.74	6.82	70.8	6.75	6.81	70.4
8.35	5.51	18.4	-	-	-
9.36	4.91	11.9	9.36	4.91	11.8
9.73	4.73	27.5	9.73	4.73	27.3
10.80	4.26	25.1	10.80	4.26	24.9
13.76	3.35	100.0	13.77	3.34	100.0
-	-	-	16.56	2.78	34.7
-	-	-	17.38	2.65	31.5
17.67	2.61	10.5	-	-	-
-	-	-	18.51	2.49	9.6
18.77	2.46	18.3	18.78	2.46	31.8

From these results it appeared that at least 5 reflections are present after reaction at both 240°C and 260°C in the same relative intensities. An attempt at indexing gave a primitive tetragonal cell with $a = 9.47$ Å and $c = 9.84$ Å ($P4_2/nmc$) which does not match any H, Li, B, N or O–containing structure reported in the Inorganic Crystal Structure Database (ICSD), although it should be stressed that no firm conclusions can be made from attempts to index so few reflections. The d–spacing of the 100% relative intensity peak in both samples was close to the inter-layer distance of BN (3.33 Å [120]) which suggests that this could be a related structure, such as a partially lithium intercalated boron nitride structure. Attempts to include boron nitride in the refinement succeeded only in fitting the most intense (002) Bragg reflection of boron nitride with 100% peak of the unidentified phase. All other predicted reflections due to boron nitride had essentially zero intensity.[†]

$Li_2B_{12}H_{12}$ has recently identified as a decomposition product of $LiBH_4$ by solid state NMR [50]. The structure of this phase (cubic, $a = 9.5771(2)$Å, $Pa\bar{3}$

[†]Other phases checked to ensure that they are not responsible for these reflections were $Li_2BH_4NH_2$ [121], LiH [122], Li_2NH [59], α-Li_3N [123], β-Li_3N [124], Li_3BN_2 ($P2_1/c$) [125] and Li_3BN_2 ($P4_22_12$) [126]. Crystal structures calculated by first–principles for the intermediate decomposition products of $LiBH_4$ ($LiBH_2$, LiBH and Li_3BH_6 [47]), as well as a model for $Li_2B_6H_6$ based on the known structure of $K_2B_6H_6$ [127] were also found not to be present.

[128]) also did not match. However, the closeness of this unit cell to the indexed tetragonal (a = 9.47 Å, c = 9.84 Å) unit cell could be an indication that this is a related species.

$Li_4BH_4(NH_2)_3$ remained as the major product (68.4(5) mol%) after heating to 260°C and similar amounts of $LiBH_4$ and $LiNH_2$ remained as with the reaction at 240°C (5.4(3) and 10.72(17) mol%, respectively). The monoclinic polymorph of lithium boron nitride ($P2_1/c$) was also observed at 8.41(10) mol% which was the first confirmation that gas must have been released from the sample. This corresponded well to the decomposition temperature observed in thermal desorption TPD-MS experiment (section 3.7) of above 245°C. The polymorph of lithium boron nitride observed was different to that reported as the decomposition product of $Li_4BH_4(NH_2)_3$ by Pinkerton *et al* [119]. After heating to 280°C the reported Li_3BN_2 ($I4_1/amd$) appeared at 23.0(5) mol%, with the $P2_1/c$ polymorph increasing to 15.2(3) mol%. $Li_4BH_4(NH_2)_3$ decreased to 42.5(9) mol%. From 300°C, $Li_4BH_4(NH_2)_3$ and the $P2_1/c$ polymorph of Li_3BN_2 were no longer present. Only Li_3BN_2 ($I4_1/amd$) and $LiNH_2$ (and Li_2O) persisted from 300°C and from 320°C to 360°C there was a relative decrease in the amount of $LiNH_2$ which could suggest partial decomposition of the remaining amide.

The decomposition of $Li_4BH_4(NH_2)_3$ appeared to predominantly proceed to form Li_3BN_2 and $LiNH_2$ with the reaction essentially complete after reaction at 300°C for 4 hours. This gives rise to the decomposition reaction in equation 3.6 which suggests a possible 8.9 wt% of hydrogen released.

$$Li_4BH_4(NH_2)_3 \rightarrow Li_3BN_2 + LiNH_2 + 4H_2 \uparrow \tag{3.6}$$

Discussion

Pinkerton *et al.* [119] reported that the Li_3BN_2 ($I4_1/amd$) structure is the dominant phase formed upon dehydrogenation of $Li_4BH_4(NH_2)_3$ and ball milled "$Li_3BN_2H_8$" mixtures, though they also reported that the monoclinic Li_3BN_2

Table 3.20: Refined and literature (in brackets) atomic coordinates for monoclinic Li_3BN_2.

Atom	x/a	y/b	z/c
Li(1)	0.260(2)	0.4798(16)	0.485(2)
	[0.24995(17)]	[0.48518(12)]	[0.49811(12)]
Li(2)	0.2548(19)	0.0051(16)	0.3701(17)
	[0.25228(18)]	[0.01212(13)]	[0.37502(13)]
Li(3)	0.759(2)	0.221(2)	0.3209(15)
	[0.74360(16)]	[0.20714(11)]	[0.31402(12)]
B	0.2240(17)	0.3257(13)	0.1767(10)
	[0.21509(7)]	[0.31982(5)]	[0.17648(5)]
N(1)	0.4384(10)	0.4388(8)	0.2176(7)
	[0.43404(6)]	[0.43735(4)]	[0.21904(5)]
N(2)	0.9915(9)	0.2092(7)	0.1337(7)
	[0.99439(6)]	[0.20472(5)]	[0.13461(5)]

($P2_1/c$) commonly occurred as a minor phase in their samples. From these data it would appear that the monoclinic phase was the first to form at lower decomposition temperatures (240°C to 280°C), and the $I4_1/amd$ polymorph preferentially forms from 300°C and above.

The literature structure of the monoclinic Li_3BN_2 polymorph gave a relatively poor fit to the observed diffraction pattern (R_{Bragg} 3.41). Refinement of the atomic positions gave an improved fit (R_{Bragg} 2.42) with relatively minor changes in the structure. Atomic coordinates before and after refinement are shown in table 3.20. Clearly a new structural determination is required for this polymorph of Li_3BN_2, although the large number of overlapping Bragg peaks in this diffraction data make it unsuitable for a definitive structural determination.

The crystal structure of the lower temperature $P2_1/c$ form is shown in figure 3.44. This appears to be more disordered than the higher temperature $I4_1/amd$ form (figure 3.45). In the $I4_1/amd$ phase the N=B=N anions align so that, when viewed down the c axis, they are on top of, and at right angles to, each other.

Pinkerton *et al.* [119] suggested that the Li_3BN_2 structure may support partial nitrogen deficiency. However, in reality they could only conclude that by

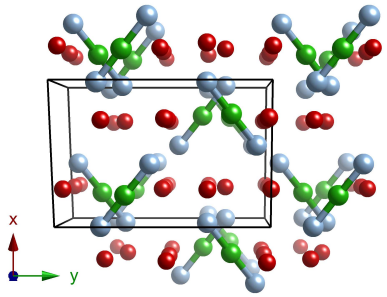

Figure 3.44: Li_3BN_2 ($P2_1/c$) structure viewed down the c axis. Boron is shown in green, nitrogen in blue and lithium in red. The unit cell is shown in black.

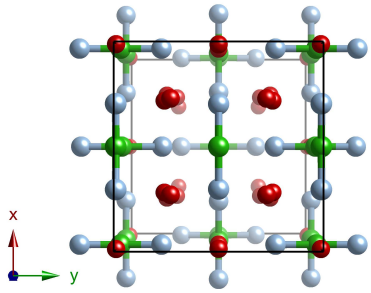

Figure 3.45: Li_3BN_2 ($I4_1/amd$) structure viewed down the c axis. Boron is shown in green, nitrogen in blue and lithium in red. The unit cell is shown in black.

using X-ray diffraction it was impossible to tell the difference between a stoichiometric Li_3BN_2 and one that is sub-stoichiometric with respect to nitrogen. Figure 3.46 shows that the unit cell volume of Li_3BN_2 ($I4_1/amd$) was smaller when formed at higher temperatures. This could be an indication of nitrogen deficiency. Figure 3.47 shows that this decrease in unit cell volume was mostly due to a contraction in a (and therefore b) lattice parameter. Figure 3.45 shows a view down the c axis of the Li_3BN_2 ($I4_1/amd$) structure. The $a \times a$ plane contains the N=B=N bonds and a contraction could be an indication of partial replacement of N=B=N with the smaller B≡N unit together with a local rearrangement. We would expect this to be reflected in a reduction in the a lattice parameter.

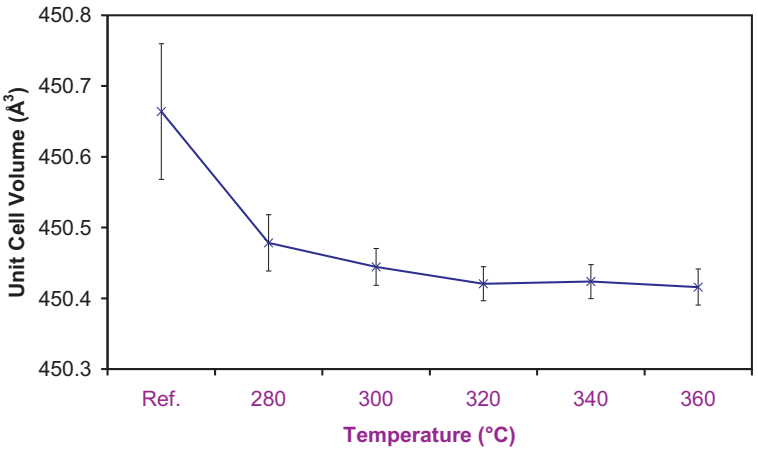

Figure 3.46: Unit cell volume of Li_3BN_2 present after heating $Li_4BH_4(NH_2)_3$ at different temperatures. The literature value for the unit cell volume [119] is also shown.

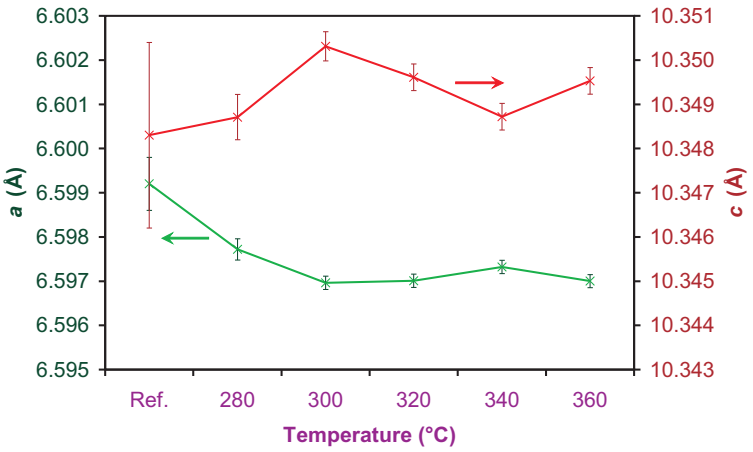

Figure 3.47: a and c lattice parameters of Li_3BN_2 present after heating $Li_4BH_4(NH_2)_3$ at different temperatures. The literature (Ref.) values [119] are also shown.

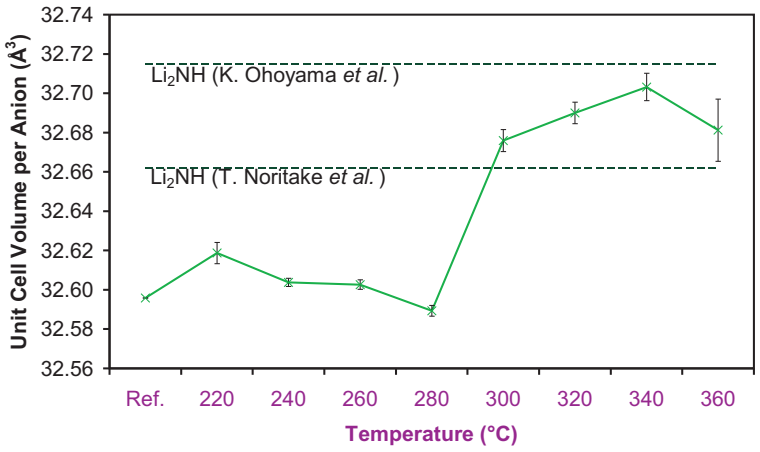

Figure 3.48: Unit cell volume per anion of $LiNH_2$ from decomposition of $Li_4BH_4(NH_2)_3$ after heating at different temperatures. A reference value is shown for $LiNH_2$ [99] and two different values for Li_2NH are also shown [129, 130].

Lithium imide was not observed in any of these diffraction patterns, which was consistent with the relatively small amount of ammonia release at temperatures up to 350°C under similar conditions in section 3.7. However, figure 3.48 shows that the unit cell volume per formula unit of the observed $LiNH_2$ phase approached the range expected for Li_2NH from reported synchrotron X-ray and neutron powder diffraction experiments. The a/c ratio for the $LiNH_2$ phase is shown in figure 3.50. This ratio did not reach a value of $1/2$ which would signify a transition to the cubic Li_2NH structure. Although there is a general increase in this ratio, even after decomposition at 360°C it still falls far short of this value and the (002) and (011) Bragg peaks, characteristic of the body centred tetragonal $LiNH_2$ structure and absent in the face centred cubic Li_2NH structure, remain prominent. It is very probable that the amide has undergone a partial decomposition to the imide with the release of a small amount of ammonia observed in TPD-MS experiments. However, attempts to determine the degree of decomposition by Rietveld refinement have failed.

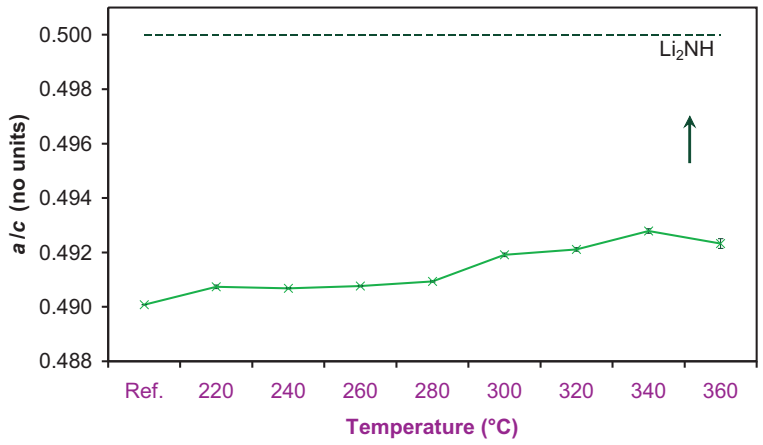

Figure 3.49: a/c ratio for $LiNH_2$ from decomposition of $Li_4BH_4(NH_2)_3$ after heating at various temperatures

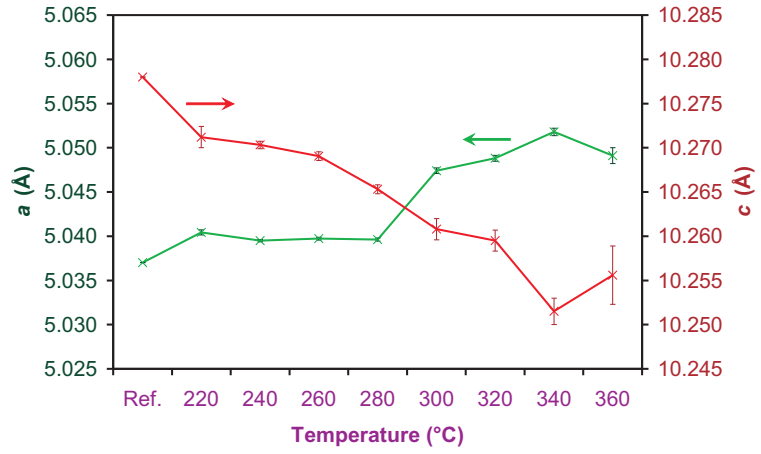

Figure 3.50: Lattice parameters of $LiNH_2$ from decomposition of $Li_4BH_4(NH_2)_3$ after heating at various temperatures

3.8 Conclusion

The complex hydride $Li_4BH_4(NH_2)_3$ has been formed by the reaction of $LiBH_4$ and $LiNH_2$ and structure solved by combined synchrotron X-ray and neutron powder diffraction techniques. Infrared and Raman spectroscopies have been used to probe the bonding in $Li_4BH_4(NH_2)_3$ and the bond strengths of the BH_4^- and NH_2^- were found to be weakened with respect to the starting materials. The thermal decomposition of $Li_4BH_4(NH_2)_3$ has been investigated by a variety of techniques and the gaseous decomposition products were found to depend on the experimental setup. Hydrogen release was observed from 245°C with ammonia observed as a minority product. *Ex-situ* diffraction techniques have been used to identify the polymorphs of Li_3BN_2 formed upon decomposition of $Li_4BH_4(NH_2)_3$ to give the reaction;

$$Li_4BH_4(NH_2)_3 \rightarrow Li_3BN_2 + LiNH_2 + 4H_2 \uparrow, \tag{3.7}$$

while remaining $LiNH_2$ may or may not decompose with the release of ammonia depending on the experimental setup.

Chapter 4

$Li_2BH_4NH_2$

4.1 Introduction

Investigations into borohydride rich reactions of $LiBH_4$ and $LiNH_2$ frequently produced diffraction patterns with peaks that could not be assigned to $LiBH_4$, $Li_4BH_4(NH_2)_3$ or $LiNH_2$. It was noted that these reactions frequently proceeded *via* a melt at temperatures as low as 120°C. Pinkerton *et al.* [131] reported that a 1:1 ball-milled mixture of $LiBH_4$ and $LiNH_2$ formed a new body centred cubic phase with a lattice constant of 10.4 Å. However, Noritake *et al.* [107] reported that ball milling a 1:1 mixture resulted in a new hexagonal phase with lattice constants of $a = 14.49$ Å and $c = 9.24$ Å. We prepared a pure phase from a 1:1 quenched melt of $LiBH_4$ and $LiNH_2$ which was indexed to the same hexagonal unit cell as Noritake *et al.* [107] and the structure was solved in rhombohedral symmetry. The spectroscopic and thermal decomposition properties of this new phase were investigated.

4.2 Experimental

Lithium amide and lithium borohydride (Sigma-Aldrich, 95% purity) were ground together in a 1:1 ratio in an argon filled glove box (>10 ppm O_2, >1 ppm H_2O)

and heated to 190°C under argon gas at 1 bar. The sample was removed from the furnace while at 190°C and quenched by immersing the reaction tube into cold water. Synchrotron X-ray powder diffraction data were collected on the ID31 diffractometer at the ESRF, Grenoble, at a wavelength and step-size of 0.80162 Å and 0.003° respectively. The sample was loaded into a glass capillary inside a nitrogen filled glove bag and sealed on a miniature gas torch. Neutron powder diffraction data were collected on GEM at the ISIS spallation neutron source at the Rutherford Appleton Laboratory. The sample was sealed inside a vanadium can with an iridium wire seal inside an argon filled glove box.

4.3 Crystal Structure Determination

The crystal structure of $Li_2BH_4NH_2$ was determined from powder diffraction data using the computer program Topas [90] and refined using the computer program GSAS [132]. During the structural determination, the crystallographic density was determined and the structure was shown to comprise a hexagonal array of discrete $(LiNH_2)_6$ clusters dispersed in a $LiBH_4$ matrix.

4.3.1 Indexing

The peak positions from the new phase were run through the indexing routine of Topas [90]. The most probable assignment was for a hexagonal unit cell with $a =$ 14.48 Å and $c = 9.24$ Å, which matched the assignment of Noritake *et al.* [107]. Inspection of the systematic absences of the diffraction pattern indicated that the phase has rhombohedral symmetry. Of the possible space groups, $R3$ (146), $R\bar{3}$ (148), $R32$ (155), $R3m$ (160) and $R\bar{3}m$ (166) (see table 4.1) were considered. The a and c lattice constants and unit cell volume were refined in a Pawley fit using Topas [90] as 14.4804(3) Å, 9.2448(3) Å and 1678.76(8) $Å^3$, respectively.

Table 4.1: Special positions available in each possible space-group (hexagonal axes of reference).

$R3$	$R\bar{3}$	$R32$	$R3m$	$R\bar{3}m$
No. 146	No. 148	No. 155	No. 160	No. 166
$9b$ (x,y,z)	$18f$ (x,y,z)	$18f$ (x,y,z)	$18c$ (x,y,z)	$36i$ (x,y,z)
$3a$ $(0,0,z)$	$9e$ $(1/2,0,0)$	$9e$ $(x,0,1/2)$	$9b$ $(x,\bar{x},z)$	$18h$ $(x,\bar{x},z)$
	$9d$ $(1/2,0,1/2)$	$9d$ $(x,0,0)$	$3a$ $(0,0,z)$	$18g$ $(x,0,1/2)$
	$6c$ $(0,0,z)$	$6c$ $(0,0,z)$		$18f$ $(x,0,0)$
	$3b$ $(0,0,1/2)$	$3b$ $(0,0,1/2)$		$9e$ $(1/2,0,0)$
	$3a$ $(0,0,0)$	$3a$ $(0,0,0)$		$9d$ $(1/2,0,1/2)$
				$6c$ $(0,0,z)$
				$3b$ $(0,0,1/2)$
				$3a$ $(0,0,0)$

4.3.2 Determining Crystallographic Density and Producing a Model

The hexagonal cell (a = 14.48 Å, c = 9.24 Å and V = 1678.76 Å^3) and the corresponding trigonal unit cell (a = 8.91 Å, α = 108.7, V = 559.59 Å^3) were investigated for similarities to the $LiBH_4$, $Li_4BH_4(NH_2)_3$ and $LiNH_2$ structures, but no obvious relationship was found.

From density and crystallographic arguments, the most probable number of formula units per unit cell were 24, 21 or 18.[†] These correspond to densities of 1.06, 0.93 and 0.80 g cm^{-3}, respectively; all these densities lie between those of the starting materials $LiBH_4$ (0.66 g cm^{-3}) and $LiNH_2$ (1.18 g cm^{-3}) [117].

24 Formula Units

The presence of 24 formula units allows for a close packed arrangement of anions which is seen in the $LiNH_2$ and $Li_4BH_4(NH_2)_3$ crystal structures by occupation of ($[l/4-n/12]$,$[m/4+n/12]$,$n/3$) sites (where l, m = 0,1,2,3 and n = 0,1,2), as illustrated in figure 4.1. This atomic arrangement was tested in all of the possible space groups using the computer program Topas [90]. The atom positions were fixed

[†]Consideration of the multiplicity of the available special positions rules out intermediate values.

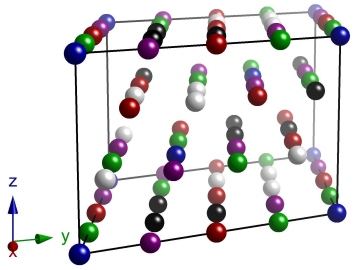

Figure 4.1: Hexagonal close packed arrangement for $Z = 24$. Example shown is in $R3$ with different crystallographic sites shown in different colours.

on the sites shown in figure 4.1 and the occupancies of each site were allowed to vary between the scattering power of B and N. None of the possible space groups produced a good fit to the diffraction data, the majority of the refinements ending with the minimum possible occupancy of each site.

Consideration of the Wyckoff sites (table 4.1) shows that, without significant disorder, a 1:1 stoichiometry is not possible, predicting instead a 7:9 stoichiometry. Reaction mixtures in the ratios $7LiBH_4$:$9LiNH_2$ and $9LiBH_4$:$7LiNH_2$ treated in the same way as the 1:1 mixture did not give a pure phase. For these reasons a structure with 24 formula units was disregarded.

21 Formula Units

The choice of 21 formula units gives a density closest to the average of the starting materials ($^1/_2[0.66 + 1.18] = 0.92$ g cm^{-3}); this is promising because the same method gave an accurate prediction of the correct density for $Li_4BH_4(NH_2)_3$.

In order for a total of 42 Li, 21 B and 21 N in the unit cell, sites of multiplicity 18 (or two 9 sites) and 3 (from table 4.1) are required for B, N and 2Li. Initially only the synchrotron X-ray powder diffraction data was investigated using the computer program Topas [90] and only the heaviest X-ray scatterers, B and N, were considered. A number of refinements were performed in each possible space

group where atoms were placed on sites adding up to the correct total number of B and N and their scattering power allowed to vary between that of B and N. Although a number of refinements produced reasonable fits to the diffraction data, in order for there to be the correct number of atoms in the unit cell without an amount of disorder, the 3*a* and 3*b* Wyckoff positions need to be occupied. This is possible considering just B and N, but once we consider that an equivalent number of Li must be present this presents a problem. This discounts $R\bar{3}$, $R32$ and $R\bar{3}m$ as there is only one possible 3*a* (0,0,0) and 3*b* (0,0,1/2) site each. These could be occupied by B and N respectively, but this would then require a disordered Li lattice for there to be 42 Li atoms in the unit cell. Attempts by Noritake *et al.* [107] to fit a disordered Li model to the structure of $Li_4BH_4(NH_2)_3$ resulted in an incorrect structural determination, and a significantly disordered structure is unlikely in such a large unit cell (1678.76(8) $Å^3$), so this possibility was discarded.

Only $R3$ and $R3m$ have the potential for the four required independent 3 multiplicity cites by multiple occupancy of 3*a* (0,0,*z*) Wyckoff positions. Li atoms were added in appropriate Wyckoff positions to the best preliminary refinements of B and N positions in both space groups. These refinements result in linear Li-B-Li-N-Li chains along the *c*-axis resulting from multiple occupancy of 3*a* (0,0,*z*) Wyckoff positions. Although the resulting Li-B and Li-N distances could be within the range expected from $LiBH_4$, $LiNH_2$ and $Li_4BH_4(NH_2)_3$, the unlikely linear geometry of the bonding and the poor fit of all attempted refinements suggested that 21 formula units was improbable.

18 Formula Units

The implausibility of 24 and 21 formula units led us finally to consider 18 formula units, which corresponds to a density that is lower than the average of the starting materials. This is plausible as it is not unusual for structures prepared through quenching from elevated temperature to have a lower density than the corresponding stable room temperature forms [133].

The synchrotron X-ray powder diffraction pattern of $Li_2BH_4NH_2$ is dominated by the scattering of B and N, and these were the first atom positions to be investigated using the computer program Topas [90]. At this stage all of the possible space groups shown in table 4.1 were considered. Starting models were chosen that consisted of 36 generic atoms in all combinations of suitable Wyckoff positions adding up to the correct total for boron and nitrogen; their positions were determined while allowing the scattering powers of the atoms to vary between that of boron and nitrogen. Many of the resultant refinements gave incorrect B : N ratios and extremely poor fits to the diffraction pattern and these atomic arrangements were immediately discarded. Of all the space groups and combinations of Wyckoff site occupations possible, the best fits were found for $R3$ and $R\bar{3}$ with all atoms on general positions and $R3m$ with two 9b (x,$\bar{x}$,z) sites and one 18c (x,y,z) site occupied. Of these possible space groups, $R3$ has the lowest symmetry with more degrees of freedom than $R\bar{3}$ and $R3m$ which could explain the good fit. The best fits for $R\bar{3}$ and $R3m$ originated from very similar structures. Both were made up of N octahedra centred around the (0,0,0) position, and therefore ($^1/_3$,$^2/_3$,$^2/_3$) and ($^2/_3$,$^1/_3$,$^1/_3$) positions by symmetry, with the B atoms occupying more open positions surrounding these octahedra. The structures differed mainly in the orientation of the N octahedra, as shown in figure 4.2.

Lithium atoms were then added to these partial structural solutions at appropriate combinations of Wyckoff positions, and 'anti-bump' penalties were introduced for short Li-B, Li-N and Li-Li distances (2.0, 1.7 and 2.2 Å respectively). At this point the $R\bar{3}$ structure became favoured, both in the visual and statistical fit. Rigid bodies for the BH_4^- and NH_2^- ions were introduced at the refined B and N positions for the $R\bar{3}$ structure. Initially BH_4^- was confined to tetrahedral geometry with a bond length of 1.2 Å and the NH_2^- ion to a bond length and angle of 1.0 Å and 105°, respectively. The rotation of these rigid bodies was then refined, followed by refinement of all atomic positions while keeping the rigid

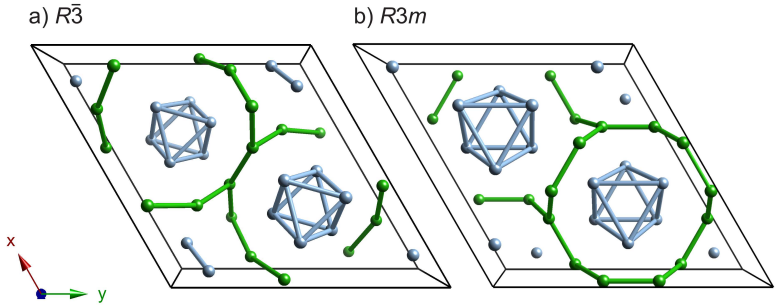

Figure 4.2: Comparison of preliminary refined structures of $Li_2BH_4NH_2$ in the space groups (a) $R\bar{3}$ and (b) $R3m$. Boron is shown in green and nitrogen in blue. The unit cell is shown in black.

body constraints. This model gave a good fit and was transferred to GSAS [132] for full Rietveld refinement using both synchrotron X-ray and neutron powder diffraction data. Hydrogen displacement parameters were constrained to be the same within each anion (BH_4^- and NH_2^-) and lithium displacement parameters were constrained to be the same on both sites; no further constraints were used. After refinement Fourier maps (not shown) were produced for the X-ray and neutron diffraction data which showed little in the way of residual scattering intensity. The final joint refinement (table 4.2) was essentially the same as that obtained from the X-ray data. The resulting crystal structure [121] is shown in figure 4.3 and the corresponding rhombohedral unit cell (between $+1/2$ and $-1/2$ in each direction) is shown including thermal ellipsoids in figure 4.4. The corresponding fits to the synchrotron X-ray and neutron diffraction data are shown in figures 4.5 and 4.6, respectively.

Selected bond lengths and angles for the refined $Li_2BH_4NH_2$ structure are shown in table 4.3. The bond angles and lengths of the BH_4^- ion refined to a slightly distorted tetrahedron, which was within the values expected from the structure of $LiBH_4$ [98] but outside the more accurate determination of $LiBD_4$ [102]. Without rigid body constraints, the NH_2^- ion significantly deformed with a very asymmetric bond lengths and unusually low bond angle. The refined

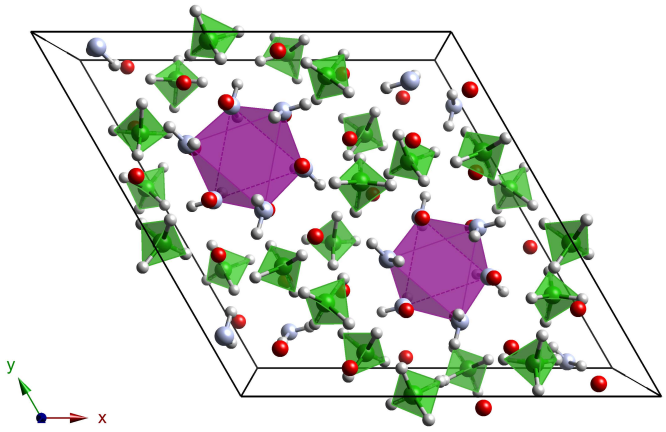

Figure 4.3: Refined crystal structure of $Li_2BH_4NH_2$. Boron is shown in green, nitrogen in blue, lithium in red and hydrogen in white. Purple N octahedra are added to guide the eye. The unit cell is shown in black.

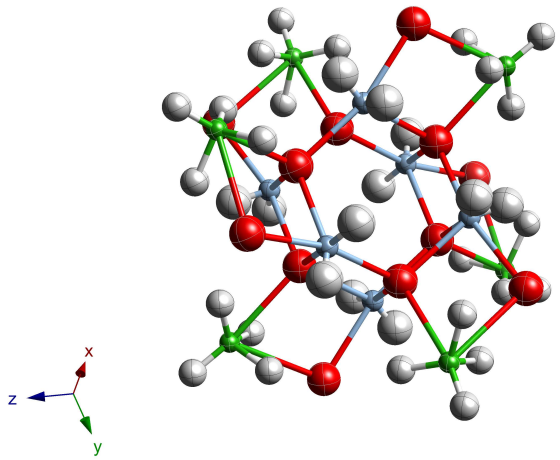

Figure 4.4: Refined crystal structure of $Li_2BH_4NH_2$ showing thermal ellipsoids. Boron is shown in green, nitrogen in blue, lithium in red and hydrogen in white. Atoms are represented as thermal ellipsoids of 50% probability.

Table 4.2: Refined crystallographic data for $Li_2BH_4NH_2$.

Atom	x/a	y/a	z/c	B_{iso}/Å
Li(1)	0.2903(9)	0.0608(9)	0.7816(11)	5.31(17)
Li(2)	0.8457(11)	0.8739(12)	0.0747(10)	Li(1)
B	0.6763(5)	0.7520(6)	0.1835(7)	1.96(16)
H(1)	0.7363(11)	0.8167(11)	0.2797(14)	3.5(2)
H(2)	0.7112(13)	0.7192(13)	0.0933(15)	H(1)
H(3)	0.6457(11)	0.8057(12)	0.1036(15)	H(1)
H(4)	0.5982(14)	0.6842(11)	0.2187(14)	H(1)
N	0.1254(4)	0.9690(3)	0.8571(4)	2.22(9)
H(5)	0.1015(17)	0.973(2)	0.7258(19)	5.9(3)
H(6)	0.1431(15)	0.9211(14)	0.829(2)	H(5)

Space group $R\bar{3}$, $a = 14.4804(3)$ Å, $c = 9.2448(3)$ Å, $V = 1678.76(8)$ Å^3.
X-ray data: $wR_p = 0.0819$, $R_p = 0.0621$.
Neutron data (banks 5 and 6): $wR_p = 0.0131$ and 0.0107 , $R_p = 0.0132$ and 0.096.
$\chi^2 = 2.264$ for 47 variables.

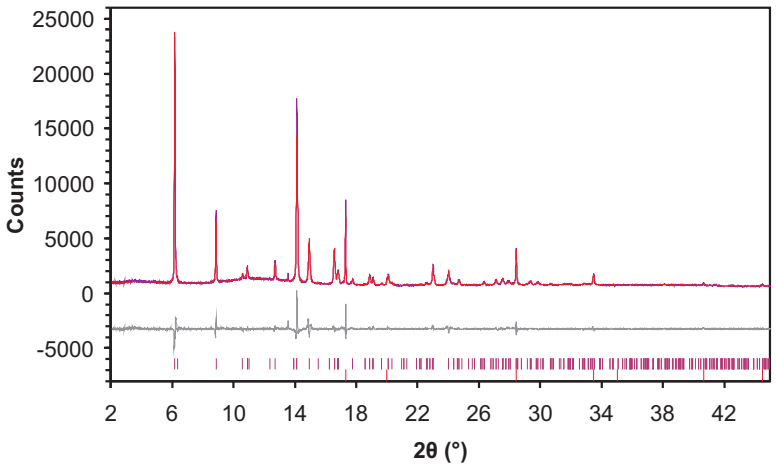

Figure 4.5: Final Rietveld plot for synchrotron X-ray diffraction data of $Li_2BH_4NH_2$ showing observed (purple), calculated (red) and difference (grey) plots. Peak positions for $Li_2BH_4NH_2$ (crimson) and Li_2O (red) are indicated.

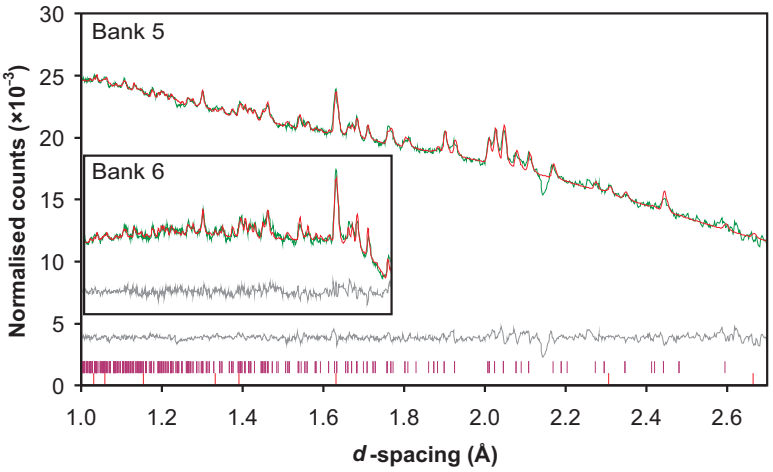

Figure 4.6: Final Rietveld plot for neutron diffraction data of $Li_2BH_4NH_2$ showing observed (green), calculated (red) and difference (grey) plots. The insert shows the data from detector bank 6. Peak positions for $Li_2BH_4NH_2$ (crimson) and Li_2O (red) are indicated.

hydrogen positions for $Li_2BH_4NH_2$ may be unreliable because of the relatively low quality of the neutron diffraction data below 1.2 Å *d*-spacing resulting from the lack of isotopic enrichment. The large difference in quality of diffraction data obtained from $Li_2BH_4NH_2$ to that of the less boron rich $Li_4BH_4(NH_2)_3$ suggest that it is the high neutron absorption of naturally occurring B (containing ^{10}B) which has the greatest affect on the quality of attainable neutron diffraction data, rather that the large incoherent neutron scattering cross section of H.

The central feature of the $Li_2BH_4NH_2$ structure is the octahedral clusters of six NH_2^- anions. These octahedral NH_2^- clusters are a common structural motif in light metal amides such as $LiNH_2$ [103], $NaNH_2$ [134], $Li_3Na(NH_2)_4$ [135] and $Mg(NH_2)_2$ [136], and are also found in the only previously reported amideborohydride, $Li_4BH_4(NH_2)_3$.

The crystal structure of $Li_2BH_4NH_2$ can be viewed as a mixture of clusters of $LiNH_2$ embedded in an $LiBH_4$ matrix. The presence of isolated NH_2^- octahedra in the $Li_2BH_4NH_2$ structure prepared from a quenched melt suggests that these units may exist in the molten state, separated by the borohydride ions. It is easy

Table 4.3: Selected refined inter atomic distances (Å) and angles (°) for $Li_2BH_4NH_2$ together with literature data for $Li_4BH_4(NH_2)_3$, $LiBH_4$, $LiBD_4$, $LiNH_2$ and $LiND_2$

Bond	$Li_2BH_4NH_2$	$Li_4BH_4(NH_2)_3$	$LiBH_4$	$LiBD_4$[†]	$LiNH_2$	$LiND_2$
B-H	1.11(2)	1.17(2)	1.04(2)	2×1.208(3)	-	-
	1.19(2)	3×1.271(11)	1.25(1)	1.213(7)	-	-
	1.27(2)	-	2×1.28(1)	1.224(5)	-	-
	1.30(2)	-	-	-	-	-
H-B-H	100.4(5)	3×107.6(4)	85.1(4)	107.2(3)	-	-
	101.2(5)	3×111.3(5)	103.2(5)	2×108.0(3)	-	-
	105.6(5)	-	2×114.3(3)	110.1(3)	-	-
	107.4(5)	-	2×120.0(5)	2×111.6(4)	-	-
	117.7(5)	-	-	-	-	-
	121.0(5)	-	-	-	-	-
N-H	0.89(2)	0.985(13)	-	-	0.70(10)	0.967(5)
	1.27(2)	1.043(15)	-	-	0.76(12)	0.978(6)
H-N-H	86.6(6)	104.9(6)	-	-	123(1)	104.0(4)
Li-B	2.41(2)	2.530(14)	2.475(4)	2.371(7)	-	-
	2.480(11)	3× 2.685(10)	2×2.521(2)	2×2.523(4)	-	-
	2.535(12)	-	2.542(4)	2.538(7)	-	-
	2.525(14)	-	-	-	-	-
Li-N	2.012(10)	3×2.035(13)	-	-	4×2.059(3)	4×2.065(3)
	2.14(2)	2×2.056(11)	-	-	2×2.064(9)	2×2.078(6)
	2.187(10)	2×2.097(9)	-	-	2×2.212(9)	2×2.191(6)
	2.190(9)	2×2.212(8)	-	-	4×2.213(3)	4×2.210(3)
Li-Li	2×2.48(2)	2.34(2)	2×3.449(4)	2×3.494(8)	4×2.519(7)	4×2.51584(4)
	2.90(2)	3×2.44(2)	-	-	2×2.524(7)	2×2.55(1)
	3.40(2)	3×3.46(2)	-	-	4×3.598(7)	4×3.59214(3)
	3.413(14)	-	-	-	-	-
Reference	[121]	[101]	[98]	[102]	[99]	[103]
Volume per cation ($Å^3$)	46.632(2)	37.90234(9)	54.1713(8)	54.615(11)	32.596	32.4569(17)

[†]This determination was performed at 3.5 K (−269.5°C).

to see how the $Li_2BH_4NH_2$ structure may form as it is reasonable to presume that the difference in energy will be small between this molecular scale mixture of $LiNH_2$ within $LiBH_4$ and the $LiNH_2$:$LiBH_4$ melt. The structural relationships between $Li_2BH_4NH_2$, $Li_4BH_4(NH_2)_3$ and the starting materials $LiBH_4$ and $LiNH_2$ are discussed in more detail in section 5.7.

4.3.3 Alternative Crystal Structure Determination

The crystal structure of $Li_2BH_4NH_2$ has subsequently been solved from scratch by Wu *et al.* [104] using an isotopically enriched sample of nominal composition $^{6/7}Li_2{}^{11}BN_2D_6$. A stoichiometric mixture of $^{7}Li^{11}BD_4$ + $LiND_2$ was repeatedly annealed at 65°C under 5 bar of deuterium gas. Constant wavelength (λ = 1.5403(2) Å) high resolution powder neutron diffraction data were collected at 5 K (−268°C), which showed predominantly the hexagonal $^{6/7}Li_2{}^{11}BD_4ND_2$ phase with some $^{6/7}Li_4{}^{11}BD_4(ND_2)_3$ and $^{7}Li^{11}BD_4$ (20.68(1) and 8.08(1) weight%, respectively).

In order to map the reported atomic coordinates of *Wu* [104] onto the reported atomic positions of *Chater* [121] an origin shift of $(0, 0, +1/2)$ is required. The transformed atomic parameters for both structures are shown in table 4.4. Although the structures look relatively similar there are significant differences, with a twisting in the relative orientation of the NH_2^- octahedra and BH_4^- chains, as shown in figure 4.7.

The determined atomic positions of *Wu* [104], in particular the hydrogen (deuterium) positions, should be more accurate than those of *Chater* [121]. The use of an isotopically enriched sample means that the neutron data will not affected by incoherent scattering from H and absorption by Li and B which resulted in the uncertainty in hydrogen positions of *Chater*. The structural determination of *Wu* was performed on data collected at 5 K (−268°C) which means that the data will be less affected by the thermal motions of the atoms, especially of the hydrogen (deuterium) atoms within the complex anions. However, this means

Table 4.4: Comparison of different crystal structure determinations

	Parameter	*Chater* [121]	*Wu*† [104]
	a (Å)	14.4804(3)	14.3944(3)
	c (Å)	9.2448(3)	9.0522(3)
	V (Å^3)	1678.76(8)	1624.337(1)
Atom			
Li(1)	x	0.1038(9)	0.0620(3)
	y	0.3764(9)	0.2911(5)
	z	0.4483(11)	0.2123(4)
	B_{iso}	5.31(17)	1.7(3)
Li(2)	x	0.0282(11)	0.1179(3)
	y	0.1543(12)	0.1527(5)
	z	0.0747(10)	0.0767(4)
	B_{iso}	Li(1)	0.8(3)
B	x	0.0757(5)	0.2478(2)
	y	0.3237(6)	0.3256(3)
	z	0.1835(7)	0.1761(4)
	B_{iso}	1.96(16)	0.134(16)
H(1)	x	0.0804(11)	0.1933(5)
	y	0.2637(11)	0.2692(2)
	z	0.2797(14)	0.2747(2)
	B_{iso}	3.5(2)	1.82(8)
H(2)	x	0.0080(13)	0.1924(5)
	y	0.2888(13)	0.3415(5)
	z	0.0933(15)	0.0887(4)
	B_{iso}	H(1)	3.00(16)
H(3)	x	0.1600(11)	0.2811(5)
	y	0.3543(12)	0.2746(5)
	z	0.1036(15)	0.1086(4)
	B_{iso}	H(1)	2.8(3)
H(4)	x	0.0860(14)	0.3167(5)
	y	0.4018(11)	0.4089(5)
	z	0.2187(14)	0.2223(7)
	B_{iso}	H(1)	1.7(4)
N	x	0.1564(4)	0.1561(3)
	y	0.1254(3)	0.0305(2)
	z	0.1429(4)	0.1475(3)
	B_{iso}	2.22(9)	0.9(3)
H(5)	x	0.1290(17)	0.1314(4)
	y	0.102(2)	0.0380(5)
	z	0.2742(19)	0.2465(6)
	B_{iso}	5.9(3)	1.02(16)
H(6)	x	0.2220(15)	0.2354(5)
	y	0.1431(14)	0.0911(5)
	z	0.171(2)	0.1522(7)
	B_{iso}	H(5)	1.3(4)

†The quoted hydrogen positions are deuterium positions. This determination was performed at 5 K (−268°C).

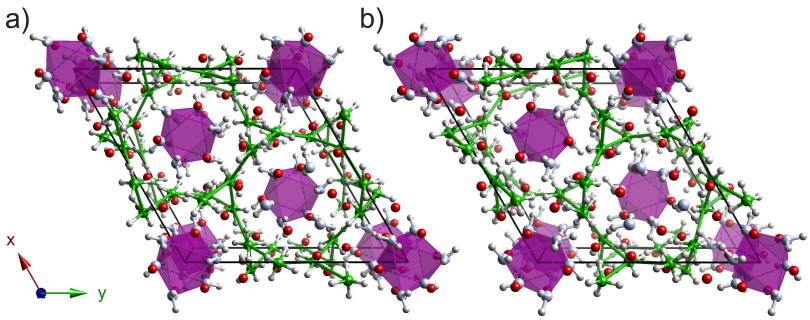

Figure 4.7: Crystal structures of $Li_4BH_4NH_2$ by (a) Chater *et al.* [121] and (b) Wu *et al.* [104]. Boron is shown in green, nitrogen in blue, lithium in red and hydrogen in white. Purple N octahedra are added to guide the eye. The unit cell is shown in black.

that the structures of *Chater* (solved using room temperature data) and *Wu* are not directly comparable. No room temperature data was published by *Wu* for the $Li_2BH_4NH_2$ structure. However, assuming that the two samples would show similar thermal expansion behaviour, there is a strong preferential expansion of the *c* lattice parameter (2.1%) compared to that of the *a* lattice parameter (0.6%) going from low temperature (*Wu*) to room temperature (*Chater*). This expansion is due to an increase in the separation of the BH_4^-/NH_2^- layers, as shown in figure 4.8(a), which are also a feature seen in $Li_4BH_4(NH_2)_3$ (4.8(b)). This increase in layer spacing would allow for the observed twist in relative orientation of the NH_2^- octahedra and BH_4^- chains between the two different structure determination to occur more easily.

The determined interatomic distances (excluding hydrogen distances) are very similar between the two models (table 4.5). Attempts to match the structure of Wu *et al.* to our neutron and X-ray diffraction data using GSAS [132] resulted in less good fits than when using our determined structure. Although the structure of Wu *et al.* [104] is certainly a more accurate determination of atomic positions than that of Chater *et al.* [121] because of the better neutron diffraction data obtained by using an enriched sample, it only represents an accurate determi-

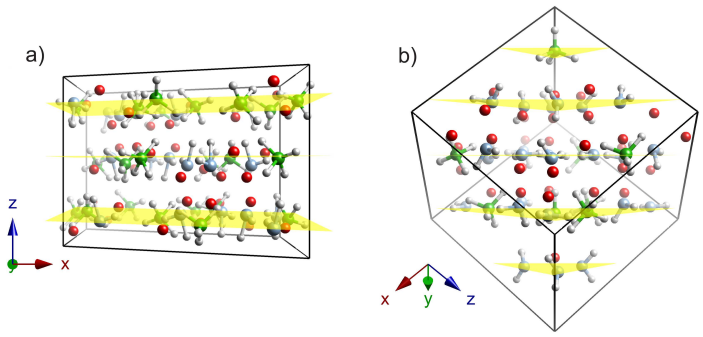

Figure 4.8: Layered structures of (a) $Li_2BH_4NH_2$ and (b) $Li_4BH_4(NH_2)_3$. The lattice planes due to (a) the (003) reflection and (b) the (222) reflection are shown in yellow.

nation of the low temperature structure. The $Li_2BH_4NH_2$ structure appears to undergo a rearrangement upon heating to room temperature to give the structure of Chater *et al.* [121]. Indeed, the observed preferential thermal expansion between the layers would facilitate such a rearrangement. Also a large degree of thermal motion in $Li_2BH_4NH_2$ at room temperature is not unexpected as the observed melting point was only 100°C (see section 5.4). A room temperature neutron diffraction study on an enriched sample of $Li_2BH_4NH_2$ is required to confirm whether the structure of Chater *et al.* [121] is indeed the correct room temperature form.

4.4 Raman Spectroscopy

In order to investigate the bonding within $Li_2BH_4NH_2$, Raman spectroscopy was performed and compared with that of the related materials, $LiBH_4$, $LiNH_2$ and $Li_4BH_4(NH_2)_3$. Group theory and comparisons with the literature, discussed previously in section 3.5, were used to assign the spectra.

Regions of the Raman spectra relating to the internal modes of the NH_2^- and BH_4^- anions of $Li_2BH_4NH_2$, together with the spectra of $Li_4BH_4(NH_2)_3$ and the starting materials $LiBH_4$ and $LiNH_2$, are shown in figure 4.9. The observed

Table 4.5: Selected refined interatomic distances (Å) and angles (°) for two $Li_2BH_4NH_2$ structure determinations.

Bond	*Chater*	*Wu*
Reference	[121]	[104]
B-H(1)	1.269(13)	1.198(8)
B-H(2)	1.190(14)	1.223(9)
B-H(3)	1.300(14)	1.222(8)
B-H(4)	1.113(13)	1.187(8)
H(1)-B-H(2)	121.0(5)	110.0(7)
H(1)-B-H(3)	105.6(4)	106.6(6)
H(1)-B-H(4)	117.7(6)	110.9(6)
H(2)-B-H(3)	100.4(5)	106.1(6)
H(2)-B-H(4)	107.4(5)	109.4(6)
H(3)-B-H(4)	101.2(5)	113.8(6)
N-H(5)	1.27(2)	0.990(7)
N-H(6)	0.89(2)	1.034(7)
H(3)-N-H(4)	86.6(6)	100.1(6)
B-Li(1)	2.480(11)	2.44(1)
B-Li(1)	2.525(14)	2.49(1)
B-Li(1)	2.535(12)	2.59(1)
B-Li(2)	2.41(2)	2.41(1)
N-Li(1)	2.187(8)	2.15(1)
N-Li(2)	2.012(10)	2.03(1)
N-Li(2)	2.135(9)	2.07(1)
N-Li(2)	2.190(14)	2.19(1)

Bond distances, angles and estimated standard deviations were calculated from the reported structures using VESTA [111].

spectra have been fully assigned, the results of which are shown in table 4.6.

In the crystal structure of $Li_2BH_4NH_2$ the BH_4^- and NH_2^- anions occupy general positions, giving the lowest possible symmetry point groups of C_1 and C_s, respectively. As such, we might expect splitting of the observed vibrational modes for $Li_2BH_4NH_2$. Instead of splitting, we observe much broader vibrational bands than for the staring materials and $Li_4BH_4(NH_2)_3$, especially for the borohydride anion. The wavenumber of the main symmetric stretch (ν_1) of the BH_4^- ion is higher than that observed in $LiBH_4$ and $Li_4BH_4(NH_2)_3$. However, the ν_3 asymmetric stretch is observed at a much lower wavenumber than in $LiBH_4$. As

Table 4.6: Observed Raman shifts ($\tilde{\nu}$) and assignments (Ass.) for $Li_2BH_4NH_2$, $LiBH_4$, $LiNH_2$ and $Li_4BH_4(NH_2)_3$.

$Li_2BH_4NH_2$		$LiBH_4$		$LiNH_2$		$Li_4BH_4(NH_2)_3$	
$\tilde{\nu}$	Ass.	$\tilde{\nu}$	Ass.	$\tilde{\nu}$	Ass.	$\tilde{\nu}$	Ass.
-	-	190	ext	236.7	ext	230	ext
288	ext	256	ext	273.7	ext	265	ext
-	-	-	-	291.2	ext	300	ext
-	-			327.1	ext	327	ext
-	-			343.8	ext	380	ext
-	-			516.2	ext	516	ext
-	-			582.3	ext	630	ext
668	ext			654.7	ext	666	ext
1098	ν_4 (BH_4^-)	1095.5	ν_4			1086	ν_4 (BH_4^-)
-	-	1235	$3\nu_L$			-	-
1255.2	ν_2 (BH_4^-)	1287.2	ν_2			1273.9	ν_2 (BH_4^-)
1325.0	ν_2' (BH_4^-)	1317.3	ν_2'			-	-
-	-			1539.1	ν_2	1558.6	ν_2 (NH_2^-)
2166	$2\nu_4$ (BH_4^-)	2161.6	$2\nu_4$			2139	$2\nu_4$ (BH_4^-)
-	-	2189.1	$2\nu_4'$			2154	$2\nu_4'$ (BH_4^-)
2241.3	ν_3 (BH_4^-)	2273.3	ν_3			-	-
2303.3	ν_1 (BH_4^-)	2297.4	ν_1			2286.4	ν_1 (BH_4^-)
-	-	2318.1	ν_3'			2316 (sh)	ν_3 (BH_4^-)
2361 (b)	com	2377	com			2360 (b)	com
2395 (b)	com	2479.8	com			2442 (b)	com
-	-	2566	com			-	-
3246.5	ν_1 (NH_2^-)			3261.6	ν_1	3244	ν_1 (NH_2^-)
3294.7	ν_3 (NH_2^-)			3313.2	ν_3	3302.1	ν_3 (NH_2^-)
-	-			3323.6	ν_3'	3304.9	ν_3' (NH_2^-)

b, broad; com, combination bands; ext, external vibrations; sh, shoulder.

Vibrations quoted to one decimal place were calculated using peak fitting with the computer program WiRE [115]. Vibrations quoted to one decimal place were from observed maxima.

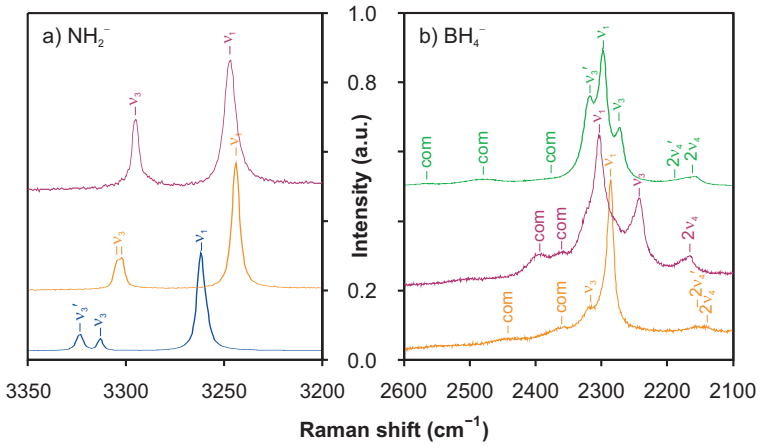

Figure 4.9: Raman spectra of (a) the NH_2^- region and (b) the BH_4^- region of $Li_2BH_4NH_2$, $LiNH_2$, $LiBH_4$ and $Li_4BH_4(NH_2)_3$. Observed spectra for $Li_2BH_4NH_2$, $LiBH_4$, $LiNH_2$ and $Li_4BH_4(NH_2)_3$ are shown in crimson, green, blue and orange, respectively.

with $Li_4BH_4(NH_2)_3$, vibrational bands due to the amide anion were observed at lower wavenumbers than in $LiNH_2$.

4.5 In-situ Diffraction

Although $Li_2BH_4NH_2$ appeared to be stable indefinitely at room temperature (no sign of degradation was observed in the X-ray diffraction pattern after 10 months), on heating to just below the melting point $Li_2BH_4NH_2$ decomposed to $Li_4BH_4(NH_2)_3$ and $LiBH_4$ confirming the intrinsic metastability of $Li_2BH_4NH_2$. This decomposition was investigated in an *in-situ* powder synchrotron X-ray diffraction experiment. A sample of $Li_2BH_4NH_2$ was taken to the ESRF, Grenoble, where it was loaded into a capillary and measured on beamline ID31.

Synchrotron X-ray diffraction data were collected at a wavelength of 0.80023(1) Å and rebinned from the original step size of 0.003° to 0.006° to improve the signal-to-noise ratio.

A cryostream was used to heat the sample. Initially the sample was heated quickly from room temperature to 90°C (10°C min^{-1}) while data were collected

in the range 2° to 28° 2θ (d-spacing 22.9 Å to 1.66 Å) with a data collection time of around 1.5 minutes per scan. Data were then collected in the range 2° to 48° 2θ (d-spacing 22.9 to 0.99 Å) with a data collection time of around 9.5 minutes per scan while the sample was held at 90°C. Once $Li_2BH_4NH_2$ had completely transformed to $Li_4BH_4(NH_2)_3$ and $LiBH_4$ the sample was heated to 180°C (above the melting point of the mixture) before cooling rapidly to room temperature. The temperatures quoted were the average temperatures over the entire scan.

Refinement Strategy

Powder diffraction data were analysed using Topas [90]. For each data set a zero point error and an 18 parameter Chebyshev background function were refined. For each phase present, lattice parameters, a pseudo-Voigt peak shape function with 6 parameters and scale factor were refined. Atomic coordinates and thermal parameters were taken from reported structures and were not refined as the quality of data recorded with relatively short scan times did not allow for meaningful refinement of atomic positions. The weight percent reported by Topas for each compound present, together with the estimated standard error, were converted into mole percent values. Molar masses per lithium ion, i.e. calculated from the chemical formula scaled to one Li (e.g. $Li(BH_4)_{0.5}(NH_2)_{0.5}$), were used to make the mole percent values comparable. At temperatures above the melting point the amount of Li_2O present was used as an internal standard for quantitative phase analysis to determine non-crystalline (liquid/amorphous) sample content, as described previously in section 3.6.

Results

Figure 4.10 shows a summary of the phase fractions obtained from the refinements at each stage of the temperature ramp to 90°C and upon holding at 90°C. Initially $Li_2BH_4NH_2$ was present with a small amount of excess $LiBH_4$ and Li_2O. The Li_2O was from the $LiNH_2$ starting material and the excess $LiBH_4$ was caused because

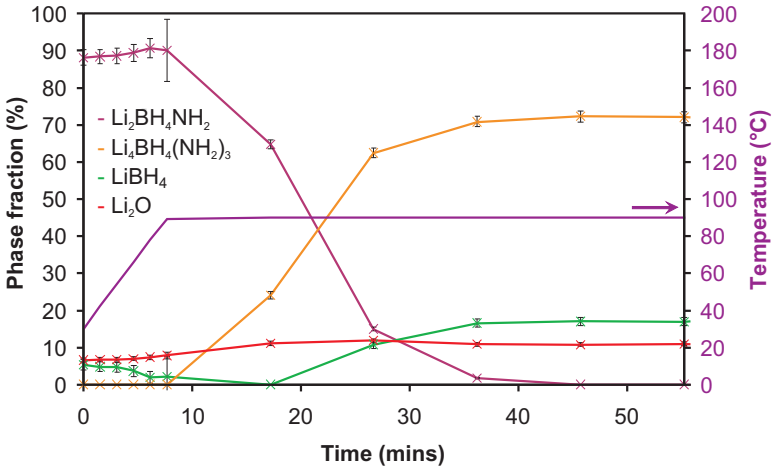

Figure 4.10: Phase fractions present upon heating $Li_2BH_4NH_2$ to 90°C.

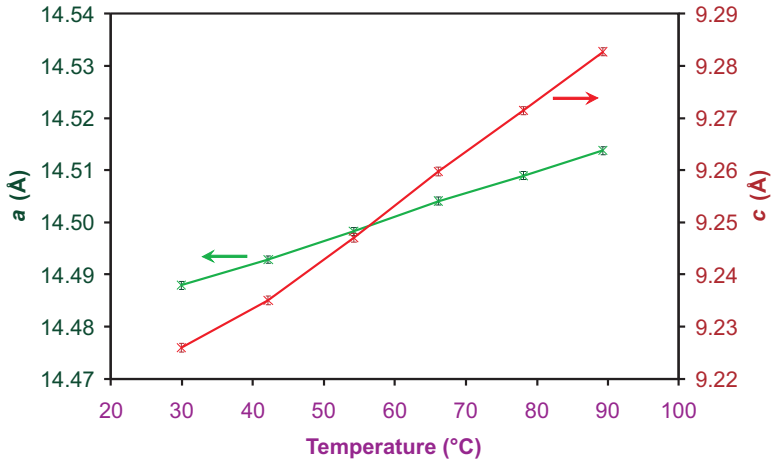

Figure 4.11: *a* and *c* lattice parameters of $Li_2BH_4NH_2$ during heating to 90°C.

the presence of Li_2O was not taken into account when weighing out the amount of $LiNH_2$ required to from $Li_2BH_4NH_2$, leading to effectively a slightly amide poor starting mixture.

The lattice parameters of the hexagonal $Li_2BH_4NH_2$ are shown in figure 4.11. Preferential expansion of the *c* lattice parameter is observed, with 0.62% expansion compared with only 0.18% for the *a* lattice parameter in the temperature range 30 to 90°C. This expansion is due to an increase in the separation of the BH_4^-/NH_2^- layers, as noted previously in section 4.3.3 when comparing crystal structure determinations performed at different temperatures.

After the fast ramp to 90°C, $Li_2BH_4NH_2$ remained. The amount of $LiBH_4$ observed during heating decreased indicating that the $Li_2BH_4NH_2$ structure may be able to accommodate extra $LiBH_4$ at elevated temperatures. After reaching 90°C the $Li_2BH_4NH_2$ gradually decomposed to $Li_4BH_4(NH_2)_3$ and $LiBH_4$ with the transformation complete after 30 minutes. The observed molar ratios after the transformation was 72.1(5)% $Li_4BH_4(NH_2)_3$ with 17.0(4)% $LiBH_4$. Assuming a 1:1 starting ratio of BH_4^-:NH_2^- we would expect 66.$\dot{6}$% $Li_4BH_4(NH_2)_3$ and 33.$\dot{3}$% $LiBH_4$ indicating that the $Li_4BH_4(NH_2)_3$ observed is borohydride rich of the form $Li_4(BH_4)_{(1+x)}(NH_2)_{(3-x)}$.

The variation of the lattice parameter with temperature of the observed $Li_4(BH_4)_{(1+x)}(NH_2)_{(3-x)}$ phase is shown in figure 4.12. During the isothermal portion of the experiment while the $Li_2BH_4NH_2$ was decomposing to $Li_4BH_4(NH_2)_3$ and $LiBH_4$ the observed lattice parameter of $Li_4(BH_4)_{(1+x)}(NH_2)_{(3-x)}$ decreased.[†] This is consistent with findings in section 3.6 during the *in-situ* formation of $Li_4BH_4(NH_2)_3$, where the more rapid decrease in the amount of $LiBH_4$ than $LiNH_2$ was interpreted as the $Li_4BH_4(NH_2)_3$ structure readily becoming borohydride rich before approaching its ideal stoichiometry upon annealing. In this case it appears that a borohydride rich $Li_4(BH_4)_{(1+x)}(NH_2)_{(3-x)}$ was initially formed with a larger lattice parameter which then upon holding at 90°C decomposed to a less borohydride rich form (with a lower lattice parameter) and $LiBH_4$. Indeed, during this isothermal section the relative amount of $LiBH_4$ compared to $Li_4BH_4(NH_2)_3$ gradually increased.

During the subsequent heated segment, the lattice parameter of $Li_4BH_4(NH_2)_3$ gradually increased with temperature as expected. The observed phase fraction of Li_2O started to increase, which was interpreted as an indication of the presence of a non-crystalline/liquid phase until, at 180°C, it accounted for 92.0(9) mol%

[†]These observed lattice parameters were significantly all larger than 10.70 Å, which was the lattice parameter observed at 90°C during the formation of $Li_4BH_4(NH_2)_3$ (section 3.6).

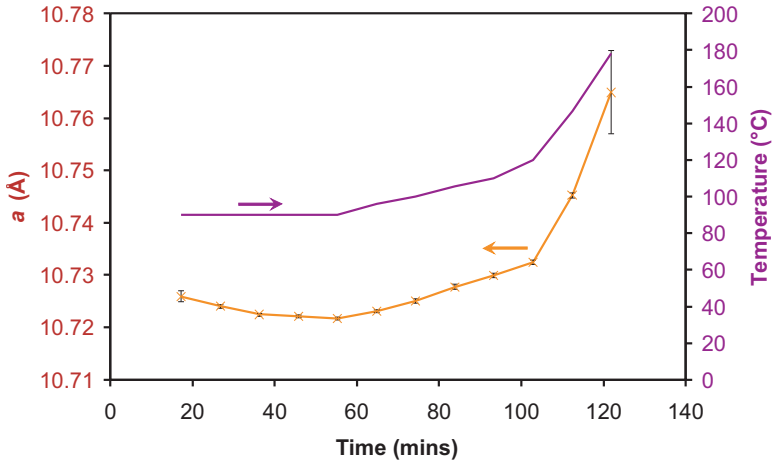

Figure 4.12: Lattice parameter of $Li_4BH_4(NH_2)_3$ formed upon heating $Li_2BH_4NH_2$.

(with some $Li_4BH_4(NH_2)_3$ remaining). Although disorder induced by rotation of the complex anions present in these structures or movement of the lithium ions will also cause an apparent loss of intensity in the diffraction pattern for the respective phase, the Bragg peaks of the observed crystalline phases remained relatively sharp, suggesting that they are not significantly disordered. The observed absolute intensity of Bragg peaks due to Li_2O did not alter significantly and a large amorphous feature centred around 14° 2θ was observed in the background of the diffraction patterns at higher temperatures which backs up the suggestion of non-crystalline content.

Using the average calculated weight fraction for Li_2O during the isothermal section as an internal standard,[†] the weight fractions were recalculated to estimate any non-crystalline content, as shown in figure 4.13.

The non-crystalline content, which has been designated as a liquid phase due to the low melting point of borohydride rich xLiBH$_4$ + yLiNH$_2$ mixtures (see chapter 5, section 5.4), started to form from 100°C, only slightly higher in temperature than in the formation of $Li_4BH_4(NH_2)_3$ (≈90°C, section 3.6). The

[†]The lower temperature data was not included in this average as it was recorded over a narrower 2θ range which only included two Bragg reflections due to Li_2O, resulting in a less accurate determination of Li_2O content.

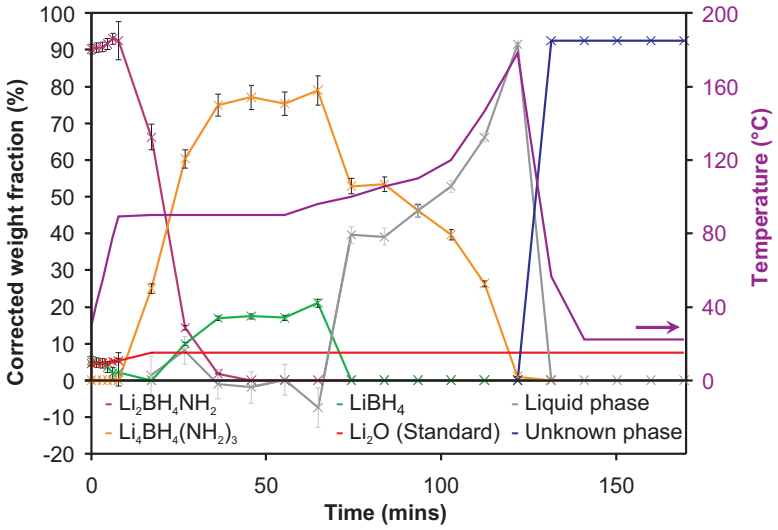

Figure 4.13: Corrected phase weight fractions present upon heating $Li_2BH_4NH_2$ after normalisation for Li_2O.

liquid content continued to increase upon heating with the concurrent loss of $Li_4BH_4(NH_2)_3$ until 180°C when only ≈1 wt% $Li_4BH_4(NH_2)_3$ remained. When the mixture was essentially molten, it was cooled rapidly to room temperature upon which $Li_2BH_4NH_2$ was expected to reform.

Although new Bragg peaks were observed upon cooling, these did not correspond to $Li_2BH_4NH_2$. A new crystalline phase formed, designated as "Unknown phase" in figure 4.13. However, after attempts to index the Bragg reflections, it became clear that these reflections were due to at least two different phases. A new face centred cubic (FCC) phase was identified with a lattice parameter of 5.62305(5) Å. The other reflections could not be identified. The assigned and unassigned reflections are shown in table 4.7 and the diffraction pattern is shown in figure 4.14.[†] Attempts to include the unknown reflections by lowering of the FCC symmetry and transforming it to related tetragonal and orthorhombic cells did not lead to an improvement in fit and the remaining reflections remain unidentified.

[†]The diffraction pattern used for indexing was a summation of data from three identical scans giving a total scan time of 28.5 minutes.

Table 4.7: Unidentified reflections and reflections due to an FCC phase after rapid cooling of molten $Li_2BH_4NH_2$.

Unknown reflections			FCC		
2θ (°)	d (Å)	I_{rel} (%)	2θ (°)	d (Å)	I_{rel} (%)
5.70	8.05	7.8	-	-	-
7.71	5.95	9.5	-	-	-
10.50	4.37	15.0	-	-	-
13.53	3.40	3.6	-	-	-
14.00	3.28	100.0	-	-	-
-	-	-	14.15	3.25	100.0
15.89	2.89	3.5	-	-	-
-	-	-	16.36	2.81	22.9
17.13	2.69	16.8	-	-	-
18.12	2.54	3.4	-	-	-
22.22	2.08	3.9	-	-	-
-	-	-	23.21	1.99	55.9
23.50	1.96	0.1	-	-	-
-	-	-	27.29	1.70	22.2
-	-	-	33.06	1.41	6.0
-	-	-	36.13	1.29	3.1

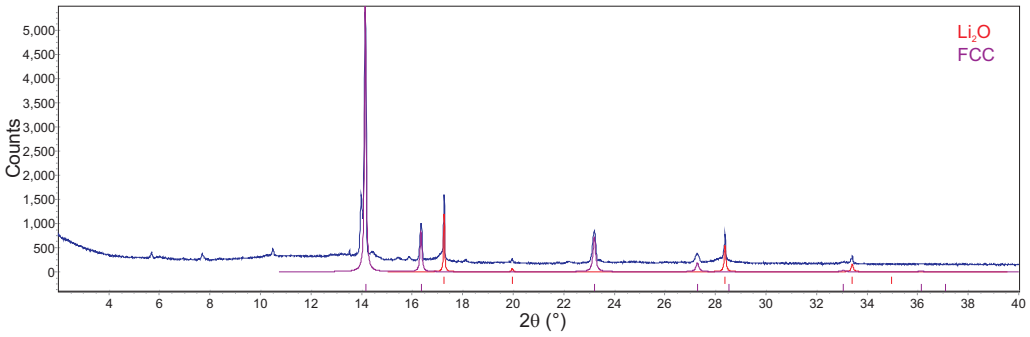

Figure 4.14: Powder X-ray diffraction pattern of the products after rapid cooling of the $Li_2BH_4NH_2$ melt. Bragg reflection positions for Li_2O and the FCC lattice are shown in red and purple respectively.

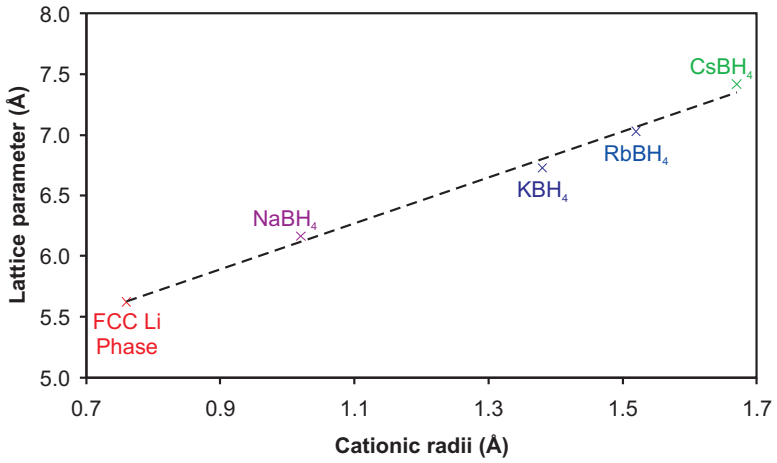

Figure 4.15: Plot of alkali metal borohydride lattice parameter [137] against cationic radii [117]. The lattice parameter of new FCC phase is shown for comparison.

Attempts to solve the structure of the new FCC phase are complicated by the sparse diffraction data available with only 11 Bragg reflections predicted in the 2θ range recorded, only 4 of which have significant intensity. The structure appears to be similar to that of the alkali metal borohydrides, other than lithium, which all share an FCC NaCl-type structure. A plot of lattice parameter [137] against cationic radii [117] (coordination number 6) for the FCC alkali metal borohydrides is given in figure 4.15, which shows that the new lithium FCC phase is consistent with a similar structure.

An FCC structure similar to that of the other alkali metal borohydrides implies a 6 coordination lithium geometry, rather than the 4 coordinate geometry observed in $LiBH_4$ [98] and $LiNH_2$ [103]. Attempts at using Rietveld refinement to fit a 6 coordinate NaCl-type structure with the occupancy of the anion site allowed to refine between $x{BH_4}^-$ and $(1-x){NH_2}^-$ resulted in a very poor match to the observed diffraction data.

Instead, a zinc blende structure type, where $x{BH_4}^-$ and $(1-x){NH_2}^-$ occupy half of the tetrahedral holes in an FCC lithium lattice gave a much better fit, although the determined value of x always tended towards 1. This structure type

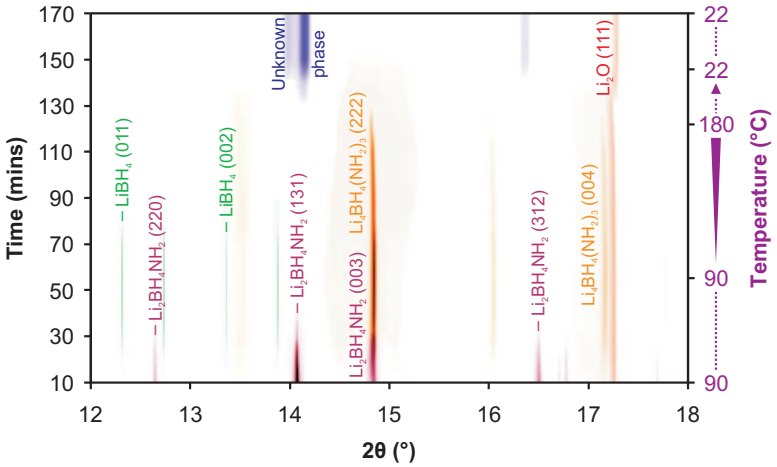

Figure 4.16: 2-D contour plot of powder diffraction data upon heating $Li_2BH_4NH_2$. A representative portion of the diffraction data containing Bragg peaks from the majority phases is shown and selected Bragg peaks are labelled. The Bragg peaks of $Li_2BH_4NH_2$, $Li_4BH_4(NH_2)_3$, $LiBH_4$, Li_2O and an unknown phase are coloured in crimson, orange, green, red and dark blue, respectively.

gives the preferred 4 coordination of lithium and it is probably close to the true structure of this new FCC phase, although this is impossible to confirm without better diffraction data.

Summary

The *in-situ* diffraction data for this experiment are summarised in a 2-D contour plot in figure 4.16. The metastability of $Li_2BH_4NH_2$ has been confirmed and it was shown to transform completely to $Li_4BH_4(NH_2)_3$ and $LiBH_4$ after 30 minutes at 90°C according to the equation:

$$3Li_2BH_4NH_2 \rightarrow Li_4BH_4(NH_2)_3 + 2LiBH_4 \tag{4.1}$$

The large observed lattice parameter of the $Li_4BH_4(NH_2)_3$ phase formed indicated that it is borohydride rich, of the form $Li_4(BH_4)_{(1+x)}(NH_2)_{(3-x)}$. Although there is no simple crystallographic transformation from the $Li_2BH_4NH_2$ structure to the $Li_4BH_4(NH_2)_3$ structure, it is interesting to note from figure 4.16 that the Bragg peak around 14.85° 2θ (d-spacing 3.1 Å) in figure 4.16 is maintained while

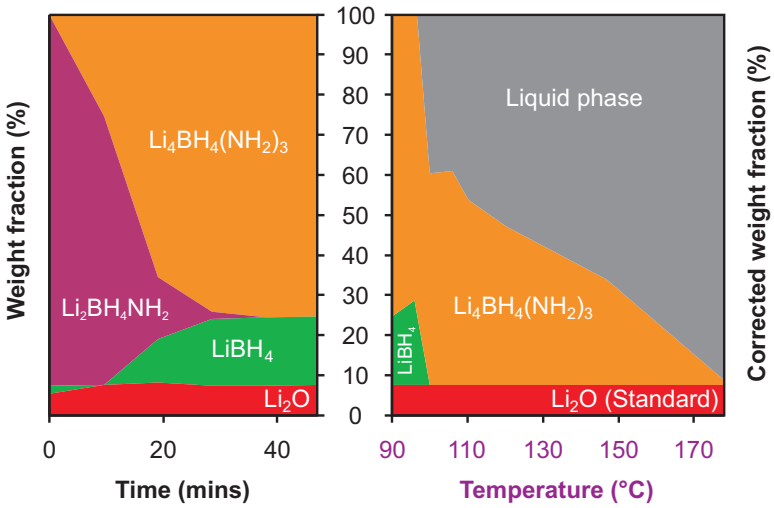

Figure 4.17: Phase map showing phases present upon heating $Li_2BH_4NH_2$. An isothermal section held at 90°C (left) and a ramped section which has been normalised for Li_2O (right) are shown.

transforming from $Li_2BH_4NH_2$ to $Li_4BH_4(NH_2)_3$ (the (003) and (222) Bragg reflections, respectively). This peak corresponds to layers that are present in each structure, as illustrated previously in figure 4.8.

As the reaction was heated above 100°C the presence of a non-crystalline phase was confirmed alongside $Li_4BH_4(NH_2)_3$, and was assigned as a borohydride rich xLiBH$_4$ + yLiNH$_2$ melt, as summarised in figure 4.17. The amount of the liquid phase continued to increase with temperature until the sample was essentially completely molten at 180°C. Upon rapidly cooling the sample from the melt a new FCC phase and other unassigned diffraction reflections were observed. The new FCC phase has been tentatively assigned as a zinc blende structure type where a disordered mixture of BH_4^- and NH_2^- anions occupy half of the tetrahedral holes in a face centred cubic lithium lattice.

4.6 Thermal Decomposition

The gaseous thermal desorption products from $Li_2BH_4NH_2$ were investigated using TPD-MS and TPD-RGA apparatus. The decomposition pathway was found

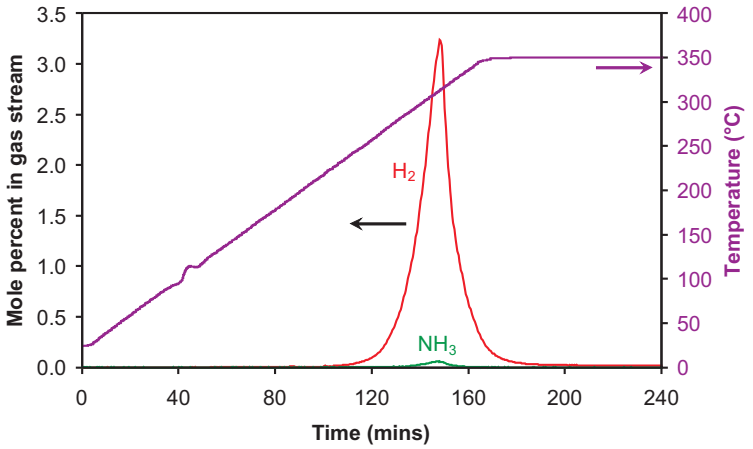

Figure 4.18: Thermal decomposition analysis of $Li_2BH_4NH_2$ in a TPD apparatus. The temperature trace is shown in purple and the mole percents of H_2 and NH_3 released are shown in red and green respectively.

to be different from that of $Li_4BH_4(NH_2)_3$ and hydrogen release was favoured over ammonia release.

4.6.1 TPD-MS

Thermal desorption data for $Li_2BH_4NH_2$ heated at a ramp rate of 2°C min^{-1} to 350°C are shown in figure 4.18. The endothermic event seen in the temperature trace starting at 95°C was due to the melting event observed in section 4.5, where the $Li_2BH_4NH_2$ phase decomposes to $Li_4BH_4(NH_2)_3$ and a borohydride rich liquid phase.

The hydrogen signal from the mass spectrometer started to increase from 160°C with significant hydrogen release from 230°C which peaked around 315°C. These temperatures were significantly lower than observed for $Li_4BH_4(NH_2)_3$ (245°C, 270°C and 340°C, respectively). At the peak of desorption, only 1.8 mol% of the gas released was NH_3 which was less than observed for $Li_4BH_4(NH_2)_3$ (4 mol%).

Figure 4.19 shows the TPD-MS data processed so as to give gravimetric data, as discussed in section 2.7. The observed weight loss from mass spectrometry

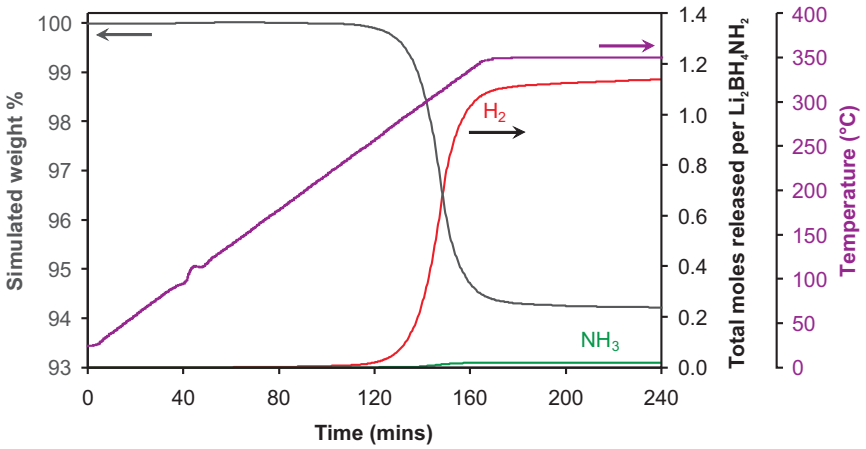

Figure 4.19: Thermal decomposition analysis of $Li_2BH_4NH_2$ in a TPD with simulated gravimetric data. The temperature trace is shown in purple, the moles of H_2 and NH_3 released are shown in red and green respectively and the simulated gravimetric data is shown in grey.

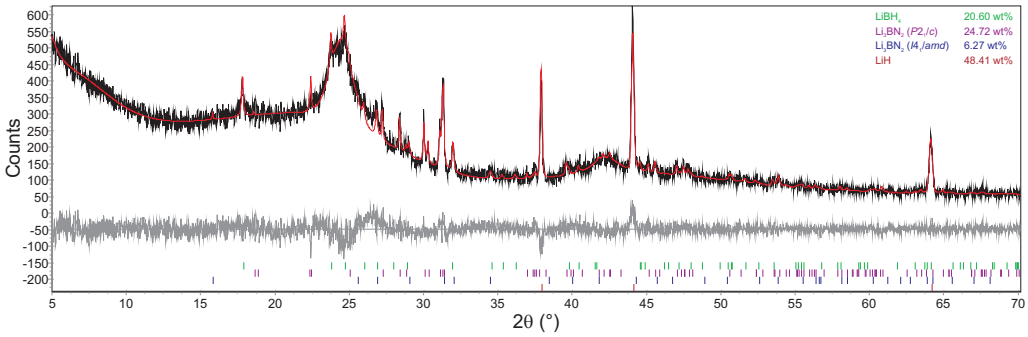

Figure 4.20: Powder XRD of $Li_2BH_4NH_2$ after heating to 350°C in TPD-MS apparatus. Bragg peak positions due to $LiBH_4$ (green), Li_3BN_2 ($P2_1/c$) (purple), Li_3BN_2 ($I4_1/amd$) (dark blue) and LiH (dark red) are indicated.

data over the total heating time was only 5.8 wt% indicating that not all of the hydrogen was released from the $Li_2BH_4NH_2$ (13.5 wt% H_2).

Powder X-ray diffraction data of the products of the TPD-MS experiment are shown in figure 4.20. LiH was the major product with the $P2_1/c$ and $I4_1/amd$ polymorphs of Li_3BN_2 present, as well as a small amount of $LiBH_4$. There was a large background observed in the diffraction pattern with broad amorphous features centred around 24.5° and 42.3° 2θ (3.6 Å and 2.1 Å d-spacing). The Raman spectrum after decomposition showed two broad peaks at 1066 cm^{-1} and

1371 cm^{-1} which correspond to the ν_1 symmetric stretch on the $BN_2{}^{3-}$ anion and B-N stretching vibration of sp^2-bonded boron nitride, respectively. The boron nitride formed can account for the amorphous phase present in the powder diffraction pattern.

The observed phases suggested two competing decomposition pathways upon heating $Li_2BH_4NH_2$. The first majority pathway was responsible for forming the lithium hydride (81(2) mol% from PXRD) and the amorphous BN phase. This reaction, shown in equation 4.2, gives a possible 9.0 wt% H_2.

$$Li_2BH_4NH_2 \rightarrow 2LiH + BN + 2H_2 \uparrow \tag{4.2}$$

The minority decomposition pathway formed Li_3BN_2 in the same way as $Li_4BH_4(NH_2)_3$, with excess $LiBH_4$ remaining, as shown in equation 4.3. As with $Li_4BH_4(NH_2)_3$, the $P2_1/c$ polymorph of Li_3BN_2 was favoured over the $I4_1/amd$ by approximately a 4:1 ratio. This alternative pathway also has the potential to release up to 9.0 wt% hydrogen.

$$2Li_2BH_4NH_2 \rightarrow Li_3BN_2 + LiBH_4 + 4H_2 \uparrow \tag{4.3}$$

Discussion

Hydrogen release from the melt of $Li_2BH_4NH_2$ occurred from 230°C. The thermal decomposition pathway of $Li_2BH_4NH_2$ varied from that of $Li_4BH_4(NH_2)_3$, with the formation of BN and LiH favoured over the formation of Li_3BN_2. This reaction occurred at lower temperatures than the Li_3BN_2 forming reaction of $Li_4BH_4(NH_2)_3$. The results from TPD-MS experiments on $Li_2BH_4NH_2$ and $Li_4BH_4(NH_2)_3$ are compared in figure 4.21.

The lower temperature decomposition of $Li_2BH_4NH_2$ matched fairly well to the shoulder on the TPD-MS data of $Li_4BH_4(NH_2)_3$ (section 3.7). The lower temperature pathway (equation 4.2) is not obvious from the decomposition products of $Li_4BH_4(NH_2)_3$ observed by powder diffraction (figure 3.35) because of the reaction of LiH with remaining $LiNH_2$ and the amorphous nature of the BN

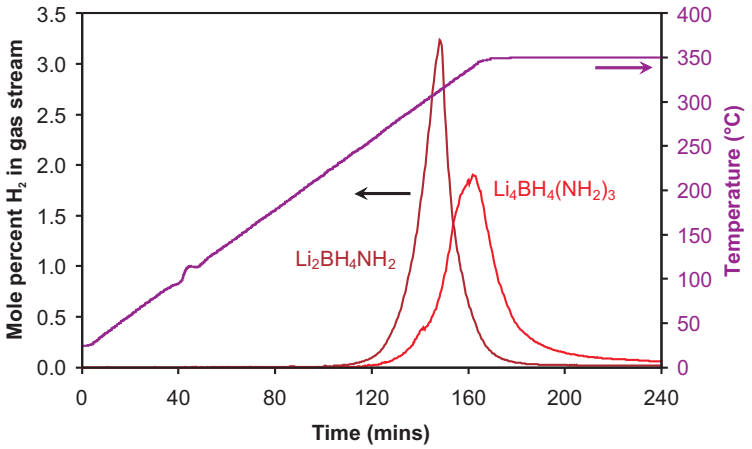

Figure 4.21: Comparison of thermal decomposition analysis of $Li_2BH_4NH_2$ and $Li_4BH_4(NH_2)_3$. The temperature trace is shown in purple and H_2 release from $Li_4BH_4(NH_2)_3$ and $Li_2BH_4NH_2$ are shown in red and dark red, respectively.

formed. Raman spectroscopy also could not confirm the present of amorphous BN so the assignment of this reaction pathway to the shoulder on the $Li_4BH_4(NH_2)_3$ TPD-MS data remains tentative.

It is worth emphasising that both $Li_2BH_4NH_2$ and $Li_4BH_4(NH_2)_3$ desorbed the majority of the hydrogen release observed from above their melting point, and so the well defined crystal structures are lost. Instead, ionic melts of the compositions $[Li^+]_2[BH_4^-][NH_2^-]$ and $[Li^+]_4[BH_4^-][NH_2^-]_3$ were responsible for the hydrogen release. As expected for melts of different ratios, reaction 4.2 was favoured when the B:N ratio was that of the reaction product, BN, and reaction 4.3 was favoured when the B:N ratio was closer to that of the reaction product, Li_3BN_2.

4.7 Conclusion

The complex hydride $Li_2BH_4NH_2$ has been formed by the reaction of $LiBH_4$ and $LiNH_2$ and structure solved by combined synchrotron X-ray and neutron powder diffraction techniques. The structure was metastable and decomposed to $Li_4BH_4(NH_2)_3$ and $LiBH_4$ upon warming. Thermal decomposition occurred

from the molten ionic mixture above 230°C with less ammonia release than $Li_4BH_4(NH_2)_3$, predominantly *via* a different decomposition pathway which formed boron nitride and lithium hydride.

Chapter 5

$n\mathrm{LiNH_2} + (1-n)\mathrm{LiBH_4}$

5.1 Introduction

When initially investigating the amide–borohydride system, reactions were performed at all stoichiometries from pure $LiBH_4$ to pure $LiNH_2$. Although $Li_4BH_4(NH_2)_3$ and $Li_2BH_4NH_2$ were the only isolatable phases present, there was a lot of subtlety with, for example, the lattice parameter of the $Li_4BH_4(NH_2)_3$ leading to the identification of this phase as a solid solution range $Li_4(BH_4)_{(1\pm x)}(NH_2)_{(3\mp x)}$. Here we present work on all compositions of amide–borohydride reactions and discuss how they relate to the $Li_4BH_4(NH_2)_3$ and $Li_2BH_4NH_2$ phases. Together with thermal desorption and calorimetry data we propose a phase diagram for the $n\mathrm{LiNH_2} + (1-n)\mathrm{LiBH_4}$ system.

5.2 Experimental

Samples of ground mixtures of lithium borohydride and lithium amide (Sigma-Aldrich, 95% purity) were prepared in an argon filled glove box (>10 ppm O_2, >1 ppm H_2O) in stoichiometries of $n\mathrm{LiNH_2} + (1-n)\mathrm{LiBH_4}$ (where $n = 0, 0.08\dot{3}, 0.16\dot{6}, 0.25, 0.33\dot{3}, 0.41\dot{6}, 0.5, 0.58\dot{3}, 0.66\dot{6}, 0.75, 0.83\dot{3}, 0.91\dot{6}$ and 1), as well as a few extra samples close to the stoichiometry required for $Li_4BH_4(NH_2)_3$; this

series of samples is referred to as *Ground*. A portion of each sample was heated under argon gas at 190°C for 12 hours and these are referred to as *Heated* samples. A portion of each *Heated* sample was subsequently ground and annealed at 90°C for 12 hours, and these are referred to as *Annealed* samples.

Powder synchrotron X-ray diffraction data were collected for the *Heated* and *Annealed* samples on the ID31 diffractometer at the ESRF, Grenoble, at a wavelength and stepsize of 0.80157 Å and 0.003°, respectively. The samples were loaded into glass capillaries inside a nitrogen filled glove bag and sealed on a miniature gas torch. Differential scanning calorimetry (DSC) and temperature programmed desorption coupled to a mass spectrometer (TPD-MS) were performed on selected *Ground* and *Annealed* samples.

5.3 Powder Diffraction Study

The powder synchrotron X-ray diffraction data collected for the *Heated* and *Annealed* samples were analysed using Topas [90]. A number of new phases were identified. However, the phase space was shown to simplify greatly upon annealing. Solubility limits for the $Li_4(BH_4)_{(1\pm x)}(NH_2)_{(3\mp x)}$ structure are proposed and crystal structure relationships are discussed.

5.3.1 Refinement Strategy

Powder diffraction data were analysed using Topas [90]. For each data set a zero point error and an 18 parameter Chebyshev background function were refined. For each phase present, lattice parameters, a pseudo-Voigt peak shape function with 6 parameters and scale factor were refined. Where possible, atomic coordinates and thermal parameters were taken from reported structures and in some cases attempts were made to refine the atomic positions and site occupancies of the majority phases. In some cases the peak shape of Bragg peaks due to $Li_4BH_4(NH_2)_3$ were highly asymmetric, so an asymmetric convolution with 4 pa-

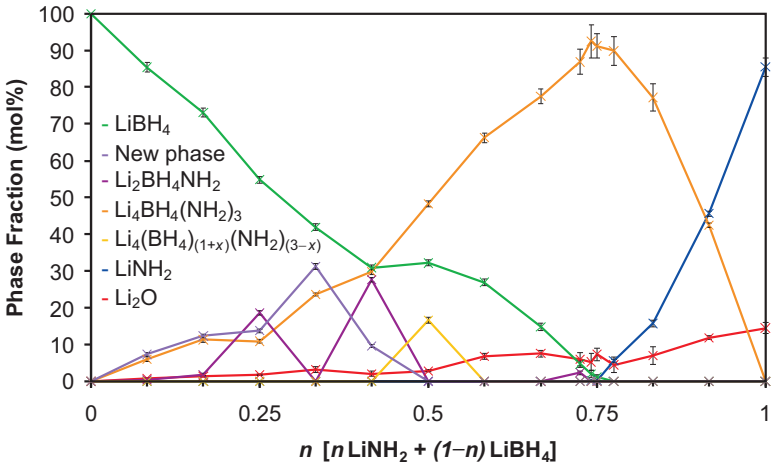

Figure 5.1: Total molar phase fractions after heating $LiBH_4$ and $LiNH_2$ in various ratios

rameters was added to the normal peak shape. The weight percent reported by Topas for each compound present, together with the estimated standard error, were converted into mole percent values. Molar masses per lithium ion, i.e. calculated from the chemical formula scaled to one Li (e.g. $Li(BH_4)_{0.25}(NH_2)_{0.75}$), were used to make the mole percent values comparable. For previously unidentified phases the phase fractions were estimated from the total X-ray scattering associated with that phase.

5.3.2 Heated Samples

Figure 5.1 shows a summary of the phase fractions obtained from the refinements at each composition for the *Heated* samples. Starting from the amide rich side of the data, from $n = 1 \rightarrow 0.75$, the phases present matched what was expected, with only $LiNH_2$ and $Li_4BH_4(NH_2)_3$ present (and Li_2O from the $LiNH_2$ starting material). If both $LiNH_2$ and $Li_4BH_4(NH_2)_3$ were present as line phases we would expect a linear decrease in the amount of $LiNH_2$ observed concurrent with a linear increase in the amount of $Li_4BH_4(NH_2)_3$ observed. Instead, we observed more $Li_4BH_4(NH_2)_3$ than expected and less $LiNH_2$ in the range $n = 1 \rightarrow 0.75$.

Figures 5.2 and 5.3 show the unit cell volume per cation for $Li_4BH_4(NH_2)_3$

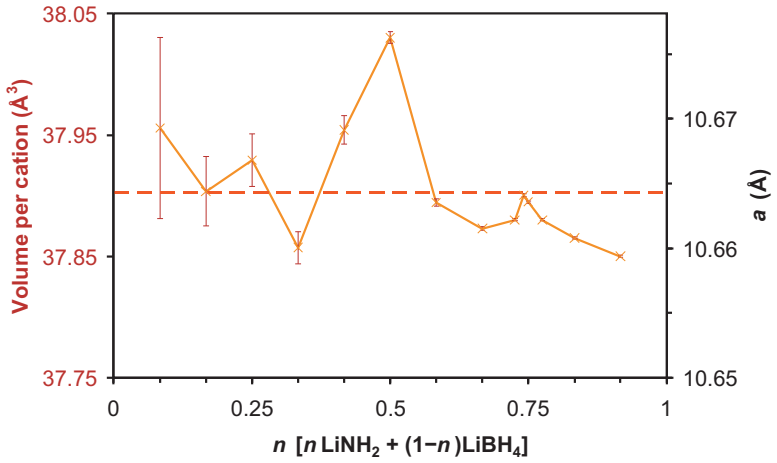

Figure 5.2: Unit cell volume per cation and lattice parameter of $Li_4BH_4(NH_2)_3$ present after heating $LiBH_4$ and $LiNH_2$ in different ratios. The literature value for $Li_4BH_4(NH_2)_3$ [101] is also shown as a dotted line.

and $LiBH_4$ and $LiNH_2$, respectively, present in the *Heated* samples. Upon introduction of $LiBH_4$ there was a slight increase in unit cell volume of $LiNH_2$ (0.04%) which could be due to partial substitution of NH_2^- by BH_4^-. The effect of the opposite substitution was more noticeable in $Li_4BH_4(NH_2)_3$ where the unit cell volume at the amide rich compositions was significantly below that expected for pure $Li_4BH_4(NH_2)_3$. The volume rose as more borohydride was added until it reached the literature value for $Li_4BH_4(NH_2)_3$ at the stoichiometric $LiBH_4$:3$LiNH_2$ ratio.

The larger than ideal amount of $Li_4BH_4(NH_2)_3$ observed compared to $LiNH_2$, coupled with the observed smaller unit cell volume of $Li_4BH_4(NH_2)_3$, is compelling evidence for a phase of the form $Li_4(BH_4)_{(1-x)}(NH_2)_{(3+x)}$. Attempts were made to estimate the degree of substitution of the $Li_4BH_4(NH_2)_3$ phase present in samples where $n = 0.91\dot{6} \rightarrow 0.75$ by Rietveld refinement. The occupancy of the BH_4^- anion was refined, allowing the boron to be replaced by nitrogen with a concurrent appropriate reduction in the occupancy of the BH_4^- hydrogen sites.[†] The results of the refinements were inconclusive, typically refin-

[†]Because of the very limited contribution to X-ray diffraction data by hydrogen atoms, attempts to refine meaningful hydrogen positions of a partially occupied, and possibly randomly

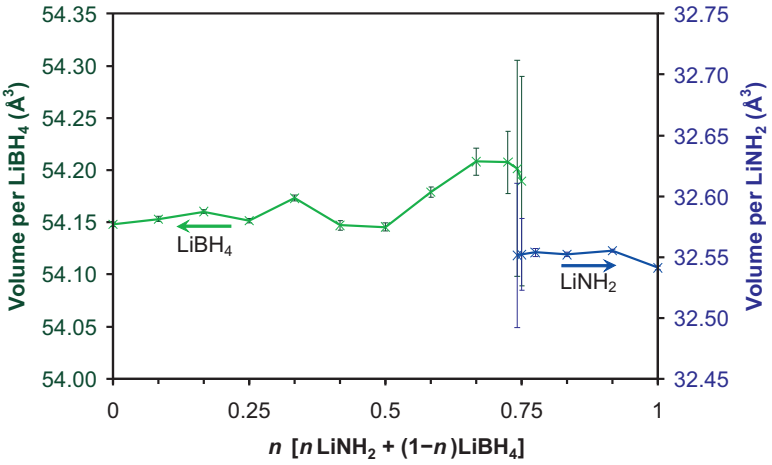

Figure 5.3: Unit cell volume per cation of $LiBH_4$ (green) and $LiNH_2$ (blue) present after heating $LiBH_4$ and $LiNH_2$ in different ratios.

ing this site occupancy to 93% borohydride (equivalent to substitution of only 0.56 borohydride anions per unit cell), although there was no link between this refined value and the lattice parameter. This is perhaps unsurprising because the BH_4^- and NH_2^- ions are isoelectronic and therefore difficult to differentiate by X-ray diffraction. Attempts to improve this refinement by refining the positions of the lithium atoms closest to boron failed to improve the consistency of this refined value. It was decided that the lattice parameter is the best indication that partial substitution may have occurred and it was reassuring that the sample where $n = 0.75$, i.e. the correct stoichiometry for $Li_4BH_4(NH_2)_3$, had essentially the same lattice parameter as the literature structure [101].

Moving past the stoichiometry of $Li_4BH_4(NH_2)_3$ to more borohydride rich mixtures ($n = 0.66\dot{6} \rightarrow 0.58\dot{3}$) there was slightly more $LiBH_4$ present than the ideal, and indeed the lattice parameter of the $Li_4BH_4(NH_2)_3$ observed was slightly below that of the ideal stoichiometry suggesting a borohydride deficient $Li_4(BH_4)_{(1-x)}(NH_2)_{(3+x)}$. This is unusual as more borohydride rich BCC phases would be expected as the borohydride concentration increases. At $n = 0.5$, two body centred cubic phases were observed. The lattice parameter of the majority

orientated, amide ion would be unrealistic.

phase most closely resembled that of pure $Li_4BH_4(NH_2)_3$ [101] with an increase of 0.11%. The second phase, denoted as $Li_4(BH_4)_{(1+x)}(NH_2)_{(3-x)}$ in figure 5.1, had a significantly larger lattice parameter of 10.8296(8) Å, an increase of 1.55%. Attempts were made to refine the degree of substitution of NH_2^- by BH_4^- in both BCC phases in a similar way as previously for the borohydride deficient BCC phases. Rietveld refinement of the NH_2^- anion, allowing the nitrogen to be replaced by boron, did not result in any change from the ideal stoichiometry of the NH_2^- anion.

A plot of unit cell volume per cation against composition (figure 5.4) gives some clues as to why attempts to determine the degree of substitution away from the ideal $Li_4BH_4(NH_2)_3$ stoichiometry using X-ray diffraction data has been inconclusive. If Vegard's law [138] were obeyed, we would expect a near linear relationship between the volume and composition. It can be seen that there is indeed a linear relationship between volume and composition going from $LiNH_2$ to $LiBH_4$ *via* the thermodynamically stable $Li_4BH_4(NH_2)_3$. This relationship can be used to predict the degree of substitution for the different observed phases with the $Li_4BH_4(NH_2)_3$-type BCC lattice, as shown in the inset in figure 5.4. The smallest unit cell BCC lattice observed in the most amide rich composition corresponds to $Li_4(BH_4)_{(1-x)}(NH_2)_{(3+x)}$ with $x = 0.014$. This very small substitution corresponds to only 0.11 anions per unit cell (out of the total of 32 anions), which would not easily be observed in powder diffraction. Applying this same method to the change in lattice parameter of $LiNH_2$ when introducing $LiBH_4$, the small increase in lattice parameter observed would correspond to only 0.15% exchange of NH_2^- for the larger BH_4^-.

Returning to the $n = 0.5$ sample, the majority BCC phase corresponded to $Li_4(BH_4)_{(1+x)}(NH_2)_{(3-x)}$ with $x = 0.019$, equivalent to only 0.15 anions per unit cell. The larger cell BCC phase corresponded to $Li_4(BH_4)_{(1+x)}(NH_2)_{(3-x)}$ with $x = 0.326$, which is approximately 1/3 borohydride, giving the formula $Li_3BH_4(NH_2)_2$, the stoichiometry needed to produce the decomposition prod-

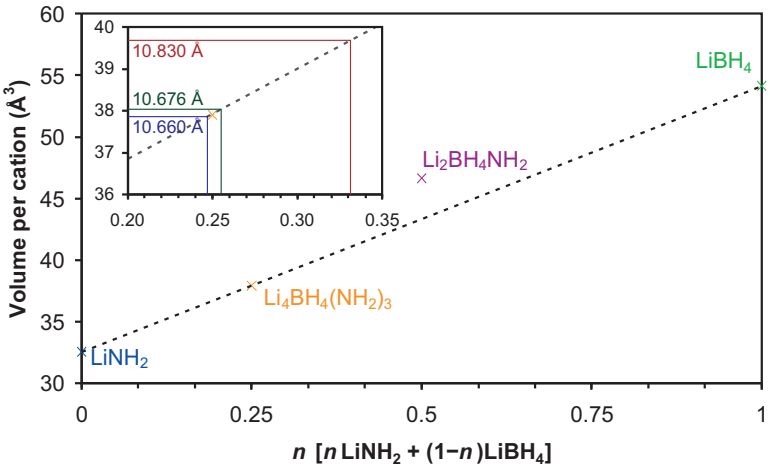

Figure 5.4: Volume per cation of $LiNH_2$, $Li_4BH_4(NH_2)_3$, $Li_2BH_4NH_2$ and $LiBH_4$ against composition. The composition predicted from the unit cell volumes of three BCC-phases are shown (inset).

uct, Li_3BN_2 (section 3.7) and the stoichiometry first reported by Pinkerton *et al.* [97] as "$Li_3BN_2H_8$". The observed lattice parameter in our study (10.83 Å) was larger than that reported for this phase (10.76 Å). This stoichiometry corresponds to substitution of 2.6̇ amide ions per unit cell by borohydride anions. No evidence for deviation from the $Li_4BH_4(NH_2)_3$ BCC symmetry was observed in the diffraction pattern suggesting that this substitution is not ordered. It is not clear why this composition seemed to be favoured to the point of forming a distinct phase, although the presence of this phase in only one of the samples over the entire composition range suggests that it has limited stability.

Although this analysis of composition from lattice parameter is very much an approximation,[†] it is unlikely that the actual levels of substitution were greater than suggested by this analysis. Any variation from the ideal stoichiometry would cause considerable local distortions of the structure around the anion, so if anything we might expect a larger lattice parameter deviation for the degree of substitution suggested by Vegard's law, and so reported degrees of substitution may be overestimates.

[†]Vegard's law is normally only applied in cases where the structrue remains constant, such as in alloys.

Moving to borohydride dominant compositions, where $n = 0.41\dot{6} \rightarrow 0.08\dot{3}$, $Li_2BH_4NH_2$ was observed for the first time in significant quantities. These compositions were molten at the reaction temperature of 190°C, and so the observation of $Li_2BH_4NH_2$ is expected if the rate of cooling is sufficient to form this phase, which can be prepared pure from a quenched melt (see section 4.2). The lattice parameter of the $Li_2BH_4NH_2$ observed was, within error, the same at all compositions indicating that anion substitution did not occur in the structure. The $Li_2BH_4NH_2$ phase was present along side a previously unidentified phase, denoted "New phase" in figure 5.1. Attempts were made to index this phase, where unidentified reflections that were present in approximately the same relative intensities in the diffraction patterns of the samples $n = 0.41\dot{6} \rightarrow 0.08\dot{3}$ were used in the indexing routine of the computer program Topas [90].

The best fit was achieved with a hexagonal unit cell with rhombohedral symmetry, which is the same as $Li_2BH_4NH_2$, but with a larger unit cell which varied considerably with composition. Typical lattice a and c lattice parameters and unit cell volume were 15.6 Å, 9.4 Å and 1980 Å^3, respectively, compared with 14.48 Å, 9.24 Å and 1679 Å^3, respectively, for $Li_2BH_4NH_2$ [121]. The dependence of lattice parameters of this phase with composition is shown in figure 5.5 and a Pawley refinement fit to the diffraction pattern for this phase in the $n = 33\dot{3}$ *Heated* sample is shown in figure 5.6. As can be seen from the Pawley refinement, many of the predicted Bragg reflections for this unit cell have little or no intensity suggesting that the indexed unit cell may be incorrect or that the peaks used in the indexing procedure may be due to more than one phase, despite only peaks with consistent relative intensities being used.

Attempts were made to determine the crystal structure of this phase. However, this was complicated by the presence of other phases and relatively little diffraction data from it. Instead, in order to estimate the mole fraction to be attributed to this phase, an appropriate scattering power was determined. An estimate of the crystallographic density and composition of this new phase can

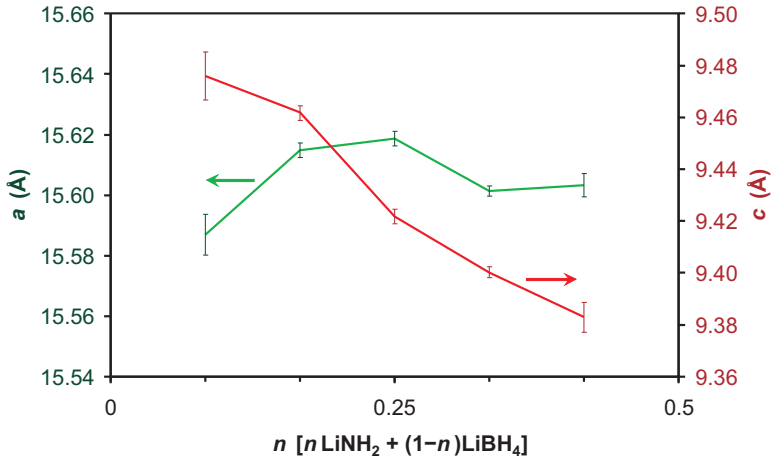

Figure 5.5: Lattice parameters of the new rhombohedral phase present after heating different compositions. The a and c lattice parameters for the hexagonal lattice are shown in green and red, respectively.

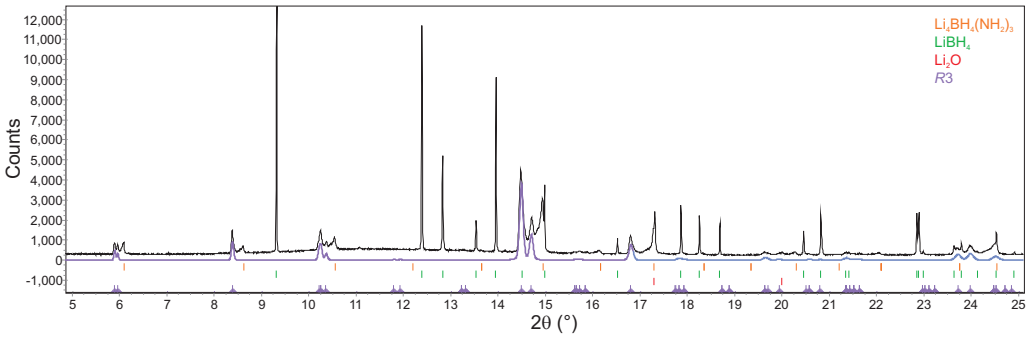

Figure 5.6: Results of Pawley refinement for the rhombohedral phase present after heating $4LiNH_2 + 8LiBH_4$. The profile due to the rhombohedral phase is shown in purple. Bragg peak positions due to $Li_4BH_4(NH_2)_3$, $LiBH_4$, Li_2O and the rhombohedral phase are shown in orange, green, red and purple, respectively.

be made from a plot of composition against volume per cation for the known compounds $LiNH_2$, $Li_4BH_4(NH_2)_3$, $Li_2BH_4NH_2$ and $LiBH_4$, as shown in figure 5.7. Assuming that this new phase has a greater borohydride concentration than $Li_2BH_4NH_2$[†] and that the crystallographic density of the phase is below that of the trend followed by the thermodynamically stable products $LiNH_2$, $Li_4BH_4(NH_2)_3$ and $LiBH_4$, which follow Vegard's law,[‡] then we can estimate

[†]This is a reasonable assumption as this phase is only present in compositions where there is more than 50% $LiBH_4$ present.

[‡]This is the case for the metastable $Li_2BH_4NH_2$.

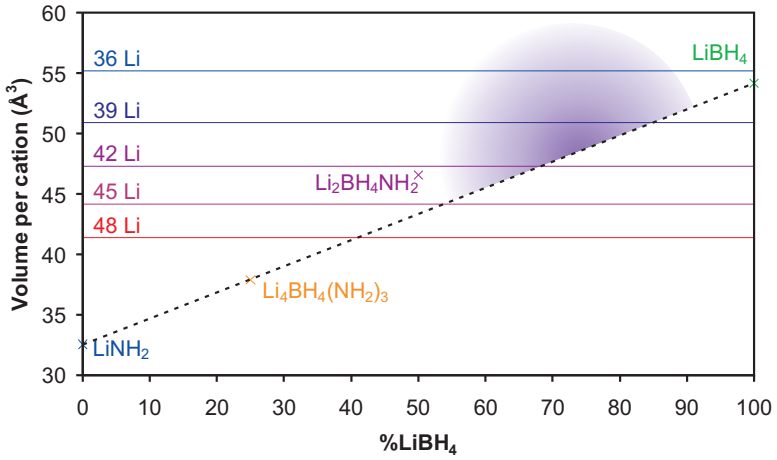

Figure 5.7: Graph of volume per cation against percentage of $LiBH_4$ used to determine the composition of a new rhombohedral phase. Possible values of unit cell volume per cation for the new phase are shown and the most probable values and compositions are highlighted in purple. Values for $LiNH_2$, $Li_4BH_4(NH_2)_3$, $Li_2BH_4NH_2$ and $LiBH_4$ are shown.

composition. Figure 5.7 shows the volume per cation for the crystallographically possible numbers of cations against the composition in terms of %$LiBH_4$ for the known phases in this system. The area highlighted in light purple in figure 5.7 corresponds to the most probable compositions for each of the possible numbers of cations in the unit cell. From this we determined that 39 cations per unit cell is the most probable which would contain approximately 70% $LiBH_4$. Looking at the available special positions in the possible rhombohedral space groups (see chapter 4, table 4.1) we see that a ratio of 12 amides to 27 borohydrides is possible giving 69% $LiBH_4$. Scattering density associated with $Li(BH_4)_{0.69}(NH_2)_{0.31}$ with 39 formula units in the unit cell was associated with this new rhombohedral phase and the molar fractions shown in figure 5.1 were thus determined.

In the borohydride rich compositions ($n = 0.41\dot{6} \rightarrow 0.08\dot{3}$) the appearance of $Li_2BH_4NH_2$ was sporadic, possibly due to random variations in cooling rate affecting which phase crystallises from the melt. The amount of the "$Li(BH_4)_{0.69}(NH_2)_{0.31}$" rhombohedral phase present was maximal at $n = 0.33\dot{3}$ and decreased at higher borohydride concentrations with $LiBH_4$ becoming pre-

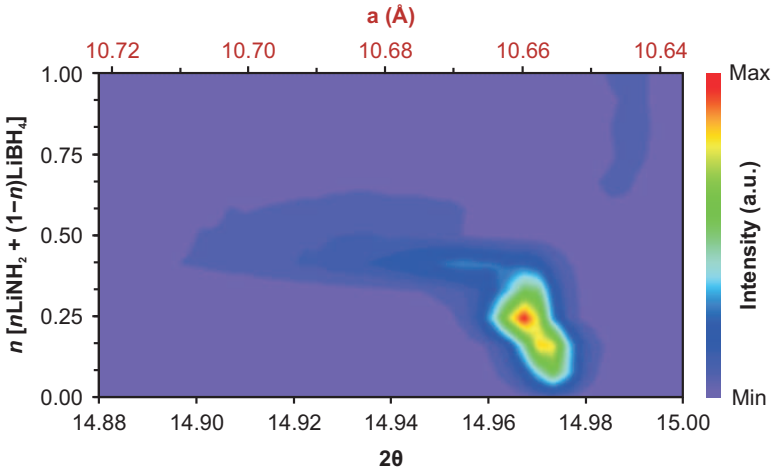

Figure 5.8: Intensity and *d*-spacing of the (222) Bragg peak and equivalent lattice parameter of $Li_4BH_4(NH_2)_3$ present in *Heated* samples.

ferred until $n = 0$ where only $LiBH_4$ was present. The errors associated with the lattice parameter of the $Li_4BH_4(NH_2)_3$ present at higher borohydride concentrations were very large (figure 5.2). This was due to the very broad and asymmetric peak shape of this phase, as illustrated in figure 5.8 showing a 2D contour plot of the most intense (222) Bragg reflection of the $Li_4BH_4(NH_2)_3$ phase.[†] The lattice parameters reported in figure 5.2 therefore represent the lattice parameter of the most dominant $Li_4BH_4(NH_2)_3$-type BCC phase. However, at higher borohydride concentrations this broadening of the $Li_4BH_4(NH_2)_3$ peaks most probably represents a range of compositions of the form $Li_4(BH_4)_{(1\pm x)}(NH_2)_{(3\mp x)}$ which overall is observed as a broad peak. The more dominant tail to lower 2θ (higher lattice parameter) again suggests that substitution of the form $Li_4(BH_4)_{(1+x)}(NH_2)_{(3-x)}$ dominates.

5.3.3 Annealed Samples

Figure 5.9 shows a summary of the phase fractions obtained from the refinements at each composition for the *Annealed* samples. The observed phase fractions

[†]The feature observed around 14.99 2θ at higher borohydride concentrations was due to the (102) Bragg reflection of $LiBH_4$.

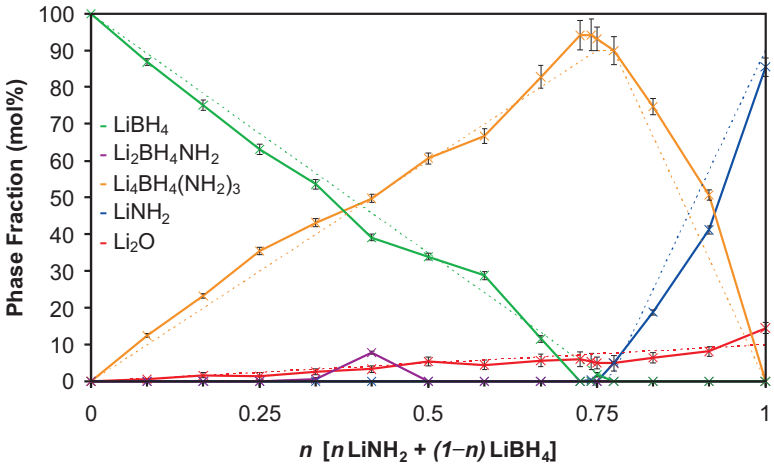

Figure 5.9: Total molar phase fractions after annealing $LiBH_4$ and $LiNH_2$ in various ratios. The predicted phase composition assuming line phases for $LiBH_4$, $Li_4BH_4(NH_2)_3$ and $LiNH_2$ are shown as dotted lines.

were very close to those predicted presuming that only the stoichiometric $LiBH_4$, $Li_4BH_4(NH_2)_3$ and $LiNH_2$ phases were present,[†] as shown by the dotted lines in figure 5.9. For both the amide rich and borohydride rich stoichiometries there was slightly more $Li_4BH_4(NH_2)_3$ present than expected indicating that the BCC phase contained more amide and more borohydride, respectively, than implied by the formula $Li_4BH_4(NH_2)_3$.

The lattice parameters of the BCC phase are shown in figure 5.10 overlaid on the data from the *Heated* samples. Lattice parameters in the amide rich region followed the trend of the *Heated* samples, suggesting that $Li_4(BH_4)_{(1-x)}(NH_2)_{(3+x)}$ with $x = 0.014$ is a consistent solid solution limit under these reaction conditions. Lattice parameters in the borohydride rich region were much more consistent in the *Annealed* samples than in the *Heated* samples. Using the Vegard's law analysis of section 5.3.2, this annealed borohydride rich BCC phase corresponds to $Li_4(BH_4)_{(1+x)}(NH_2)_{(3-x)}$ with $x = 0.008$ (only 0.06 anions per unit cell), which could be the upper stable solid solution limit for the $Li_4BH_4(NH_2)_3$ structure. Very little variation was observed in the lattice

[†] Li_2O from the $LiNH_2$ starting material was also present.

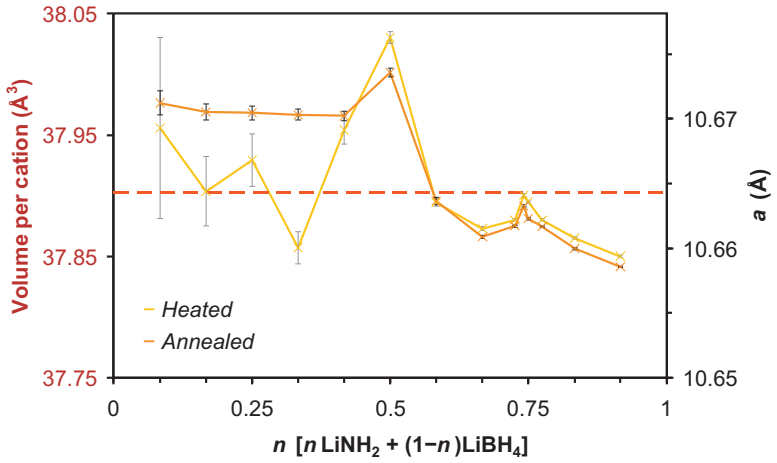

Figure 5.10: Unit cell volume per cation and lattice parameter of $Li_4BH_4(NH_2)_3$ present after heating (orange) and annealing (yellow) $LiBH_4$ and $LiNH_2$ in different ratios.

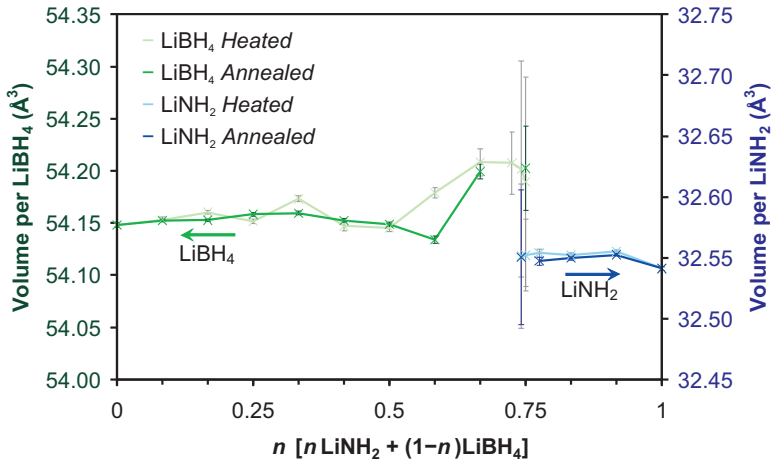

Figure 5.11: Unit cell volume per cation and lattice parameter of $LiBH_4$ (green) and $LiNH_2$ (blue) present after heating $LiBH_4$ and $LiNH_2$ in different ratios.

parameters of the $LiBH_4$ and $LiNH_2$ phases observed (figure 5.11).

Only $n = 0.41\dot{6}$ had any phase present other than the predicted $Li_4BH_4(NH_2)_3$ or the end members $LiNH_2$ or $LiBH_4$. $Li_2BH_4NH_2$ was present, but at a much reduced quantity (7.8 mol%) compared to in the equivalent *Heated* sample (27.6 mol%), indicating that annealing at 90°C reduced, but did not completely remove, the $Li_2BH_4NH_2$ phase.

5.3.4 Summary

Samples of $n\mathrm{LiNH_2} + (1-n)\mathrm{LiBH_4}$ (where $n = 0 \rightarrow 1$) were investigated. Although $\mathrm{Li_4BH_4(NH_2)_3}$ dominated the phase space, after heating at 190°C, $\mathrm{Li_2BH_4NH_2}$ was observed at higher borohydride concentrations and phases corresponding to a BCC phase approximating to $\mathrm{Li_3BH_4(NH_2)_2}$ and a new rhombohedral phase of approximate composition $\mathrm{Li(BH_4)_{0.69}(NH_2)_{0.31}}$ were also identified.

After annealing at 90°C the majority of these other phases were replaced by the thermodyamically stable products, $\mathrm{LiBH_4}$, $\mathrm{Li_4BH_4(NH_2)_3}$ and $\mathrm{LiNH_2}$. Vegard's law was used to estimate the degree of substitution into the BCC $\mathrm{Li_4BH_4(NH_2)_3}$ structure and stable solid solution limits of $\mathrm{Li_4(BH_4)_{(1+x)}(NH_2)_{(3-x)}}$ where $0.008 \geq x \geq -0.014$ were proposed.

5.4 Differential Scanning Calorimetry Study

The thermal properties of the lithium amide–borohydride mixtures, as well as $\mathrm{Li_4BH_4(NH_2)_3}$ and $\mathrm{Li_2BH_4NH_2}$ were investigated by differential scanning calorimetry. Samples were accurately weighed to 0.001 mg in aluminium crucibles and loaded into a DSC housed inside an argon filled glove box.

The accuracy of the calibration of the DSC was first tested using pure $\mathrm{LiBH_4}$. The orthorhombic to hexagonal phase transition was observed at 114°C which is consistent with the observed increase in conductivity recently reported (115°C [139]) which coincides with this phase transition. The enthalpy of the phase change was measured to be 4.6 kJ $\mathrm{mol^{-1}}$, slightly higher than quoted in the literature (4.2 to 4.3 kJ $\mathrm{mol^{-1}}$ [140]).

5.4.1 $\mathrm{Li_4BH_4(NH_2)_3}$

DSC data for $\mathrm{Li_4BH_4(NH_2)_3}$ and a *Ground* sample of $\mathrm{LiBH_4} + 3\mathrm{LiNH_2}$ are shown in figure 5.12. For the *Ground* sample there was a slight exotherm at 99°C which was absent for $\mathrm{Li_4BH_4(NH_2)_3}$. This can be attributed to the for-

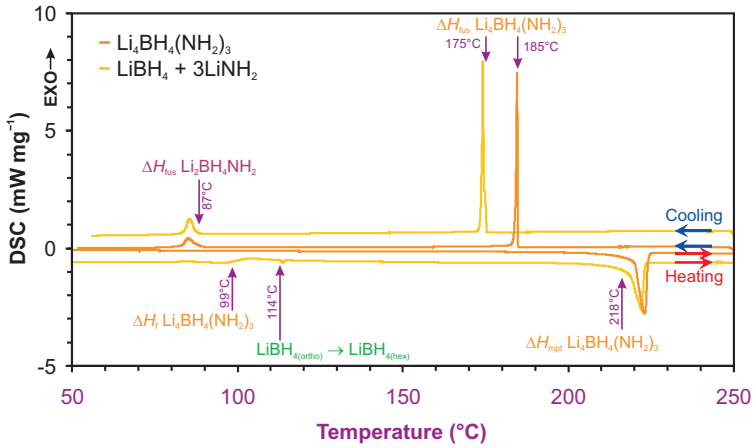

Figure 5.12: DSC data for $Li_4BH_4(NH_2)_3$ and a starting mixture of $LiBH_4$ + $3LiNH_2$. DSC data for the starting mixture is shifted in the y direction for clarity by -0.5 and $+0.5$ upon heating and cooling respectively.

mation of $Li_4BH_4(NH_2)_3$ which is consistent with *in-situ* diffraction data (section 3.6). There was a small endotherm due to the phase transition of $LiBH_4$ observed at 114°C indicating that the formation of $Li_4BH_4(NH_2)_3$ was not complete by this temperature. A value of approximately -4.6 kJ mol^{-1} was determined for the formation of $Li_4BH_4(NH_2)_3$, which is slightly less than that predicted by density functional theory (-6 kJ mol^{-1} [109]). Both the *Ground* sample and $Li_4BH_4(NH_2)_3$ showed the same broad endotherm due to melting, with an onset around 218°C, estimated to be 23.5 kJ mol^{-1} for one formula unit of $Li_4BH_4(NH_2)_3$.

Upon cooling, the crystallisation of $Li_4BH_4(NH_2)_3$ was observed at 185°C and 175°C for $Li_4BH_4(NH_2)_3$ and *Ground* samples, respectively. Discrepancies in the temperature are due to differences in nucleation rates of the supercooled liquid. The exotherm due to solidification upon cooling was significantly less than the endotherm upon melting. Also a second exotherm was observed in both DSC traces at 87°C. Both of these observations can be explained by the relatively quick cool rate of 2°C min^{-1}. It appears that the $Li_4BH_4(NH_2)_3$ majority phase crystallised first, and that a small amount of $Li_2BH_4NH_2$ may also have crystallised at this lower temperature of 87°C. This is consistent with the powder

diffraction study of the *Heated* samples (figure 5.1); even at a composition very close to that expected to form pure $Li_4BH_4(NH_2)_3$ a small amount of $Li_2BH_4NH_2$ was also observed.

5.4.2 $Li_2BH_4NH_2$

DSC data for $Li_2BH_4NH_2$ and a ground mixture of $LiBH_4$ + $LiNH_2$ are shown in figure 5.13. For the *Ground* $LiBH_4$ + $LiNH_2$ sample a melting event was observed, starting at 91°C. The melting of the sample was still not complete until above 114°C as the phase transition of $LiBH_4$ was still observed. Indeed, the DSC trace stayed slightly, but significantly endothermic until just above 170°C when melting was complete. For $Li_2BH_4NH_2$ an endotherm was observed at the lower temperature of 80°C. This is concurrent with the gradual transformation of $Li_2BH_4NH_2$ to $Li_4BH_4(NH_2)_3$ and $LiBH_4$, as observed in section 4.5. The endotherm became more pronounced from 91°C which is attributed to the onset of melting. As with the *Ground* sample, the DSC trace remained endothermic long past this main endothermic event until the temperature of 156°C; at this temperature the sample was deemed to be completely molten as no further thermal events were observed. For $Li_2BH_4NH_2$, the melting event was much more pronounced than for the *Ground* sample and the phase change of $LiBH_4$ was not observed; this is attributed to starting from $Li_2BH_4NH_2$ allowing for a more intimate mixture of amide and borohydride from the offset than was possible in the *Ground* sample. It is presumably a mixture of $LiNH_2$ and $LiBH_4$ which melted at these low temperatures and an intimate mixture would allow for a more pronounced melting point.

For the *Ground* sample, the main endothermic melting event was calculated to be 4.0 kJ mol^{-1} per lithium present.[†] For $Li_2BH_4NH_2$, the main endothermic event was calculated to be 5.2 kJ mol^{-1} per lithium, which reduces to 4.4 kJ mol^{-1}

[†]The endotherm due to the lithium borohydride phase transition was excluded from this calculation.

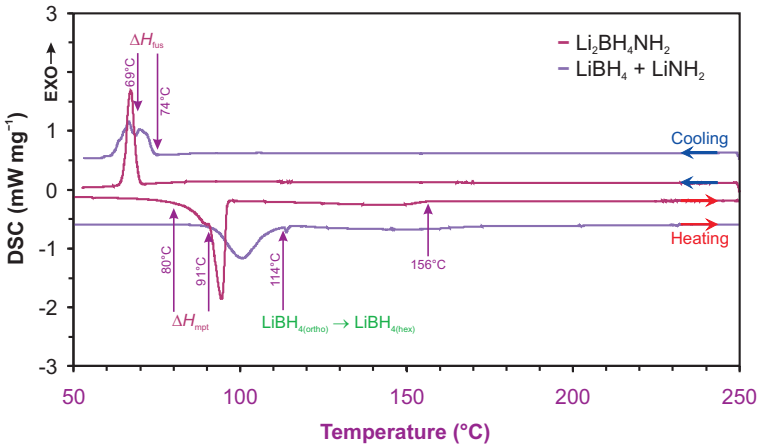

Figure 5.13: DSC data for $Li_2BH_4NH_2$ and a starting mixture of $LiBH_4 + LiNH_2$. DSC data for the starting mixture is shifted in the y direction for clarity by -0.5 and $+0.5$ upon heating and cooling respectively.

for the melting event if the initial lower temperature endotherm was indeed due to segregation of $Li_2BH_4NH_2$ to $Li_4BH_4(NH_2)_3$ and $LiBH_4$. The discrepancy between these determined values was due to the very broad melting event.

Upon cooling, the solidification was observed for the $Li_2BH_4NH_2$ and *Ground* samples at 69°C and 74°C, respectively. As in the previous section, the discrepancy in the temperature was due to differences in nucleation rates of the supercooled liquid. For the *Ground* sample, two distinct exothermic events were observed which may have been due to nucleation of different phases, such as those observed in section 5.3.2.

5.4.3 Heating Overview

The DSC results from the heating regime of all *Ground* samples are summarised as a 2D contour plot in figure 5.14. Starting from the amide rich region, for pure $LiNH_2$ no thermal events were observed up to 250°C. Upon addition of $LiBH_4$ a slight exotherm was observed around 100°C due to the formation of $Li_4BH_4(NH_2)_3$, which was maximal around the $LiBH_4 + 3LiNH_2$ composition required to form the mixed complex hydride pure. For these amide dominated

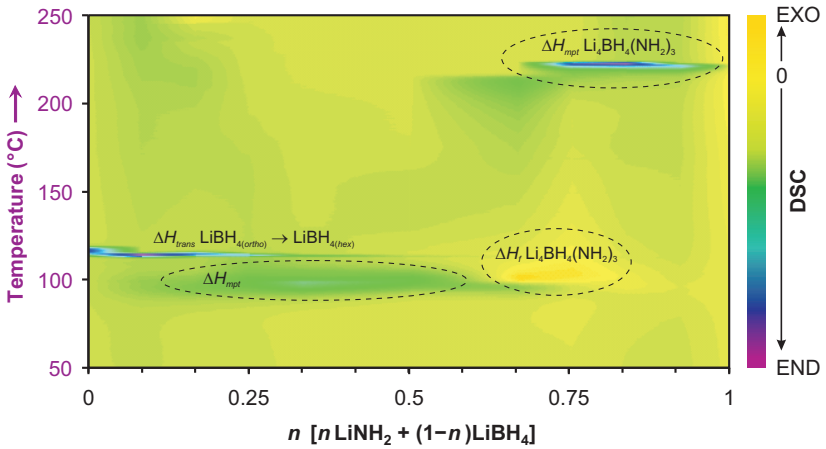

Figure 5.14: 2D contour plot of DSC data upon heating *Ground* samples of $LiBH_4$ + $LiNH_2$ in different ratios. Colours due to exothermic (EXO) and endothermic (END) events are shown on the right. Significant thermal events are labelled.

compositions an endothermic melting event was then observed at 220°C, however the onset of an endothermic event was observed from 160°C which may be due to increased motion of the complex anions or cations leading up to the melting event.

For samples made up of half borohydride or greater an endothermic melting event was observed around 95°C, which was maximal at the $LiNH_2$ + $2LiBH_4$ composition. Clearly this melting event was not complete for the entire sample as the phase transition of $LiBH_4$ was still observed at 114°C and indeed became more pronounced at more borohydride rich compositions.

Linking these observations with *in-situ* powder diffraction data looking at the formation of $Li_4BH_4(NH_2)_3$ from a mixture of $LiBH_4$ and $LiNH_2$ (section 3.6), and the phase evolution of $Li_2BH_4NH_2$ upon heating (section 4.5), we can now discern that the endothermic event at 95°C was due to a melt of the approximate composition $[(Li^+)_3(BH_4^-)_2(NH_2^-)]_{(l)}$. In section 3.6 (figure 3.32) it was noted that from 100°C $Li_4BH_4(NH_2)_3$ was the only observed crystalline phase with an indication of a large amount of amorphous content. Because of the 1:1 starting ratio of $LiBH_4$ + $LiNH_2$, this amorphous phase was attributed to a borohydride

rich melt, which is consistent with the formation of $[(Li^+)_3(BH_4{}^-)_2(NH_2{}^-)]_{(l)}$ from 95°C, as suggested by the DSC data.

In section 4.5 (figure 4.13) a significant amount of amorphous content was also present above 90°C alongside $Li_4BH_4(NH_2)_3$ from a starting sample of $Li_2BH_4NH_2$ (a 1:1 amide to borohydride mix). The amount of amorphous content continued to rise with the loss of $Li_4BH_4(NH_2)_3$ up to the maximum temperature reached of 180°C.[†] This implies that at higher temperatures more amide rich compositions than $[(Li^+)_3(BH_4{}^-)_2(NH_2{}^-)]$ also became molten. Indeed, at borohydride dominated compositions a second melting event was not observed in the DSC data, suggesting a gradual melting event, i.e. the solubility of $LiNH_2$ in $[(Li^+)_3(BH_4{}^-)_2(NH_2{}^-)]_{(l)}$ increased with temperature. These observations, and others, will be discussed in section 5.6 in relation to the construction of a phase diagram for the $n\mathrm{LiNH_2} + (1-n)\mathrm{LiBH_4}$ system.

5.4.4 Cooling Overview

The DSC data from the cooling step of all *Ground* samples are summarised as a 2D contour plot in figure 5.15. The temperatures of the exothermic events observed upon cooling were inherently inconsistent due to differences in nucleation rates. In general, for the amide rich samples a distinct fusion event was observed in the range 175 to 200°C. For the borohydride rich samples, the phase transition of $LiBH_4$ was observed around 105°C indicating that some $LiBH_4$ had crystallised out of the melt by this temperature, although only minor exotherms were observed around 195°C and 150°C for a few different samples, indicating that this was a gradual process. Towards the centre of the composition diagram, exothermic events were observed in the region 60 to 80°C. This is attributed to the crystallisation of any remaining molten phase, although as illustrated in figure 5.1, it is by no means certain which phase will crystallise in this temperature

[†]This effect was also noted in section 4.5 but to a lesser extent due to the lower maximum temperature of 150°C.

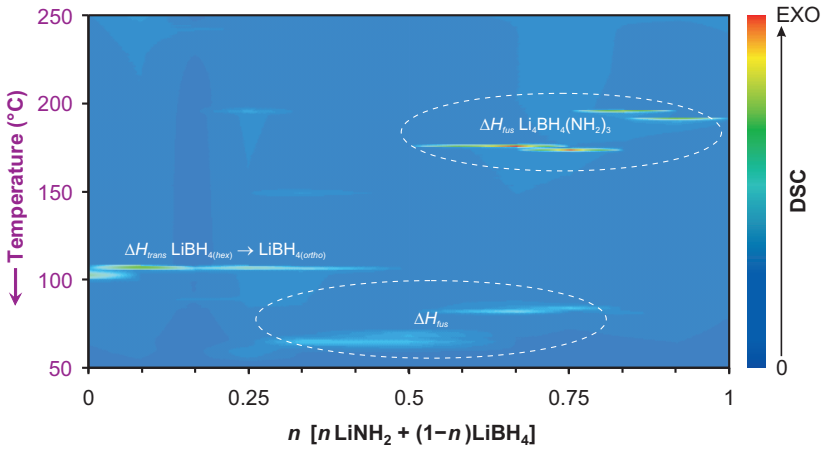

Figure 5.15: 2D contour plot of DSC data upon cooling *Ground* samples of $LiBH_4$ + $LiNH_2$ in different ratios. Colours due to exothermic (EXO) events are shown on the right. Significant thermal events are labelled.

range.

5.4.5 Conclusion

The DSC data reported here provides a valuable insight into the thermal properties of the $LiNH_2$ + $LiBH_4$ system and backs up observations from separate *in-situ* diffraction studies. A ΔH_f of -4.6 kJ mol^{-1} was estimated for the formation of $Li_4BH_4(NH_2)_3$ from the constituent $LiBH_4$ + $3LiNH_2$ and the enthalpy of melting, ΔH_{mpt}, was estimated at 23.5 kJ mol^{-1}. A melting event was observed around 95°C leading to the assignment of $[(Li^+)_3(BH_4^-)_2(NH_2^-)]_{(l)}$ as a low temperature eutectic. These observations will be further discussed in relation to construction of a phase diagram for $LiBH_4$ + $LiNH_2$ in section 5.6.

5.5 Thermal Decomposition Study

The gaseous thermal desorption products from various *Ground* samples were investigated using TPD-MS at a ramp rate of 2°C min^{-1} to 350°C. Results were compared with those of the end members $LiNH_2$ and $LiBH_4$ and previous results from $Li_4BH_4(NH_2)_3$ and $Li_2BH_4NH_2$ samples.

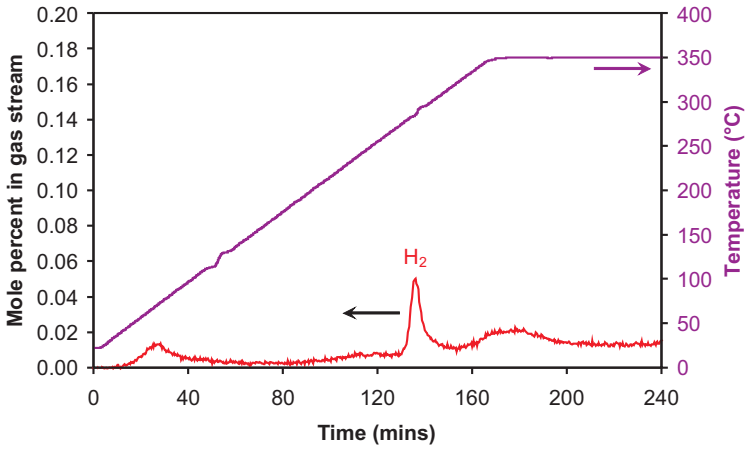

Figure 5.16: Thermal decomposition analysis of $LiBH_4$. The temperature trace is shown in purple and the mole percents of H_2 and NH_3 released are shown in red and green respectively.

5.5.1 $LiBH_4$

Thermal desorption data from pure $LiBH_4$ are shown in figure 5.16. Very little hydrogen was observed up to the maximum temperature of 350°C. The endothermic events observed at 110°C and 280°C in the temperature trace corresponded to the orthorhombic to hexagonal phase transition [98] and melting point [117], respectively. There was a minor hydrogen release which accompanied the melting.

The thermal properties of $LiBH_4$ were investigated by Fedneva *et al.* [141] where two endothermic events corresponding to the phase change and melting point were observed in the temperature range covered by this experiment. The melting event was accompanied by a release of around 2% of the total hydrogen which is consistent with our findings. The first study where $LiBH_4$ was investigated as a potential hydrogen storage material by Züttel *et al.* [40], where hydrogen release was not observed during melting, has now been superseded by a study by the same authors where it was [45]. The main hydrogen release is reported in all previous studies not to occur until above 400°C, and so it was not observed in this experiment.

PXRD after the TPD-MS experiment showed two minor reflections at 42.81°

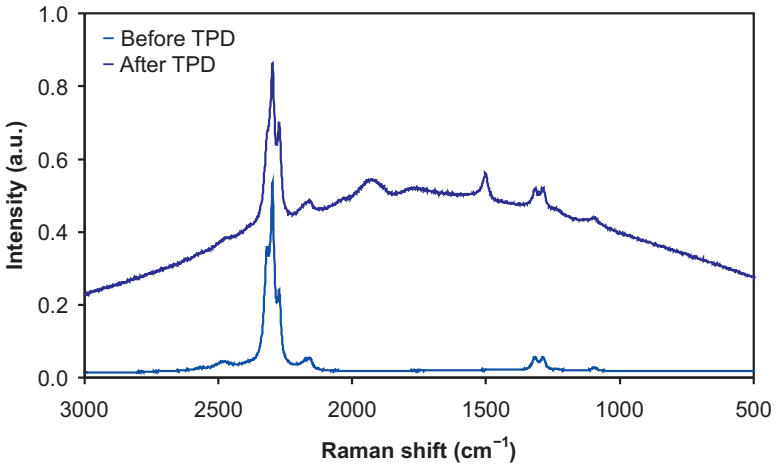

Figure 5.17: Raman spectra of $LiBH_4$ before (light blue) and after (dark blue) TPD-MS.

and 62.19° 2θ (2.11 Å and 1.49 Å d-spacing) which could not be identified as boron, LiH [122] or $Li_2B_{12}H_{12}$ [128], the known decomposition products of $LiBH_4$ [40, 50]. Raman spectroscopy (figure 5.17) showed a larger background after the TPD experiment with a new broad peak centred around 1920 cm^{-1} and a more well defined peak at 1500 cm^{-1}. These new peaks could not be assigned as $B_{12}H_{12}{}^{2-}$ stretches [142], or as due to LiH or boron [143, 144] (or possible oxidation products). The identity of the phase(s) responsible for the extra reflections in the PXRD and extra modes observed in Raman spectroscopy remains uncertain.

Although a very small hydrogen released was observed from $LiBH_4$ up to 350°C, it is clear from PXRD and Raman spectroscopy that the majority of the $LiBH_4$ remained unchanged in this temperature range. This is consistent with previous reports where significant hydrogen release was not observed until above 400°C [45, 40].

5.5.2 $LiNH_2$

Thermal desorption data from pure $LiNH_2$ are shown in figure 5.18. A small amount of ammonia release was observed from 210°C, just above the background noise of the mass spectrum signal, which corresponded to a mass loss of less

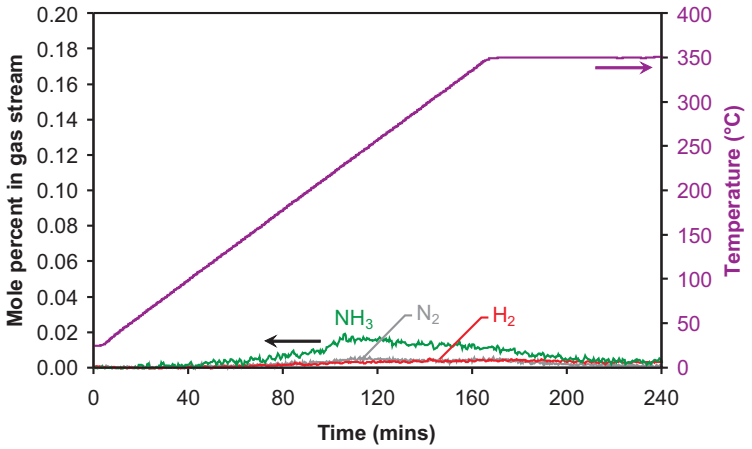

Figure 5.18: Thermal decomposition analysis of $LiNH_2$. The temperature trace is shown in purple and the mole percents of H_2, NH_3 and N_2 released are shown in red, green and grey respectively.

than 2% of the ammonia available in $LiNH_2$. No significant hydrogen or nitrogen release was observed up to 350°C.

$LiNH_2$ was reported to decompose with the release of NH_3 in vacuum [145]. A more recent study by Chen *et al.* [61] reported that decomposition begins from 200°C with significant ammonia release above 350°C together with small amounts of N_2 and H_2 also observed, which is consistent with our results. PXRD and Raman spectroscopy after TPD showed no difference from the $LiNH_2$ staring material which is consistent with the very small amount of decomposition products observed in the TPD-MS experiment.

5.5.3 $3LiNH_2 + LiBH_4$

Thermal desorption data from a *Ground* sample of $3LiNH_2 + LiBH_4$ are shown in figure 5.19. As expected, the desorption profile was similar to that of $Li_4BH_4(NH_2)_3$, also included in figure 5.19. A slight exotherm was observed in the temperature trace at 105°C which was attributed to the formation of $Li_4BH_4(NH_2)_3$, and an endothermic melting event was observed at 220°C.

As with $Li_4BH_4(NH_2)_3$, hydrogen release was observed from around 245°C.

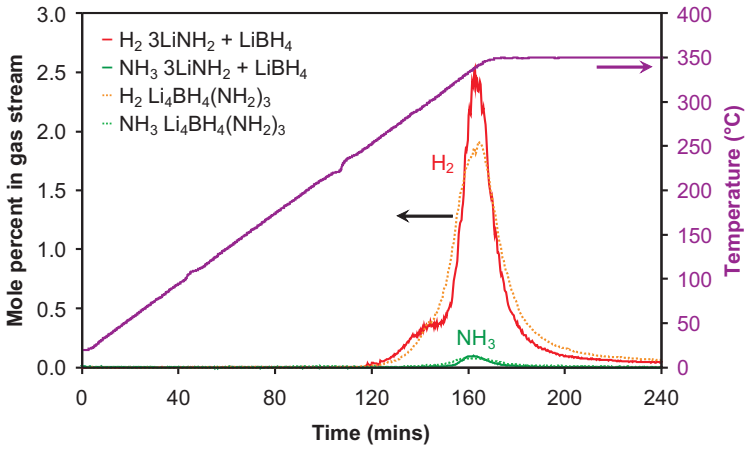

Figure 5.19: Thermal decomposition analysis of $3LiNH_2 + LiBH_4$. The temperature trace is shown in purple and the mole percents of H_2 and NH_3 released are shown in red and green respectively. For comparison, mole percents of H_2 and NH_3 desorbed from $Li_4BH_4(NH_2)_3$ are shown as dotted lines in orange and light green, respectively.

Two distinct hydrogen releasing events were observed: the first, smaller hydrogen release peaked around 300°C with the second major hydrogen release dominating from 310°C and peaking at 340°C. For $Li_4BH_4(NH_2)_3$, a shoulder was observed in the hydrogen release profile around 300°C suggesting a two step decomposition pathway. For the *Ground* starting mixture $3LiNH_2 + LiBH_4$ the two decomposition events were much more distinct.

In section 4.6, the lower temperature shoulder in the decomposition profile of $Li_4BH_4(NH_2)_3$ was attributed to a decomposition pathway forming boron nitride and lithium hydride, which appeared to be favoured in the more borohydride rich $Li_2BH_4NH_2$. For the *Ground* $3LiNH_2 + LiBH_4$ mixture the two starting reagents will not be as intimately mixed as in $Li_4BH_4(NH_2)_3$, therefore, locally there could be borohydride rich regions and amide rich regions. We hypothesise that the more prominent lower temperature hydrogen release from $3LiNH_2 + LiBH_4$ is due to hydrogen release from borohydride rich portions of the sample to form LiH and BN. Only at higher temperatures above the melting point would the mixture be completely homogenous and the major hydrogen releasing pathway to form

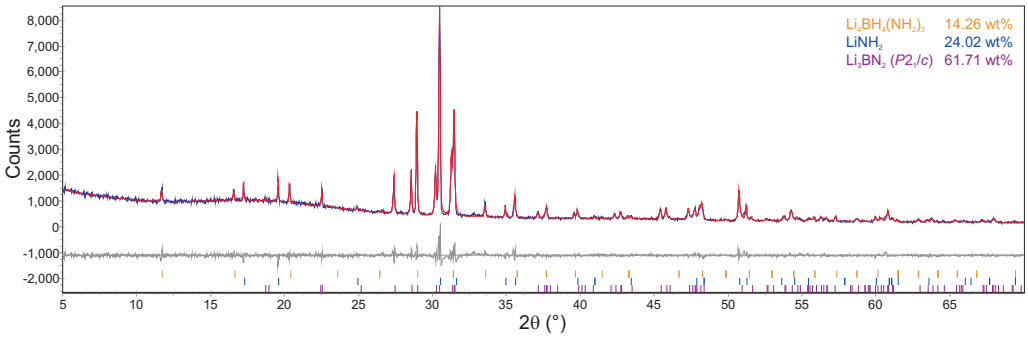

Figure 5.20: Powder XRD of $3LiNH_2 + LiBH_4$ after heating to 350°C in TPD-MS apparatus. Bragg peak positions due to $Li_4BH_4(NH_2)_3$ (orange), $LiNH_2$ (light blue) and Li_3BN_2 ($P2_1/c$) (purple) are indicated.

Li_3BN_2 become favoured.

PXRD of the reaction products after the TPD-MS experiment are shown in figure 5.20. The decomposition product was Li_3BN_2, with $LiNH_2$ and $Li_4BH_4(NH_2)_3$ remaining which is consistent with the reaction pathway suggested in section 3.7.2 (equation 3.6). Only the $P2_1/c$ polymorph of Li_3BN_2 was observed, whereas for $Li_4BH_4(NH_2)_3$ a very small amount of the $I4_1/amd$ polymorph was also present (section 3.7.1, figure 3.35). LiH, which was assigned as a decomposition product of the lower temperature hydrogen release, was not observed. Any LiH formed could react with the residual $LiNH_2$ to form Li_2NH. No distinct Li_2NH phase was observed. However, studies have shown that the $LiNH_2$ and Li_2NH structures can support non-stoichiometry [64]. It is possible that the $LiNH_2$ structure can accommodate imide anions as the two structures are closely related.

Ammonia accounted for 3.6 mol% of the total gas released at the peak of desorption, approximately the same as observed for $Li_4BH_4(NH_2)_3$. It is worth noting that for the *Ground* sample of $3LiNH_2 + LiBH_4$ significant ammonia release did not commence until 320°C, which was concurrent with the major hydrogen release attributed to the decomposition reaction forming Li_3BN_2. It is tentatively suggested that the reaction mechanism for this decomposition path-

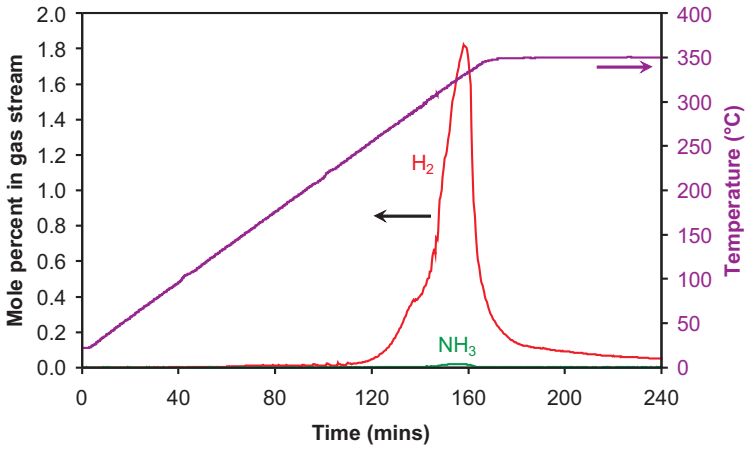

Figure 5.21: Thermal decomposition analysis of $2LiNH_2 + LiBH_4$. The temperature trace is shown in purple and the mole percents of H_2 and NH_3 released are shown in red and green respectively.

way may proceed *via* ammonia. This reaction was certainly responsible for the majority of ammonia release from this reaction mixture rather than the lower temperature LiH and BN forming reaction.

5.5.4 $2LiNH_2 + LiBH_4$

Thermal desorption data from a *Ground* sample of $2LiNH_2 + LiBH_4$ are shown in figure 5.21. This reaction mixture is the correct stoichiometry to completely form the lithium boron nitride decomposition product according to equation 5.1 and so should display maximal hydrogen release.

$$2LiNH_2 + LiBH_4 \rightarrow Li_3BN_2 + 4H_2 \uparrow \tag{5.1}$$

A minor exotherm was observed in the temperature trace at 100°C which was attributed to the partial formation of $Li_4BH_4(NH_2)_3$ and an endothermic melting event was observed from 210°C. A two stage hydrogen release was again observed, however the lower temperature hydrogen release was less pronounced than for the $3LiNH_2 + LiBH_4$ sample, appearing as a shoulder in the major hydrogen peak. Hydrogen was again released from 245°C with the main hydrogen release peaking

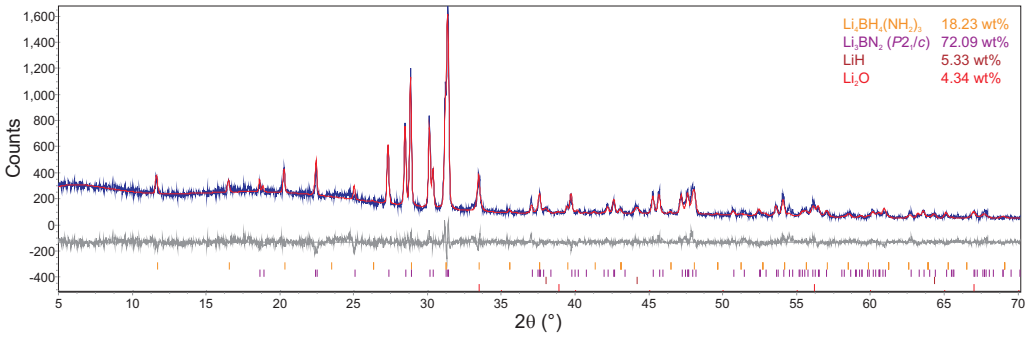

Figure 5.22: XRD of $2LiNH_2 + LiBH_4$ after heating to 350°C in a TPD-MS apparatus. Bragg peak positions due to $Li_4BH_4(NH_2)_3$ (orange), Li_3BN_2 ($P2_1/c$) (purple), LiH (dark red) and Li_2O (red) are indicated.

at 335°C. At the peak of desorption 3.0 mol% of the gas released was ammonia, slightly less than for the amide rich $3LiNH_2 + LiBH_4$ sample.

PXRD of the reaction products after the TPD-MS experiment are shown in figure 5.22. The majority decomposition product observed was again the $P2_1/c$ polymorph of Li_3BN_2 formed *via* reaction 5.1, with a small amount of LiH present attributed to the reaction shown in equation 5.2. Some $Li_4BH_4(NH_2)_3$ remained unreacted in the timescale of the TPD-MS experiment.

$$LiNH_2 + LiBH_4 \rightarrow 2LiH + BN + 2H_2 \uparrow \tag{5.2}$$

At the $2LiNH_2 + LiBH_4$ reaction stoichiometry there should be no excess $LiNH_2$ remaining after decomposition, as was the case for the $3LiNH_2 + LiBH_4$ reaction. As such, no $LiNH_2$ is available for any LiH formed from the lower temperature decomposition pathway (equation 5.2) to react with and so at this composition LiH was observed in the diffraction pattern of the decomposition products. The estimated relative amounts of Li_3BN_2 and LiH observed in the diffraction pattern of the decomposition products suggest that, over the entire TPD-MS experiment, the Li_3BN_2 forming reaction (equation 5.1) was favoured over the LiH forming reaction (equation 5.2) by a ratio of approximately 3.6:1.[†]

[†]The errors associated with determining the amount of LiH present in a sample by X-ray

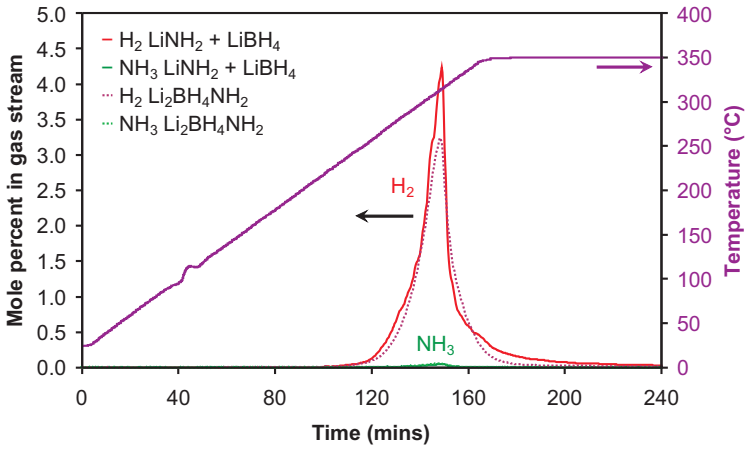

Figure 5.23: Thermal decomposition analysis of $LiNH_2$ + $LiBH_4$. The temperature trace is shown in purple and the mole percents of H_2 and NH_3 released are shown in red and green respectively. For comparison, mole percents of H_2 and NH_3 desorbed from $Li_2BH_4NH_2$ are shown as dotted lines in crimson and light green, respectively.

5.5.5 $LiNH_2$ + $LiBH_4$

Thermal desorption data from a *Ground* sample of $LiNH_2$ + $LiBH_4$ compared to data for $Li_2BH_4NH_2$ are shown in figure 5.23. An endothermic event was observed in the temperature trace from 95°C which was attributed to a melting event. Unlike for amide rich compositions, only a single hydrogen release was observed from 245°C which peaked at 315°C. The desorption profile for the *Ground* sample closely matched that of $Li_2BH_4NH_2$. At the peak of desorption, ammonia made up only 1.7% of the gaseous desorption products which was considerably less than for the amide rich compositions.

PXRD of the reaction products after the TPD-MS experiment are shown in figure 5.24. The majority decomposition product observed was LiH from the decomposition reaction shown in equation 5.2. The background for the diffraction pattern was very large with significant broad features around 25° and 42° 2θ which could be due to amorphous BN. Despite being the correct stoichiometry

diffraction are large due to the minimal amount of interaction of the low number of electrons present in LiH with X-rays and the small number of Bragg reflections present for LiH over the 2θ range measured. As such this value is only very approximate.

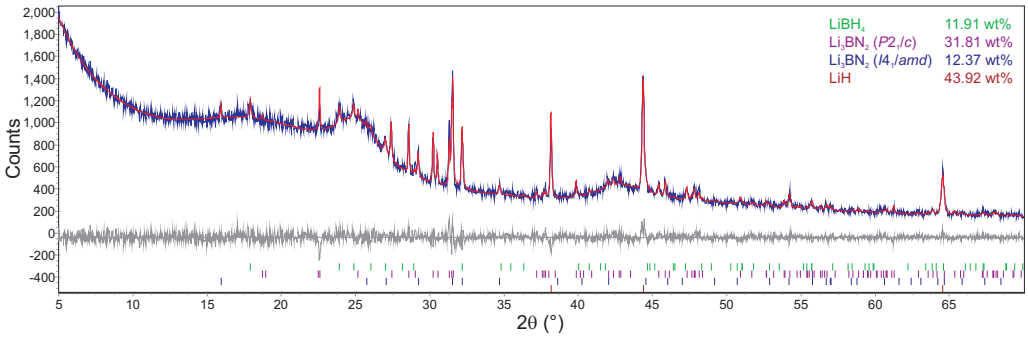

Figure 5.24: Powder XRD of $LiNH_2 + LiBH_4$ after heating to 350°C in a TPD-MS apparatus. Bragg peak positions due to $LiBH_4$ (green), Li_3BN_2 ($P2_1/c$) (purple), Li_3BN_2 ($I4_1/amd$) (blue) and LiH (dark red) are indicated.

for reaction 5.2 to go to completion, significant amounts of Li_3BN_2 were also observed with the $P2_1/c$ polymorph favoured over the $I4_1/amd$ polymorph by a ratio of 2.6:1. Unreacted $LiBH_4$ was also observed. As described for the previous sample, the LiH forming reaction (equation 5.2) was favoured over the Li_3BN_2 forming reaction (equation 5.1) by a ratio of approximately 7.5:1.

5.5.6 $LiNH_2 + 2LiBH_4$

Thermal desorption data from a *Ground* sample of $LiNH_2 + 2LiBH_4$ are shown in figure 5.25. The same endothermic melting event was observed, again at 95°C. The same onset temperature of 245°C was also observed, however hydrogen release peaked at the slightly lower temperature of 305°C. Even less ammonia release was observed from this sample, making up only 0.8% of the gaseous desorption products at the peak of desorption.

PXRD of the reaction products after the TPD-MS experiment showed only LiH and $LiBH_4$ with no Li_3BN_2 observed (figure 5.26). It appeared that at this stoichiometry the lower temperature reaction (equation 5.2) went to completion under the conditions of the TPD-MS experiment. The excess of borohydride present in this reaction mixture, which is an ionic melt at the temperature of hydrogen release, makes the BN forming reaction much more likely. A reaction

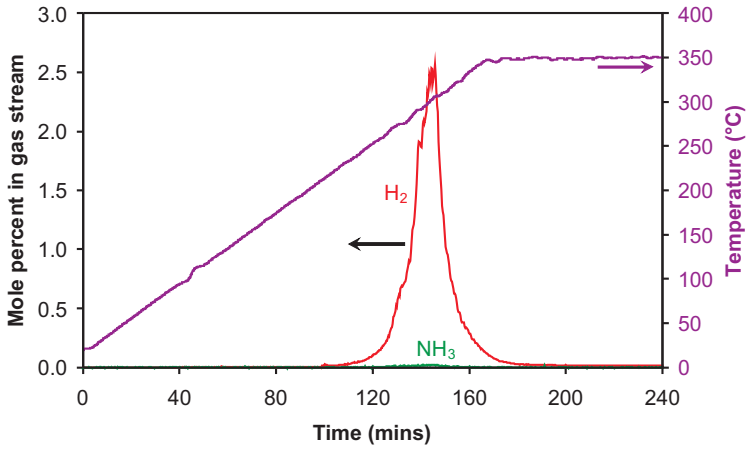

Figure 5.25: Thermal decomposition analysis of $LiNH_2$ + $2LiBH_4$. The temperature trace is shown in purple and the mole percents of H_2 and NH_3 released are shown in red and green respectively.

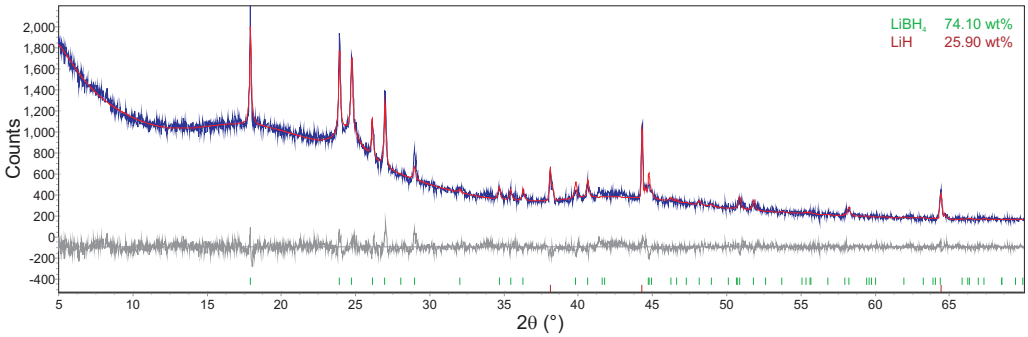

Figure 5.26: Powder XRD of $LiNH_2$ + $2LiBH_4$ after heating to 350°C in a TPD-MS apparatus. Bragg peak positions due to $LiBH_4$ (green) and LiH (dark red) are indicated.

to form Li_3BN_2 would require at some point the coming together of two amide ions with a borohydride ion, as discussed previously in section 4.6, which becomes less likely in borohydride rich mixtures.

5.5.7 $LiNH_2$ + $3LiBH_4$

Thermal desorption data from a *Ground* sample of $LiNH_2$ + $3LiBH_4$ are shown in figure 5.27. The desorption profile was very similar to that of the $LiNH_2$ + $2LiBH_4$ sample only with less hydrogen released and a similar amount of ammonia release was observed (0.9%).

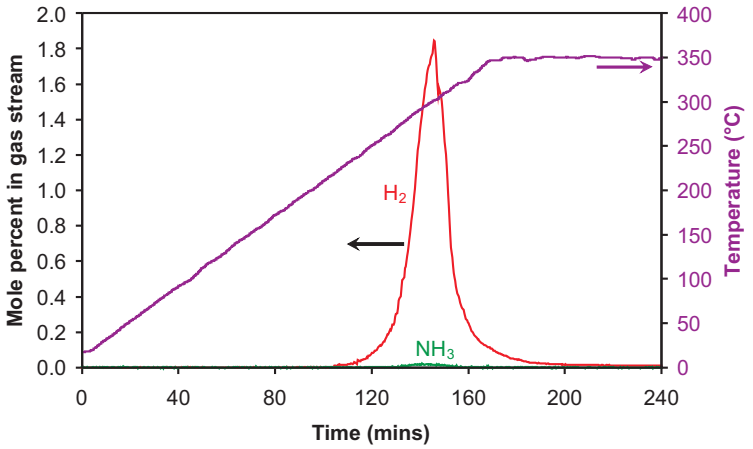

Figure 5.27: Thermal decomposition analysis of $LiNH_2$ + $3LiBH_4$. The temperature trace is shown in purple and the mole percents of H_2 and NH_3 released are shown in red and green respectively.

The diffraction pattern of the decomposition products (not shown) was very similar to that in section 5.5.6, with $LiBH_4$ as the majority phase (83.7 wt%) and LiH (16.3 wt%). No boron rich decomposition products were observed and as such the amount of hydrogen release observed dropped with the introduction of more borohydride than the 1:1 sample.

5.5.8 Summary and Discussion

The hydrogen desorption profile of $LiBH_4$ + $LiNH_2$ mixtures differed greatly from that of the starting materials, $LiBH_4$ and $LiNH_2$, which were found not to decompose to a significant degree up to 350°C. Figure 5.28 shows a summary the TPD-MS data for *Ground* $LiBH_4$ + $LiNH_2$ samples processed so as to give quantitative hydrogen release data, as discussed in section 2.7. The amount of hydrogen released and the fraction of ammonia release observed are summarised in table 5.1.

The instantaneous hydrogen release (figure 5.28(b)) for the amide rich compositions showed a two stage hydrogen release. Two decomposition pathways were identified; at low temperatures and at borohydride rich compositions a reaction

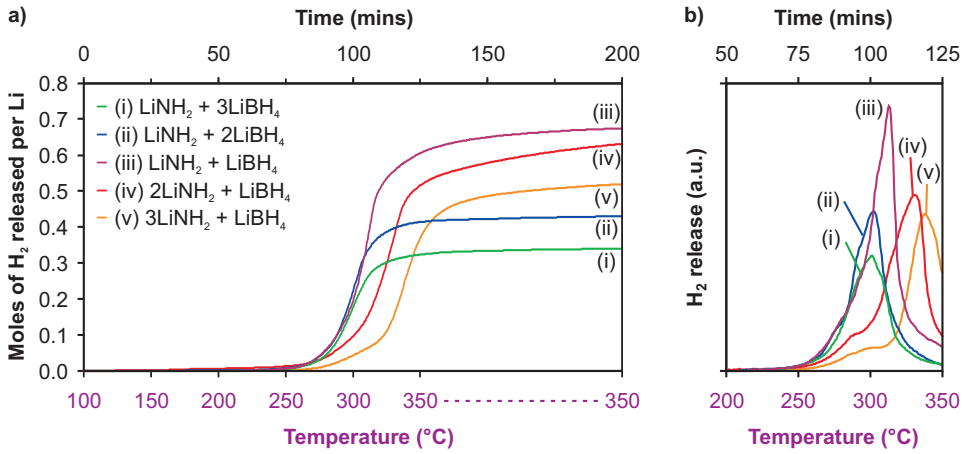

Figure 5.28: Comparison of thermal decomposition from $LiBH_4 + LiNH_2$ samples showing (a) cumulative hydrogen release and (b) instantaneous hydrogen release.

Table 5.1: Summary of TPD-MS data for $LiNH_2 + LiBH_4$ samples.

Composition	$LiNH_2$ + $3LiBH_4$	$LiNH_2$ + $2LiBH_4$	$LiNH_2$ + $LiBH_4$	$2LiNH_2$ + $LiBH_4$	$3LiNH_2$ + $LiBH_4$
H_2 released (mol)	0.34	0.43	0.67	0.63	0.52
NH_3 released (mol%)	0.9	0.8	1.11	3.0	3.6
T_{dec}† (°C)	275	272	271	276	294

†Temperature at which 0.03 moles of H_2 had been released from the sample.

forming LiH and BN was favoured (equation 5.2) whereas at higher temperatures in amide rich compositions the formation of Li_3BN_2 was favoured (equation 5.1).

Reaction 5.1 is capable of releasing 4/3 H_2 per lithium which equates to 11.9 wt% H_2. Reaction 5.2 forms a hydrogen containing decomposition product (LiH) leading to only one H_2 released per lithium and a reduced hydrogen capacity (9.0 wt% H_2). In practice, the amounts of hydrogen observed by the quantification of TPD-MS data (table 5.1) fell short of the values expected for complete decomposition. In some cases this was due to incomplete decomposition as evidenced by the presence of undecomposed hydrogen containing materials in the post-TPD PXRD pattern. This was attributed to either incomplete decomposition in the

relatively short timescale of the TPD-MS experiment[‡] or due to some sample moving out of the hot zone of the TPD-MS furnace.

The maximum hydrogen release was observed for the $LiNH_2 + LiBH_4$ sample, whereas the theoretical maximum amount of hydrogen release is predicted for the $2LiNH_2 + LiBH_4$ sample. For the 1:1 sample hydrogen release was essentially complete, as evidenced by the flattening off of the hydrogen release curve in figure 5.28(a). For the 2:1 sample hydrogen release was not complete as the hydrogen release curve continued to rise at the end of the experiment.

As expected, the amount of ammonia release observed increased with amide concentration. This is contrary to a previous study by Meisner *et al.* [131] where more significant ammonia release was observed for borohydride rich compositions. The lower temperature hydrogen release pathway (equation 5.2) was not mentioned in this study and no LiH formation was observed. We hypothesise that the formation of LiH by a lower temperature reaction was responsible for the reduction in ammonia release observed as LiH can react with NH_3 released to form $LiNH_2$ with the release of hydrogen.

5.6 Proposed Phase Diagram

A previous attempt to produce a phase diagram for the $LiNH_2 + LiBH_4$ system has been made by Meisner *et al.* [131] where a very complex phase diagram was proposed. Differences between our observed results and the published results of Meisner *et al.* led us to propose a new phase diagram for the $LiNH_2 + LiBH_4$ system.

Meisner *et al.* [131] adopted ball milling as the synthesis route to their starting samples of the form $(LiNH_2)_x(LiBH_4)_{(1-x)}$. This highly non-equilibrium synthesis technique led to the assignment of four distinct phases present at room temperature, which were assigned as α ($Li_4BH_4(NH_2)_3$) and β ($Li_2BH_4NH_2$ in-

[‡]Each sample was held at the ultimate temperature of 350°C for only one hour.

correctly assigned as a body centred cubic phase with a = 10.4 Å) and two unindexed phases labelled δ (present in one amide rich sample where $x = 0.75$) and γ (present where $0.556 \geq x \geq 0.655$). These observations disagree with our observations in section 5.3.3, where $Li_4BH_4(NH_2)_3$ was the only observed stable phase. Variable temperature powder diffraction and thermogravimetric analysis linked to a mass spectrometer were used by Meisner *et al.* [131] to analyse the crystalline phases present and the gases released upon heating. The observed decomposition products were different to those observed in our study for borohydride rich compositions with only Li_3BN_2 observed rather than LiH and BN. The gaseous desorption products also showed a greater degree of ammonia release than our TPD-MS study. A new phase diagram consistent with our observations is proposed.

5.6.1 Results

We have compiled phase information from *in-situ* and *ex-situ* powder diffraction experiments, DSC data and TPD-MS data in order to produce a phase diagram of the $LiNH_2$ + $LiBH_4$ system from room temperature to 350°C. The proposed phase diagram is shown in figure 5.29.

Starting from $LiBH_4$, the phase transition from orthorhombic to hexagonal [98] was observed in the DSC trace at 114°C and the melting point was observed as an endothermic event in the TPD-MS temperature trace. Although a very small hydrogen release was observed in the TPD-MS experiment at the melting point, and Raman spectroscopy indicated that new phases may be present, the majority phase observed in the diffraction pattern after decomposition at 350°C was still $LiBH_4$ and so this is the only phase listed in the phase diagram.

Upon addition of $LiNH_2$ to $LiBH_4$, $Li_4BH_4(NH_2)_3$ formed as the only other stable room temperature phase (section 5.3.3). In the borohydride rich region of the phase diagram, $Li_4BH_4(NH_2)_3$ is labelled $Li_4(BH_4)_{(1+x)}(NH_2)_{(3-x)}$ due to observations in section 5.3.3 where a stable solid solution where x = 0.008

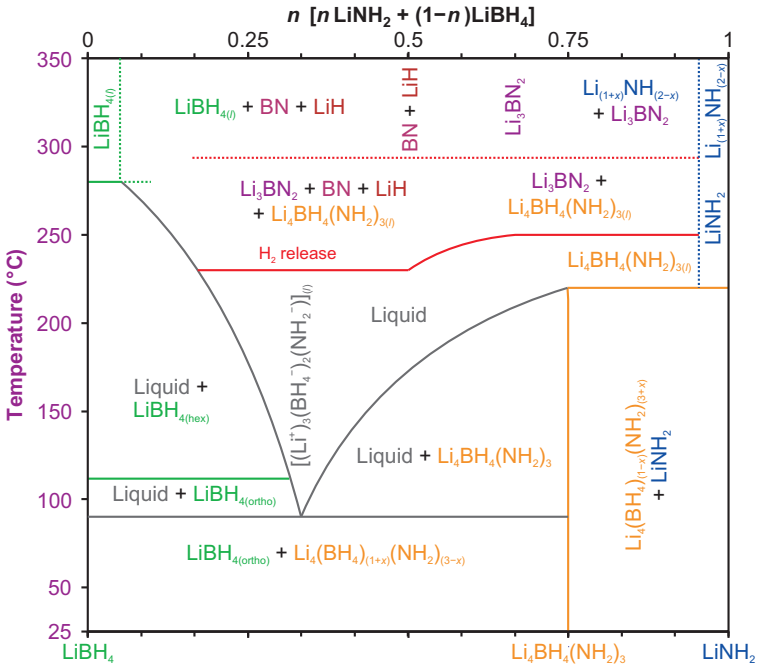

Figure 5.29: Proposed phase diagram for $LiNH_2$ + $LiBH_4$.

was proposed. In the amide rich region of the phase diagram $Li_4BH_4(NH_2)_3$ is similarly labelled $Li_4(BH_4)_{(1-x)}(NH_2)_{(3+x)}$ to represent the proposed alternative solid solution limit where $x = 0.014$.

Upon heating borohydride rich compositions above 90°C an endothermic event was observed in the DSC data (section 5.4.3), which was most prominent at the $2LiBH_4 + LiNH_2$ composition. Observations in *in-situ* diffraction studies on samples of $LiBH_4$ + $LiNH_2$ composition indicated that amorphous content started to form from this temperature, which was assigned as a molten borohydride rich phase (section 4.5). Combining these observations together with physical observations of samples heated to different temperatures, the $LiBH_4$ + $LiNH_2$ system was designated as a eutectic with the eutectic point at 90°C at the $2LiBH_4$ + $LiNH_2$ composition, labelled in figure 5.29 as $[(Li^+)_3(BH_4^-)_2(NH_2^-)]_{(l)}$. Upon heating, the solubility of both amide and borohydride in the ionic melt increased, as evidenced by the gradual loss of $Li_4BH_4(NH_2)_3$ in *in-situ* diffraction experiments (section 4.5). In the amide rich region, the melting point of $Li_4BH_4(NH_2)_3$

was reached at 218°C. However, $LiNH_2$ did not melt in the temperature range investigated (T_{mpt} 380°C [117]). For the borohydride rich region the amount of liquid phase present increased with temperature until 280°C where $LiBH_4$ was also completely molten.

Two red lines are included in the phase diagram (figure 5.29); the first red line at the lower temperature represents the onset of significant hydrogen release from the different mixtures. The second dotted red line represents the temperature at which hydrogen release was complete when held at temperature for around 4 hours. Although technically only the thermodynamically stable products should be listed in the phase diagram, the nature of the ramped temperature experiments used to construct this phase diagram make assigning the temperatures of the true thermodynamically stable products difficult. As such, the onset temperature is shown as the first temperature line and an approximate temperature for complete decomposition is shown as the second dotted temperature line. It has recently been demonstrated that although hydrogen release can occur from $2LiNH_2 + LiBH_4$ at 240°C, the reaction was not complete even after 5 days [146]. As such, the demarcation of decomposition temperature in this way is justified.

Although the line due to $Li_4BH_4(NH_2)_3$ is represented as a solid line, rather than a solid solution, the width of the solid solution is so small in annealed samples that is it not significant on the scale of the phase diagram. Strictly speaking, the end members themselves should not be included on the phase diagram directly. However, for clarity of showing the melting point of $LiBH_4$ and the slow decomposition point of $LiNH_2$ at higher temperatures it was felt that the inclusion was warranted.

The proposed phase diagram presented here represents our best guess at the true phase diagram of this complicated multiphase system and is consistent with our observations using various and varied instrumental techniques.

5.7 Crystal Structure Comparisons

The structural similarities between $Li_4BH_4(NH_2)_3$ and $LiNH_2$ have been noted previously (e.g. see section 3.3 and figures 3.14 and 3.15). Although the crystal structures of $Li_2BH_4NH_2$ and $Li_4BH_4(NH_2)_3$ appear very different there are in fact a lot of similarities between the structures and the $LiNH_2$ end member, such as the preservation of the N octahedra. The nitrogen ions in $LiNH_2$ adopt a slightly distorted face centred cubic configuration which can be viewed as edge shared octahedral clusters (figures 5.30(a) and 5.31(a)). In $Li_4BH_4(NH_2)_3$ only one quarter of the edges of the NH_2^- octahedra are shared and the amide framework is penetrated by spiral chains of BH_4^- ions running in three orthogonal directions through this cubic structure (figures 5.30(b) and 5.31(b)). In contrast, for $Li_2BH_4NH_2$ the NH_2^- octahedra are completely isolated in the structure (figures 5.30(c) and 5.31(c)).

This type of analysis was extended by Wu *et al.* [104] where the structures of $LiNH_2$, $Li_4BH_4(NH_2)_3$, $Li_2BH_4NH_2$ and $LiBH_4$ were described in terms of the tetrahedral coordination around lithium ions.

The $LiNH_2$ structure [105] has three crystallographically distinct Li^+ sites, all of which are tetrahedrally coordinated by a single crystallographic NH_2^-, as shown in figure 5.32(a). The $Li_4BH_4(NH_2)_3$ structure [101] has three different tetrahedral Li^+ sites (figure 5.32(b)). These three sites, present in a ratio of 3:3:2, have NH_2^-:BH_4^- ratios of 2:2, 4:0 and 3:1 respectively. For $Li_2BH_4NH_2$ [121], there are two crystallographically distinct Li^+ sites present in an equal ratio in the structure, one of which is ¼ NH_2^- and one of which is ¼ BH_4^- (figure 5.32(c)). The $LiBH_4$ structure [98] has a single Li^+ site tetrahedrally coordinated to BH_4^- (figure 5.32(d)).

The way these tetrahedra are arranged in each of the structures is shown in figure 5.33 which illustrates structural relationships between all of the members of the lithium amide–borohydride family. The structural similarities between

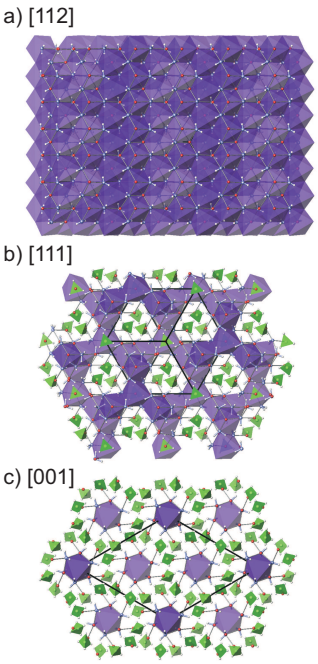

Figure 5.30: Diagram showing the relationship between the N octahedra of (a) $LiNH_2$, (b) $Li_4BH_4(NH_2)_3$ and (c) $Li_2BH_4NH_2$. H atoms are depicted in white, Li in red, B in green and N in blue. N octahedra are shown in purple. The viewing directions shown are all perpendicular to the [110] direction.

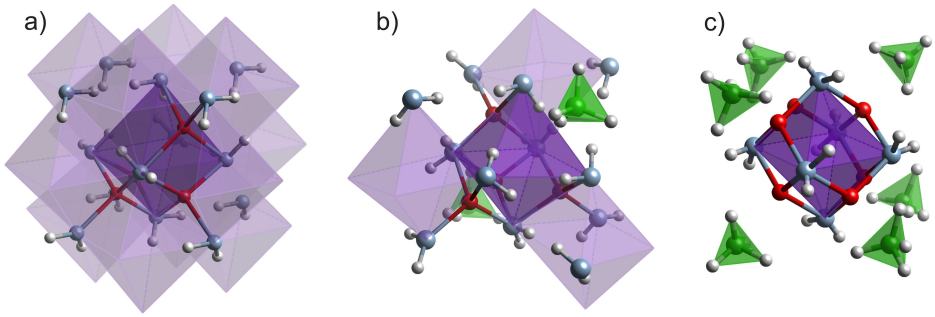

Figure 5.31: Diagram showing the local structure around a single N octahedron in (a) $LiNH_2$, (b) $Li_4BH_4(NH_2)_3$ and (c) $Li_2BH_4NH_2$. H atoms are depicted in white, Li in red, B in green and N in blue. N octahedra are shown in purple.

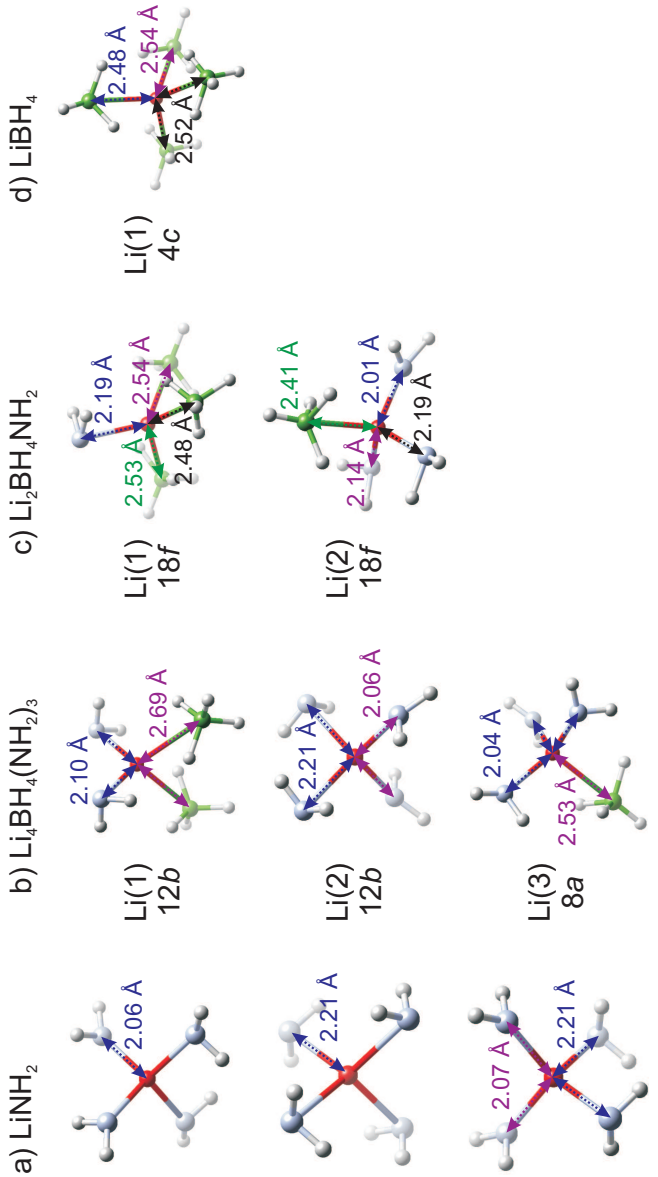

Figure 5.32: Comparison of local lithium environments in $LiNH_2$, $Li_4BH_4(NH_2)_3$, $Li_2BH_4NH_2$ and $LiBH_4$. Nitrogen is shown in blue, boron in green, lithium in red and hydrogen in white.

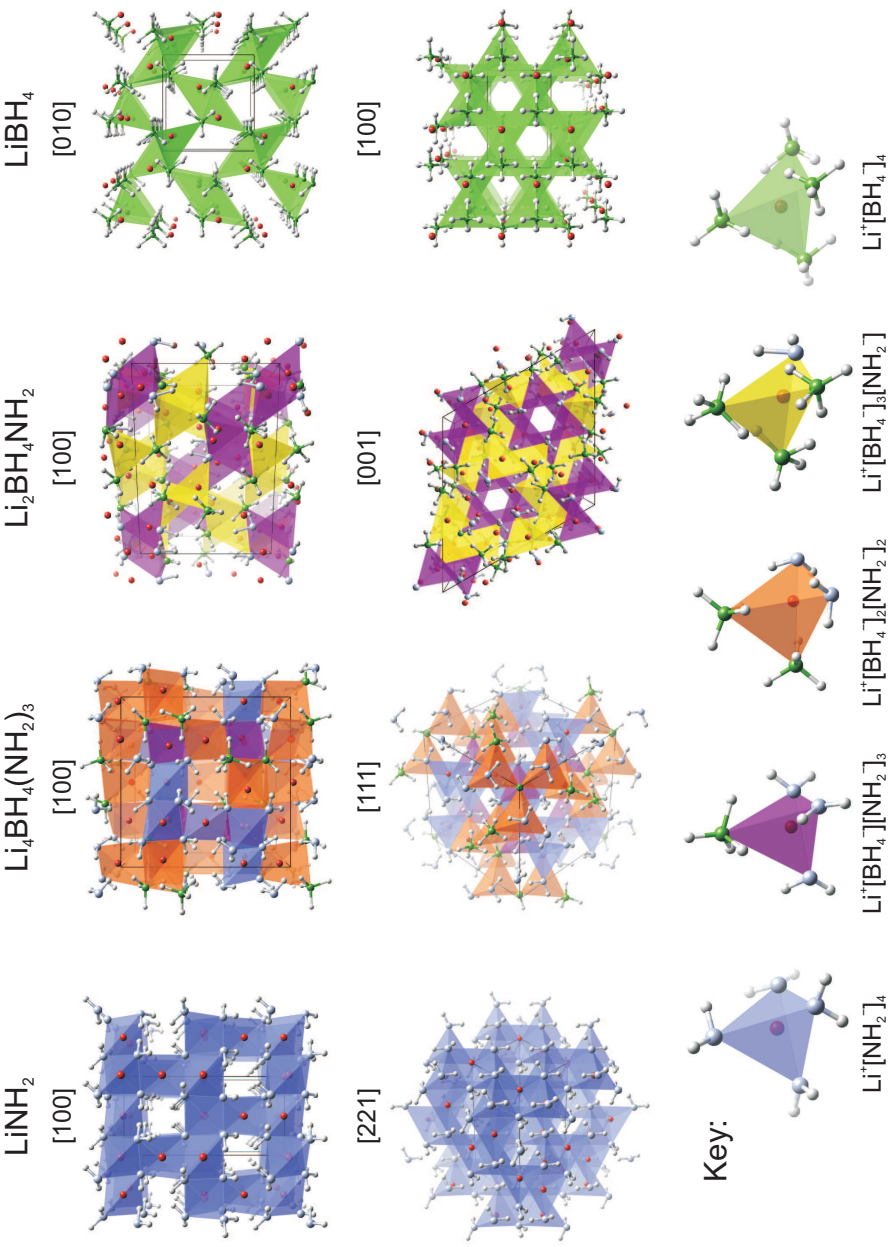

Figure 5.33: Comparison of the structures of $LiNH_2$, $Li_4BH_4(NH_2)_3$, $Li_2BH_4NH_2$ and $LiBH_4$. Nitrogen is shown in blue, boron in green, lithium in red and hydrogen in white. The unit cell is shown in black. Different lithium tetrahedra coordination environments are shown in different colours.

$LiNH_2$ and $Li_4BH_4(NH_2)_3$ are clear as previously noted, indeed, 37.5% of the lithium tetrahedra are purely $Li^+[NH_2^-]_4$. The $Li_4BH_4(NH_2)_3$ structure contains a number of different lithium environments; $Li^+[NH_2^-]_4$, $Li^+[BH_4^-][NH_2^-]_3$ and $Li^+[BH_4^-]_2[NH_2^-]_2$. The range of environments in this structure may explain why this structure appears capable of accommodating a range of stoichiometries.

Wu *et al.* [104] noted that of the possible configuration of the lithium tetrahedra, $Li^+[BH_4^-]_2[NH_2^-]_2$ is the most distorted due to the differing sizes of BH_4^- and NH_2^-. This was proposed as a reason for the rigid stoichiometry of $Li_2BH_4NH_2$ as opposed to the variable stoichiometry of $Li_4BH_4(NH_2)_3$. $Li_2BH_4NH_2$ is made up entirely of $Li^+[BH_4^-][NH_2^-]_3$ and $Li^+[BH_4^-]_3[NH_2^-]$ tetrahedra. The substitution of one of either anion to form $Li^+[BH_4^-]_2[NH_2^-]_2$ tetrahedra would then affect and distort all surrounding tetrahedra. Substitution causing the formation of $Li^+[BH_4^-]_4$ or $Li^+[NH_2^-]_4$ tetrahedra would cause segregation to form $LiBH_4$ or $Li_4BH_4(NH_2)_3$ respectively.

5.8 Conclusion

The system $n\mathrm{LiNH_2} + (1-n)\mathrm{LiBH_4}$ has been investigated in detail using *ex-situ* powder X-ray diffraction, TPD-MS and DSC. Data from these varied techniques have been pooled together to compile a phase diagram for the $n\mathrm{LiNH_2} + (1-n)\mathrm{LiBH_4}$ system at temperatures up to 350°C. Two decomposition pathways have been identified with the lower temperature pathway releasing less hydrogen, but also less ammonia.

Although the proposed phase diagram was derived from a large amount of data, the majority of the diffraction data were collected *ex-situ*. As such, the observed phases may not truly represent the thermodynamically stable phases at elevated temperatures. For example, the solid solution range of $Li_4BH_4(NH_2)_3$ is expected to increase upon heating, although this could not be proved from purely *ex-situ* data. Further work to determine the true phase diagram would require

in-situ diffraction data at a range of temperatures to determine the thermodynamically stable products.

Chapter 6

$Li_4BH_4(NH_2)_3 + nMH_x$

6.1 Introduction

Investigations into whether the decomposition pathway of $Li_4BH_4(NH_2)_3$ could be altered by the incorporation of alkali and alkali earth metal hydrides was undertaken. It was found that the metal hydrides interacted with the amide present in $Li_4BH_4(NH_2)_3$ and as such reaction mixtures in the ratio of one amide ion to one hydride ion were investigated. Addition of all of the studied metal hydrides decreased the level of ammonia released. However, little change in the temperature of release was observed except in the case of magnesium hydride, MgH_2, where a lower temperature hydrogen releasing reaction was observed.

6.2 Experimental

$Li_4BH_4(NH_2)_3$ was prepared by the method described in section 3.2. LiH (Sigma-Aldrich, $\leq$95% purity), NaH (Sigma-Aldrich, 95% purity), MgH_2 (Alfa Aesar, 98%) and CaH_2 (Sigma-Aldrich, 99.99% purity) were used as received.

The hydrides were ground with the $Li_4BH_4(NH_2)_3$ in the desired molar ratio and heated on the TPD-MS apparatus described in section 2.7. Approximately 0.1 g of sample was used and all results presented in this section were normalised

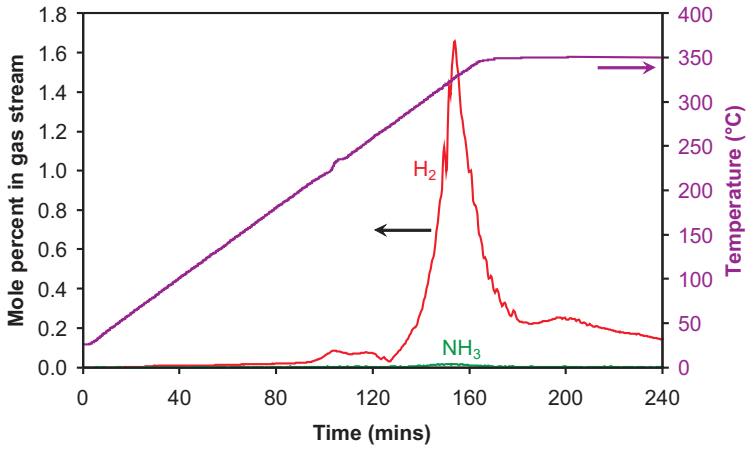

Figure 6.1: Thermal decomposition analysis of $Li_4BH_4(NH_2)_3$ + 3LiH in a TPD apparatus. The temperature trace is shown in purple and the mole percents of H_2 and NH_3 released are shown in red and green respectively.

to 0.1 g of sample. Powder diffraction data were collected for the products after the TPD-MS experiments.

6.3 $Li_4BH_4(NH_2)_3$ + 3LiH

Thermal desorption data from $Li_4BH_4(NH_2)_3$ + 3LiH heated at a ramp rate of 2°C min^{-1} to 350°C are shown in figure 6.1. Two main desorption events were observed; the first minor hydrogen peak started from 205°C and the second main hydrogen release started from 270°C, peaking at 330°C. An endothermic event was observed in the temperature trace at 220°C, which is consistent with the melting of $Li_4BH_4(NH_2)_3$.

The lower temperature hydrogen release was consistent with the observed onset temperature of the reaction of LiH with $LiNH_2$ to form Li_2NH with the release of hydrogen [147]. PXRD of the reaction products after the TPD-MS experiment (figure 6.2) confirmed the presence of Li_2NH, unlike for the decomposition of pure $Li_4BH_4(NH_2)_3$ where $LiNH_2$ was observed in the diffraction pattern of the TPD-MS products (figure 3.35).

The main hydrogen releasing reaction started from 270°C, the same tempera-

ture as observed for significant hydrogen release from pure $Li_4BH_4(NH_2)_3$ (section 3.7.1).

As with thermal decomposition of $Li_4BH_4(NH_2)_3$, the $P2_1/c$ polymorph of Li_3BN_2 appeared favoured (24.17 wt%) over the $I4_1/amd$ polymorph (15.47 wt%) by a ratio of 1.6:1, but to a much lesser extent than for pure $Li_4BH_4(NH_2)_3$ (27.6:1).

The reaction appeared to proceed *via* two pathways. At low temperatures $LiNH_2$ from the $Li_4BH_4(NH_2)_3$ structure reacted with LiH to form Li_2NH according to equation 6.1. This reaction appeared to be much slower than for pure $LiNH_2$ with LiH, with significantly less hydrogen release observed than for an equivalent $LiNH_2$ + LiH sample [147]. This is an indication that the $Li_4BH_4(NH_2)_3$ structure stabilises $LiNH_2$ with respect to the reaction with LiH. The small hydrogen release indicated that only a small proportion of $LiNH_2$ from the $Li_4BH_4(NH_2)_3$ structure reacted in this way at these lower temperatures.

$$LiNH_2 + LiH \rightarrow Li_2NH + H_2 \uparrow \tag{6.1}$$

The second higher temperature decomposition was the normal decomposition pathway of $Li_4BH_4(NH_2)_3$ to form Li_3BN_2 according to equation 6.2. This then results in more $LiNH_2$, which can react with the remaining LiH, again according to equation 6.1. This explains why significant hydrogen release from the $Li_4BH_4(NH_2)_3$ + 3LiH reaction continued long after reacting the maximum experimental temperature of 350°C.

$$Li_4BH_4(NH_2)_3 \rightarrow Li_3BN_2 + LiNH_2 + 4H_2 \uparrow \tag{6.2}$$

The amount of ammonia released was significantly less than observed for pure $Li_4BH_4(NH_2)_3$. At the peak of hydrogen desorption, only 0.8 mol% of the gas released was due to ammonia compared to 4.0 mol% for pure $Li_4BH_4(NH_2)_3$. This can be attributed to the reaction of LiH with released ammonia according

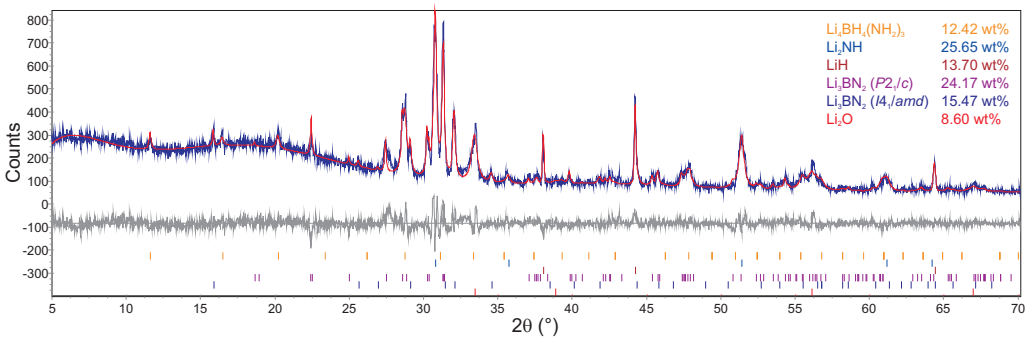

Figure 6.2: Powder XRD of $Li_4BH_4(NH_2)_3$ + 3LiH after heating to 350°C in a TPD-MS apparatus. Bragg peak positions due to $Li_4BH_4(NH_2)_3$ (orange), Li_2NH (blue), LiH (dark red), Li_3BN_2 ($P2_1/c$) (purple), Li_3BN_2 ($I4_1/amd$) (dark blue) and Li_2O (red) are indicated.

to equation 6.3 [148].

$$LiH + NH_3 \rightarrow LiNH_2 + H_2 \uparrow \tag{6.3}$$

Figure 6.3 shows the TPD-MS data processed to give simulated gravimetric data. The inferred weight loss from mass spectroscopic data over the total heating time was only 4.9 wt%. If the reaction went to completion with the $LiNH_2$ and $LiBH_4$ constituents of $Li_4BH_4(NH_2)_3$ reacting in a 2:1 ratio to form Li_3BN_2 and the remaining mole of $LiNH_2$ reacting with one mole of LiH according to equation 6.4, this would give a theoretical maximum of 8.8 wt% H_2. However, this leaves two moles of LiH as essentially dead weight in the reaction.

$$Li_4BH_4(NH_2)_3 + 3LiH \rightarrow Li_3BN_2 + Li_2NH + 2LiH + 5H_2 \uparrow \tag{6.4}$$

Although the addition of LiH to $Li_4BH_4(NH_2)_3$ appears to produce a beneficial reduction in the amount of ammonia released, no significant difference in the temperature or pathways of decomposition was observed.

6.4 $Li_4BH_4(NH_2)_3$ + 3NaH

Thermal desorption data from $Li_4BH_4(NH_2)_3$ + 3NaH heated at a ramp rate of 2°C min^{-1} to 350°C are shown in figure 6.4. Two main peaks were observed in the

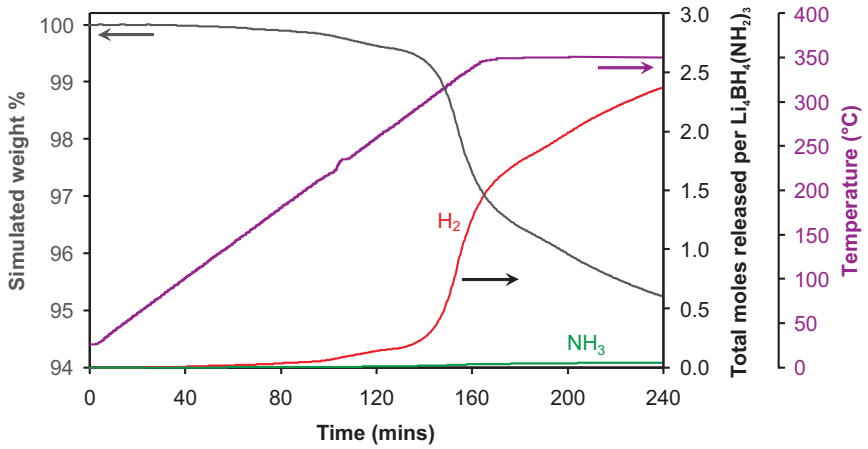

Figure 6.3: Thermal decomposition analysis of $Li_4BH_4(NH_2)_3$ + 3LiH in a TPD apparatus with simulated gravimetric data. The temperature trace is shown in purple, the moles of H_2 and NH_3 released per $Li_4BH_4(NH_2)_3$ are shown in red and green respectively, and the simulated gravimetric data is shown in grey.

desorption profile, the first starting from 220°C and peaking at 290°C, and the second dominating from 325°C and, unusually, peaking after the maximum temperature of 350°C was achieved. The entire desorption profile was much broader than observed for pure $Li_4BH_4(NH_2)_3$ and $Li_4BH_4(NH_2)_3$ mixed with other metal hydrides. Ammonia release appeared to be suppressed with the ammonia signal just above the background noise of the mass spectrometer equating to less than 1% of the total gas released.

PXRD of the reaction products after the TPD-MS experiment are shown in figure 6.5. The majority decomposition products were the $P2_1/c$ polymorph of Li_3BN_2 and Li_2NH while a large amount of NaH remained unreacted. Two mixed lithium–sodium amides, $LiNa_2(NH_2)_3$ and $Li_3Na(NH_2)_4$, were also observed [135, 149]. The observation of Li_2NH, as opposed to $LiNH_2$ for pure $Li_4BH_4(NH_2)_3$, combined with the observation of mixed Li–Na amides suggests a partial metathesis as shown in equation 6.5. Any $NaNH_2$ formed can react with remaining $LiNH_2$ to explain the existence of the mixed Li–Na amides. This reaction also produces LiH which can also react with remaining $LiNH_2$ to form Li_2NH with the release of hydrogen. This explains the existence of Li_2NH in the

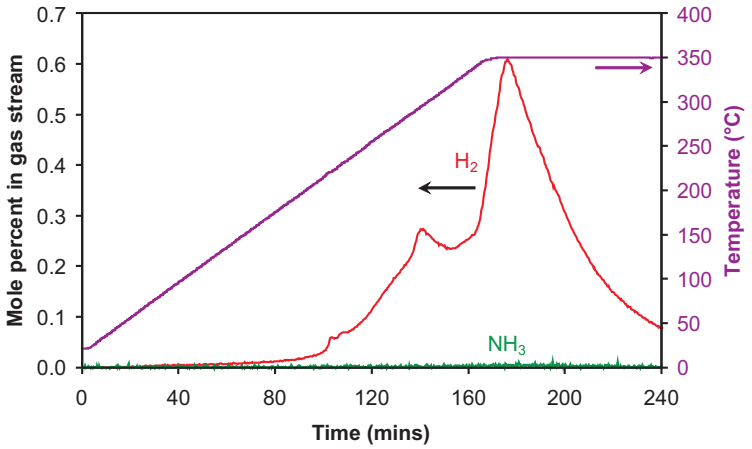

Figure 6.4: Thermal decomposition analysis of $Li_4BH_4(NH_2)_3$ + 3NaH in a TPD apparatus. The temperature trace is shown in purple and the mole percents of H_2 and NH_3 released are shown in red and green respectively.

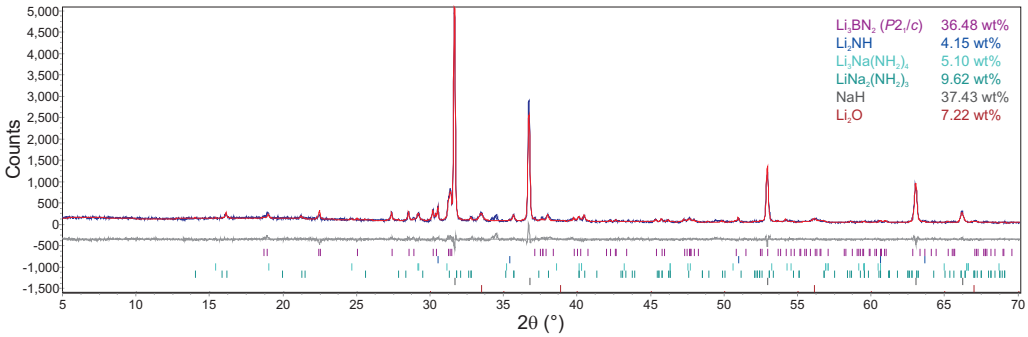

Figure 6.5: Powder XRD of $Li_4BH_4(NH_2)_3$ + 3NaH after heating to 350°C in a TPD-MS apparatus. Bragg peak positions due to Li_3BN_2 ($P2_1/c$) (purple), Li_2NH (blue), $Li_3Na(NH_2)_4$ (turquoise), $LiNa_2(NH_2)_3$ (dark turquoise), NaH (grey) and Li_2O (red) are indicated.

decomposition products.

$$LiNH_2 + NaH \rightarrow LiH + NaNH_2 \tag{6.5}$$

The TPD-MS data interpreted to give gravimetric data are shown in figure 6.6. A total of 2.55 moles of H_2 was inferred per $Li_4BH_4(NH_2)_3$ over the timescale of the TPD-MS experiment, which is similar to that observed for the experiment with LiH. The broadness of the hydrogen release could be due to the metathesis reaction creating $NaNH_2$, which does not react in the same way as $LiNH_2$. In-

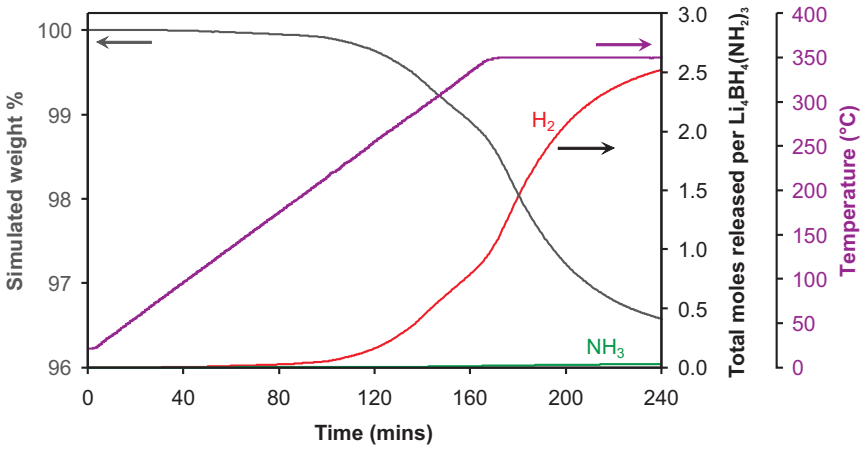

Figure 6.6: Thermal decomposition analysis of $Li_4BH_4(NH_2)_3$ + 3NaH in a TPD apparatus with simulated gravimetric data. The temperature trace is shown in purple, the moles of H_2 and NH_3 released per $Li_4BH_4(NH_2)_3$ are shown in red and green respectively and the simulated gravimetric data is shown in grey.

deed, no sodium containing decomposition product was observed. As such, the formation of $NaNH_2$ may effectively partially block the decomposition reaction.

6.5 $2Li_4BH_4(NH_2)_3 + 3MgH_2$

Thermal desorption data from $2Li_4BH_4(NH_2)_3 + 3MgH_2$ heated at a ramp rate of 2°C min^{-1} to 350°C are shown in figure 6.7. Two very distinct peaks were observed in the desorption profile, the first starting from 190°C and peaking at 225°C and the second dominating from 290°C and peaking at 330°C.

The decomposition products after heating to 350°C were predominantly Li_3BN_2, Mg_3N_2 [150] and LiH (figure 6.7). Unusually, the $P4_22_12$ polymorph of Li_3BN_2 [126] was preferred with a smaller amount of the $I4_1/amd$ polymorph and none of the most commonly observed $P2_1/c$ polymorph was seen. The presence of a magnesium containing decomposition product and the appearance of a different polymorph of Li_3BN_2 clearly indicate that the presence of MgH_2 alters the decomposition pathway of $Li_4BH_4(NH_2)_3$ and it was decided to investigate this system in more detail by *ex-situ* synchrotron X-ray diffraction and gravimet-

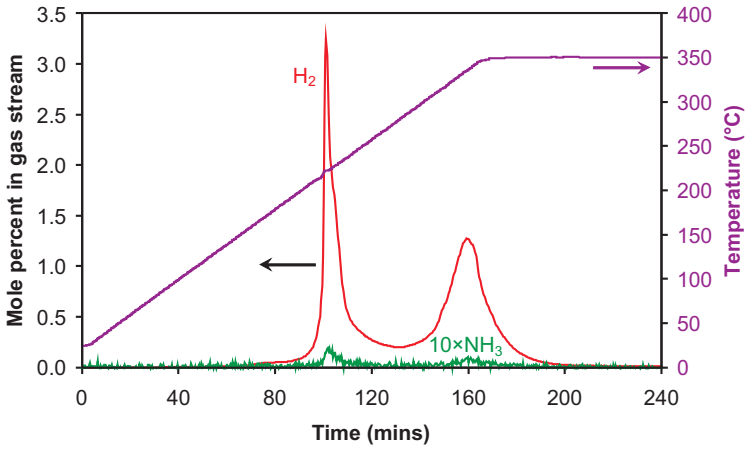

Figure 6.7: Thermal decomposition analysis of $2Li_4BH_4(NH_2)_3 + 3MgH_2$ in a TPD apparatus. The temperature trace is shown in purple and the mole percents of H_2 and NH_3 (magnified by a factor of 10) released are shown in red and green respectively.

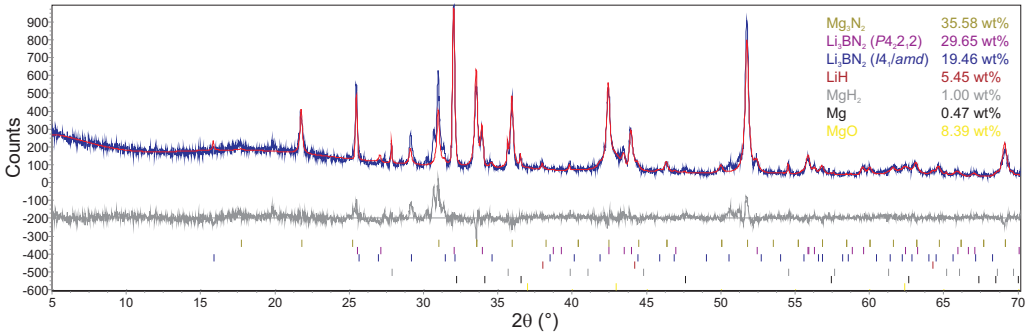

Figure 6.8: Powder XRD of $2Li_4BH_4(NH_2)_3 + 3MgH_2$ after heating to 350°C in a TPD-MS apparatus. Bragg peak positions due to Mg_3N_2 (olive), Li_3BN_2 ($P4_22_12$) (purple), Li_3BN_2 ($I4_1/amd$) (dark blue), LiH (dark red), MgH_2 (grey), Mg (black) and MgO (yellow) are indicated.

ric methods.

6.5.1 Low Temperature Desorption

The first distinct hydrogen release was investigated separately in an equivalent TPD-MS experiment where $2Li_4BH_4(NH_2)_3 + 3MgH_2$ was heated at a ramp rate of 2°C min^{-1} to 220°C (figure 6.10). Synchrotron X-ray powder diffraction data for the decomposition products are shown in figure 6.10. The majority

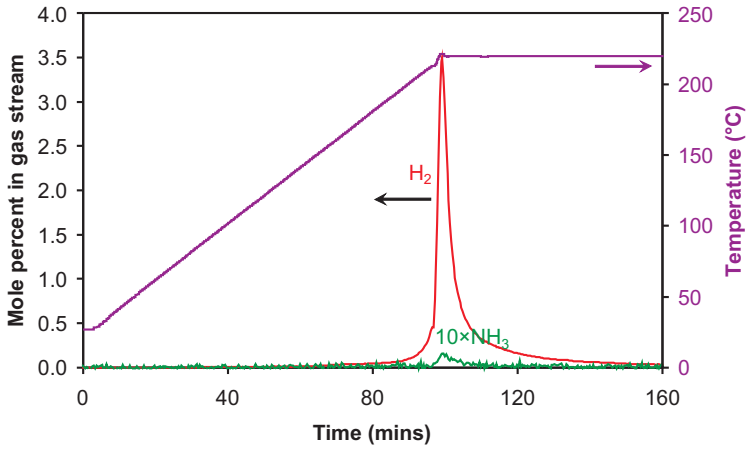

Figure 6.9: Thermal decomposition analysis of $2Li_4BH_4(NH_2)_3 + 3MgH_2$ in a TPD apparatus up to 220°C. The temperature trace is shown in purple and the mole percents of H_2 and NH_3 (magnified by a factor of 10) released are shown in red and green respectively.

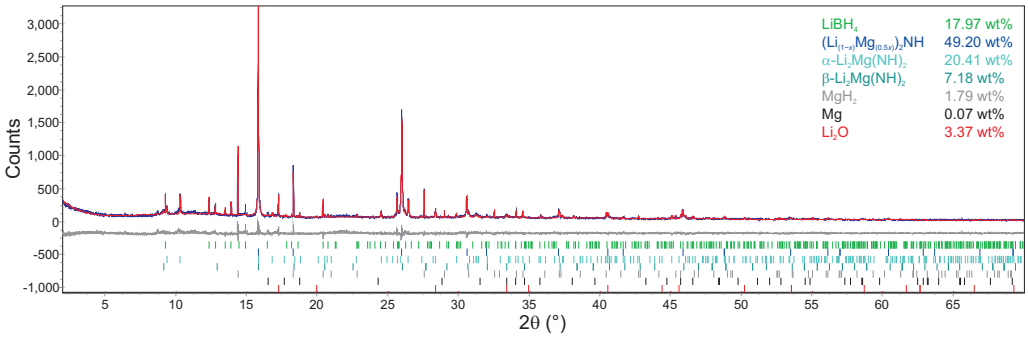

Figure 6.10: Powder synchrotron XRD data of $2Li_4BH_4(NH_2)_3 + 3MgH_2$ after heating to 220°C in a TPD-MS apparatus. Bragg peak positions due to $LiBH_4$ (green), $(Li_{(1-x)}Mg_{(0.5x)})_2NH$ (blue), α–$Li_2Mg(NH)_2$ (light turquoise), β–$Li_2Mg(NH)_2$ (dark turquoise), MgH_2 (grey), Mg (black) and Li_2O (red) are indicated.

decomposition product was a face centred cubic Li_2NH-like phase, although the fit of the calculated relative intensities of the Bragg reflections for Li_2NH to the observed data was relatively poor. α– and β–$Li_2Mg(NH)_2$ were also observed [69], but in the case of primitive cubic β–$Li_2Mg(NH)_2$ the majority of the Bragg reflections overlap with those of the face centred cubic Li_2NH–like phase and is only directly evidenced by the presence of the (001) peak.

The structures of the primitive cubic β–$Li_2Mg(NH)_2$ and the face centred

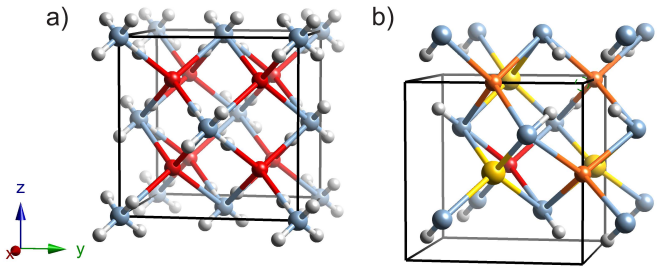

Figure 6.11: Crystal structures of (a) Li_2NH and (b) β-$Li_2Mg(NH)_2$. H atoms are depicted in white, Li in red and N in blue. The unit cells are shown in black. In (a) hydrogen sites are a quarter occupied. In (b) orange sites represent fractional occupancies of 0.59 Li and 0.08 Mg and yellow sites represent 0.41 Li and 0.59 Mg and a vacancy site is highlighted in green.

cubic Li_2NH are very similar, as shown in figure 6.11. In the β–$Li_2Mg(NH)_2$ structure there is an ordering of the cation sites giving one lithium site, two mixed metal sites and one vacancy resulting in primitive symmetry. The relatively poor fit of the Li_2NH structure to the observed diffraction pattern led us to consider that it may also be a mixed Li–Mg imide, but without the ordering required to form the orthorhombic α–$Li_2Mg(NH)_2$ structure or the primitive β–$Li_2Mg(NH)_2$ structure. We modelled substitution in the Li_2NH structure by refining a level of disordered substitution of the form $(Li_{(1-x)}Mg_{(0.5x)})_2NH$. Upon refinement in this manner the R_{Bragg} value for this phase dropped from 4.80 for a pure Li_2NH phase to 2.56 for a formula of $(Li_{(1-x)}Mg_{(0.5x)})_2NH$ with $x = 0.159(9)$. The overlapping nature of these phases makes a definitive assignment of phases difficult. Rather than forming distinct phases the phases present in this reaction mixture are probably a whole range of lithium–magnesium imides with various degrees of ordering.

$LiBH_4$ remained unreacted and no boron containing decomposition products were observed after decomposition at 220°C. $LiNH_2$ from the $Li_4BH_4(NH_2)_3$ structure appears to react with MgH_2 according to the known reaction shown

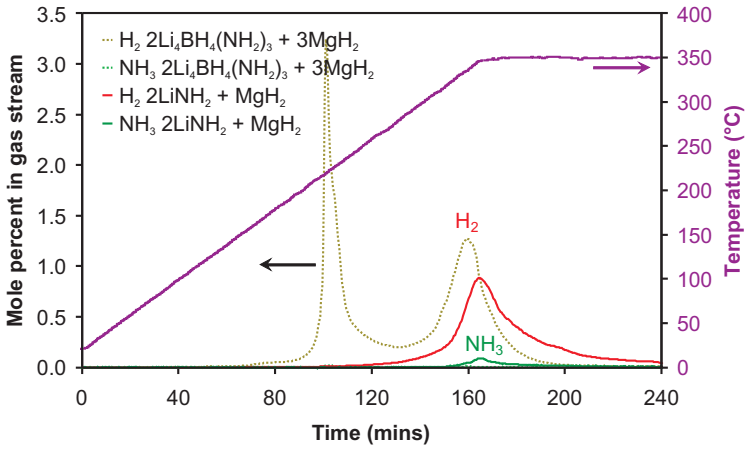

Figure 6.12: Thermal decomposition analysis of $2LiNH_2 + MgH_2$ in a TPD apparatus. The temperature trace is shown in purple and the mole percents of H_2 and NH_3 released are shown in red and green respectively. For comparison, mole percents of H_2 and NH_3 released for $2Li_4BH_4(NH_2)_3 + 3MgH_2$ are shown as dotted lines in dark yellow and light green, respectively.

in equation 6.6 [67, 69].

$$2LiNH_2 + MgH_2 \rightarrow Li_2Mg(NH)_2 + 2H_2 \uparrow \tag{6.6}$$

The apparent lack of participation of $LiBH_4$ in the reaction lead us to investigate just the reaction of $2LiNH_2 + MgH_2$ in our TPD-MS apparatus, as shown in figure 6.12.

Hydrogen release from $2LiNH_2 + MgH_2$ occurred at a much higher temperature than in the $2Li_4BH_4(NH_2)_3 + 3MgH_2$ sample. Significant hydrogen release was not observed until 290°C compared to around 205°C for the first desorption step of the $2Li_4BH_4(NH_2)_3 + 3MgH_2$ sample. At the peak of desorption, 9.0% of the gas released was NH_3 compared to only 0.6% for $2Li_4BH_4(NH_2)_3 + 3MgH_2$.

PXRD of the post TPD-MS $2LiNH_2 + MgH_2$ sample are shown in figure 6.13 and shows α– and β–$Li_2Mg(NH)_2$ together with some $LiNH_2$ and MgH_2 which remained unreacted in the timescale of the TPD-MS experiment. These observed decomposition products are similar to those of the first low temperature reaction step for the $2Li_4BH_4(NH_2)_3 + 3MgH_2$. No disordered cubic $(Li_{(1-x)}Mg_{(0.5x)})_2NH$

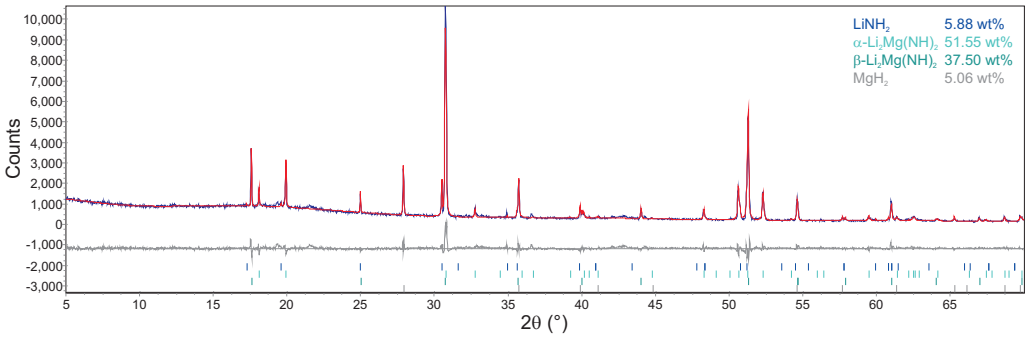

Figure 6.13: Powder XRD of $2LiNH_2 + MgH_2$ after heating to 350°C in a TPD-MS apparatus. Bragg peak positions due to $LiNH_2$ (blue), α–$Li_2Mg(NH)_2$ (light turquoise), β–$Li_2Mg(NH)_2$ (dark turquoise) and MgH_2 (grey) are indicated.

was observed, which is probably due to the annealing of this disordered phase to the more ordered α– and β–$Li_2Mg(NH)_2$ structures upon heating to 350°C.

The reaction products of $2Li_4BH_4(NH_2)_3 + 3MgH_2$ at 220°C closely matched those of $2LiNH_2 + MgH_2$ at 350°C. Clearly the presence of $LiBH_4$ in $Li_4BH_4(NH_2)_3$ has a dramatic effect on the reactivity of $LiNH_2$ towards MgH_2. A similar effect of $LiBH_4$ has been noted previously in the decomposition of MgH_2, although in that case the effect appeared to be purely kinetic [30]. The vastly lower temperature of hydrogen release implies that the effect of $LiBH_4$ in this case may be thermodynamic in nature.

In the case of $2Li_4BH_4(NH_2)_3 + 3MgH_2$, Mg_3N_2 was observed after heating to 350°C, whereas for $2LiNH_2 + MgH_2$ the reaction did not progress further than the mixed Li–Mg imide at these temperatures. Clearly the reaction pathway is very different in the presence of $LiBH_4$. A detailed study of the phases present upon heating $2Li_4BH_4(NH_2)_3 + 3MgH_2$ was undertaken using *ex-situ* synchrotron X-ray powder diffraction in order to determine how the reaction progresses.

6.5.2 Ex-situ Synchrotron X-ray Powder Diffraction

A range of partially decomposed samples of $2Li_4BH_4(NH_2)_3 + 3MgH_2$ were prepared by heating at 4°C min^{-1} to the desired temperature and holding for 4 hours.

Temperatures investigated were 100°C, 140°C and from 170°C to 350°C in 20°C steps. The solid crystalline products were then determined using synchrotron X-ray powder diffraction.

Refinement Strategy

Synchrotron X-ray powder diffraction data were collected at a wavelength of 0.79987(1) Å and rebinned from the original step size of 0.003° to 0.006° to improve the signal-to-noise ratio. Data were collected in the range 2° to 48° 2θ (d-spacing 23.0 to 0.98 Å) with a data collection time of around 12 minutes. Due to a problem with data collection which caused steps in the diffraction data at low angle, the data below 5° 2θ were discarded. Powder diffraction data were refined using Topas [90]. For each data set a zero point error and an 18 parameter Chebyshev background function were refined. For each phase present, lattice parameters, a pseudo-Voigt peak shape function with 6 parameters and scale factor were refined. Atomic coordinates were taken from reported structures and were not refined. In the case of the Li_2NH structure, a disordered substitution of the form $(Li_{(1-x)}Mg_{(0.5x)})_2NH$ was refined as discussed previously (section 6.5.1).

Results

Figure 6.14 shows a summary of the weight percents obtained for each phase from the refinements using Topas [90]. At 100°C only $Li_4BH_4(NH_2)_3$ and MgH_2 were present with a small Li_2O impurity from the $LiNH_2$ starting material and Mg metal from the MgH_2 starting material. At the slightly higher temperature of 140°C a small amount of a new phase was observed which was identified as magnesium amide [136]. This suggests that a metathesis reaction occurred with lithium amide from $Li_4BH_4(NH_2)_3$ and magnesium hydride, as shown in equation 6.7.

$$2LiNH_2 + MgH_2 \rightarrow Mg(NH_2)_2 + 2LiH \tag{6.7}$$

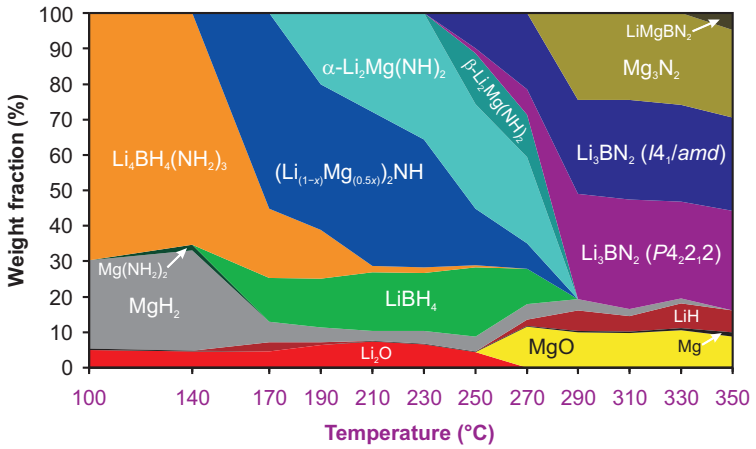

Figure 6.14: Total molar phase fractions after heating $2Li_4BH_4(NH_2)_3$ + $3MgH_2$ at various temperatures.

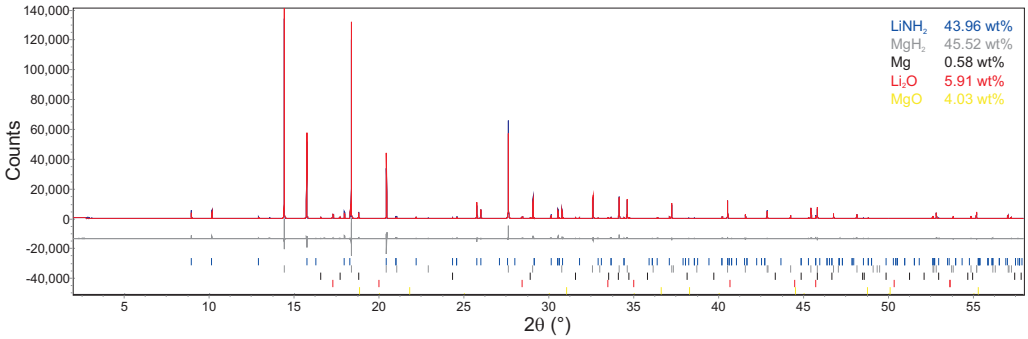

Figure 6.15: Powder synchrotron XRD of $2LiNH_2$ + MgH_2 after heating to 140°C. Bragg peak positions due to $LiNH_2$ (blue), MgH_2 (grey), Mg (black), Li_2O (red) and MgO (yellow) are indicated.

Heating of $2LiNH_2$ + MgH_2 at similar temperatures did not produce any metathesis reaction (e.g. see figure 6.15). The mixing of $LiBH_4$ with $LiNH_2$ has the effect of dramatically decreasing the melting point of the system (see section 5.6). We suggest that the presence of BH_4^- in the $Li_4BH_4(NH_2)_3$ structure allows for increased ionic motion of amide anions compared to the structurally related $LiNH_2$. This ionic motion may be significant even below the melting point of $Li_4BH_4(NH_2)_3$ which could facilitate the metathesis reaction.

The presence of $Mg(NH_2)_2$ at this low temperatures opens up the possibility that the low temperature reaction is in fact the reaction of $Mg(NH_2)_2$ with LiH,

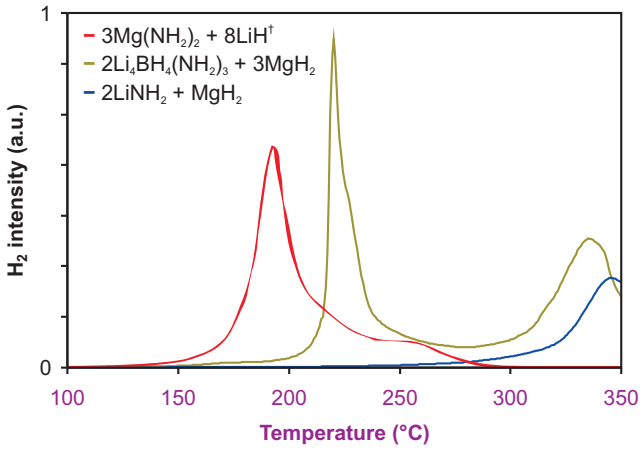

Figure 6.16: Thermal decomposition analysis of $2Li_4BH_4(NH_2)_3 + 3MgH_2$ in a TPD apparatus (olive) compared with literature data for $3Mg(NH_2)_2 + 8LiH$ (red) [68]†. For comparison, hydrogen release from $2LiNH_2 + MgH_2$ is also shown (blue).

shown in equation 6.8.

$$Mg(NH_2)_2 + 2LiH \rightarrow Li_2Mg(NH)_2 + 2H_2 \uparrow \tag{6.8}$$

Figure 6.16 shows a comparison of hydrogen release from $2Li_4BH_4(NH_2)_3 + 3MgH_2$ with literature data for a ball milled sample of $3Mg(NH_2)_2 + 8LiH$ [68].† It is clear that hydrogen release from the $3Mg(NH_2)_2 + 8LiH$ reaction occurred at temperatures significantly lower than for $2LiNH_2 + MgH_2$. Hydrogen release from the ball milled $3Mg(NH_2)_2 + 8LiH$ sample was at temperatures lower than for $2Li_4BH_4(NH_2)_3 + 3MgH_2$, although this may be attributed to the ball milling process.

The presence of a small amount of $Mg(NH_2)_2$ at 140°C does not prove that the low temperature hydrogen release from $2Li_4BH_4(NH_2)_3 + 3MgH_2$ was due to reaction 6.8, although the temperature of hydrogen release is more consistent with this reaction than reaction 6.6. At 170°C $Mg(NH_2)_2$ was no longer observed and instead the decomposition product $(Li_{(1-x)}Mg_{(0.5x)})_2NH$ was observed. The absence of $Mg(NH_2)_2$ and the presence of a decomposition product is consistent

†An excess of LiH was used in this study to suppress the amount of ammonia released in the reaction

with a metathesis reaction forming $Mg(NH_2)_2$ which then preferentially reacts with the LiH produced to form mixed Li–Mg imides.

The appearance of $(Li_{(1-x)}Mg_{(0.5x)})_2NH$ at 170°C was concurrent with a decrease in the amount of $Li_4BH_4(NH_2)_3$ and MgH_2 and the appearance of $LiBH_4$. After reaction at higher temperatures of up to 230°C the amount of $Li_4BH_4(NH_2)_3$ and MgH_2 continued to decrease with an increase in the amount of the mixed Li–Mg phases $(Li_{(1-x)}Mg_{(0.5x)})_2NH$ and α–$Li_2Mg(NH)_2$ observed. Between 190°C and 230°C the α–$Li_2Mg(NH)_2$ structure became favoured over that of the $(Li_{(1-x)}Mg_{(0.5x)})_2NH$ structure, which is attributed to the annealing of the disordered $(Li_{(1-x)}Mg_{(0.5x)})_2NH$ structure to the more ordered α–$Li_2Mg(NH)_2$ structure. The overall reaction in the temperature range 170°C to 230°C can by summarised by equation 6.9, which has the theoretical hydrogen capacity of 4.7 wt%.

$$2Li_4BH_4(NH_2)_3 + 3MgH_2 \rightarrow 3Li_2Mg(NH)_2 + 2LiBH_4 + 6H_2 \uparrow \quad (6.9)$$

At temperatures of 250°C and 270°C the boron containing decomposition product Li_3BN_2 was observed indicating that the $LiBH_4$ had started to decompose. This is a similar temperature to that at which pure $Li_4BH_4(NH_2)_3$ was observed to decompose to form Li_3BN_2 (section 3.7.2). Unlike for pure $Li_4BH_4(NH_2)_3$, decomposition of $2Li_4BH_4(NH_2)_3 + 3MgH_2$ formed the $I4_1/amd$ and $P4_22_12$ polymorphs of Li_3BN_2.

At temperatures of 290°C and above the decomposition was essentially complete, forming Li_3BN_2, Mg_3N_2 and LiH as the ultimate decomposition products. Although there appeared to be a relatively small amount of LiH present, this was due to the very light nature of LiH and it in fact represents a similar molar quantity to Li_3BN_2. At 330°C and 350°C the amount of residual MgH_2 decreased with a concurrent increase in the amount of Mg observed indicating that the MgH_2 was decomposing. At the highest temperature of 350°C $LiMgBN_2$ [151] was also observed, but only in a very small quantity. The reaction in the higher

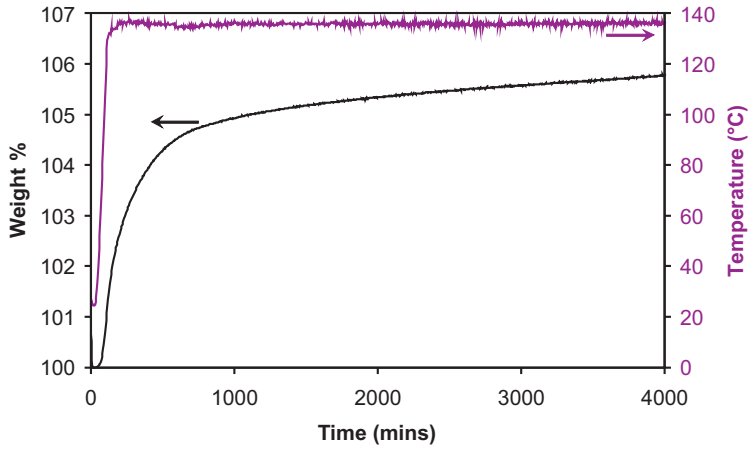

Figure 6.17: Hydrogen absorption of decomposed $2Li_4BH_4(NH_2)_3 + 3MgH_2$ in an IGA at 18 bar H_2. The gravimetric trace is shown in black and the temperature trace is shown in purple.

temperature range 290°C to 350°C can by summarised by equation 6.10.

$$3Li_2Mg(NH)_2 + 2LiBH_4 \rightarrow 2Li_3BN_2 + Mg_3N_2 + 2LiH + 6H_2 \uparrow \quad (6.10)$$

This high temperature reaction releases a theoretical 4.9 wt% hydrogen, giving a total theoretical capacity of the $2Li_4BH_4(NH_2)_3 + 3MgH_2$ system up to temperatures of 350°C of 9.3 wt% H_2.

6.5.3 Reversibility Studies

The hydrogenation properties of the low temperature hydrogen releasing reaction (equation 6.9) were investigated using an Intelligent Gravimetric Analyser (IGA). A sample of $2Li_4BH_4(NH_2)_3 + 3MgH_2$ decomposed in a TPD-MS experiment up to 220°C (73.0 mg) was inertly loaded into an IGA an placed under a hydrogen atmosphere at 18 bar and heated at 2°C min^{-1} to 135°C. A gradual mass increase was observed, as shown in figure 6.17, which reached 5.8 wt% after 3 days.

This mass increase is larger than the theoretical maximum for the reverse of reaction 6.9 (5.2 wt%). Also the sample mass continued to increase linearly which is an indication that oxidation may be occurring and as such the gravimetric

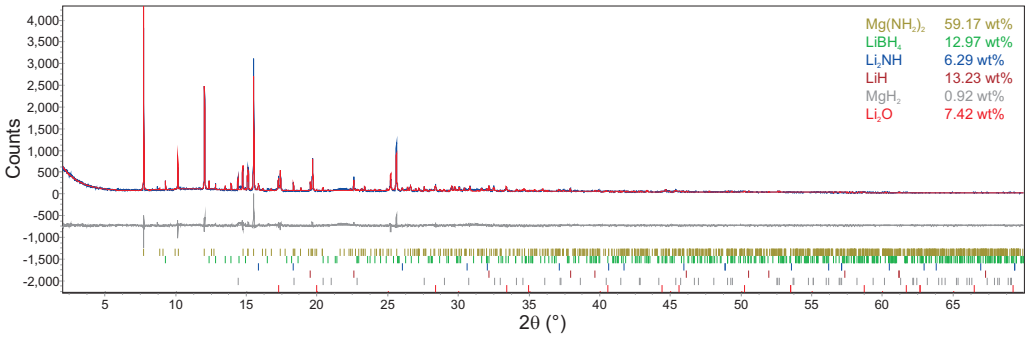

Figure 6.18: Powder synchrotron XRD of $2Li_4BH_4(NH_2)_3 + 3MgH_2$ after heating to 220°C in a TPD-MS apparatus and subsequent hydrogenation in an IGA. Bragg peak positions due to $Mg(NH_2)_2$ (olive), $LiBH_4$ (green), Li_2NH (blue), LiH (dark red), MgH_2 (grey) and Li_2O (red) are indicated.

data was declared unreliable. The sample was inertly removed from the IGA and synchrotron X-ray powder diffraction data were collected (figure 6.18).

Rather than containing $Li_4BH_4(NH_2)_3$ and MgH_2 as expected if reaction 6.9 is reversible, $Mg(NH_2)_2$ was observed as the majority phase together with $LiBH_4$, LiH and some Li_2NH. The presence of $Mg(NH_2)_2$ and LiH suggest that the true reversible reaction is the reaction presented in equation 6.11.

$$3Li_2Mg(NH)_2 + 2LiBH_4 + 6H_2 \rightarrow 3Mg(NH_2)_2 + 6LiH + 2LiBH_4 \qquad (6.11)$$

This observation is the same as made for $Li_2Mg(NH)_2$ formed from the reaction of $LiNH_2$ with MgH_2 [152]. Upon hydrogenation, $Mg(NH_2)_2$ and LiH form in preference to $LiNH_2$ and MgH_2.

The cycling properties of this system were tested in an IGA. A new sample of $2Li_4BH_4(NH_2)_3 + 3MgH_2$ (81.4 mg) was inertly loaded onto an IGA. The thermal desorption properties were measured by heating at 2°C min^{-1} to 215°C under flowing argon at 1 bar and a mass spectrometer was used to observe the gaseous desorption products. The thermal desorption data are shown in figure 6.19.

Thermal desorption observed in the IGA commenced around 50°C with a re-

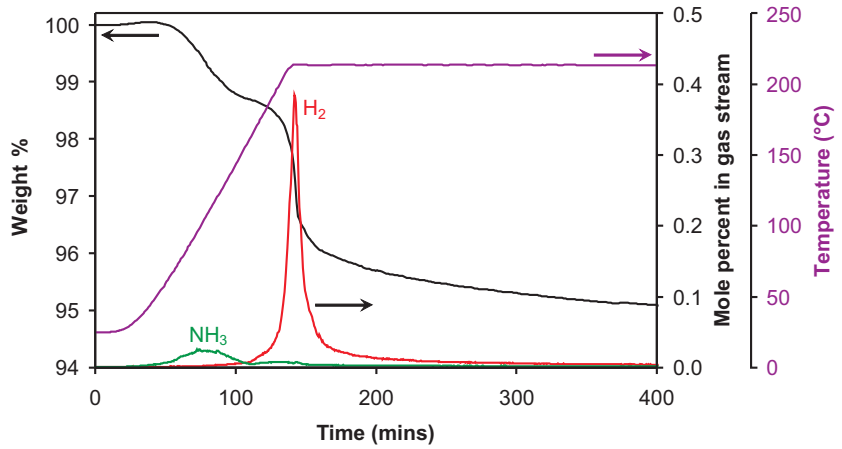

Figure 6.19: Thermo-gravimetric analysis of $2Li_4BH_4(NH_2)_3 + 3MgH_2$ in an IGA. The gravimetric trace is shown in black, the temperature trace is shown in purple and the mole percents of H_2 and NH_3 released are shown in red and green respectively.

lease of ammonia which was not observed in TPD-MS experiments (figure 6.9). This is similar to $Li_4BH_4(NH_2)_3$ investigated by IGA-MS where a low temperature ammonia release was also observed (see section 3.7.1). Significant Hydrogen release from $2Li_4BH_4(NH_2)_3 + 3MgH_2$ was observed from 160°C which was below the temperature observed in TPD-MS experiments (190°C). The apparent lowering of the hydrogen release temperature was also observed in between IGA-MS and TPD-MS experiments on $Li_4BH_4(NH_2)_3$.

Figure 6.20 shows the IGA-MS data where the calculated mass loss due to the amount of desorbed gases has been fitted to the observed mass loss by refining the relative H_2:NH_3 sensitivity, as discussed previously in section 3.7.1.

During the hydrogen release, 3.5 moles of H_2 were released per $2Li_4BH_4(NH_2)_3 + 3MgH_2$ in 400 minutes, which is less than the 6 moles predicted from equation 6.9. Ammonia release contributed 0.3 moles of gas released per $2Li_4BH_4(NH_2)_3 + 3MgH_2$ and made up 7.1% of the total gas released. The sample was held at temperature for a total of 1000 minutes during which time the sample mass continued to drop and when heating was stopped a total of 4.5 moles of H_2 per $2Li_4BH_4(NH_2)_3 + 3MgH_2$ was released, which when combined with the observed

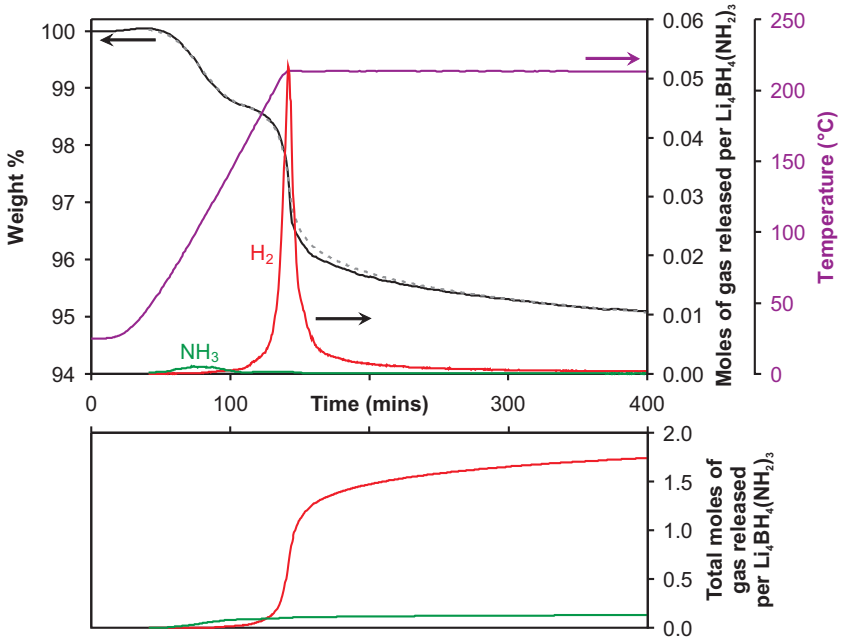

Figure 6.20: Thermo-gravimetric analysis of $2Li_4BH_4(NH_2)_3 + 3MgH_2$ in an IGA. The gravimetric trace is shown in black, the fitted calculated gravimetric trace from mass spectrometer data is shown in grey, the temperature trace is shown in purple. The number of moles of H_2 and NH_3 released per mole of $Li_4BH_4(NH_2)_3$ are shown in red and green respectively and a cumulative plot for these gases is shown below.

ammonia release is close to accounting for all of the expected hydrogen release.

The IGA was then cooled to room temperature, evacuated and purged with hydrogen at 0.5 bar. Hydrogen was admitted up to a pressure of 18 bar H_2 and the sample temperature was ramped to 150°C at 2°C min^{-1}. The resulting gravimetric trace is shown in figure 6.21. While at 150°C the sample mass rose due to hydrogenation, it did so very slowly. After two hours at 150°C the sample temperature was ramped to the slightly higher temperature of 170°C to test for any improvement in the kinetics of hydrogenation at higher temperatures. Rather than increasing the rate of hydrogenation, dehydrogenation occured evidenced by a gradual mass loss of 0.1 wt% in 90 minutes. The sample temperature was then decreased to 135°C where the sample mass started to increase once more, this time at a faster rate than at 150°C. This behaviour suggests a reversible hydrogenation

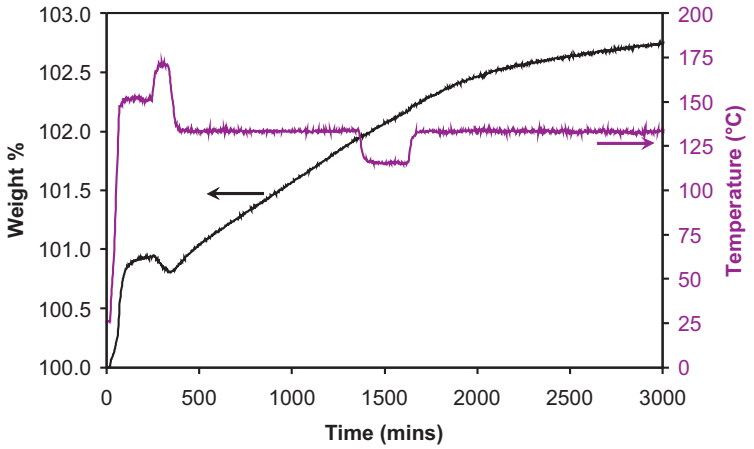

Figure 6.21: Subsequent absorption of decomposed $2Li_4BH_4(NH_2)_3 + 3MgH_2$ in an IGA at 18 bar H_2. The gravimetric trace is shown in black and the temperature trace is shown in purple.

reaction where the equilibrium temperature at 18 bar H_2 is around 160°C. An even lower hydrogenation temperature of 115°C was attempted. Although the sample mass continued to increase there was little affect on the observed rate of hydrogenation.

After a total hydrogenation time of 2 days, the sample has adsorbed a total of 2.8 wt% H_2. This is considerably less than the theoretical maximum of 5.2 wt%. The hydrogenation was not complete in the timescale of the experiment with the sample mass continuing to rise. Also ammonia release during the desorption step will have reduced the amount of nitrogen in the sample and therefore reduced the capacity of the system.

The sample was cooled to room temperature and the IGA was purged with Ar at 1 bar. A second desorption experiment was performed under flowing Ar gas at 1 bar and the results compared with those of the first desorption experiment in figure 6.22.

MS data was not available for the second desorption experiment. However, it is apparent that the initial mass loss which was attributed to ammonia release in the first desorption was much reduced in the second desorption. This is an indication that much less ammonia was released upon cycling. The initial low

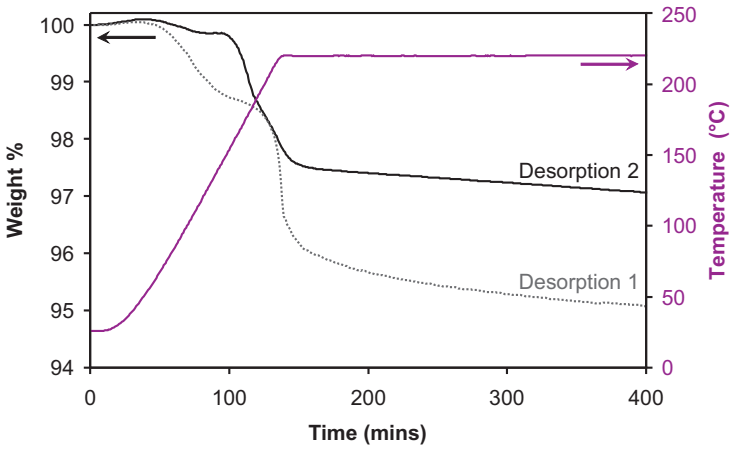

Figure 6.22: Initial and subsequent mass losses from $2Li_4BH_4(NH_2)_3 + 3MgH_2$ in an IGA. The mas loss upon first desorption is shown in grey and the subsequent desorption after absorption is shown in black. The temperature trace is shown in purple.

temperature mass loss for the second desorption was approximately 0.2 wt% compared to 1.3 wt% for ammonia release from the first desorption. On the second desorption a sharp mass loss was observed from 155°C which equates to 2.4 wt%, a similar amount to that absorbed. The mass loss was much sharper than for the first desorption. Although the mass continued to drop after this initial mass decrease, the subsequent mass loss appeared completely linear which is an indication that this may be due to an instrumental effect of the IGA rather than continuing dehydrogenation.

6.5.4 Summary

The addition of MgH_2 to $Li_4BH_4(NH_2)_3$ significantly changed the desorption profile giving rise to a two step hydrogen release; the first started at 190°C and the second at 290°C. The low temperature decomposition was identified as forming mixed Li-Mg imides, which do not form until much higher temperatures from $2LiNH_2 + MgH_2$. The decomposition was followed using *ex-situ* diffraction and a reaction scheme was suggested.

Hydrogenation of the products of the low temperature decomposition step

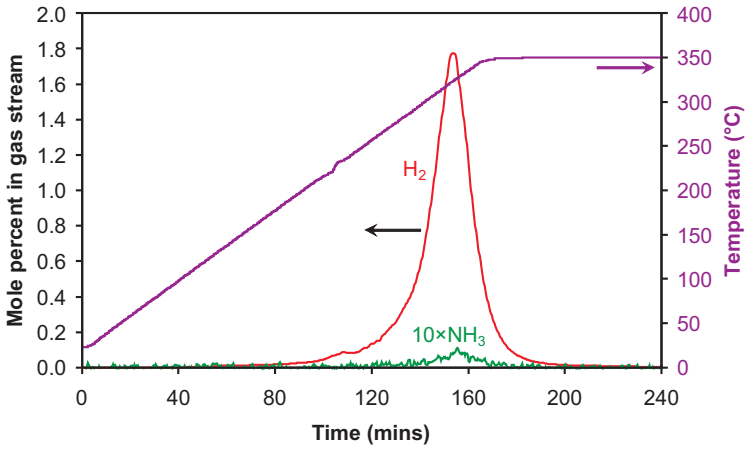

Figure 6.23: Thermal decomposition analysis of $2Li_4BH_4(NH_2)_3 + 3CaH_2$ in a TPD apparatus. The temperature trace is shown in purple and the mole percents of H_2 and NH_3 released are shown in red and green respectively.

resulted in the formation of $Mg(NH_2)_2$, indicating that the true reversible reaction can be represented by equation 6.12.

$$Li_2Mg(NH)_2 + 2H_2 \leftrightarrow Mg(NH_2)_2 + 2LiH \tag{6.12}$$

Although the role of $LiBH_4$ in the initial desorption appears to involve the promotion of the metathesis reaction, it is currently unclear from this study as to whether $LiBH_4$ has an effect on the cycling ability of the system.

6.6 $2Li_4BH_4(NH_2)_3 + 3CaH_2$

Thermal desorption data from $2Li_4BH_4(NH_2)_3 + 3CaH_2$ heated at a ramp rate of 2°C min^{-1} to 350°C are shown in figure 6.23. The gradual onset of hydrogen release was observed from 190°C with significant hydrogen release from 260°C which peaked at 325°C. At the peak of desorption, only 0.6% of the gas released was ammonia. Unusually, hydrogen release was essentially complete after around 20 minutes at 350°C.

PXRD of the reaction products after the TPD-MS experiment are shown in figure 6.24. The majority decomposition products were the $P2_1/c$ and $I4_1/amd$

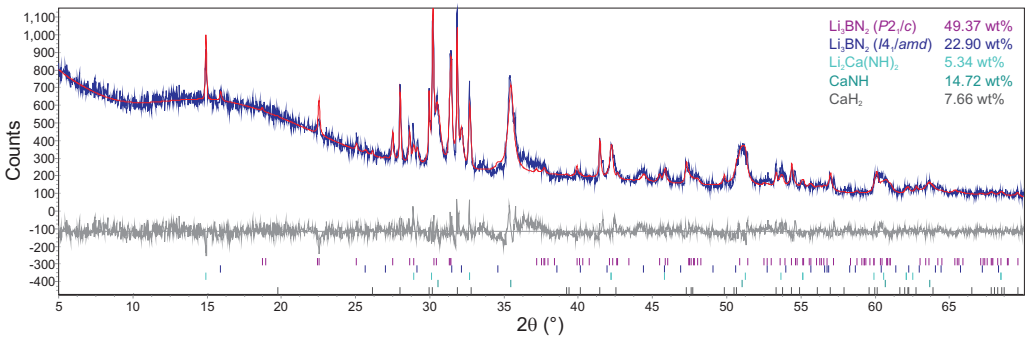

Figure 6.24: Powder XRD of $2Li_4BH_4(NH_2)_3 + 3CaH_2$ after heating to 350°C in a TPD-MS apparatus. Bragg peak positions due to Li_3BN_2 ($P2_1/c$) (purple), Li_3BN_2 ($I4_1/amd$) (dark blue), $Li_2Ca(NH)_2$ (light turquoise), CaNH (dark turquoise) and CaH_2 (grey) are indicated.

polymorphs of Li_3BN_2. Two calcium containing imides, CaNH [153] and $Li_2Ca(NH)_2$ [70], were also observed. Some CaH_2 also remained unreacted. The observed onset temperature of 190°C is consistent with the reported temperature of reaction of $LiNH_2$ with CaH_2 to form $Li_2Ca(NH)_2$ [70].

For CaNH to form, a nitrogen containing calcium phase, such as $Ca(NH_2)_2$, would be expected to be present as a precursor. It is reported that CaNH is formed from the reaction of $Ca(NH_2)_2$ with CaH_2 at temperatures of up to 350°C [154]. The presence of CaNH could indicate a metathesis of CaH_2 with $LiNH_2$ from the structure of $Li_4BH_4(NH_2)_3$ to produce $Ca(NH_2)_2$. However, although the relative intensities of the CaNH phase observed matched reasonably well, the observed lattice parameter was 1.6% smaller than in the literature structure and the Bragg peaks due to this phase were very broad. This suggests that, in a similar way to the magnesium containing system (6.5), this may be a disordered Li–Ca imide. As such, a CaNH–like Li–Ca imide phase could form from the direct reaction of CaH_2 with $LiNH_2$ from $Li_4BH_4(NH_2)_3$ without the need for a metathesis. Further experiments are required to confirm the nature of the CaNH–type phase.

The major decomposition pathway for $2Li_4BH_4(NH_2)_3 + 3CaH_2$ appears to be dominated by the usual decomposition reaction of $Li_4BH_4(NH_2)_3$ to form

Li_3BN_2. The $LiNH_2$ remaining from this decomposition may react with CaH_2 to form mixed Li–Ca imides in a similar way to that observed for $Li_4BH_4(NH_2)_3$ + 3LiH (section 6.3). The lower onset of hydrogen release compared with pure $Li_4BH_4(NH_2)_3$ suggests that the reaction of CaH_2 with $LiNH_2$ from $Li_4BH_4(NH_2)_3$ occurs slowly at a low temperature. However, on the timescale of the ramped TPD-MS experiment this reaction does not go to completion before the main Li_3BN_2 forming reaction can take over at higher temperatures. The overall idealised reaction scheme is shown in equation 6.13.

$$2Li_4BH_4(NH_2)_3 + 3CaH_2 \rightarrow 2Li_3BN_2 + Li_2Ca(NH)_2 + 2CaH_2 + 10H_2 \uparrow \quad (6.13)$$

6.7 Summary and Discussion

The effect of the addition of metal hydrides to $Li_4BH_4(NH_2)_3$ was investigated. In all cases the amount of ammonia released was reduced compared to pure $Li_4BH_4(NH_2)_3$. The amount of hydrogen release with temperature is summarised for all samples in figure 6.25. The addition of metal hydrides allowed for the reaction of $LiNH_2$ from $Li_4BH_4(NH_2)_3$ to react to form imides. Upon the addition of LiH, hydrogen release was observed at a lower temperature due to the reaction forming Li_2NH. Upon reaction of $Li_4BH_4(NH_2)_3$ with NaH a mixed Li–Na imide was not observed. Instead a metathesis reaction was suggested forming $NaNH_2$ and LiH; the LiH in turn reacted with remaining $LiNH_2$ from $Li_4BH_4(NH_2)_3$ to again give Li_2NH. The observed hydrogen release profile was very broad, which was attributed to the relatively slow rate of the metathesis reaction affecting hydrogen release.

Upon the addition of MgH_2 a different two step reaction was observed. A more detailed *ex-situ* powder diffraction study was used to elucidate the reaction mechanism, as summarised in equations 6.14 and 6.15.

$$2Li_4BH_4(NH_2)_3 + 3MgH_2 \rightarrow 3Mg(NH_2)_2 + 6LiH + 2LiBH_4 \quad (6.14)$$

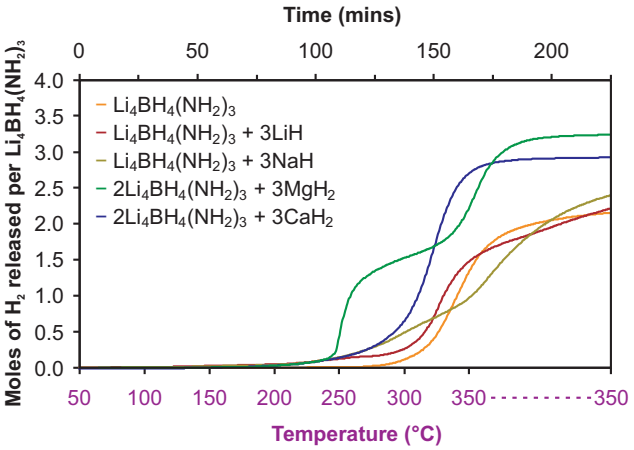

Figure 6.25: Comparison of hydrogen release from $Li_4BH_4(NH_2)_3$ mixed with metal hydrides in a TPD apparatus.

$$Mg(NH_2)_2 + 2LiH \leftrightarrow Li_2Mg(NH)_2 + 2H_2 \uparrow \tag{6.15}$$

The reversibility of this system was tested using an IGA and hydrogen was absorbed at 130°C at a pressure of 18 bar. A significant amount of ammonia release was observed on the first desorption which was reduced in the second desorption.

For the reaction $2Li_4BH_4(NH_2)_3 + 3CaH_2$ a mixed Li-Ca imide, $Li_2Ca(NH)_2$, formed. The majority decomposition products observed were still Li_3BN_2 from the dominant decomposition pathway of $Li_4BH_4(NH_2)_3$, with the mixed imide attributed to a reaction of CaH_2 with the remaining $LiNH_2$.

A recent study by Yang *et al.* [155] on the reaction composition $2LiNH_2 + LiBH_4 + MgH_2$ investigated this system in detail using *in-situ* diffraction. Broadly this study agreed with our findings reported here for the $2Li_4BH_4(NH_2)_3 + 3MgH_2$ system. One area in which Yang *et al.*'s interpretation of their results differed from our own was in the exact nature of the low temperature hydrogen release. Yang *et al.* observed a shoulder in the low temperature desorption step which they interpreted as two desorption steps; the main desorption was attributed to a direct reaction of $Li_4BH_4(NH_2)_3$ with MgH_2 to form $Li_2Mg(NH)_2$ and the higher temperature shoulder was attributed to $Mg(NH_2)_2$ and LiH from

a lower temperature metathesis reacting to form $Li_2Mg(NH)_2$. We did not observe a shoulder in the low temperature hydrogen release. We suggest that the reaction $2Li_4BH_4(NH_2)_3 + 3MgH_2$ proceeds *via* the metathesis reaction, which at temperatures above 155°C is rapidly followed by reaction of the $Mg(NH_2)_2$ and LiH formed to give $Li_2Mg(NH)_2$.

In the study by Yang *et al.* [155] they observed that 2.5 wt% hydrogen could be reversibly stored in this system with hydrogen release complete after 20 minutes at 160°C. Hydrogenation was performed at 160°C under a hydrogen pressure of 100 bar although no timescale for hydrogenation was reported. These findings are consistent with our reversibility data (section 6.5.3).

This report sparked a number of investigations into similar systems [156, 157, 158, 159]. It was confirmed that $2LiNH_2 + MgH_2$ completely transforms to $Mg(NH_2)_2 + 2LiH$ in the presence of $LiBH_4$ at 120°C and that as a result the hydrogen release properties of $2LiNH_2 + MgH_2 + LiBH_4$ was essentially the same as from $Mg(NH_2)_2 + 2LiH + LiBH_4$ [158]. The presence of a relatively small amount of $LiBH_4$ was also shown to have a favourable effect on the kinetics of both dehydrogenation and hydrogenation steps of the $Mg(NH_2)_2 + 2LiH$ [157]. The rate of hydrogen release was doubled at 140°C by the introduction of 3 mol% $LiBH_4$ while the release of ammonia was also suppressed. Essentially complete hydrogenation was possible within 12 hours at 100°C under a hydrogen pressure of 78 bar.

This $LiBH_4$ catalysed $Mg(NH_2)_2 + 2LiH$ system formed from $2Li_4BH_4(NH_2)_3 + 3MgH_2$ remains to date one of the most promising hydrogen storage systems providing a moderate reversible hydrogen capacity with relatively fast rates of (de)hydrogenation compared to most complex hydrides at relatively low temperatures. More work is needed to develop appropriate catalysts to further improve both the rate of hydrogenation and the amount of ammonia released during dehydrogenation.

Chapter 7

$Na_2BH_4NH_2$

7.1 Introduction

In a series of experiments, different mixtures of $NaBH_4$ and $NaNH_2$ over the entire composition range were heated and it was identified that a body centred cubic phase with a unit cell of around 4.7 Å was always present across the full compositional range. A new mixed amide–borohydride of sodium was identified and the thermal desorption properties of the $NaBH_4$ + $NaNH_2$ system have been investigated. The structure of this sodium amide–borohydride was investigated.

7.2 Crystal Structure Investigation

The crystal structure of $Na_2BH_4NH_2$ was investigated using powder diffraction data and the computer program Topas [90]. The structure was found to be heavily disordered and reasons for this are proposed based on the structures of the starting materials, $NaBH_4$ and $NaNH_2$.

7.2.1 Experimental

Sodium amide (Sigma-Aldrich, 95% purity) and sodium borohydride (Sigma-Aldrich, $\geq$ 98% purity) were ground together in a 1:1 ratio in an argon filled glove

box (>10 ppm O_2, >1 ppm H_2O) and heated under a mixture of H_2 and N_2 gas (1:9) at 1 bar and 190°C for 12 hours. A slight excess of amide was used in order to redress the difference in quoted purities of the starting reagents. The sample was reground and annealed at 190°C to drive the reaction to completion and improve the crystallinity of the sample. Powder synchrotron X-ray diffraction data were collected on the ID31 diffractometer at the ESRF, Grenoble, at a wavelength and stepsize of 0.80022 Å and 0.003°, respectively. The sample was loaded into a glass capillary inside a nitrogen filled glove bag and sealed on a miniature gas torch. Neutron powder diffraction data were collected on HRPD at the ISIS spallation neutron source at the Rutherford Appleton Laboratory. The sample was sealed inside a vanadium can with an iridium wire seal, inside an argon filled glove box. Synchrotron X-ray data were collected in the range 2° to 55° 2θ (d-spacing 22.9 to 0.87 Å) and the backscattering bank of the HRPD neutron data was used (d-spacing 2.49 to 0.73 Å). The resulting sample was predominantly $Na_2BH_4NH_2$ with a very small $NaNH_2$ impurity.

7.2.2 Indexing and Space Group Selection

The regular spacing of observed Bragg reflections suggested a cubic lattice. A trial-and-error method utilising ChekCell [95] to provide a graphical indication of fit gave a lattice parameter of ∼4.7 Å. Investigation of the systematic absences of the diffraction pattern indicated that the phase has primitive symmetry with $P23$, $Pm\bar{3}$, $P432$, $P\bar{4}3m$ and $Pm\bar{3}m$ as the most probable space groups. The lattice constant and unit cell volume were refined in a Pawley fit of the synchrotron X-ray diffraction data using Topas [90] (figure 7.1) to be 4.6970(7) Å and 103.62(5) Å^3, respectively. Consideration of the volumes of a single formula unit of $NaBH_4$ (V = 58.54 Å^3) and $NaNH_2$ (V = 47.29 Å^3), from diffraction data collected in this experiment, led to an assignment of two anion-cation pairs in the unit cell of 103.62(5) Å^3, i.e. a single $Na_2BH_4NH_2$ unit in the unit cell.

By looking at the Wyckoff positions available in each of the possible space

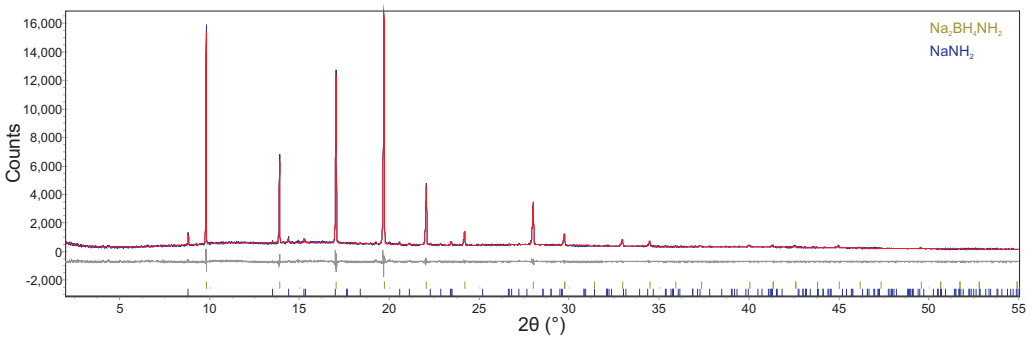

Figure 7.1: Powder synchrotron X-ray diffraction pattern of the products of the reaction $NaBH_4$ + $NaNH_2$. Bragg reflection positions for $Na_2BH_4NH_2$ and $NaNH_2$ are shown in dark yellow and blue, respectively.

Table 7.1: Special positions available in each possible space group.

$P23$	$Pm\bar{3}$	$P432$	$P\bar{4}3$	$Pm\bar{3}m$
No. 195	No. 200	No. 207	No. 215	No. 221
$12j$ (x, y, z)	$24l$ (x, y, z)	$24k$ (x, y, z)	$12j$ (x, y, z)	$48n$ (x, y, z)
$6i$ $(x, 1/2, 1/2)$	$12k$ $(1/2, y, z)$	$12j$ $(1/2, y, y)$	$12i$ (x, x, z)	$24m$ (x, x, z)
$6h$ $(x, 1/2, 0)$	$12j$ $(0, y, z)$	$12i$ $(0, y, y)$	$12h$ $(x, 1/2, 0)$	$24l$ $(1/2, y, z)$
$6g$ $(x, 0, 1/2)$	$8i$ (x, x, x)	$12h$ $(x, 1/2, 0)$	$6g$ $(x, 1/2, 1/2)$	$24k$ $(0, y, z)$
$6f$ $(x, 0, 0)$	$6h$ $(x, 1/2, 1/2)$	$8g$ (x, x, x)	$6f$ $(x, 0, 0)$	$12j$ $(1/2, y, y)$
$4e$ (x, x, x)	$6g$ $(x, 1/2, 0)$	$6f$ $(x, 1/2, 1/2)$	$4e$ (x, x, x)	$12i$ $(0, y, y)$
$3d$ $(1/2, 0, 0)$	$6f$ $(x, 0, 1/2)$	$6e$ $(x, 0, 0)$	$3d$ $(1/2, 0, 0)$	$12h$ $(x, 1/2, 0)$
$3c$ $(0, 1/2, 1/2)$	$6e$ $(x, 0, 0)$	$3d$ $(1/2, 0, 0)$	$3c$ $(0, 1/2, 1/2)$	$8g$ (x, x, x)
$1b$ $(1/2, 1/2, 1/2)$	$3d$ $(1/2, 0, 0)$	$3c$ $(0, 1/2, 1/2)$	$1b$ $(1/2, 1/2, 1/2)$	$6f$ $(x, 1/2, 1/2)$
$1a$ $(0, 0, 0)$	$3c$ $(0, 1/2, 1/2)$	$1b$ $(1/2, 1/2, 1/2)$	$1a$ $(0, 0, 0)$	$6e$ $(x, 0, 0)$
	$1b$ $(1/2, 1/2, 1/2)$	$1a$ $(0, 0, 0)$		$3d$ $(1/2, 0, 0)$
	$1a$ $(0, 0, 0)$			$3c$ $(0, 1/2, 1/2)$
				$1b$ $(1/2, 1/2, 1/2)$
				$1a$ $(0, 0, 0)$

groups (table 7.1) it quickly became clear that a single $Na_2BH_4NH_2$ unit could not easily be accommodated in this unit cell without significant disorder. Each of the available space groups have only two single multiplicity sites, which may each, for example, be occupied by an anion. However, there are then no sites of low enough multiplicity for the two sodium ions to occupy without disorder. Because of this necessary disorder it was decided to investigate the crystal structure in the highest symmetry space group, $Pm\bar{3}m$.

7.2.3 Producing a Model

As with $Li_4BH_4(NH_2)_3$, infrared spectroscopy was performed in order to determine whether the BH_4^- and NH_2^- groups remained intact from the starting materials. The infra-red spectrum of the amide–borohydride phase, analysed in more detail in section 7.4, showed the characteristic BH_4^- and NH_2^- stretches centred around 2300 cm^{-1} and 3200 cm^{-1}, respectively, confirming that these groups remained intact. This lead to our assignment of this phase as a sodium amide–borohydride, $Na_2BH_4NH_2$.

The structures of the starting materials, $NaBH_4$ [160] and $NaNH_2$ [134] (figures 7.2 and 7.3, respectively), were investigated as possible starting points for structural determination. Unlike for the lithium amide–borohydride system, where both $LiNH_2$ and $LiBH_4$ contain 4 coordinate lithium, $NaNH_2$ contains 4 coordinate sodium and $NaBH_4$ contains 6 coordinate sodium. $NaBH_4$ has a sodium chloride-type structure with the BH_4^- at a site of octahedral symmetry [137] whereas in $NaNH_2$ amide ions adopt a near ideal tetrahedral arrangement around the sodium ion, although the tetrahedron formed by sodium ions around the amide ion is highly distorted due to the bent shape of the NH_2^- ion [161]. The local structures around the anion in $NaBH_4$ and $NaNH_2$ are shown in figure 7.4 and selected inter atomic distances and angles are shown in table 7.2.

Attempting to accommodate these observed atomic arrangements of the starting materials in a primitive cubic unit cell with a lattice parameter of $\sim$4.7 Å is

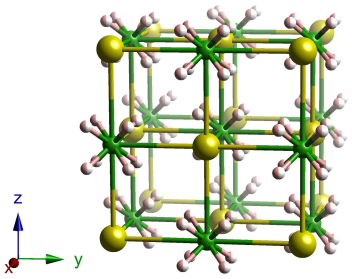

Figure 7.2: Crystal structure of $NaBH_4$. Boron is shown in green, sodium in yellow and half occupied hydrogen sites in grey/pink.

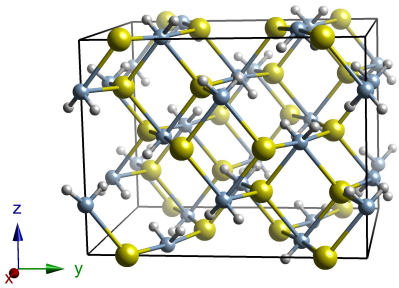

Figure 7.3: Crystal structure of $NaNH_2$. Nitrogen is shown in blue, sodium in yellow and hydrogen in grey. The unit cell is shown in black.

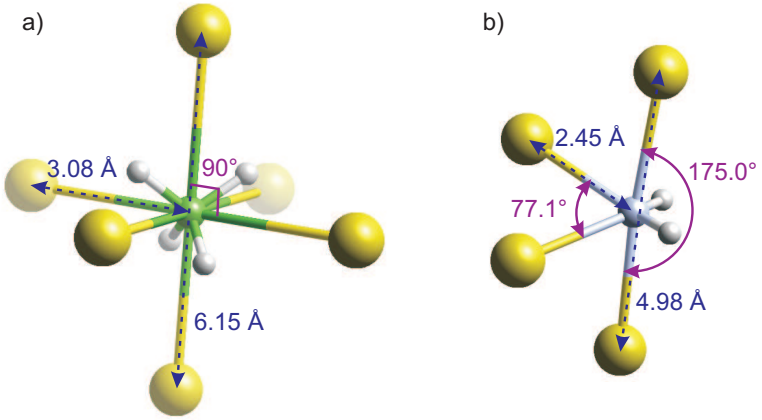

Figure 7.4: Local structures around the anion of (a) $NaBH_4$ and (b) $NaNH_2$. Boron is shown in green, nitrogen in blue, sodium in yellow and hydrogen in grey.

Table 7.2: Selected inter atomic distances (Å) and angles (°) for $NaBD_4$ and $NaND_2$.

Bond	$NaBD_4$	$NaND_2$
(B/N)-D	4×1.168(4)	2×0.94(2)
H-(B/N)-D	6×109.5(2)	95.4(6)
Na-(B/N)	6×3.069(4)	2×2.437(2)
	-	2×2.494(2)
Na-Na	12×4.340(4)	3.036(3)
	-	2×3.0406(14)
	-	4×3.987(2)
	-	2×4.588(2)
Na-(B/N)-Na	12×90.0	2×76.14(6)
	-	77.07(7)
	-	2×77.07(7)
	-	175.00(11)
(B/N)-Na-(B/N)	12×90.0	102.93(8)
	-	2×103.86(6)
	-	2×107.93(6)
	-	127.86(7)
Reference	[160]	[134]
Volume per cation ($Å^3$)	57.78(11)	47.14(5)

impossible. However, the structures of the starting materials may be indicative of the local ordering of the disordered $Na_2BH_4NH_2$ structure.

A wider search for related structures that may provide a model for structural refinement resulted in one report of a sodium amide-bromide, $Na_4Br(NH_2)_3$ [162]. The ionic radius of the Br^- ion (1.96 Å [117]) is similar to that of the BH_4^- ion (2.03 Å [137]) and so it is possible that the structure of $Na_4Br(NH_2)_3$ would share structural characteristics with $Na_2BH_4NH_2$. The crystal structure of $Na_4Br(NH_2)_3$ is shown in figure 7.5 and selected inter atomic distances are given in table 7.3.

It can be seen how the structure of the cubic $Na_2BH_4NH_2$ could be related to the local structure around the Br^- ion in $Na_4Br(NH_2)_3$ (figure 7.6). Indeed, the average lattice parameter of this pseudo cube is 4.59 Å, only slightly below that of $Na_2BH_4NH_2$ (4.70 Å) which contains the slightly larger BH_4^- ion.

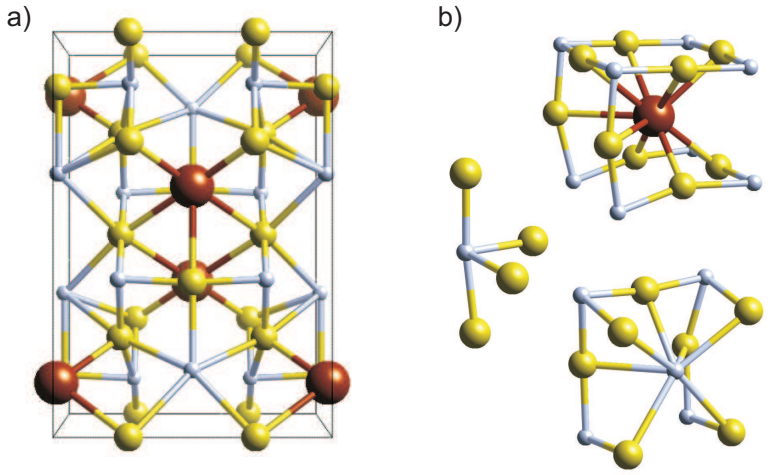

Figure 7.5: (a) Crystal structure of $Na_4Br(NH_2)_3$ and (b) local environment around Br and N atoms. Nitrogen is shown in blue, sodium in yellow and bromine in brown. The unit cell is shown in black. Hydrogen positions were not determined.

Table 7.3: Selected inter atomic distances for $Na_4Br(NH_2)_3$ [162].

Atom 1	Atom 2	Distance (Å)	Atom 1	Atom 2	Distance (Å)
Br	Na(1)	2×3.176(13)	Na(1)	Br	2×3.176(13)
	Na(2)	3.203(14)		N(1)	2×3.07(2)
		3.213(13)		N(2)	2×2.407(13)
		3.377(14)	Na(2)	Br	3.203(14)
	Na(3)	2.407(13)			3.213(13)
		2×3.555(10)			3.377(14)
N(1)	Na(1)	2×3.07(2)		N(1)	2.82(2)
	Na(2)	2.82(2)		N(2)	2×2.38(2)
	Na(3)	2×3.002(13)	Na(3)	Br	2.796(10)
		2×3.005(12)			3.555(10)
N(2)	Na(1)	2.407(13)		N(1)	3.002(13)
	Na(2)	2.38(2)			3.005(12)
	Na(3)	2.40(2)		N(2)	2.40(2)
		2.47(2)			2.47(2)

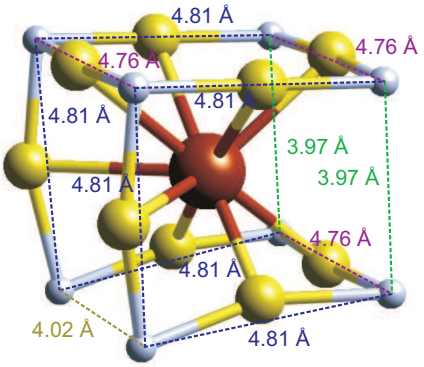

Figure 7.6: Pseudo cubic arrangement around the Br ion in $Na_4Br(NH_2)_3$. Nitrogen is shown in blue, sodium in yellow and bromine in brown.

Consideration was now given to how best to incorporate this disordered cubic structural model in $Pm\bar{3}m$ symmetry in the cubic unit cell. An obvious choice is to place the B of the borohydride ion on the $1b$ ($1/2$,$1/2$,$1/2$) position, in a similar position to the pseudo cubic environment of Br^- in $Na_4Br(NH_2)_3$. The N of the amide ion was then placed on a $1a$ (0,0,0) site, although the true local position of this atom will vary depending on the orientation of the anisotropic NH_2^- ion. For the modelling of the position of the Na ions, two options present themselves. The first is for an Na atom located on the $3b$ ($1/2$,0,0) position at an occupancy of $2/3$ with an anisotropic thermal parameter used to indicate the disordered position around the axis. The second is for occupation of the $12j$ ($1/2$,y,y) site, where a real displacement from the axis is refined, but with the consequence of a much larger multiplicity of the Na site, which therefore will involve the refinement of the atomic position of an Na site with an occupancy of $1/6$. It was decided to test both possible options during Rietveld refinement.

The refinement of meaningful atomic positions for hydrogen also presents a challenge. Hydrogen cannot simply be disregarded, as is frequently the case for structure solution of hydrogen containing materials, because it contributes a significant proportion of the total scattering of the unit cell contents. However, the hydrogen arrangements will certainly be disordered, and so refinement of

Table 7.4: Construction of the hydrogen sphere around boron in the structural model.

Atom	Site	Equation	Starting occupancy
-	-	$\delta = r_{BH}/a$	-
H(1)	$6f$ (x,1/2,1/2)	$x = 1/2 + \delta$	4/26
H(2)	$12j$ (1/2,y,y)	$y = 1/2 + \delta/\sqrt{2}$	4/26
H(3)	$8g$ (x,x,x)	$x = 1/2 + \delta/\sqrt{3}$	4/26

r_{BH} = refinable B-H bond length. a = lattice parameter.

specific positions, such as a tetrahedron for BH_4^-, may be misleading. Instead it was decided to model the hydrogen as a sphere around the B/N position with a refineable radius which represents the bond length. For the B position, this was done by occupation of $6f$ (x,1/2,1/2), $8g$ (x,x,x) and $12j$ (1/2,y,y) sites where the refineable fractional atomic coordinates were related back to a refinable bond length, as shown in table 7.4.

The same approach was taken for hydrogen of the amide anion with the sphere centred around (0,0,0) by placing hydrogen on $6e$ (x,0,0), $12i$ (0,y,y) and $8g$ (x,x,x) sites, where starting occupancies for the sites was 2/26. The total occupancy of BH_4^- and NH_2^- hydrogen sites were fixed at 4 and 2, respectively, while the relative occupation of each site was refined.

In order to test whether alternative atomic arrangements may better match the observed powder diffraction data a 'simulated annealing' structure solution was performed using the computer program Topas [90] jointly on the neutron and synchrotron X-ray diffraction data. Two Na atoms and rigid bodies for BH_4 and NH_2 were allowed to move and rotate freely within the unit cell with no symmetry constraints (space group $P1$) and 'anti-bump' penalties introduced for short Na-B and Na-N distances (2.0 Å). Typical results of this refinement resulted in the BH_4 ion at approximately (+1/2,+1/2,+1/2) relative to the NH_2 ion and the Na atoms spread throughout the remaining space in the cell. This was reasonably consistent with the previously suggested disordered $Pm\bar{3}m$ model, and so this

model was used for Rietveld refinement.

7.2.4 Rietveld Refinement

Because of the relatively sparse diffraction data available because of the highly symmetrical unit cell of $Na_2BH_4NH_2$, Rietveld refinement was performed simultaneously on both the powder synchrotron X-ray and neutron diffraction data from the start using Topas [90].

The model where Na sites on a $3b$ ($1/2$,0,0) site with an occupancy of $2/3$ was considered first. Initially thermal parameters were not included and the H site occupancies were fixed at their starting values for both anions while the B–H and N–H bond length was refined. This resulted in a very poor fit to the observed diffraction data. Anisotropic thermal displacement parameters were introduced for the Na atoms where atomic motion along the unit cell edges was allowed to refine separately to motion perpendicular to the edges. This allows for disorder of the Na either along the unit cell edge or perpendicular to the edge. Refinement showed that motion perpendicular to the cell edge was favoured, but fits were poor. This was attributed to only the displacement of Na being taken into account, whereas other atoms almost certainly also have significant displacement from their ideal positions. Simultaneous refinement of displacement parameters for B and N resulted in negative values for B and very large values for N. It was decided that modelling the disordered position of Na with displacement parameters was underestimating the total scattering by Na, and as such was resulting in a meaningless refinement.

Instead, the model where Na occupies the $12j$ ($1/2$,y,y) site was preferred. Initially thermal parameters were not considered. The Na position was refined from a starting value of ($1/2$,0.1,y) and the H site occupancies were fixed at their starting values for both anions while the B–H and N–H bond lengths of the hydrogen spheres were refined. This resulted in an improved fit compared with the previous model which included anisotropic displacement parameters for

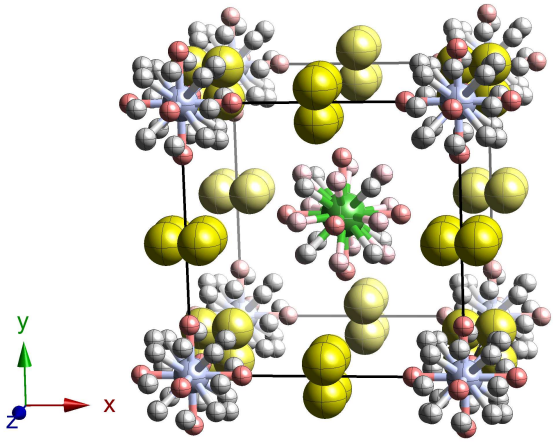

Figure 7.7: Refined crystal structure of $Na_2BH_4NH_2$. Boron is shown in green, nitrogen in blue and sodium in yellow. Preferentially occupied hydrogen sites are shown in pink and unoccupied sites are shown in white. Atoms are represented as thermal ellipsoids of 50% probability.

sodium. The relative occupation of each of the hydrogen sites was now added to the refinement. This resulted in an improvement in fit, with occupation of the $6f$ (x,1/2,1/2) and $6e$ (x,0,0) sites favoured for the BH_4^- and NH_2^- ions, respectively. Thermal displacement parameters (B_{iso}) were introduced to the refinement for B, N, Na and H and refined from starting values of 1 Å^2. The thermal parameters for each type of hydrogen (H(B) and H(N)) were constrained at the same value. Refinement resulted in very large thermal parameter values for hydrogen and negative values for the other atoms. These large thermal parameters for hydrogen equate to large overlap of the thermal ellipsoids of neighbouring hydrogens in the hydrogen sphere. It was decided to fix the hydrogen displacement parameters at a value of 1 Å^2 (no significant overlap with neighbouring hydrogens) while allowing the other thermal parameters, the Na position and the B-H and N-H bond lengths to refine. The resultant crystal structure and Rietveld plots for the X-ray and neutron data are shown in figures 7.7, 7.8 and 7.9, respectively, and the refined crystallographic data is shown in table 7.5.

Table 7.6 shows selected bond distances from the crystal structure refinement

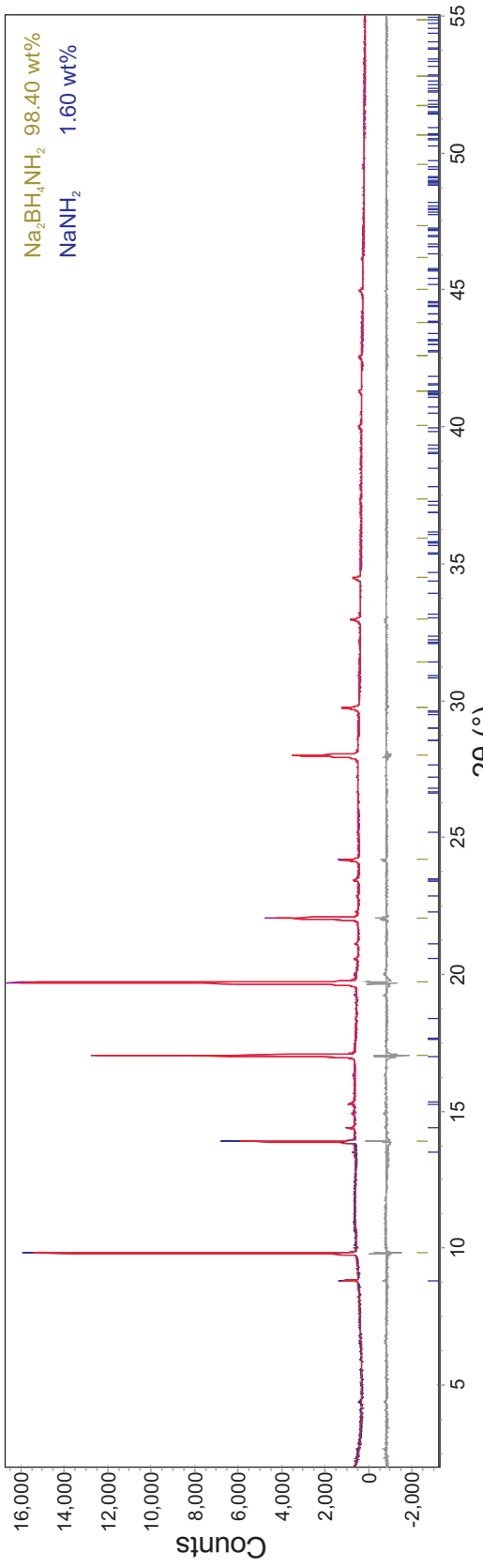

Figure 7.8: Final Rietveld plot for X-ray diffraction data of $Na_2BH_4NH_2$ showing observed (purple), calculated (red) and difference (grey) plots. Peak positions for $Na_2BH_4NH_2$ (dark yellow) and $NaNH_2$ (blue) are indicated.

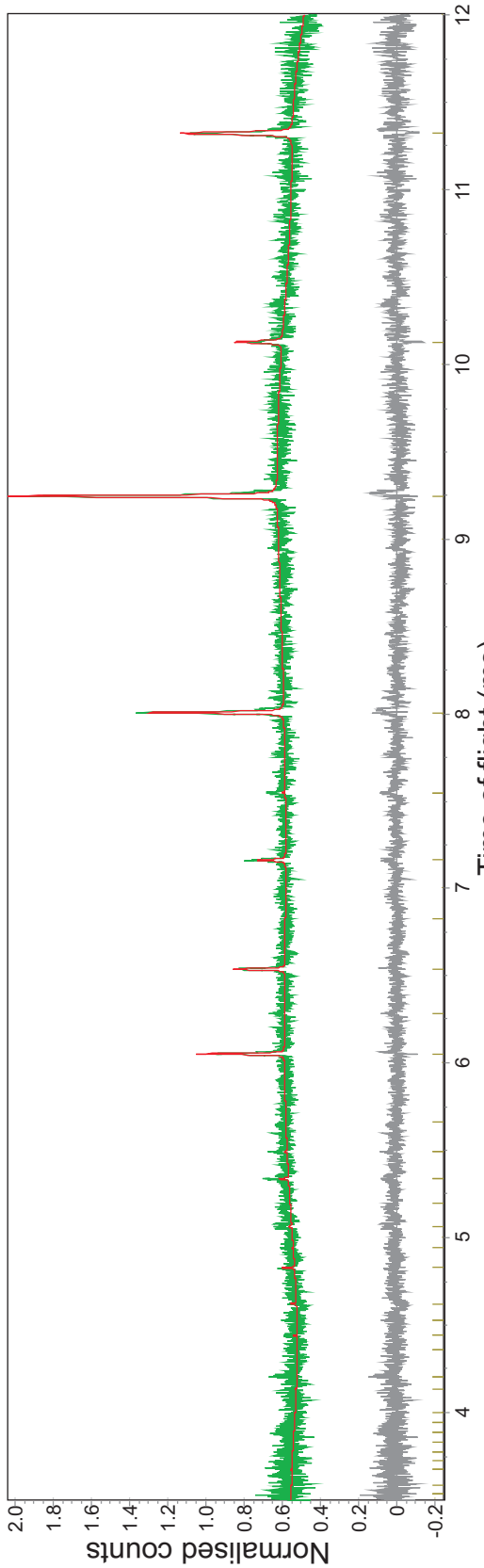

Figure 7.9: Final Rietveld plot for neutron diffraction data of $Na_2BH_4NH_2$ showing observed (green), calculated (red) and difference (grey) plots. Peak positions for $Na_2BH_4NH_2$ (dark yellow) are indicated.

Table 7.5: Refined crystallographic data for $Na_2BH_4NH_2$.

Atom	Site	x/a	y/a	z/a	Occupancy	B_{iso}/Å
B	$1b$	1/2	1/2	1/2	1	5.27(8)
H1	$6f$	0.7158(13)	1/2	1/2	0.51(5)	1
H2	$12j$	1/2	0.6526(9)	y	0.08(4)	1
H3	$8g$	0.6246(7)	x	x	0.00(5)	1
N	$1a$	0	0	0	1	3.15(5)
H4	$6e$	0.187(3)	0	0	0.33(9)	1
H5	$12i$	0	0.133(2)	y	0.00(9)	1
H6	$8g$	0.108(2)	x	x	0.00(10)	1
Na	$12j$	1/2	0.9392(3)	y	1/6	4.57(5)

Space group $Pm\bar{3}m$, $a = 4.6970(7)$ Å.
$r_{\mathrm{BH}} = 1.014(6)$, $r_{\mathrm{NH}} = 0.880(14)$.
X-ray data: $R_{\mathrm{wp}} = 6.472$, $R_{\mathrm{exp}} = 7.087$, $\chi^2 = 0.91$.
Neutron data: $R_{\mathrm{wp}} = 5.307$, $R_{\mathrm{exp}} = 171.787$, $\chi^2 = 0.031$.

of $Na_2BH_4NH_2$ together with selected distances for related structures. It can be seen that, broadly speaking, the refined bond distances are consistent with observed distances in the related structures. Although there are clearly limitations to this description of $Na_2BH_4NH_2$ we believe it to be a good representation of a highly disordered structure.

7.3 Powder Diffraction Study

When investigating the sodium amide–borohydride system, reactions were performed at a range of stoichiometries between pure $NaBH_4$ to pure $NaNH_2$. Unlike for the lithium system where a variety of phases formed, the cubic $Na_2BH_4NH_2$ phase was the only new phase present. There was, however, a lot of subtle variation in with the conclusion that there might be a solid solution range of the form $Na_2(BH_4)_{(1-x)}(NH_2)_{(1+x)}$.

Table 7.6: Selected refined inter atomic distances (Å) for $Na_2BH_4NH_2$ together with literature data for $NaBD_4$, $NaND_2$ and $Na_4Br(NH_2)_3$.

Bond	$Na_2BH_4NH_2$	$NaBD_4$	$NaND_2$	$Na_4Br(NH_2)_3$
B-H	1.0136(2)	1.168(4)	-	-
N-H	0.88(2)	-	0.94(2)	-
(B/Br)-Na	2.917(10)	3.069(4)	-	2.407(13)
	3.346(11)	-	-	3.176(13)
	3.725(10)	-	-	3.203(14)
	-	-	-	3.213(13)
	-	-	-	3.377(14)
	-	-	-	3.555(10)
N-Na	2.383(2)	-	2.437(2)	2.38(2)
	-	-	2.494(2)	2.40(2)
	-	-	-	2.82(2)
	-	-	-	3.005(12)
Na-Na	2.917(14)	4.340(4)	3.036(3)	3.054(13)
	3.769(14)	-	3.0406(14)	3.340(10)
	4.13(2)	-	3.987(2)	3.357(13)
	-	-	4.588(2)	3.49(2)
	-	-	-	4.002(12)
Reference	-	[160]	[134]	[162]

7.3.1 Experimental

Samples of ground mixtures of $NaBH_4$ (Sigma-Aldrich, $\leq$98% purity) and $NaNH_2$ (Sigma-Aldrich, 95% purity) were prepared in an argon filled glove box (>10 ppm O_2, >1 ppm H_2O) in stoichiometries of $n\mathrm{NaNH_2} + (1-n)\mathrm{NaBH_4}$ (where $n = 0, 0.08\dot{3}, 0.16\dot{6}, 0.25, 0.33\dot{3}, 0.41\dot{6}, 0.5, 0.58\dot{3}, 0.66\dot{6}, 0.75, 0.83\dot{3}, 0.91\dot{6}$ and 1). Each sample was evacuated and sealed inside a quartz tube which was heated at 180°C for 12 hours and then annealed at 90°C for 12 hours.

Powder synchrotron X-ray diffraction data were collected on the ID31 diffractometer at the ESRF, Grenoble, at a wavelength and stepsize of 0.80157 Å and 0.003°, respectively. The samples were loaded into a glass capillary inside a nitrogen filled glove bag and sealed on a miniature gas torch. Differential scanning calorimetry (DSC) and temperature programed desorption coupled to a mass spectrometer (TPD-MS) and thermogravimetric analysis were performed on se-

lected samples and starting mixtures.

7.3.2 Refinement Strategy

Powder diffraction data were analysed using Topas [90]. For each data set a zero point error and an 18 parameter Chebyshev background function were refined. For each phase present, lattice parameters, a pseudo-Voigt peak shape function with 6 parameters and scale factor were refined. In some of the more amide rich samples, the peak shape of Bragg peaks due to $Na_2BH_4NH_2$ were highly asymmetric, so an asymmetric convolution with 4 parameters was added to the normal peak shape. Atomic coordinates and thermal parameters were taken from reported structures for $NaBH_4$ [160] and $NaNH_2$ [134] and the crystal structure determined in section 7.2 was used for $Na_2BH_4NH_2$. The weight percent reported by Topas for each compound present, together with the estimated standard error, were converted into mole percent values. The molar mass of $Na(BH_4)_{0.5}(NH_2)_{0.5}$ was used for $Na_2BH_4NH_2$ to make the mole percent values directly comparable to that of the starting materials.

7.3.3 Results

Figure 7.10 shows a summary of the phase fractions obtained from the refinements at each composition for the samples. It can be seen that this $Na_2BH_4NH_2$ was present at every mixed composition, although, unlike in the case of $Li_4BH_4(NH_2)_3$, this new phase was not pure at any composition, instead existing alongside the starting materials. This is an indication that either further annealing is required to produce a pure phase or that the phase is metastable with respect to decomposition back to the starting materials.

If $Na_2BH_4NH_2$ was present as a line phase we would expect a linear decrease in the amount of $NaBH_4$ and $NaNH_2$ observed concurrent with a linear increase in the amount of $Na_2BH_4NH_2$ observed. Although this is broadly true for the borohydride rich compositions, for the amide rich compositions there was less

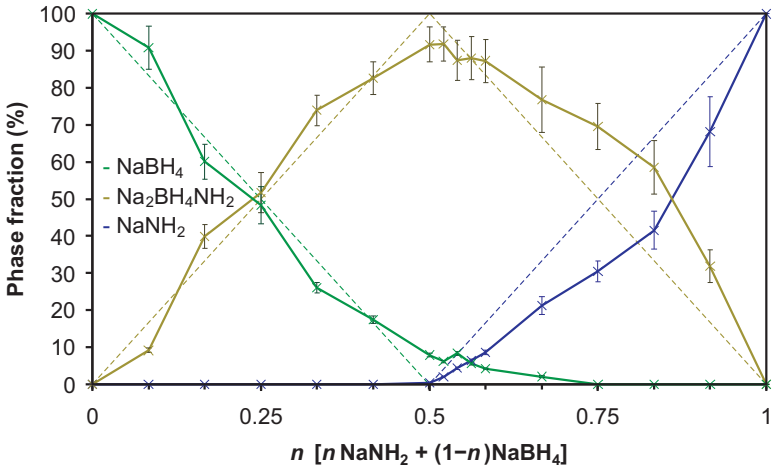

Figure 7.10: Phase fractions present after heating $NaBH_4$ and $NaNH_2$ in various ratios.

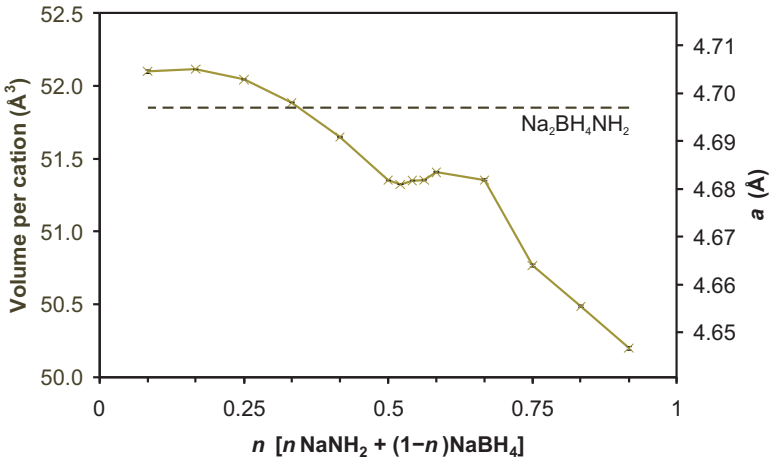

Figure 7.11: Unit cell volume per cation and lattice parameter of $Na_2(BH_4)_{(1-x)}(NH_2)_{(1+x)}$ present after heating $NaBH_4$ and $NaNH_2$ in different ratios.

$NaNH_2$ observed than expected. This suggests that $Na_2BH_4NH_2$ can support over-stoichiometry with respect to amide of the form $Na_2(BH_4)_{(1-x)}(NH_2)_{(1+x)}$.

The lattice parameter and unit cell volume per cation of $Na_2BH_4NH_2$ varies greatly with composition, as shown in figure 7.11. At borohydride rich compositions the unit cell volume of $Na_2BH_4NH_2$ is larger than at amide rich compositions, indicating a greater proportion of the larger borohydride anion. The largest observed lattice parameter was 4.70608(4) Å, 0.19% larger than the refined lattice

parameter observed during the crystal structure solution of $Na_2BH_4NH_2$. It is highly unlikely that the crystal structure of $Na_2BH_4NH_2$ can accommodate more of the larger BH_4^- ion within the structure as this would necessitate short Na-B distances. It is therefore suggested that 4.70608(4) Å represents the true lattice parameter of stoichiometric $Na_2BH_4NH_2$ and that the sample used for structure solution may have had partial substitution of the form $Na_2(BH_4)_{(1-x)}(NH_2)_{(1+x)}$.

The smallest observed lattice parameter at the most amide rich composition was 4.64770(12) Å, 1.24% smaller than the largest observed sodium amide–borohydride phase. A rough estimation of the composition of the observed $Na_2(BH_4)_{(1-x)}(NH_2)_{(1+x)}$ phases can be made using Vegard's law [138], as shown in figure 7.12. The unit cell volume value for the largest observed $Na_2BH_4NH_2$ phase was taken as the true 1:1 stoichiometric phase ($n = 0.5$ in figure 7.12). Unlike for $Li_4BH_4(NH_2)_3$ where Vegard's law correct predicts the unit cell volume from the volumes of the starting materials, $Na_2BH_4NH_2$ sits below the line joining the starting materials $NaNH_2$ and $NaBH_4$, which is an indication that Vegard's law is not obeyed. This is most probably because of the very different coordination environments in the different structures. The region of figure 7.12 where $0 \leq n \leq 0.5$ was used to estimate the composition of the observed $Na_2(BH_4)_{(1-x)}(NH_2)_{(1+x)}$ phases. For the sample used in structure solution, this returns a value for x of 0.063, a relatively small substitution. For the smallest observed cubic phase this returns a value of only 30.1 % borohydride, i.e. $x = 0.40$. This is a strong indication that the $Na_2BH_4NH_2$ structure can accommodate very large substitution of the borohydride ion by the smaller amide ion. This is perhaps not surprising as the only other known related structure, $Na_4Br(NH_2)_3$, is predominantly amide.

Figure 7.13 shows the unit cell volume per cation for $NaBH_4$ and $NaNH_2$. There is little evidence for significant anion substiution into the structures of $NaBH_4$ or $NaNH_2$. Although there is a slight increase in unit cell volume for $NaNH_2$ in the more borohydride rich compositions which may suggest partial

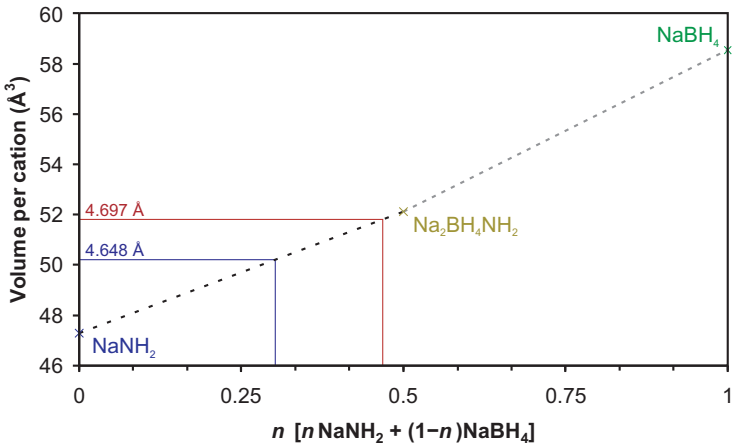

Figure 7.12: Unit cell volume per cation for $NaNH_2$, $Na_2BH_4NH_2$ and $NaBH_4$. The unit cell volume per cation values for the sample of $Na_2BH_4NH_2$ used for structure solution and the smallest observed $Na_2BH_4NH_2$-type phase are shown in red and blue, respectively.

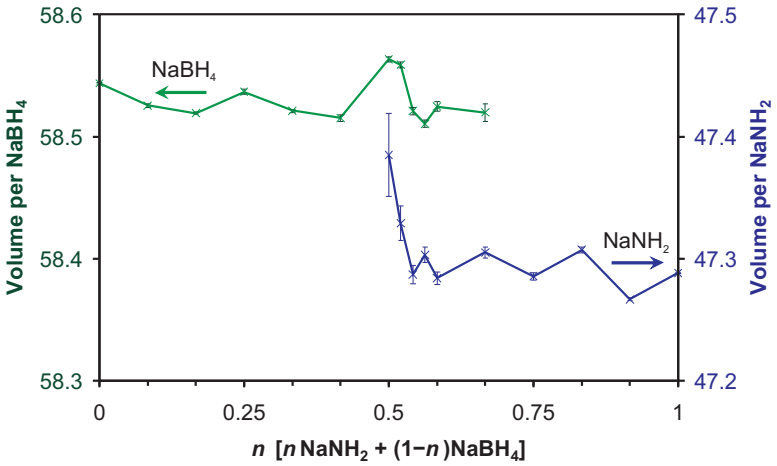

Figure 7.13: Unit cell volume per cation of $NaBH_4$ (green) and $NaNH_2$ (blue) present after heating $NaBH_4$ and $NaNH_2$ in different ratios.

substitution by the larger borohydride ion, this was when very small amounts of $NaNH_2$ were present (figure 7.10) and so errors associated with calculating unit cell volumes were larger leading to uncertainty in this conclusion.

Looking in more detail at the amide rich side of the data, from $n = 0.91\dot{6} \rightarrow 0.83\dot{3}$, there is a small Bragg peak at 6.58° 2θ (d-spacing 6.97 Å) which was unaccounted for by $NaNH_2$ or the cubic $Na_2(BH_4)_{(1-x)}(NH_2)_{(1+x)}$. This opens up the possibility of a lowering of the cubic symmetry. For $NaBH_4$ there is a

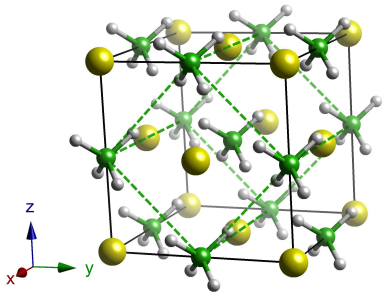

Figure 7.14: Crystal structure of $NaBH_4$ showing the unit cell of the low temperature modification. Boron is shown in green, sodium in yellow and hydrogen in grey. The room temperature unit cell is shown in black and the low temperature unit cell is shown in green.

known phase transition upon cooling below −83°C (190 K) from cubic ($a = 6.16$) to tetragonal ($a = 4.35$ Å, $c = 5.91$ Å), which corresponds to an ordering of the BH_4^- units [137], as shown in figure 7.14. The possibility of a similar ordering to form a tetragonal unit cell with a equal to the cubic unit cell lattice parameter (4.65 Å) and c equal to the d-spacing of this new unassigned peak (6.97 Å) was investigated. For a similar modification to the $NaBH_4$ structure, we would expect the new c lattice parameter to be related to the a lattice parameter by a factor of $\sqrt{2}$, which gives a new c lattice parameter of 6.58 Å, 5.9% smaller than the observed d-spacing of the unassigned peak. Although the use of this tetragonal unit cell with a equal to 6.97 Å resulted in a fit to the unassigned peak as well a second very small peak at 13.16° 2θ (d-spacing 3.49 Å), the major Bragg reflection due to the (111) of the cubic unit cell could not be fit with this unit cell. We can hypothesise that this extra Bragg reflection may be due to some local tetragonal ordering, but that overall the phase remains cubic.

Moving towards more borohydride rich compositions from $n = 0.75 \rightarrow 0.5$ the Bragg reflections due to the $Na_2(BH_4)_{(1-x)}(NH_2)_{(1+x)}$ phase had shoulders due to a second, very similar cubic phase. Although the lattice parameters presented in figure 7.11 represent the majority phase present, a more accurate analysis can

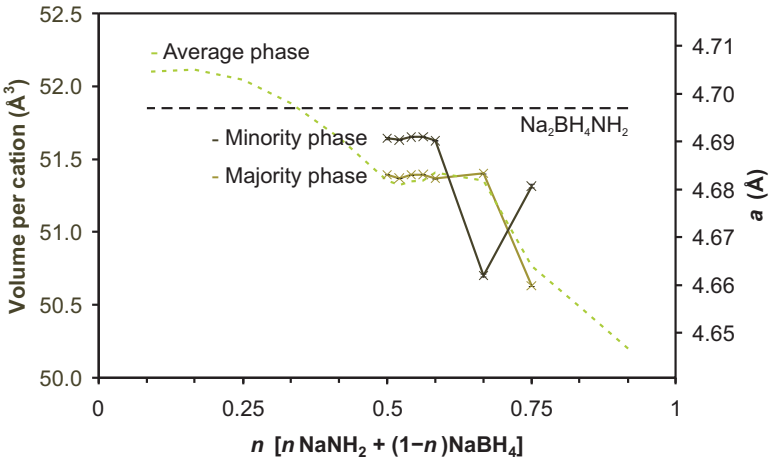

Figure 7.15: Unit cell volume per cation and lattice parameter of major and minor $Na_4(BH_4)_{(1-x)}(NH_2)_{(1+x)}$ phases present after heating $NaBH_4$ and $NaNH_2$ in different ratios. The average observed unit cell and the unit cell from section 7.2 are also shown as a dotted lines.

be made by refining the lattice parameter of the shoulders as a second minority cubic phase, as shown in figure 7.15.

This analysis suggests that there may be a favoured compositions of $Na_2(BH_4)_{(1-x)}(NH_2)_{(1+x)}$ with a more consistent lattice parameter in the range $n = 0.75 \rightarrow 0.5$ calculated to be 4.6838(9) Å. The Vegard's law analysis described previously gives a value of $x = 0.15$ (42% borohydride). Although this value is nothing special, a value of $x = 0.13$ would equate to the substitution of one borohydride by one amide in a 2×2 super-cell of the original cubic unit cell. It is possible that the Vegard's law analysis is overestimating the degree of substitution and that this preferred unit cell volume is indeed due to local ordering into a 2×2 super-cell. A search for Bragg reflections to back up the existence of this ordering was unsuccessful.

7.3.4 Summary

A cubic $Na_2BH_4NH_2$ phase was present after reaction of all mixed $NaBH_4$ + $NaNH_2$ compositions. The lattice parameter of the cubic phase was highly variable with an upper limit of 4.70608(4) Å, observed in the most borohydride rich

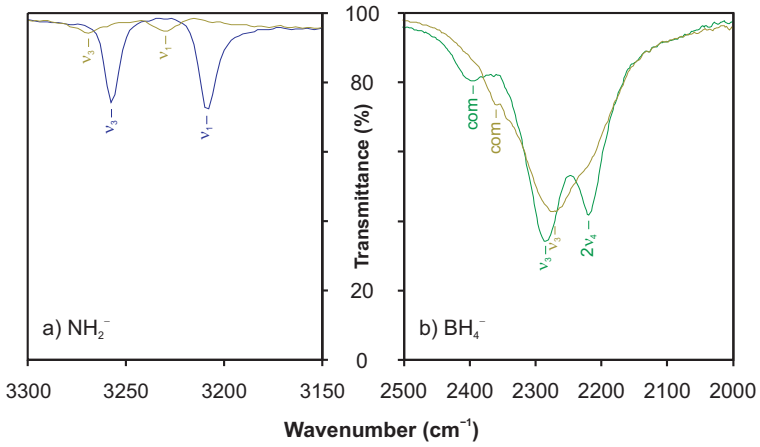

Figure 7.16: Infrared spectra of (a) the NH_2^- region and (b) the BH_4^- region of $NaNH_2$, $NaBH_4$ and $Na_2BH_4NH_2$. Observed spectra for $NaBH_4$, $NaNH_2$ and $Na_2BH_4NH_2$ are shown in green, blue and dark yellow, respectively.

compositions, which was assigned to be the true lattice parameter of stoichiometric $Na_2BH_4NH_2$. Cubic phases with smaller lattice parameters were attributed to more amide rich phases of the form $Na_2(BH_4)_{(1-x)}(NH_2)_{(1+x)}$ where $0 \leq x \leq 0.40$.

7.4 Spectroscopy

Regions of the FTIR and Raman spectra relating to the internal modes of the NH_2^- and BH_4^- anions of $Na_2BH_4NH_2$, together with the spectra of the starting materials $NaBH_4$ and $NaNH_2$, are shown in figures 7.16 and 7.17, respectively.

The FTIR and Raman spectrum of $NaBH_4$ has been fully assigned by Renaudin *et al.* [163] and the Raman spectrum of $NaNH_2$ has been assigned by Cunningham *et al.* [164]. Using these literature assignments, and the analysis discussed in the section 3.5, the observed vibrational spectra of $Na_2BH_4NH_2$, $NaNH_2$ and $NaBH_4$ have been fully assigned, the results of which are shown in tables 7.7 and 7.8.

In the crystal structures of both $NaBH_4$ [160] and $NaNH_2$ [134] the anions occupy sites of ideal symmetry (point groups T_d and C_{2v}, respectively). For both $NaBH_4$ and $NaNH_2$ the observed FTIR and Raman spectra are consistent

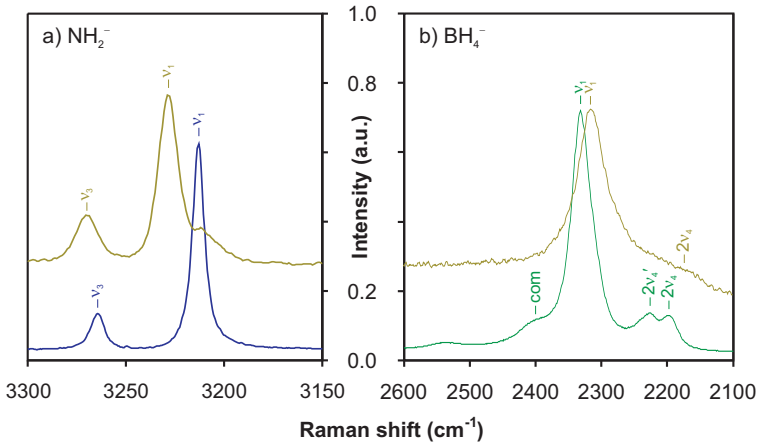

Figure 7.17: Raman spectra of (a) the NH_2^- region and (b) the BH_4^- region of $NaNH_2$, $NaBH_4$ and $Na_2(BH_4)_{(1-x)}(NH_2)_{(1+x)}$. Observed spectra for $NaBH_4$, $NaNH_2$ and $Na_2(BH_4)_{(1-x)}(NH_2)_{(1+x)}$ are shown in green, blue and dark yellow, respectively.

Table 7.7: Literature (Lit.) and observed (Obs.) infrared frequencies ($\tilde{\nu}$) and assignments (Ass.) for $NaBH_4$ with observed data for $NaNH_2$ and $Na_2BH_4NH_2$.

$NaBH_4$				$NaNH_2$		$Na_2BH_4NH_2$	
Lit. [163]		Obs.		Obs.		Obs.	
$\tilde{\nu}$	Ass.	$\tilde{\nu}$	Ass.	$\tilde{\nu}$	Ass.	$\tilde{\nu}$	Ass.
1110	ν_4	1111	ν_4	-	-	1097	ν_4 (BH_4^-)
-	-	-	-	1529	ν_2	1528	ν_2 (NH_2^-)
2217	$2\nu_4$	2219	$2\nu_4$	-	-	-	-
2284	ν_3	2285	ν_3	-	-	2274 (b)	ν_3 (BH_4^-)
2404	$\nu_2 + \nu_4$	2400	com	-	-	2360	com
-	-	-	-	3209	ν_1	3230	ν_1 (NH_2^-)
-	-	-	-	3257	ν_3	3269	ν_3 (NH_2^-)

b, broad; com, combination bands.

Table 7.8: Literature (Lit.) and observed (Obs.) Raman shifts ($\tilde{\nu}$) and assignments (Ass.) for $NaBH_4$ and $NaNH_2$ with observed data for $Na_2BH_4NH_2$.

$NaBH_4$				$NaNH_2$				$Na_2BH_4NH_2$	
Lit. [163]		Obs.		Lit. [164]		Obs.		Obs.	
$\tilde{\nu}$	Ass.	$\tilde{\nu}$	Ass.	$\tilde{\nu}$	Ass.	$\tilde{\nu}$	Ass.	$\tilde{\nu}$	Ass.
1124	ν_4	1122	ν_4	-	-	-	-	-	-
1274	ν_2	1276	ν_2	-	-	-	-	1250 (b)	ν_2 (BH_4^-)
-	-	-	-	1550	ν_2	1534	ν_2	1567	ν_2 (NH_2^-)
2197	$2\nu_4$	2195	$2\nu_4$	-	-	-	-	2183 (b)	$2\nu_4$ (BH_4^-)
2231	$2\nu_4$	2225	$2\nu_4$	-	-	-	-	-	-
2321	ν_3	-	-	-	-	-	-	-	-
2340	ν_1	2332	ν_1	-	-	-	-	2312 (b)	ν_1 (BH_4^-)
2416	$\nu_2 + \nu_4$	2400 (sh)	com	-	-	-	-	-	-
2553	$2\nu_2$	2537	com	-	-	-	-	-	-
-	-	-	-	-	-	-	-	3211	ν_1 ($NaNH_2$)
-	-	-	-	3218	ν_1	3213	ν_1	3228	ν_1 (NH_2^-)
-	-	-	-	3267	ν_3	3264	ν_3	3270	ν_3 (NH_2^-)

b, broad; com, combination bands; sh, shoulder.

with this ideal geometry.[†] For $NaBH_4$ the observed FTIR spectrum was very similar to the literature values, whereas for the Raman spectra the ν_1 symmetric stretch was observed at a slightly lower energy. For $NaNH_2$ the observed Raman spectra gave wavenumber values slightly below that reported in the literature. The peak at 3211 cm^{-1} is attributed to some excess $NaNH_2$ present in the sample of $Na_2BH_4NH_2$.

In the structure of $Na_2BH_4NH_2$ both anions are expected to be significantly disordered and possibly distorted from ideal geometry. The disorder of the BH_4^- anion was reflected in the very broad peaks due to the asymmetric stretch (ν_3) in the FTIR spectrum (figure 7.16) and the symmetric stretch (ν_1) in the Raman spectrum (figure 7.17), with very few other discernible features in the BH_4^- region of the spectra. No evidence for symmetric stretch (ν_1) or symmetric bend (ν_2) of the borohydride ion was observed in the FTIR spectrum, which would be an indication of lowering from tetragonal symmetry of this anion. As such,

[†]The absence of the ν_1 symmetric stretch and ν_2 symmetric bend of the borohyride ion from the FTIR spectrum of $NaBH_4$ is an indication of ideal T_d symmetry.

we attribute disorder in the orientation of the BH_4^- anion as the main cause of broadening in the observed spectra, rather than significant distortion from ideal tetrahedral geometry.

The stretches due to the internal modes of the NH_2^- ion were more defined, indicating that this anion may be more ordered than the BH_4^- ion. Unlike for $Li_4BH_4(NH_2)_3$, upon formation of $Na_2BH_4NH_2$ the N–H bond strength in the NH_2^- ion was significantly increased compared to in $NaNH_2$, although the bonding in BH_4^- did appear to weaken. The apparent strengthening of the NH_2^- bonding is consistent with the observation that ammonia is not released from the mixed $Na_2BH_4NH_2$ at temperatures where the starting material $NaNH_2$, where the bonding was weaker, was observed to release NH_3 (see section 7.5).

7.5 Thermal Decomposition

7.5.1 In-situ Decomposition

The gaseous thermal desorption products from various stoichiometries of $NaNH_2$ + $NaBH_4$ as well as the starting materials $NaBH_4$ and $NaNH_2$ were investigated using TPD-MS. $Na_2BH_4NH_2$ was investigated using IGA-MS. Hydrogen was the majority gaseous decomposition product for $Na_2BH_4NH_2$ although some ammonia was also observed.

$NaBH_4$

Thermal desorption data from $NaBH_4$ are shown in figure 7.18. Very little hydrogen release was observed up to the maximum temperature of 350°C with the mass spectrum signal barely above the background level. The mass spectrum signal for the other possible desorption product, diborane, and its fragmentation products, did not rise above the background level. No thermal events were visible in the temperature trace of the TPD.

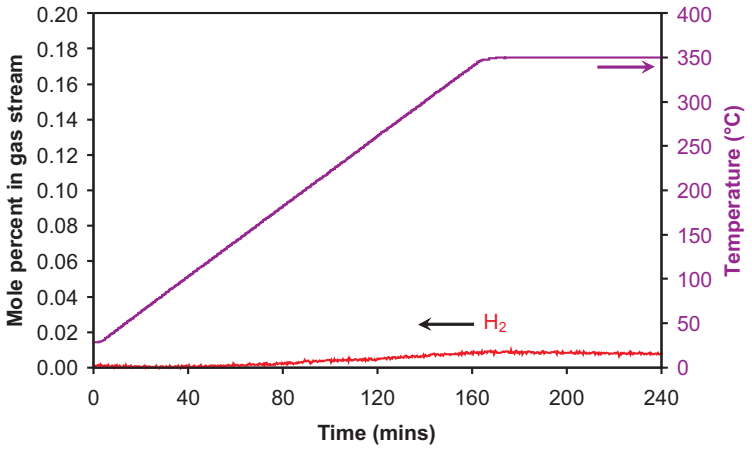

Figure 7.18: Thermal decomposition analysis of $NaBH_4$ in a TPD apparatus. The temperature trace is shown in purple and the mole percent of H_2 released is shown in red.

This is consistent with literature reports of slow thermal desorption above 400°C in vacuum [41] and a melting point of 497°C [165]. As expected, no difference was observed in the powder diffraction pattern of $NaBH_4$ after the TPD-MS experiment.

$2NaBH_4 + NaNH_2$

Thermal desorption data from a $2NaBH_4 + NaNH_2$ mixture are shown in figure 7.19. Clearly the introduction of $NaNH_2$ dramatically changed the decomposition pathway from that of $NaBH_4$, with the onset of gas release starting from 265°C and peaking at 350°C, the maximum temperature in this experiment.

There was a minor thermal event at 160°C which is currently unassigned and a larger thermal event at 215°C which was just above the reported melting point of $NaNH_2$ (210°C [117]). Figure 7.20 shows the TPD-MS data processed so as to give simulated gravimetric data, as discussed in section 2.7. The observed weight loss from mass spectroscopic data over the total heating time was only 2.7 wt%, much less than the amount of hydrogen present in the starting materials (8.8 wt%). At the peak of the desorption 1.8% of the gas released was NH_3 and overall this made up 3.4% of the total gas released. No trace of N_2 release was

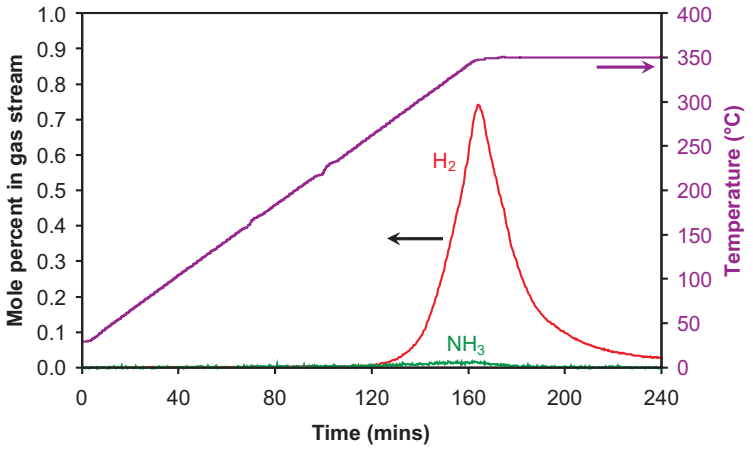

Figure 7.19: Thermal decomposition analysis of $2NaBH_4 + NaNH_2$ in a TPD apparatus. The temperature trace is shown in purple and the mole percents of H_2 and NH_3 released are shown in red and green respectively.

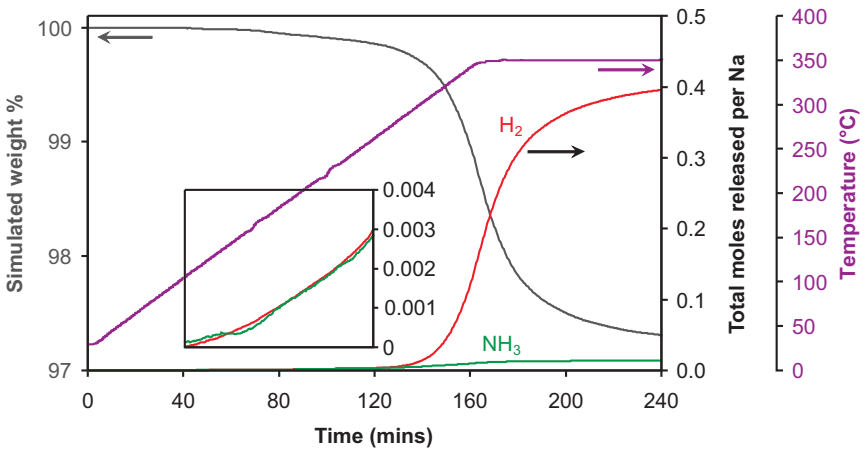

Figure 7.20: Thermal decomposition analysis of $2NaBH_4 + NaNH_2$ in a TPD apparatus with simulated gravimetric data. The temperature trace is shown in purple and the mole percents of H_2 and NH_3 released are shown in red and green, respectively, and the simulated gravimetric data is shown in grey. The inset shows a magnified y scale area.

observed above the background signal of the mass spectrometer. The inset in figure 7.20 shows thermal desorption first proceeds with the near equal evolution of H_2 and NH_3 with H_2 release only becoming favoured at temperatures exceeding 280°C.

XRD after TPD-MS showed only $NaBH_4$ and NaH present at a composition of 70.9(6) wt% and 29.1(6) wt%, respectively. Although these are the only

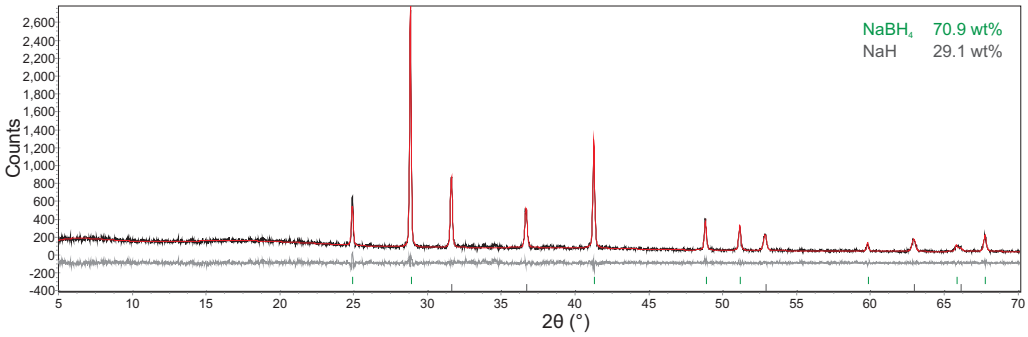

Figure 7.21: Powder XRD of $2NaBH_4 + NaNH_2$ after heating to 350°C in TPD-MS apparatus. Bragg peak positions due to $NaBH_4$ (green) and NaH (grey) are indicated.

crystalline phases observed there must be a further nitrogen containing phase present since the small amount of ammonia release observed was not sufficient to account for the amount of nitrogen present in the starting mixture. This must be an amorphous phase, perhaps amorphous boron nitride, though Raman spectroscopy showed no signs of B-N stretches.

$NaBH_4 + NaNH_2$

Figure 7.22 shows thermal desorption data from a stoichiometric mixture of $NaBH_4$ and $NaNH_2$. The temperatures of gas release were essentially the same as for the $2NaBH_4 + NaNH_2$ stoichiometry with the onset at 265°C and peak hydrogen release at 350°C. For the 1:1 stoichiometry the thermal event at 160°C was more pronounced than the event at 215°C. It is likely that the first thermal event is due to the formation of $Na_2BH_4NH_2$ from the starting materials. Attempts to probe the thermal properties further using DSC failed because of the reactivity of $NaNH_2$ towards the aluminium sample holders.

Figure 7.23 shows the TPD-MS data processed so as to give simulated gravimetric data. A larger weight loss of 3.7 wt% was observed compared with the $2NaBH_4 + NaNH_2$ stoichiometry, but this still corresponds to less than half of the hydrogen present in the starting materials (7.9 wt% H_2). At the peak of the desorption 2.7% of the gas released was NH_3 and overall this made up 3.8% of

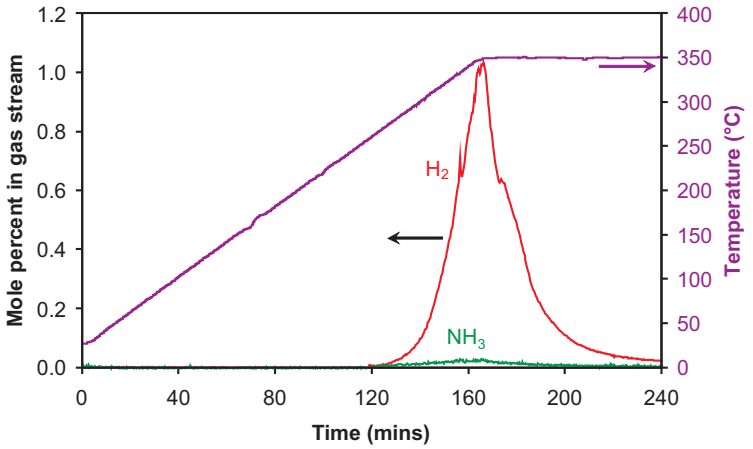

Figure 7.22: Thermal decomposition analysis of $NaBH_4$ + $NaNH_2$ in a TPD apparatus. The temperature trace is shown in purple and the mole percents of H_2 and NH_3 released are shown in red and green respectively.

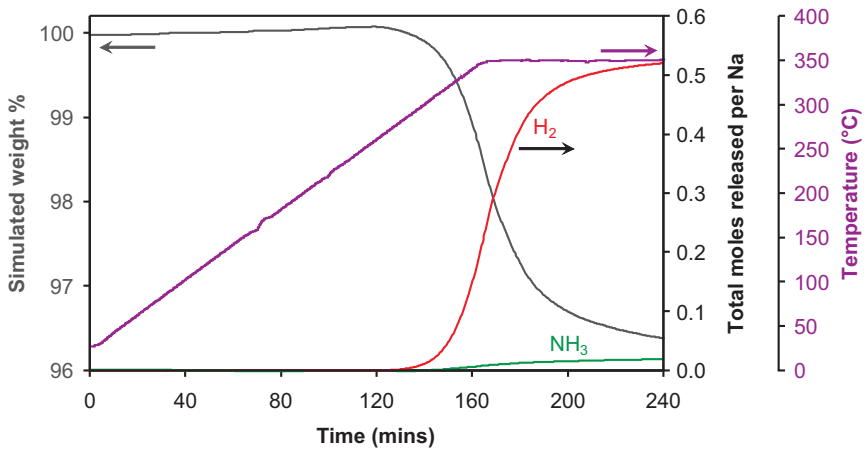

Figure 7.23: Thermal decomposition analysis of $NaBH_4$ + $NaNH_2$ in a TPD apparatus with simulated gravimetric data. The temperature trace is shown in purple, the mole percents of H_2 and NH_3 released are shown in red and green, respectively, and the simulated gravimetric data is shown in grey.

the total gas released.

Powder XRD after the TPD experiment again showed $NaBH_4$ and NaH present, this time with NaH as the majority phase, making up 78.2(9) wt% of the observed crystalline phases. There were also some minor Bragg reflections which could not be accounted for. These reflections were more intense in the $NaBH_4$ + $2NaNH_2$ composition and so will be discussed in the following section.

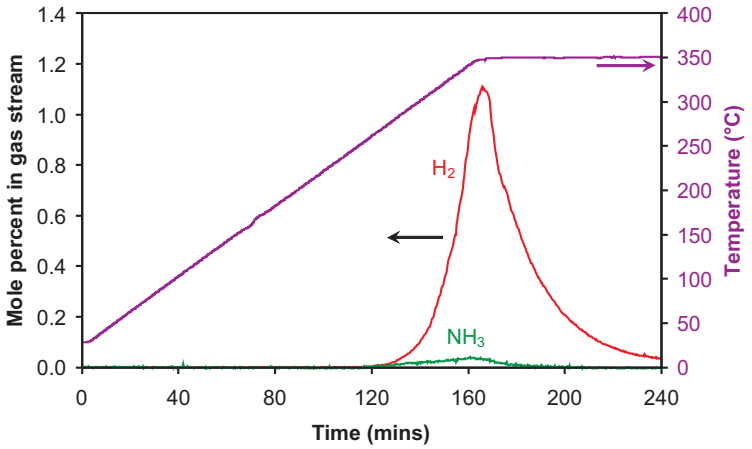

Figure 7.24: Thermal decomposition analysis of $NaBH_4$ + $2NaNH_2$ in a TPD apparatus. The temperature trace is shown in purple and the mole percents of H_2 and NH_3 released are shown in red and green respectively.

$NaBH_4$ + $2NaNH_2$

Thermal desorption data from the $NaBH_4$ + $2NaNH_2$ sample are shown in figure 7.24. Again, the temperatures of gas release were essentially the same as for the other samples with the onset at 265°C and peak of hydrogen release at 350°C. At the peak of the desorption 3.0% of the gas released was NH_3, slightly higher than for the more borohydride rich compositions.

Figure 7.25 shows the TPD-MS data processed to give simulated gravimetric data. A larger still weight loss of 4.1 wt% was observed compared with the more borohydride rich stoichiometries. A total of 0.64 moles of hydrogen per sodium were released during the total heating time giving only 1.9 H_2 molecules released for the reaction $NaBH_4$ + $2NaNH_2$.

Powder XRD after the TPD experiment (figure 7.26) showed NaH as the only assignable phase present. However, there were also some Bragg reflections which could not be accounted for which were also present in smaller intensities in the $NaBH_4$ + $NaNH_2$ composition. The peak positions and relative intensities for these unidentified reflections are given in table 7.9. Attempts to index these reflections using the computer program Topas [90] have failed. These re-

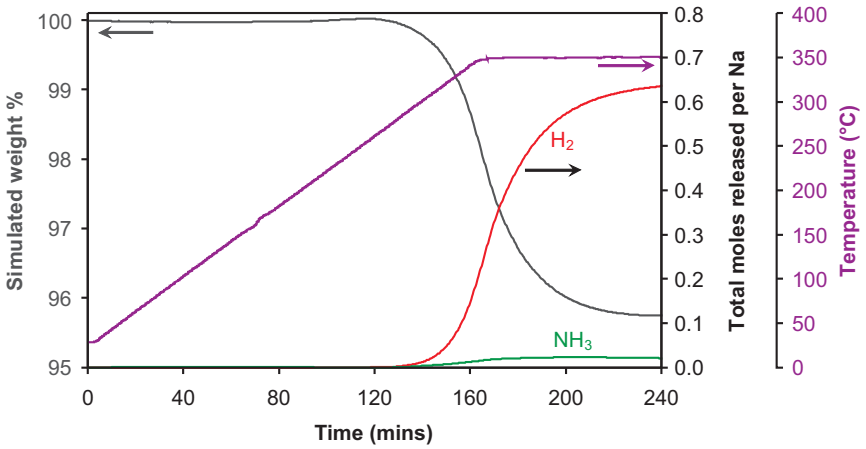

Figure 7.25: Thermal decomposition analysis of $NaBH_4$ + $2NaNH_2$ in a TPD apparatus with simulated gravimetric data. The temperature trace is shown in purple and the mole percents of H_2 and NH_3 released are shown in red and green, respectively, and the simulated gravimetric data is shown in grey.

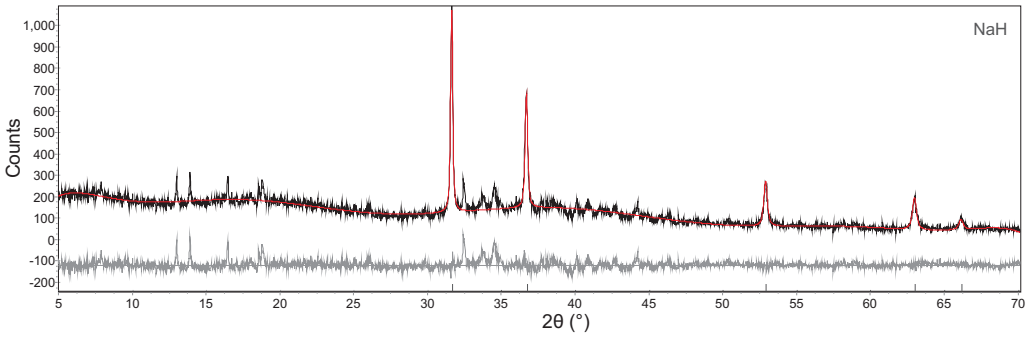

Figure 7.26: Powder XRD of $NaBH_4$ + $2NaNH_2$ after heating to 350°C in TPD-MS apparatus. Bragg peak positions due to NaH (grey) are indicated.

flections are not due to the reported Na_3BN_2 [166]; the reported synthesis for this phase involves high pressure and temperature (4 GPa, 1000°C) and has not been repeated in the literature. For the lithium system there are three known polymorphs of Li_3BN_2 [126, 118, 119]. It may be that these reflections are due to a hitherto undiscovered polymorph of Na_3BN_2, but better diffraction data is needed to confirm this. Raman spectroscopy of the solid decomposition products could not confirm the presence of the BN_2^{3-} anion.

Table 7.9: Unidentified reflections after TPD of $NaBH_4$ + $NaNH_2$ and $NaBH_4$ + $2NaNH_2$.

$NaBH_4$ + $NaNH_2$			$NaBH_4$ + $2NaNH_2$		
2θ (°)	d (Å)	I_{rel} (%)	2θ (°)	d (Å)	I_{rel} (%)
7.97	11.08	15.0	7.94	11.13	16.6
13.10	6.75	23.4	13.06	6.77	29.0
14.03	6.31	21.3	13.97	6.34	36.9
16.60	5.34	32.2	16.51	5.36	36.8
18.73	4.73	12.3	18.63	4.76	17.3
18.97	4.67	34.4	18.87	4.70	42.9
-	-	-	26.07	3.42	16.6
-	-	-	29.86	2.99	11.7
32.65	2.74	100.0	32.52	2.75	84.0
33.92	2.64	49.6	33.80	2.65	66.7
34.66	2.59	76.3	34.59	2.59	100.0
-	-	-	37.81	2.38	22.4
-	-	-	40.19	2.24	13.7
-	-	-	40.92	2.20	25.5
-	-	-	42.73	2.11	20.7
-	-	-	44.25	2.05	28.4

$NaNH_2$

Thermal desorption data from $NaNH_2$ are shown in figure 7.27. Ammonia release was observed with an onset around 240°C, peaking at the maximum temperature of 350°C. The endothermic melting of $NaNH_2$ is clearly visible in the temperature trace at 205°C. Hydrogen was observed as a minor decomposition product, making up 12% of the desorbed gases.

$NaNH_2$ is reported to decompose in the range 335–400°C with the release of H_2 and N_2 according to equation 7.1 with ammonia as a minor product [167].

$$2NaNH_2 \rightarrow 2NaH + H_2 \uparrow + N_2 \uparrow \tag{7.1}$$

The upper temperature for this experiment is close to the lower limit of the reported decomposition temperature. More recent studies have failed to characterise better the decomposition pathway of $NaNH_2$ because of the reactivity of molten $NaNH_2$ towards Au and Al sample holders [168, 169]. Although there

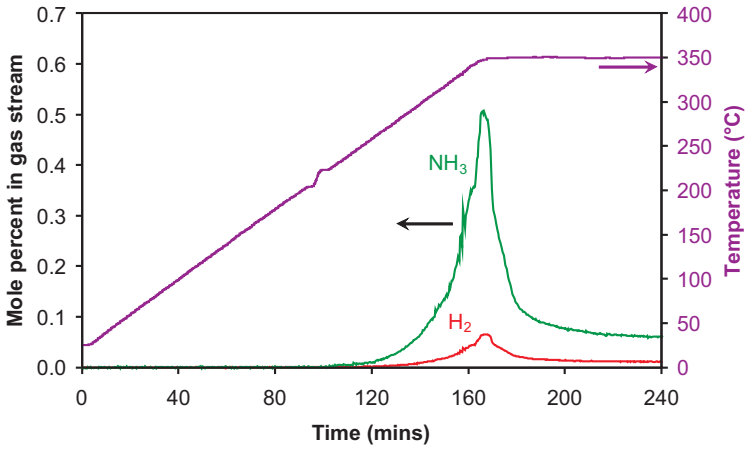

Figure 7.27: Thermal decomposition analysis of $NaNH_2$ in a TPD apparatus. The temperature trace is shown in purple and the mole percents of H_2 and NH_3 released are shown in red and green, respectively.

was significant discolouration of the quartz sample tube used in this TPD-MS experiment for the $NaNH_2$ sample we believe that the ammonia releasing decomposition pathway of $NaNH_2$ observed in this experiment is favoured at lower temperatures (≤ 350°C).

XRD after the TPD experiment showed a new set of Bragg reflections which were not due to $NaNH_2$ or NaH which suggested an imide-like structure, analogous to the lithium system, according to equation 7.2. Sodium imide is not known and thought not to exist [167].

$$2NaNH_2 \rightarrow Na_2NH + {}^3/_2H_2 \uparrow \tag{7.2}$$

Further investigations into the decomposition pathway of $NaNH_2$ are currently under way in a separate project [170].

Discussion

It is clear that the decomposition profile of mixed $NaBH_4$ + $NaNH_2$ samples varies greatly from that of the pure starting materials. Whereas $NaBH_4$ releases very little hydrogen up to 350°C and $NaNH_2$ releases predominantly ammonia above 240°C, the mixed system releases predominantly hydrogen. Ammonia was

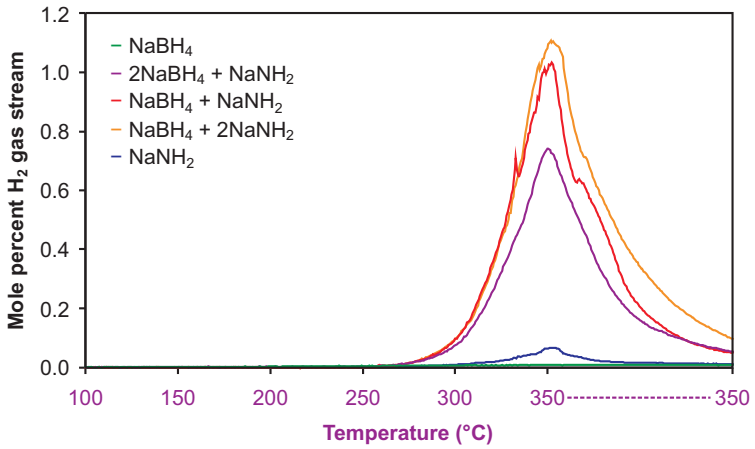

Figure 7.28: Comparison of thermal decomposition from $NaBH_4$ + $NaNH_2$ samples.

a minor desorption product making up less than 4% of the desorbed gas. The amount of ammonia observed was greater for the more $NaNH_2$–rich compositions. Despite the composition differences between the mixed samples, the hydrogen desorption profiles were very similar, with the onset of hydrogen desorption at 265°C and peak at 350°C. The hydrogen release profiles for each of the samples tested are compared in figure 7.28. The same onset temperature for hydrogen release suggests the same reaction mechanism for the different compositions. Hydrogen is only released from these mixed systems above the temperature at which $NaNH_2$ is releasing ammonia, suggesting that ammonia may be important in the reaction mechanism, as suggested for the $LiNH_2$ + LiH system [63]. Indeed, figure 7.28 shows that the presence of more $NaNH_2$, and therefore more available NH_3, increases the total amount of hydrogen release from the system, although the difference is smaller between the $NaBH_4$ + $NaNH_2$ and $NaBH_4$ + $2NaNH_2$ samples.

Analysis of the XRD patterns of the post-TPD samples suggests two possible reaction mechanisms. The identification of $2NaBH_4$ and NaH as the only crystalline phases from $NaBH_4$ + $NaNH_2$, and the presence of NaH only from $NaBH_4$ + $NaNH_2$, suggest a reaction to give amorphous BN (equation 7.3, 5.3 wt% H_2)

is possible.

$$NaBH_4 + NaNH_2 \rightarrow 2NaH + BN + 2H_2 \uparrow \quad (7.3)$$

The presence of unidentified Bragg reflections in the XRD pattern of the post-TPD $NaBH_4$ + $NaNH_2$ and $NaBH_4$ + $2NaNH_2$ samples suggest a second equation to form a hitherto unidentified Na_3BN_2 phase could be favoured at more amide rich compositions (equation 7.4, 7.0 wt% H_2).

$$NaBH_4 + 2NaNH_2 \rightarrow Na_3BN_2 + 4H_2 \uparrow \quad (7.4)$$

Indeed, greater hydrogen release is observed for amide rich samples, for which a more hydrogen rich decomposition pathway is suggested. There is a second possible assignment of the unindexed peaks in the amide rich samples. If the decomposition proceeds purely *via* equation 7.3, then for the $NaBH_4$ + $2NaNH_2$ reaction there is a possibility for the excess $NaNH_2$ to react further with the NaH to form a previously unknown sodium imide (equation 7.2). Work by others on the $NaNH_2$ + NaH system suggests that the observed Bragg reflections in this study are not due to the reaction of $NaNH_2$ with NaH [170], and so the formation of Na_3BN_2 *via* equation 7.4 is tentatively suggested as a possibility. Raman spectroscopy of the decomposition products failed to confirm the presence of BN or Na_3BN_2.

7.5.2 IGA-MS

A sample of $NaBH_4$ + $NaNH_2$ (105 mg), pre-reacted at 180°C for 12 hours, was inertly loaded into an IGA connected to a mass spectrometer. Figure 7.29 shows the thermogravimetric data overlaid with the mass spectrometric data for the observed desorption products. The sample heated in the IGA showed significant ammonia release with an onset temperature of 245°C, just above the temperature observed previously for ammonia release from $NaNH_2$ in a TPD-MS (240°C). Hydrogen release occurred at slightly higher temperatures and hydrogen release

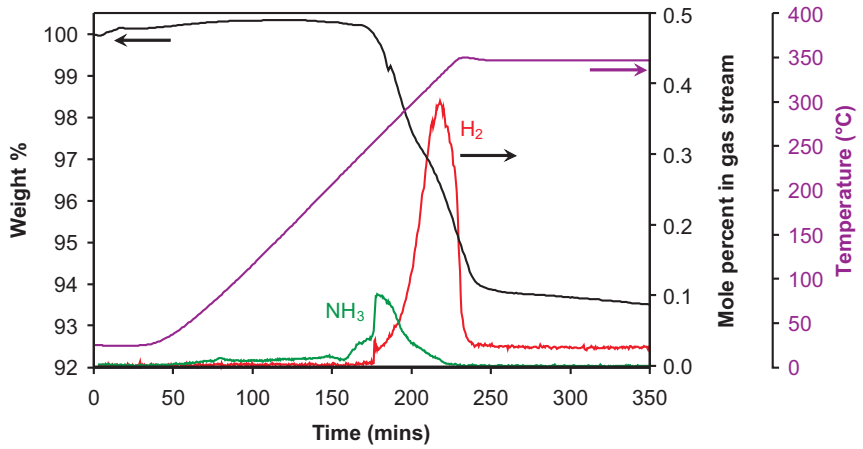

Figure 7.29: Thermo-gravimetric analysis of $NaBH_4$ + $NaNH_2$ in an IGA. The gravimetric trace is shown in black, the temperature trace is shown in purple and the mole percents of H_2 and NH_3 are shown in red and green, respectively.

overtook ammonia as the major decomposition product from 280°C, with peak hydrogen desorption at 340°C. This decomposition corresponds to 6.1 wt% which is predominantly due to hydrogen release. After this first major decomposition the sample mass continued to decrease upon holding at 350°C with continuing hydrogen release going on to a further 3.5 wt%.

The weight loss of 6.1 wt% is consistent with equation 7.3 (5.3 wt% H_2) with some ammonia release. The further continued weight loss due to only hydrogen was attributed to the slow decomposition of NaH to sodium metal and hydrogen. Attempts to rehydride this sample on the IGA (190°C, 10 bar H_2, 2 days) resulted in a minor absorption of 0.2 wt% which was attributed to a slow partial hydrogenation of the sodium metal to reform NaH.

As with $Li_4BH_4(NH_2)_3$, ammonia release was favoured at lower temperatures from sodium amide–borohydride in the IGA-MS experimental set-up compared with the TPD-MS where much less ammonia was observed. The fact that the desorption of ammonia was suppressed in our TPD experiments suggests that it may be the primary desorption product and that hydrogen is produced only upon reaction of desorbed ammonia with the sample. In the IGA experiment, where contact time between any desorbed ammonia and the desorbing sample will be

less due to a continuous gas flow directly over the sample surface, ammonia release is initially strongly favoured over that of hydrogen at lower temperatures. Our results are therefore consistent with the suggestion that NH_3 is an intermediate in the evolution of hydrogen from the $Na_2BH_4NH_2$ system.

7.6 Conclusion

The complex hydride $Na_2BH_4NH_2$ has been formed by the reaction of $NaBH_4$ and $NaNH_2$ and its disordered structure solved by Rietveld refinement against combined powder synchrotron X-ray and neutron diffraction data. The thermal decomposition of the xNaBH$_4$ + yNaNH$_2$ system has been investigated and the decomposition products were found to depend on the stoichiometry of the reaction. Hydrogen release was observed from 265°C with some ammonia also released. Two possible decomposition pathways to form boron nitride and a sodium boron nitride are proposed.

References

[1] A. Sartbaeva, V. L. Kuznetsov, S. A. Wells, and P. P. Edwards, *Energy Environ. Sci.*, 2008, **1**(1), 79–85. [cited at p. 1]

[2] A. Züttel, *Naturwissenschaften*, 2004, **91**, 157–172. [cited at p. 1, 4, 9, 10]

[3] T. M. Letcher, *Climate Change - Observed Impacts on Planet Earth*, Elsevier, 2009. [cited at p. 2]

[4] P. P. Edwards, V. L. Kuznetsov, and W. I. F. David, *Phil. Trans. R. Soc. A*, 2007, **365**, 1043–1056. [cited at p. 2, 8]

[5] K. Agbossou, R. Chahine, J. Hamelin, F. Laurencelle, A. Anouar, J. M. St-Arnaud, and T. K. Bose, *J. Power Sources*, 2001, **96**(1), 168–172. [cited at p. 3]

[6] W. Kreuter and H. Hofmann, *Int. J. Hydrogen Energ.*, 1998, **23**(8), 661–666. [cited at p. 3]

[7] S. Baykara, *Int. J. Hydrogen Energ.*, 2004, **29**(14), 1451–1458. [cited at p. 4]

[8] F. Hawkes, R. Dinsdale, D. Hawkes, and I. Hussy, *Int. J. Hydrogen Energ.*, 2002, **27**(11-12), 1339–1347. [cited at p. 4]

[9] S. C. N. Martínez-Pérez, G. Premier, R. Dinsdale, D. Hawkes, F. Hawkes, G. Kyazze, and A. Guwy, *Biomass Bioenerg.*, 2007, **31**, 95–104. [cited at p. 4]

[10] L. Schlapbach and A. Züttel, *Nature*, 2001, **414**, 23–31. [cited at p. 5]

[11] U. Bossel Well-to-Wheel Studies, Heating Values, and the Energy Conservation Principle Technical Report E10, European Fuel Cell Forum, Morgenacherstrasse 2F, CH-5452 Oberrohrdorf, Switzerland, 2003. [cited at p. 5]

[12] L. M. Das, *Int. J. Hydrogen Energ.*, 1990, **15**(6), 425–443. [cited at p. 5]

[13] C. M. White, R. R. Steeper, and A. E. Lutz, *Int. J. Hydrogen Energ.*, 2006, **31**, 1292–1305. [cited at p. 5]

[14] P. P. Edwards, V. L. Kuznetsov, W. I. F. David, and N. P. Brandon, *Energ. Policy*, 2008, **36**(12), 4356–4362. [cited at p. 6]

[15] F. Barbir and T. Gómez, *Int. J. Hydrogen Energ.*, 1997, **22**(10-11), 1027–1037. [cited at p. 6]

[16] X. Cheng, Z. Shi, N. Glass, L. Zhang, J. Zhang, D. Song, Z. Liu, H. Wang, and J. Shen, *J. Power Sources*, 2007, **165**(2), 739–756. [cited at p. 6]

[17] R. Hammerschlag and P. Mazza, *Energ. Policy*, 2005, **33**(16), 2039–2043. [cited at p. 7]

[18] S. Dunn, *Int. J. Hydrogen Energ.*, 2002, **27**, 235–264. [cited at p. 7]

[19] S. M. Aceves, G. D. Berry, J. Martinez-Frias, and F. Espinosa-Loza, *Int. J. Hydrogen Energ.*, 2006, **31**, 2274–2283. [cited at p. 8]

[20] N. Takeichi, H. Senoh, T. Yokota, H. Tsuruta, K. Hamada, H. T. Takeshita, H. Tanaka, T. Kiyobayashi, T. Takano, and N. Kuriyama, *Int. J. Hydrogen Energ.*, 2003, **28**, 1121–1129. [cited at p. 8]

[21] G. Walker, *Solid-state hydrogen storage: Materials and chemistry*, Woodhead Publishing, 2008. [cited at p. 9]

[22] H. W. Langmi, D. Book, A. Walton, S. R. Johnson, M. M. Al-Mamouri, J. D. Speight, P. P. Edwards, I. R. Harris, and P. A. Anderson, *J. Alloys Compd.*, 2005, **404**, 637–642. [cited at p. 9]

[23] Z. Yang, Y. Xia, and R. Mokaya, *J. Am. Chem. Soc.*, 2007, **129**, 1673–1679. [cited at p. 9]

[24] X. Lin, J. Jia, X. Zhao, K. M. Thomas, A. J. Blake, G. S. Walker, N. R. Champness, P. Hubberstey, and M. Schröder, *Angew. Chem., Int. Ed.*, 2006, **45**, 7358–7364. [cited at p. 9]

[25] P. Budd, J. Selbie, K. Mahmood, N. B. McKeown, B. Ghanem, K. Msayib, D. Book, and A. Walton, *Phys. Chem. Chem. Phys.*, 2007, **9**, 1802–1808. [cited at p. 9]

[26] A. W. C. van den Berg and C. O. Areán, *Chem. Commun.*, 2008, **6**, 668–681. [cited at p. 10]

[27] T. Spassov, P. Solsona, S. Bliznakov, S. Suriñach, and M. D. Baró, *J. Alloys Compd.*, 2003, **356-357**, 639–643. [cited at p. 10]

[28] B. Bogdanović, K. Bohmhammel, B. Christ, A. Reiser, K. Schlichte, R. Vehlen, and U. Wolf, *J. Alloys Compd.*, 1999, **282**(1-2), 84–92. [cited at p. 11]

[29] O. Gutfleisch, N. S. de Boer, N. Ismail, M. Herrich, A. Walton, J. Speight, I. R. Harris, A. S. Pratt, and A. Züttel, *J. Alloys Compd.*, 2003, **356-357**(1-2), 598–602. [cited at p. 11]

[30] S. R. Johnson, P. A. Anderson, P. P. Edwards, I. Gameson, J. W. Prendergast, M. Al-Mamouri, D. Book, I. R. Harris, J. D. Speight, and A. Walton, *Chem. Commun.*, 2005, **22**, 2823–2825. [cited at p. 11, 215]

[31] S. Orimo, Y. Nakamori, J. R. Eliseo, A. Züttel, and C. M. Jensen, *Chem. Rev.*, 2007, **107**, 4111–4132. [cited at p. 11]

[32] W. Grochala and P. P. Edwards, *Chem. Rev.*, 2004, **104**, 1283–1315. [cited at p. 11, 13, 14, 18]

[33] B. Bogdanović, R. A. Brand, A. Marjanović, M. Schwickardi, and J. Tölle, *J. Alloys Compd.*, 2000, **302**, 36–58. [cited at p. 11]

[34] B. Bogdanović and M. Schwickardi, *J. Alloys Compd.*, 1997, **253-254**, 1–9. [cited at p. 12]

[35] B. Bogdanović, M. Felderhoff, A. Pommerin, F. Schüth, and N. Spielkamp, *Adv. Mater.*, 2006, **18**(9), 1198–1201. [cited at p. 12]

[36] J. Chen, N. Kuriyama, Q. Xu, H. T. Takeshita, and T. Sakai, *J. Phys. Chem. B*, 2001, **105**, 11214–11220. [cited at p. 12]

[37] S. S. Srinivasan, H. W. Brinks, B. C. Hauback, D. Sun, and C. M. Jensen, *J. Alloys Compd.*, 2004, **377**(1-2), 283–289. [cited at p. 12]

[38] H. I. Schlesinger and H. C. Brown, *J. Am. Chem. Soc.*, 1940, **62**(12), 3429–3435. [cited at p. 12]

[39] T. J. Marks and J. R. Kolb, *Chem. Rev.*, 1977, **77**(2), 263–293. [cited at p. 12, 13]

[40] A. Züttel, P. Wenger, S. Rentsch, P. Sudan, P. Mauron, and C. Emmenegger, *J. Power Sources*, 2003, **118**, 1–7. [cited at p. 12, 107, 182, 183]

[41] H. I. Schlesinger, H. C. Brown, H. R. Hoekstra, and L. R. Rapp, *J. Am. Chem. Soc.*, 1953, **75**(1), 199–204. [cited at p. 12, 256]

[42] Y. Nakamori, H. W. Li, K. Miwa, S. Towata, and S. Orimo, *Mater. Trans.*, 2006, **47**(8), 1898–1901. [cited at p. 13, 14]

[43] E. A. Nickels, M. O. Jones, W. I. F. David, S. R. Johnson, R. L. Lowton, M. Sommariva, and P. P. Edwards, *Angew. Chem. Int. Edit.*, 2008, **47**(15), 2817–2819. [cited at p. 13, 14]

[44] S. Orimo, Y. Nakamori, H. W. Li, M. Matsuo, T. Sato, N. Ohba, K. Miwa, and S. Towata In *Materials Issues in a Hydrogen Economy*, pp. 124–129, 2009. [cited at p. 13]

[45] P. Mauron, F. Buchter, O. Friedrichs, A. Remhof, M. Bielmann, C. N. Zwicky, and A. Züttel, *J. Phys. Chem. B*, 2008, **112**, 906–910. [cited at p. 13, 182, 183]

[46] A. Züttel, S. Rentsch, P. Fischer, P. Wenger, P. Sudan, P. Mauron, and C. Emmenegger, *J. Alloys Compd.*, 2003, **356-357**, 515–520. [cited at p. 13]

[47] J. K. Kang, S. Y. Kim, Y. S. Han, R. P. Muller, and W. A. Goddard III, *Appl. Phys. Lett.*, 2005, **87**, 111904. [cited at p. 13, 122]

[48] N. Ohba, K. Miwa, M. Aoki, T. Noritake, S. Towata, Y. Nakamori, S. Orimo, and A. Züttel, *Phys. Rev. B*, 2006, **74**(7), 075110. [cited at p. 13]

[49] S. Orimo, Y. Nakamori, N. Ohba, K. Miwa, M. Aoki, S. Towata, and A. Züttel, *Appl. Phys. Lett.*, 2006, **89**, 021920. [cited at p. 13]

[50] S.-J. Hwang, R. C. Bowman Jr., J. W. Reiter, J. Rijssenbeek, G. L. Soloveichik, J.-C. Zhao, H. Kabbour, and C. C. Ahn, *J. Phys. Chem. C*, 2008, **112**, 3164–3169. [cited at p. 13, 122, 183]

[51] S. Orimo, Y. Nakamori, G. Kitahara, K. Miwa, N. Ohba, S. Towata, and A. Züttel, *J. Alloys Compd.*, 2005, **404-406**, 427–430. [cited at p. 13]

[52] J. J. Vajo, S. L. Skeith, and F. Mertens, *J. Phys. Chem. B*, 2005, **109**(9), 3719–3722. [cited at p. 14]

[53] U. Bösenberg, S. Doppiu, L. Mosegaard, G. Barkhordarian, N. Eigen, A. Borgschulte, T. R. Jensen, Y. Cerenius, O. Gutfleisch, T. Klassen, M. Dornheim, and R. Bormann, *Acta Mater.*, 2007, **55**(11), 3951–3958. [cited at p. 14]

[54] G. Barkhordarian, T. Klassen, M. Dornheim, and R. Bormann, *J. Alloys Compd.*, 2007, **440**, L18–L21. [cited at p. 14]

[55] Y. Nakamori, K. Miwa, A. Ninomiya, H. Li, N. Ohba, S. Towata, A. Züttel, and S. Orimo, *Phys. Rev. B*, 2006, **74**, 045126. [cited at p. 14]

[56] D. Ravnsbæk, Y. Filinchuk, Y. Cerenius, H. J. Jakobsen, F. Besenbacher, J. Skibsted, and T. R. Jensen, *Angew. Chem. Int. Ed.*, 2009, **48**, 6659–6663. [cited at p. 14]

[57] A. Züttel In *Hydrogen Storage Materials*. MRS Proceedings, 2009. [cited at p. 14]

[58] F. W. Bergstrom and W. C. Fernelius, *Chem. Rev.*, 1933, **12**(1), 43–179. [cited at p. 14]

[59] R. Juza and K. Opp, *Z. Anorg. Allg. Chem.*, 1951, **266**, 325–330. [cited at p. 14, 122]

[60] P. Chen, Z. Xiong, J. Luo, J. Lin, and K. L. Tan, *Nature*, 2002, **420**, 302–304. [cited at p. 15]

[61] P. Chen, Z. Xiong, J. Luo, J. Lin, and K. L. Tan, *J. Phys. Chem. B*, 2003, **107**(39), 10967–10970. [cited at p. 15, 23, 184]

[62] T. Ichikawa, S. Isobe, N. Hanada, and H. Fujii, *J. Alloys Compd.*, 2004, **365**, 271–276. [cited at p. 15]

[63] T. Ichikawa, N. Hanada, S. Isobe, H. Leng, and H. Fujii, *J. Phys. Chem. B*, 2004, **108**, 7887–7892. [cited at p. 15, 264]

[64] W. I. F. David, M. O. Jones, D. H. Gregory, C. M. Jewell, S. R. Johnson, A. Walton, and P. P. Edwards, *J. Am. Chem. Soc.*, 2007, **129**(6), 1594–1601. [cited at p. 15, 186]

[65] D. H. Gregory, *J. Mater. Chem.*, 2008, **18**, 2321–2330. [cited at p. 15]

[66] Z. Xiong, G. Wu, J. Hu, and P. Chen, *Adv. Mater.*, 2004, **16**, 1522–1525. [cited at p. 15]

[67] W. Luo, *J. Alloys Compd.*, 2004, **381**, 284–287. [cited at p. 15, 214]

[68] H. Y. Leng, T. Ichikawa, S. Hino, N. Hanada, S. Isobe, and H. Fujii, *J. Phys. Chem. B*, 2004, **108**, 8763–8765. [cited at p. 15, 218]

[69] J. Rijssenbeek, Y. Gao, J. Hanson, Q. Huang, C. Jones, and B. Toby, *J. Alloys Compd.*, 2008, **454**(1-2), 233–244. [cited at p. 15, 212, 214]

[70] G. Wu, Z. Xiong, T. Liu, Y. Liu, J. Hu, P. Chen, Y. Feng, and A. T. S. Wee, *Inorg. Chem.*, 2007, **46**, 517–521. [cited at p. 15, 227]

[71] K. Tokoyoda, S. Hino, T. Ichikawa, K. Okamoto, and H. Fujii, *J. Alloys Compd.*, 2007, **439**(1-2), 337–341. [cited at p. 16]

[72] US Department of Energy Targets for Onboard Hydrogen Storage Systems for Light-Duty Vehicles Technical report, Office of Energy Efficiency and Renewable Energy and The FreedomCAR and Fuel Partnership, 2009. [cited at p. 16]

[73] H. R. Kemp, *J. Chem. Educ.*, 1987, **64**(6), 482–484. [cited at p. 19]

[74] National Institute of Standards and Technology NIST Standard Reference Database 69: NIST Chemistry WebBook; http://webbook.nist.gov, 2008. [cited at p. 22, 59]

[75] Q. Ge, *J. Phys. Chem. A*, 2004, **108**, 8682–8690. [cited at p. 23]

[76] G. Burns and A. M. Glazer, *Space Groups for Solid State Scientists*, Academic Press, 1978. [cited at p. 26, 27]

[77] R. E. Dinnebier and S. J. L. Billinge, *Powder Diffraction. Theory and Practice*, RSC Publishing, 2008. [cited at p. 32, 34, 38, 48]

[78] C. Hammond, *The Basics of Crystallography and Diffraction*, IUCr Monographs on Crystallography, Oxford University Press, 2nd ed., 2001. [cited at p. 33]

[79] J. I. Langford and A. J. C. Wilson, *J. Appl. Cryst.*, 1978, **11**, 102–113. [cited at p. 36]

[80] H. M. Rietveld, *J. Appl. Cryst.*, 1969, **2**, 65–71. [cited at p. 42]

[81] R. A. Young, *The Rietveld Method*, Oxford University Press, 1993. [cited at p. 42]

[82] GSAS: General Structure Analysis System, user manual. A. C. Larson and R. B. Von Dreele; Los Alamos National Laboratory, 2004. [cited at p. 42]

[83] Topas technical reference manual. A. Coelho; Bruker AXS, 2005. [cited at p. 42, 43]

[84] R. A. Young and D. B. Wiles, *J. Appl. Cryst.*, 1982, **15**, 430–438. [cited at p. 43]

[85] R. J. Hill and C. J. Howard, *J. Appl. Cryst.*, 1987, **20**, 467–474. [cited at p. 48]

[86] D. L. Bish and S. A. Howard, *J. Appl. Cryst.*, 1988, **21**, 86–91. [cited at p. 48]

[87] A. G. De la Torre and M. A. G. Aranda, *J. Appl. Cryst.*, 2003, **36**, 1169–1176. [cited at p. 48, 49]

[88] I. C. Madsen, N. V. Y. Scarlett, L. M. D. Cranswick, and T. Lwinc, *J. Appl. Cryst.*, 2001, **34**, 409–426. [cited at p. 48, 49]

[89] W. I. F. David, K. Shankland, L. McCusker, and C. Baerlocher, *Structure Determination from Powder Diffraction Data*, IUCr Monographs on Crystallography, Oxford University Press, 2002. [cited at p. 48]

[90] Topas, general profile and structure analysis software for powder diffraction data. A. A. Coelho; Bruker AXS, Karlsruhe, Germany, 3.0 ed., 2004. [cited at p. 49, 71, 72, 76, 78, 102, 117, 131, 132, 133, 135, 148, 163, 169, 216, 231, 232, 239, 240, 246, 260]

[91] Absorbdx. Socabim; Bruker-AXS, v1.1.4 ed., 2003. [cited at p. 51]

[92] C. Dass, *Fundamentals of Contemporary Mass Spectrometry*, Wiley, 2007. [cited at p. 53]

[93] M. E. Brown, *Introduction to Thermal Analysis: Techniques and Applications*, Kluwer Academic Publishers, 2nd ed., 2001. [cited at p. 64]

[94] G. W. Höhne, W. F. Hemminger, and H. J. Flammersheim, *Differential Scanning Calorimetry*, Springer, 2nd ed., 2003. [cited at p. 64]

[95] Chekcell. J. Laugier and B. Bochu; Laboratoire des Matériaux et du Génie Physique, 2002. [cited at p. 71, 232]

[96] W. I. F. David, K. Shankland, and N. Shankland, *Chem. Commun.*, 1998, **8**, 931–932. [cited at p. 72]

[97] F. E. Pinkerton, G. P. Meisner, M. S. Meyer, M. P. Balogh, and M. D. Kundrat, *J. Phys. Chem. B*, 2005, **109**, 6–8. [cited at p. 72, 73, 103, 168]

[98] J.-P. Soulié, G. Renaudin, R. Černý, and K. Yvon, *J. Alloys Compd.*, 2002, **346**, 200–205. [cited at p. 73, 74, 83, 84, 107, 120, 121, 136, 140, 154, 182, 195, 198]

[99] H. Jacobs and R. Juza, *Z. anorg. allg. Chem.*, 1972, **391**, 3247–3259. [cited at p. 73, 74, 75, 83, 84, 120, 121, 127, 140]

[100] H. Putz, J. C. Schön, and M. Jansen, *J. Appl. Crystallogr.*, 1999, **32**, 864–870. [cited at p. 75]

[101] P. A. Chater, W. I. F. David, S. R. Johnson, P. P. Edwards, and P. A. Anderson, *Chem. Commun.*, 2006, **23**, 2439–2441. [cited at p. 83, 86, 87, 90, 91, 105, 119, 120, 121, 140, 165, 166, 167, 198]

[102] M. R. Hartman, J. J. Rush, T. J. Udovic, R. C. Bowman Jr., and S.-J. Hwang, *J. Solid State Chem.*, 2007, **180**, 1298–1305. [cited at p. 83, 84, 91, 136, 140]

[103] M. H. Sørby, Y. Nakamura, H. W. Brinks, T. Ichikawa, S. Hino, H. Fujii, and B. C. Hauback, *J. Alloys Compd.*, 2007, **428**, 297–301. [cited at p. 83, 84, 139, 140, 154]

[104] H. Wu, W. Zhou, T. J. Udovic, J. J. Rush, and T. Yildirim, *Chem. Mater.*, 2008, **20**, 12451247. [cited at p. 84, 86, 87, 90, 91, 141, 142, 143, 145, 198, 202]

[105] M. Nagib and H. Jacobs, *Atomkernenerg./Kernt*, 1973, **21**, 275–278. [cited at p. 84, 198]

[106] Y. E. Filinchuk, K. Yvon, G. P. Meisner, F. E. Pinkerton, and M. P. Balogh, *Inorg. Chem.*, 2006, **45**, 1433–1435. [cited at p. 86, 87, 89, 90, 91, 101]

[107] T. Noritake, M. Aoki, S. Towata, A. Ninomiya, Y. Nakamori, and S. Orimo, *Appl. Phys. A*, 2006, **83**(2), 277–279. [cited at p. 86, 87, 88, 91, 130, 131, 134]

[108] J. B. Yang, X. J. Wang, Q. Cai, W. B. Yelon, and W. J. James, *J. Appl. Phys.*, 2007, **102**, 033507. [cited at p. 86, 87, 89, 90, 91]

[109] J. F. Herbst and L. G. Hector Jr., *Appl. Phys. Lett.*, 2006, **88**, 231904. [cited at p. 86, 90, 91, 176]

[110] D. J. Siegel, C. Wolverton, and V. Ozoliņš, *Phys. Rev. B*, 2007, **75**, 014101. [cited at p. 86, 90, 91]

[111] VESTA, Visualization for Electronic and STructural Analysis. K. Momma and F. Izumi; Department of Earth and Planetary Materials Science, Tohoku University, Aoba, Sendai, Miyagi 980-0044, Japan, 1.0.2b ed., 2007. [cited at p. 90, 145]

[112] K. B. Harvey and N. R. McQuaker, *Can. J. Chem.*, 1971, **49**, 3282–3286. [cited at p. 98, 100]

[113] S. Gomes, H. Hagemann, and K. Yvon, *J. Alloys Compd.*, 2002, **346**, 206–210. [cited at p. 98, 99, 101]

[114] J. P. O. Bohger, R. R. Essmann, and H. Jacobs, *J. Mol. Struct.*, 1995, **348**, 325–328. [cited at p. 98, 99, 101]

[115] WiRE. Renishaw Software; Renishaw, v3.1 ed., 2002. [cited at p. 99, 146]

[116] PowderCell for Windows. W. Kraus and G. Nolze; Federal Institute for Materials Research and Training, Rudower Chaussee 5, 12489 Berlin, Germany, 2.4 ed., 2000. [cited at p. 107]

[117] ed. D. R. Lide, *CRC Handbook of Chemistry and Physics*, Taylor and Francis, Boca Raton, FL, 87th ed., 2007. [cited at p. 109, 132, 154, 182, 197, 236, 256]

[118] H. Yamane, S. Kikkawa, H. Horiuchi, and M. Koizumi, *J. Solid State Chem.*, 1986, **65**, 6–12. [cited at p. 120, 261]

[119] F. E. Pinkerton and J. F. Herbst, *J. Appl. Phys.*, 2006, **99**, 113523. [cited at p. 120, 123, 124, 126, 261]

[120] R. S. Pease, *Acta Cryst.*, 1952, **5**(3), 356–361. [cited at p. 122]

[121] P. A. Chater, W. I. F. David, and P. A. Anderson, *Chem. Commun.*, 2007, **45**, 4770–4772. [cited at p. 122, 136, 140, 141, 142, 143, 144, 145, 169, 198]

[122] R. S. Calder, W. Cochran, D. Griffiths, and R. D. Lowde, *J. Phys. Chem. Solids*, 1962, **23**, 621–632. [cited at p. 122, 183]

[123] A. Rabenau and H. Schulz, *J. Less-Common Met.*, 1976, **50**, 155–159. [cited at p. 122]

[124] H. J. Beister, S. Haag, R. Kniep, K. Strøssner, and K. Syassen, *Angew. Chem., Int. Ed. Engl.*, 1988, **27**, 1101–1103. [cited at p. 122]

[125] K. Cenzual, L. M. Gelato, M. Penzo, and E. Parthe, *Acta Crystallogr., Sect. B: Struct. Sci.*, 1991, **47**, 433–439. [cited at p. 122]

[126] H. Yamane, S. Kikkawa, and M. Koizumi, *J. Solid State Chem.*, 1987, **71**, 1–11. [cited at p. 122, 210, 261]

[127] I. Y. Kuznetsov, D. M. Vinitskii, K. A. Solntsev, N. T. Kuznetsov, and L. A. Butman, *Russ. J. Inorg. Chem.*, 1987, **32**, 1803–1804. [cited at p. 122]

[128] J.-H. Her, M. Yousufuddin, W. Zhou, S. S. Jalisatgi, J. G. Kulleck, J. A. Zan, S.-J. Hwang, R. C. Bowman Jr., and T. J. Udovic, *Inorg. Chem.*, 2008, **47**(21), 9757–9759. [cited at p. 123, 183]

[129] K. Ohoyama, Y. Nakamori, S. Orimo, and K. Yamada, *J. Phys. Soc. Japan*, 2005, **74**(1), 483–487. [cited at p. 127]

[130] T. Noritake, H. Nozaki, M. Aoki, S. Towata, G. Kitahara, Y. Nakamori, and S. Orimo, *J. Alloys Compd.*, 2005, **393**, 264–268. [cited at p. 127]

[131] G. P. Meisner, M. L. Scullin, M. P. Balogh, F. E. Pinkerton, and M. S. Meyer, *J. Phys. Chem. B*, 2006, **110**, 4186–4192. [cited at p. 130, 194, 195]

[132] General Structure Analysis System (GSAS). A. C. Larson and R. B. V. Dreele; Los Alamos National Laboratory, report laur 86-748 ed., 2004. [cited at p. 131, 136, 143]

[133] T. Threlfall, *Org. Process Res. Dev.*, 2003, **7**, 1017–1027. [cited at p. 134]

[134] M. Nagib, H. Kistrup, and H. Jacobs, *Atomkernenergie*, 1975, **26**(2), 87–90. [cited at p. 139, 234, 236, 245, 246, 252]

[135] H. Jacobs and B. Harbrechet, *J. Less-Common Met.*, 1982, **85**(1), 87–95. [cited at p. 139, 208]

[136] H. Jacobs, *Z. Anorg. Allg. Chem.*, 1971, **382**(2), 97–109. [cited at p. 139, 216]

[137] S. C. Abrahams and J. Kalnajs, *J. Chem. Phys.*, 1954, **22**, 434–436. [cited at p. 154, 234, 236, 250]

[138] A. R. Denton and N. W. Ashcroft, *Phys. Rev. A*, 1991, **43**(6), 3161–3164. [cited at p. 167, 248]

[139] H. Maekawa, M. Matsuo, H. Takamura, M. Ando, Y. Noda, T. Karahashi, and S. Orimo, *J. Am. Chem. Soc.*, 2009, **131**(3), 894–895. [cited at p. 175]

[140] N. A. Zarkevich and D. D. Johnson, *Phys. Rev. Lett.*, 2008, **100**(4), 040602. [cited at p. 175]

[141] E. M. Fedneva, V. L. Alpatova, and V. I. Mikheeva, *Russ. J. Inorg. Chem.*, 1964, **9**, 826–827. [cited at p. 182]

[142] E. K. Muetterties, R. E. Merrifield, H. C. Miller, W. H. Knoth Jr., and J. R. Downing, *J. Am. Chem. Soc.*, 1962, **84**(13), 2506–2508. [cited at p. 183]

[143] U. Kuhlmann, H. Werheit, T. Lundström, and W. Robers, *J. Phys. Chem. Solids*, 1994, **55**(7), 579–587. [cited at p. 183]

[144] O. Madelung, U. Rössler, and M. Schulz, *Non-Tetrahedrally Bonded Elements and Binary Compounds I*, Vol. 41C of *Landolt-Börnstein - Group III Condensed Matter*, Springer-Verlag, 1998. [cited at p. 183]

[145] R. Juza and K. Opp, *Z. Anorg. Allg. Chem.*, 1951, **266**, 313–324. [cited at p. 184]

[146] H. O'Brien, Private communication. [cited at p. 197]

[147] P. A. Chater, P. A. Anderson, J. W. Prendergast, A. Walton, V. S. J. Mann, D. Book, and W. I. F. David, *J. Alloys Compd.*, 2007, **446-447**, 350–354. [cited at p. 205, 206]

[148] Y. H. Hu and E. Ruckenstein, *J. Phys. Chem. A*, 2003, **107**(46), 9737–9739. [cited at p. 207]

[149] R. L. Lowton, M. O. Jones, W. I. F. David, S. R. Johnson, M. Sommariva, and P. P. Edwards, *J. Mater. Chem.*, 2008, **18**, 2355–2360. [cited at p. 208]

[150] O. Reckeweg and F. J. DiSalvo, *Z. Anorg. Allg. Chem.*, 2001, **627**, 371–377. [cited at p. 210]

[151] U. Herterich, J. Curda, K. Peters, M. Somer, and H. G. Schering, *Z. Kristallogr.*, 1994, **209**(7), 617. [cited at p. 219]

[152] T. Ichikawa, K. Tokoyoda, H. Leng, and H. Fujii, *J. Alloys Compd.*, 2005, **400**(1-2), 245–248. [cited at p. 221]

[153] T. Sichla and H. Jacobs, *Z. Anorg. Allg. Chem.*, 1996, **622**(12), 2079–2082. [cited at p. 227]

[154] S. Hino, T. Ichikawa, H. Leng, and H. Fujii, *J. Alloys Compd.*, 2005, **398**, 62–66. [cited at p. 227]

[155] J. Yang, A. Sudik, D. J. Siegel, D. Halliday, A. Drews, R. O. Carter, C. Wolverton, G. J. Lewis, J. W. A. Sachtler, J. J. Low, S. A. Faheem, D. A. Lesch, and V. Ozolinš, *Angew. Chem. Int. Ed.*, 2008, **47**, 882–887. [cited at p. 229, 230]

[156] A. Sudik, J. Yang, D. Halliday, and C. Wolverton, *J. Phys. Chem. C*, 2008, **112**(11), 4384–4390. [cited at p. 230]

[157] J. Hu, Y. Liu, G. Wu, Z. Xiong, Y. S. Chua, and P. Chen, *Chem. Mater.*, 2008, **20**(13), 4398–4402. [cited at p. 230]

[158] J. Hu, M. Fichtner, and P. Chen, *Chem. Mater.*, 2008, **20**(22), 7089–7094. [cited at p. 230]

[159] A. Sudik, J. Yang, D. J. Siegel, C. Wolverton, R. O. Carter III, and A. R. Drews, *J. Phys. Chem. C*, 2009, **113**(5), 2004–2013. [cited at p. 230]

[160] R. L. Davis and C. H. L. Kennard, *J. Solid State Chem.*, 1985, **59**, 393–396. [cited at p. 234, 236, 245, 246, 252]

[161] A. Zalkin and D. H. Templeton, *J. Phys. Chem.*, 1956, **60**(6), 821–823. [cited at p. 234]

[162] H. Barlage and H. Jacobs, *Z. Anorg. Allg. Chem.*, 1996, **622**, 895–897. [cited at p. 236, 237, 245]

[163] G. Renaudin, S. Gomes, H. Hagemann, L. Keller, and K. Yvon, *J. Alloys Compd.*, 2004, **375**, 98–106. [cited at p. 252, 253, 254]

[164] P. T. Cunningham and V. A. Maroni, *J. Chem. Phys.*, 1972, **57**(4), 1415–1418. [cited at p. 252, 254]

[165] S. Orimo, Y. Nakamori, and A. Züttel, *Mater. Sci. Eng. B-Adv.*, 2004, **108**, 51–53. [cited at p. 256]

[166] J. Evers, M. Münsterkötter, G. O. K. Polborn, and B. Sendlinger, *J. Less-Common Met.*, 1990, **162**(1), 17–22. [cited at p. 261]

[167] R. Juza, *Angew. Chem. Int. Edit.*, 1964, **3**(7), 471–481. [cited at p. 262, 263]

[168] H. Leng, T. Ichikawa, S. Isobe, N. H. S. Hino, and H. Fujii, *J. Alloys Compd.*, 2005, **404-406**, 443–447. [cited at p. 262]

[169] H. Leng, T. Ichikawa, S. Hino, N. Hanada, S. Isobe, and H. Fujii, *J. Power Sources*, 2006, **156**, 166–170. [cited at p. 262]

[170] A. Kersting, Private communication. [cited at p. 263, 265]

List of Symbols and Abbreviations

Abbreviation	Description	Definition
a.u.	arbitrary units	-
DFT	density functional theory	-
DSC	differential scanning calorimetry	page 63
DTA	differential thermal analysis	page 64
ESD	estimated standard deviation	-
ESRF	European Synchrotron Radiation Facility	-
FTIR	fourier transform infrared (spectroscopy)	page 67
ICE	internal combustion engine	page 5
PEM	proton exchange membrane (fuel cell)	page 6
QPA	quantitative phase analysis	page 48
XRD	X-ray diffraction	page 37
XRF	X-ray fluorescence	page 50

List of Figures

List of Tables